Target Shadow Profile Reconstruction in Forward Scatter Radar

Stanislav Zdravkov Hristov

A thesis submitted to
The University of Birmingham
for the degree of
DOCTOR OF PHILOSOPHY

School of Electrical, Electronic and Systems
Engineering
31st March 2017

ABSTRACT

This thesis is dedicated to the matter of imaging (further explained as profile reconstruction) in Forward Scatter Radars (FSR). Firstly, an introduction to radar systems, including forward scatter radar, is made, then an introduction to the scalar theory of diffraction and principles of holography follows. The application of holographic imaging principles in the microwave domain is studied. The practical modelling of forward scatter radar target signals is made, based on the theoretical expectations and approximations outlined. Theoretical background of the imaging in FSR is made, based on previously published work. A novel approach for profile reconstruction is introduced based on the practices of holographic imaging, together with simulated results. Experimental set-ups used in the feasibility proof are described and experimental results are presented for 8 different targets in both a single-node and multistatic configurations. Preliminary accuracy analysis of these reconstructed target profiles is done, outlining practical application issues and domain of accuracy. Quantitative measures of the accuracy of the reconstructed images are defined.

ACKNOWLEDGEMENTS

First and foremost I want to thank Dr. Marina Gashinova and Prof. Mike Cherniakov for giving me the possibility to grasp the exciting world of scientific research, and all their help and guidance along the way. But mostly for their patience during my PhD studies.

Also, I want to thank all the colleagues within the group - Dimitris Tzagkas, Alp Sayin, Alessandro De Luca, to name a few, and Liam Daniel and Edward Hoare, for their help and all the constructive discussions we have had.

And I'd like to thank my mother, my father, my friends for the nice memories and good time during the years of my PhD study.

CONTENTS

LIST OF FIGURES

LIST OF TABLES

LIST OF SYMBOLS

Symbol	*Meaning*
R	range
c	speed of light
t_s	time delay
v	velocity
f_0	transmitted frequency
λ	wavelength
f_d	Doppler shift
β	bistatic angle
P_r	target return at receiver
G_t	gain of transmit antenna
G_r	gain of receiver antenna
P_t	transmit power
σ	RCS of the target
R_t	range transmitter - target
R_r	range receiver-target

t_c	time gap between two present targets
τ	duration of a pulse at the output of the transmitter
τ_{obs}	observational time
ΔR_m	range resolution of monostatic radar
ΔR_b	range resolution of bisatic radar
Δf	bandwidth of the transmitted signal
Δv_m	velocity resolution in monostatic radar
Δf_d^m	Doppler resolution of monostatic radars
Δv_b	velocity resolution in bistatic radar
L_{eff}	effective length of a synthetic aperture antenna
β_b	half-power bandwidth of antenna
δ_α	azimuth linear resolution
D	largest dimension of the aperture
C	contrast of reconstructed target profile in FSR
r	range from a point on a target to receiver
l	length of the target
h	height of the target
E_{sh}	shadow radiation
E_i	incident time-dependent harmonic wave
A	projected shadow contour of the target
d_{max}	largest dimension of the target
E_{sh}^{FF}	shadow radiation in the far field
x'	point of a target in the x'-axis
y'	point of a target in the y'-axis
θ_x	diffraction angle in the x'-axis

θ_y	diffraction angle in the y'-axis
$\sigma_{FS_{max}}$	maximum of FSCS
σ_{mono}	monostatic RCS
(xp, yp, zp)	Cartesian coordinates of the centre of a target
dT	crossing distance, with respect to the transmitter
ϕ	crossing angle
BL	baseline
U_{inc}	incident CW plane wave
A_{inc}	amplitude of the incident CW plane wave
U_{LKG}	leakage signal
U_{Rx}	FSR signal at the receiving antenna
A_{Tg}	amplitude of the forward scattered signal
S_{IQ}	quadrature channel received signal in baseband
S_{RSSI}	quadrature channel received signal in baseband
ω_d	angular Doppler frequency
$L(t)$	sum of time-varying ranges R_Tx and R_Rx
R_{Tx}	range transmitter-target in FSR system
R_{Rx}	range receiver-target in FSR system
x_0	target trajectory starting point in the x-axis
y_0	target trajectory starting point in the y-axis
v_x	component of the target velocity in x-axis
v_y	component of the target velocity in y-axis
$t_{n,k}$	crossing time for the n,k - node
$d_{Tx/Rx}$	distance between Rx/Tx which are next to each other
R	distance between source and detector

a	area of closed surface S
v_s	volume of closed surface S
r_c	radius of a circular aperture
E_{RS}^{I}	solution of the RS integral of first kind
E_{RS}^{II}	solution of the RS integral of second kind
E_{FK}	Fresnel-Kirchoff diffraction integral solution
U_1	field due to presence of opening in opaque space
U_2	field due to presence of a opaque object
$I(x, y)$	intensity of EM field in holography
ψ_{ref}	reference wave, i.e. incident wave
A_{ref}	amplitude of the reference wave
ϕ_{ref}	phase of the reference wave
ψ_{obj}	object wave, i.e. scattered wave
A_{obj}	amplitude of the object wave
ψ_{obj}	phase of the object wave
L_{screen}	length of the receiver screen in holography
M_I	magnification factor in holography
M_II	magnification factor in holography
λ_{ref}	wavelength of reference wave
λ_{obj}	wavelength of object wave
$\mathcal{F}$	Fourier transform
K	propagation kernel
R_h	range of each point on the object to the receiver
x''	transformed x' axis
y''	transformed y' axis

$\Gamma(x, y, z)$ complex amplitude of the object image

$\mathrm{F}^{-1} inverseFouriertransform$

ΔR_{DIH} resolution of the object image in DIH

N number of pixels on the recording screen

Δs size of each screen on the receiver

$S(t)$ complex Doppler signature at baseband in time domain

α_v vertical diffraction angle with respect to transmitter

α_h horizontal diffraction angle with respect to receiver

β_v vertical diffraction angle with respect to receiver

β_h horizontal diffraction angle with respect to receiver

Ω parameter inversely proportional to the local Fresnel radius

r_f local Fresnel radius

H complex profile function

γ term of Doppler phase change information in SISAR modelling

Q amplitude scaling due to the geometry of the system in SISAR imaging

T_{obs} observation time

E_{Rx} complex received signal in time domain at baseband

σ_{FS} Forward scatter cross section

Γ_{TSPR} complex amplitude of the target profile

θ_v angle between the Tx/Rx plane and trajectory of the target

$\Delta R_{L_{1D}}$ resolution of a one dimensional target profile

Z transformed curve through Procrustes analysis

b scale component of the Procrustes linear transformation

T rotation and reflection component of the Procrustes transformation

ϵ translation component of the Procrustes linear transformation

$Y(t)$	the curved subject to Procrustes superimposition
A	curve of size m samples
B	curve of size n samples
L_{NF}	distance target-receiver for the reactive near-field

LIST OF ABBREVIATIONS

Abbrev.	*Meaning*
Radar	RAdio Detection and Ranging
EM	electromagnetic
Tx	transmitter
Rx	receiver
FSR	Forward Scatter Radar
SAR	synthetic aperture radar
ISAR	inverse synthetic aperture radar
SISAR	shadow inverse synthetic aperture radar
ATC	automatic target classification
RHS	radio holographic signal
LoS	line-of-sight
FSCS	forward scatter cross section
SCR	signal-to-clutter ratio
UHF	ultra high frequency
TSPR	target shadow profile reconstruction
RCS	radar cross-section
CW	continuous wave

Rx/Tx transmit-receive system

RSSI received signal strength indicator

MIMO multi-input-multi-output

SNR signal-to-noise ratio

VHF very high frequency

PSD power spectral density

PDF probability density function

FK Fresnel-Kirchoff diffraction theory

DIH Digital in-line holography

FFT Fast Fourier transform

FS Forward scattering

RR Range Rover

RS Rayleigh-Somerfield diffraction theory

CPF complex profile function

STFT short-time Fourier transform

MISO multi-input-single-output

DTW dynamic time warping

SSE sum of squared errors

RMSE root-mean square error

BB Black Box 1.2 GHz single-node FSR transciever

SDR software defined radio

USRP Universal Software Radio Peripheral

UHD USRP Hardware Driver

FPGA Filed-programmable gate array

CHAPTER 1

INTRODUCTION

1.1 Basics of Radar

The presented research is dedicated to moving target profile reconstruction in Forward Scatter Radar (FSR) which is a specific configuration of a bistatic radar, where the bistatic angle is close to π.

Radar (**RA**dio **D**etection **A**nd **R**anging) are systems and sensors, intended for detection of various objects (targets) remotely and estimation of their positions and trajectories by means of electromagnetic waves transmission and reception. More recently new functions of radar have been exploited, namely automatic target classification and recognition which gain the highest priority in the latest radar related research. The important peculiarities of radar compared to visual or acoustic observation are the abilities to:

- Operate in light or darkness over a long range;
- Operate in all weather conditions;
- Extract the target‘s true range and radial speed, as well as spatial coordinates.

Fig. 1.1 shows a simplified radar structure, where electromagnetic (EM) waves (EMW) are transmitted and reflections of these waves from a target are received. The reflected return contains information about the target, which can be extracted in the signal processing stage [6].

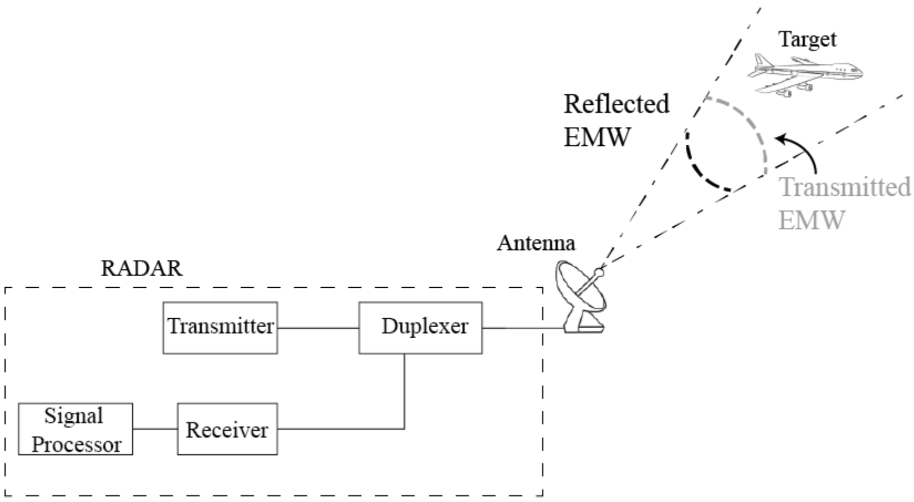

Figure 1.1: A typical radar system

Considering Fig. 1.1, where the target is located within the illumination beam of the radar antenna at some distance away, the time delay between the transmission of the radar signal and receiving the target return, can be expressed as [6, 7]:

$$t_s = \frac{2R}{c}, \tag{1.1}$$

where R is the line-of-sight (LoS) distance between the target and the radar. It must be noted here that this thesis does not consider over-the-horizon radars.

When the target is moving at some velocity, $\mathbf{v}$, relative to the radar, the carrier frequency of the target return will differ from the transmitted signal (carrier) frequency, f_0, with wavelength λ. This difference is described by [6, 7]:

$$f_d = \frac{2v}{\lambda}, \tag{1.2}$$

where f_d is the Doppler shift and v is the velocity component of the target towards the radar, i.e. radial speed. Thus by equation 1.2 the target radial speed can be estimated.

Target angular position, can be estimated by the use of narrow-beam antennas for the transmission and/or reception of the signals [6] [8, Chapter 1].

The operation of radar can be summarized as [8, Chapter 1]:

- EMW are radiated into space by an antenna
- Some of the radiated energy falls on a reflecting object, called a target
- The intercepted energy is re-radiated in many directions
- Some of this re-radiated energy (target echo) is returned towards the radar and received in the receive antenna
- After amplification and signal processing a decision on the presence of a target echo is made and further information for the target, i.e. position, trajectory, etc, is extracted.

The ability of a radar system to detect and measure the parameters of targets is based on three physical phenomena [6]:

- The rectilinear propagation of radio waves in free space at a practically constant speed - speed of light, $c \approx 3 \cdot 10^8$ m/s;
- The ability of objects to scatter electromagnetic waves;
- The Doppler effect.

Radars are used in a variety of applications from long range air traffic control to near field subsurface imaging.

The presence of a target is detected by the radar when the received target echo is larger than that of a pre-set threshold. This threshold must be chosen according to automatic target detection theory [7, Chapter 15] - if it is too low there are going to be too many false alarms, while if it is too high, targets present might not be detected [8, Chapter 1].

Just the detection of targets in modern application of radars is usually not a final goal and other information about the target (kinematics, position and class) is of high interest. Thus radars have evolved to be able to extract information about the target, as well as its presence.

One of the important features of radar is the ability to determine the range to a target by the measurement of the time taken for the EM radar signal to travel to the target and back. To measure range the transmitted wave must have a particular timing mark, which can be a short pulse or frequencym or phase modulation of the signal. The accuracy of the range measurement depends on the the bandwidth of the signal and signal-to-noise ratio at the reception side.

Radial velocity is measured by the rate of change of the range over a period of time or the Doppler shift of the target return. An accurate measurement of the radial velocity requires prolonged observation of the target, which has a physical limit equal to the coherency interval of the reflected signal. Thus this time interval is the basic property describing the quality of the measurement. The speed and trajectory of the target can be obtained from its track, which is obtained by long measurement of the target location, and using signal processing algorithms further target movement can be predicted.

The direction to a target is measured by determining the angle where the target echo is strongest in the case of scanning and the received difference is largest in the case of monopulse. This is usually done by the use of a narrow-beam scanning or tracking antenna, where the beam is shaped as a monopulse or has a special, e.g. conical, scanning pattern.

If the radar has sufficient resolution in range and/or angle it can provide a two dimensional image of the target or scene, such as a portion of the earth's surface, and is referred to as an imaging radar. High range resolution is obtained by the use of large bandwidth of the transmit signal, while high cross-range resolution by the use of very narrow-beam antennas which may be a physical radiation beam over a short range. The beamwidth of an antenna is limited by its electrical size, i.e. the size of the antenna in wavelengths. Further improvement of cross range resolution can be achieved by means of aperture synthesis [8, Chapter 17], briefly introduced in sections 1.3.2 and 1.3.3.

With sufficient resolution in both dimensions, the target shape can be extracted, which is one way for Automatic Target Classification (ATC). ATC is the ability of a system to define the class of a target based on the parameters of the target obtained [9, Chapter 14]. It should be noted here that ATC can be implemented on the basis of both parameters of the target signature and the result of target imaging.

Research interest in ATC is growing to enable the usage of such algorithms in both civil border security, railway and subway safety systems, autonomous vehicles; and defence applications.

A basic radar consists of Transmitter (Tx) and Receiver (Rx), antennas and a signal processor. Radar classification can be based on topology: monostatic (MR), bistatic (BR) and forward scatter radars (FSR), where Fig. 1.2 shows these three main types.

Monostatic radar, which represents the majority of radars, (Fig. 1.2(a)) is a type of radar, where the transmitter and receiver are co-located, while bistatic radars (Fig. 1.2(b)) consist of transmitter and receiver which are separated by a considerable distance, comparable with the distance to the target [8, Chapter 23] [7].

This thesis is dedicated to a special case of bistatic radar, where the bistatic angle, β is close

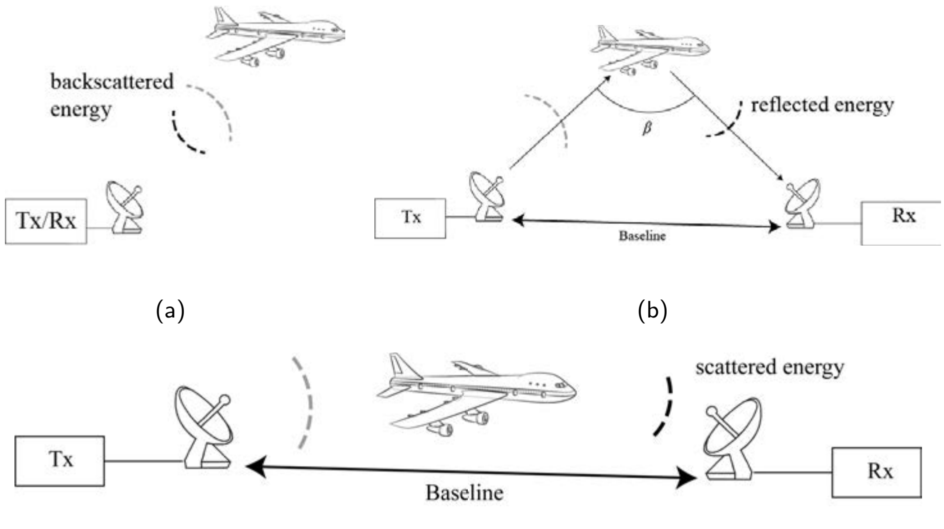

(a) (b)

(c)

Figure 1.2: Radar classification by topology: monostatic (a), bistatic (b) and forward scatter (c) radar systems.

or equal to π and the target dimensions are larger than the wavelength [6]. This system is called a Forward Scatter Radar and target returns are described by shadowing of the Direct Path (DPS) or Leakage signal (LS), rather than back scattering. FSR properties have been discussed in [3, 6, 10] and its main peculiarities are going to be discussed in section 2.

1.2 Topology of bistatic radar systems

In this section the basic properties identifying a bistatic radar system are going to be presented.

A bistatic radar topology (Fig. 1.2(b)) is most commonly represented in the so called north-referenced coordinate system [6], shown in Fig. 1.3.

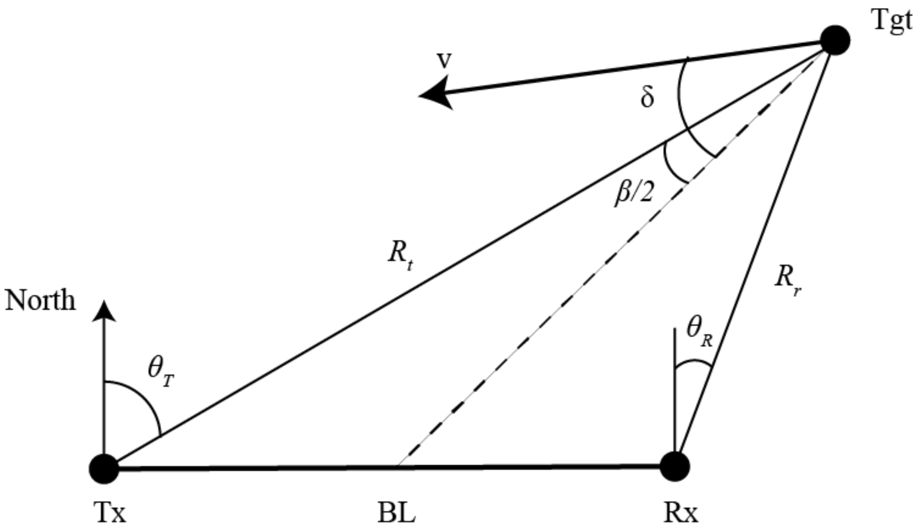

Figure 1.3: 2D Bistatic radar geometry in a north-referenced coordinate system

The look angle, θ_T, of the transmitter and the look angle, θ_R, of the receiver are defined as the clockwise angle between the north and the direction of the ranges R_t and R_r, respectively. The bistatic angle, β, is the angle given by the relationship $\beta = \theta_T - \theta_R$, and can be within the interval of $-\pi$ to π. The plane Tx-Tgt-Rx is referred to as the bistatic plane. In case of $\beta = \pi$ the geometry is referred as forward scatter, while in the case of $\beta = 0$, the configuration is known as monostatic. The baseline, BL, is the line-of-sight separation between the transmitter and receiver.

From Fig. 1.3, a simple relationship between the range change and the target velocity can be made, where the only assumptions are that the transmitter and receiver are stationary. Considering the target to be north of the baseline, as in Fig. 1.3 [6]:

$$\begin{aligned}\frac{\mathrm{d}}{\mathrm{d}t}R_t &= \mathbf{v}\cos(\delta - \beta/2)\\ \frac{\mathrm{d}}{\mathrm{d}t}R_r &= \mathbf{v}\cos(\delta + \beta/2),\end{aligned} \tag{1.3}$$

where δ is the angle between the target velocity, $\mathbf{v}$, and the bistatic bisector, measured clockwise. Thus the time-varying range sum is given by [6]:

$$\frac{\mathrm{d}}{\mathrm{d}t}R_t + \frac{\mathrm{d}}{\mathrm{d}t}R_r = 2v_b \cos\left(\frac{\beta}{2}\right), \tag{1.4}$$

where v_b is the projection of the target velocity in the direction of the bistatic bisector and is given by: $v_b = v\cos(\delta)$.

Equations 1.3 and 1.4 define the relationships between the target motion and the two bistatic ranges, and equation 1.4 will be used further to derive the Doppler resolution and the Doppler frequency in bistatic and forward scatter radar.

1.2.1 The radar equation for bistatic radar

The radar range equation represents the fundamental relationship between the radar parameters, the target and the transmitted and received signal [8, Chapter 23], [6]. The target return power at the receiver, P_r, is given by:

$$P_r = \frac{P_t G_t G_r \lambda^2 \sigma_\beta}{(4\pi)^3 R_t^2 R_r^2 L_{PT} L_{RT} L_o}, \tag{1.5}$$

where G_t and G_r are the gains of the transmit and receive antennas, P_t is transmit average power, σ_β is the target bistatic Radar Cross Section (RCS), and R_t and R_r are the ranges target-transmitter and target-receiver, respectively and L_{PT} and L_{PR} are losses that appear during wave propagation in the area transmitter-target and target-receiver, respectively. L_o are general unaccounted losses.

It is important to stress here that the bistatic RCS, σ_β, is different from the monostatic RCS and essentially depends on the bistatic angle and target geometry.

Also, it should be noted that the received power, P_r, in bistatic radar is dependent on particular bistatic ranges, where the minimum of the received power for a particular system and target is when $R_t = R_r$.

Using the bistatic radar equation the signal-to-noise ratio (SNR) can be estimated. An extensively used form of constant SNR range sums are the Ovals of Cassini. Such ovals are seen in Fig. 1.4 for different SNR values ranging from 0 to 15 dB.

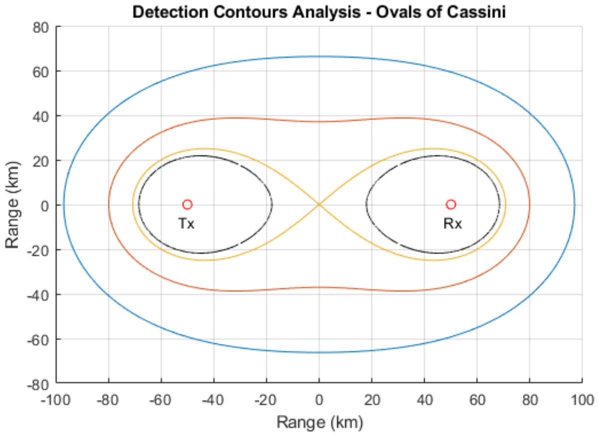

Figure 1.4: Ovals of Cassini for a reference bistatic radar system for constant SNR values of 0, 5, 10 and 15 dB.

The power budget of a radar system is an important consideration, as well as its resolution in range, angle and velocity, discussed further.

1.2.2 Resolution in Bistatic Radar

The resolution of a radar system corresponds to its ability to detect and measure the properties of two closely positioned targets, of similar RCS, separately [6]. Resolution is defined in range, angle (space) and velocity (Doppler) and each will be briefly discussed below.

1.2.2.1 Range resolution

In bistatic radars, the range resolution (also called width of a bistatic range cell) is defined as the separation, ΔR_b, between two confocal concentric isorange (or isophase) contours in the direction of the bistatic bisector, as shown in Fig. 1.5.

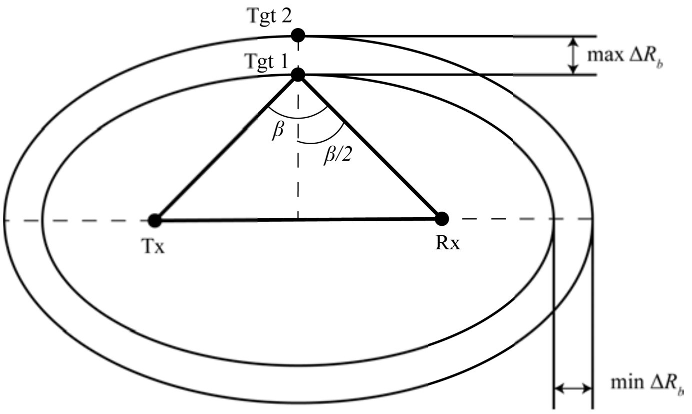

Figure 1.5: Bistatic range cells

The bistatic range resolution is given by [6]:

$$\Delta R_b = \frac{c}{2\Delta f \cos(\beta/2)}, \tag{1.6}$$

where Δf is the bandwidth of the transmitted signal. The direction of the bistatic range resolution is referred along the bisector of the bistatic angle.

The bistatic range resolution degrades by $\cos(\beta/2)$ in comparison with monostatic radar. In the quasi-monostatic case the range resolution is maximum, while in forward scatter geometry, there is no range resolution, i.e. it is known that target is between transmitter and receiver, but not where along the baseline, though indication of the range can be done by signal processing [11–13].

1.2.2.2 Doppler resolution

Doppler separation between two targets which are in the same range cell and of similar amplitude, but having different speed and is taken to be inversely proportional to the coherent processing time, τ. It is important to mention here that τ itself is restricted by the coherency interval of the target return.

In the case of bistatic radar, from equation 1.4, the minimum required difference between the velocities of two targets for sufficient Doppler resolution is given by [6]:

$$\Delta v_b = \frac{\lambda}{2\tau \cos(\beta/2)}, \tag{1.7}$$

where Δv_b is the minimum separation between the two velocity vectors projected on the bistatic bisector to enable separate Doppler estimation for the two targets.

Again as for the range resolution, the Doppler resolution degrades as the target approaches the baseline and $\beta \to \pi$, and there is complete loss of resolution and, in fact, Doppler information at the baseline.

1.2.2.3 Angular resolution

The accuracy of measurement of the angular position of a target is a function of the directivity of the two antennas. In BR these are generally designed so that the transmit antenna beamwidth is larger than that of the receiver antenna to avoid pulse chasing problem [14], thus it is not taken into account for the calculation of the angular resolution [6].

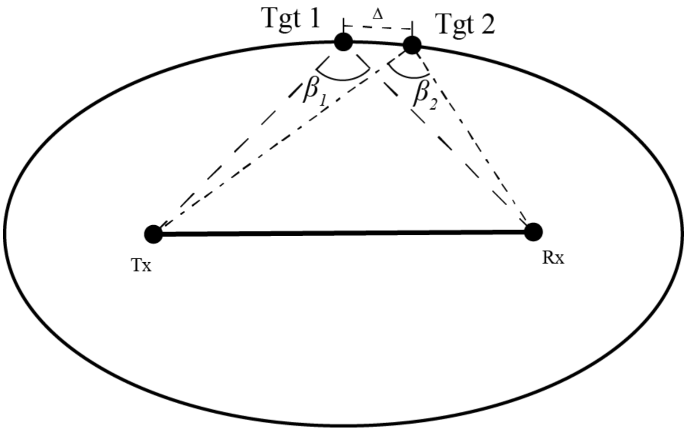

Figure 1.6: Geometry for angle resolution in bistatic radar

In bistatic radar in order to achieve cross range separation of $R_r\Delta\theta_R$, two targets, lying on the same isophase contour, must be physically separated by a distance Δ [6], as shown in Fig. 1.6:

$$\Delta = \frac{R_r\Delta\theta_R}{\cos(\beta/2)}, \tag{1.8}$$

where $\Delta\theta_R$ is the 3-dB beamwidth of the receive antenna and all angular parameters are given in radians.

In bistatic radar the resolution depends on the bistatic angle, β, and is less than that of the monostatic radar. From the discussion above it follows that with an increase of the bistatic angle, the resolution decreases, while in the particular case of FSR the resolution tends to 0.

1.3 Radar Imaging

Radar imaging is the process of high-resolution estimation of the electromagnetic radiation scattered towards the radar receiver from stationary or moving objects. This application of radar generates a spatial image of a target or observational area in one or two dimensions, which can be any combination of range, cross-range and Doppler of the target [9].

In this section the basic principles of high resolution real time radars and synthetic aperture radars, will be introduced.

1.3.1 Real Aperture Radar

The size and shape of the target are two of the fundamental ways for recognizing one type of a target from another [8, Chapter 1]. A high resolution radar can obtain the profile of a target or observation area in both range and cross range and thus provide target classification capability. Such high resolution systems will operate with large ranging signal bandwidth for high range resolution and narrow beam antennas for high angular resolution, according to the corresponding relationships shown in section 1.2.2.

Systems which operate with a narrow physical antenna beam can image an area in real time, and are called real aperture radars (RAR). The utilization of such system is challenging due to the large electrical size of antennas needed, but still operating over a rather short range.

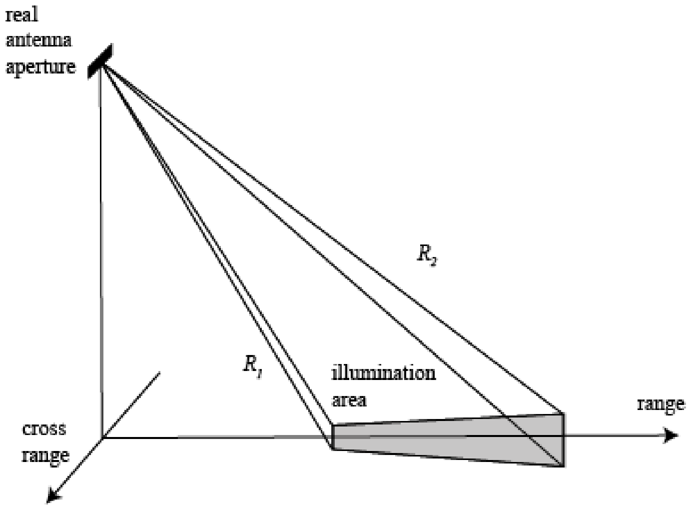

Figure 1.7: Side-looking airborne RAR

Considering a quasi-monostatic case ($\beta = 0$), from equation 1.8 and considering the antenna beamwidth, $\Delta\theta_R$ to be given by:

$$\Delta\theta_R \cong \lambda/D[rad], \tag{1.9}$$

where D is the antenna aperture size, thus cross-range resolution is given by:

$$\delta_{cr} \approx \frac{R\lambda}{D}, \tag{1.10}$$

where R is the range to the target. From equations 1.10 and 1.9 it can be shown that for an antenna of 0.5 degrees two-way beamwidth (this is referred as a narrow-beam antenna), cross-range resolution of 0.5 m, can be achieved at range of ≤ 60 meters. It follows that such systems can operate only at short ranges. For a target located 10 km away from the aperture for radar with $\lambda = 0.01$ m, the antenna aperture has to have length of 200 m, having a beamwidth of 0.00005 rad. Such antenna sizes and their manufacturing tolerances are impractical for most radar applications but could be used in radio astronomy, while a range resolution of 0.5 m would require, a technically achievable, signal bandwidth of 300

MHz, according to equation 1.6, which, though, could be restricted by spectrum allocation regulations.

1.3.2 Synthetic Aperture Radar

The need of large antenna aperture for small cross range resolution has given rise to research into Synthetic Aperture Radars (SAR). In SAR a large antenna aperture is synthesised due to the radar motion. So synthetic aperture could be formed in a radar where at least one end, transmitter or receiver, is moving [8, Chapter 17], as it is schematically shown in Fig. 1.8. The processing required to achieve the fine resolution of SAR, includes adjustments of the phases of the received signals at each point of the synthetic aperture antenna, in order to make these signals of equal phase for each target [8, Chapter 17].

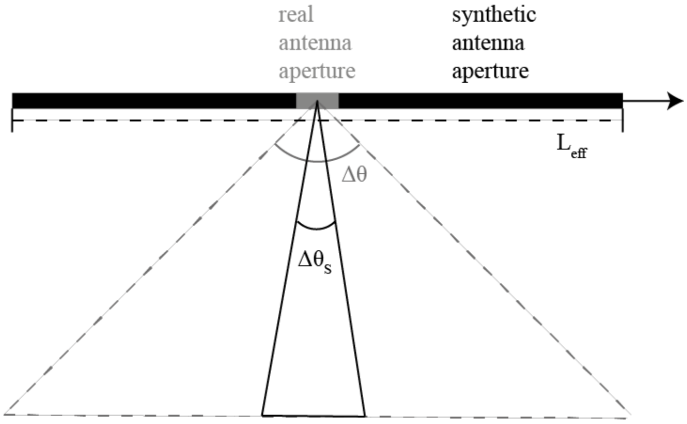

Figure 1.8: Illustration of the difference between real antenna aperture beamwidth, $\Delta\theta$, and synthetic aperture beamwidth, $\Delta\theta_S$

The potentially achievable cross range resolution in stripmap monostatic SAR, with physical aperture of effective length, L_{eff}, is about half of the physical antenna size:

$$\delta_{cr} \approx \frac{\lambda}{2\Delta\Theta} \approx \frac{L_{eff}}{2} \tag{1.11}$$

and could be further enhanced in a spotlight or circular trajectory mode. Resolution of modern airborne SAR is about 0.3x0.3 m [15] and for space-borne SAR is 4x4 m or less [16]. Stripmap SAR is defined as a mode where the radar antenna is fixed in a direction broadside to the platform track, where spotlight SAR is a mode in which the antenna is steered to a particular target.

Thus it follows that using the motion of a platform, sub-meter cross-range resolution can be achieved at large ranges, with particular feasible antenna apertures.

1.3.3 Inverse SAR

A stationary radar and a moving target, till some extent, may be considered as equivalent to a moving radar and a stationary target. Generally, for a case such that most of the motion in target-centred coordinates is caused by the rotation of the target, the term Inverse Synthetic Aperture Radar (ISAR) is used [17, Chapter 6].

As an example a scattering point on a turntable, rotating with angular velocity, Ω, the centre of which is at the origin, is considered. The scattering point has polar coordinates r, φ relative to the centre of the turntable, as shown in Fig. 1.9(a). The rotational speed of the point is $r\Omega$, while the line-of-sight velocity in the x-axis, v_{LOS}, is $-r\Omega\sin\varphi = -y\Omega$. Thus this speed is proportional to the cross-range coordinate y and independent of the range coordinate, x.

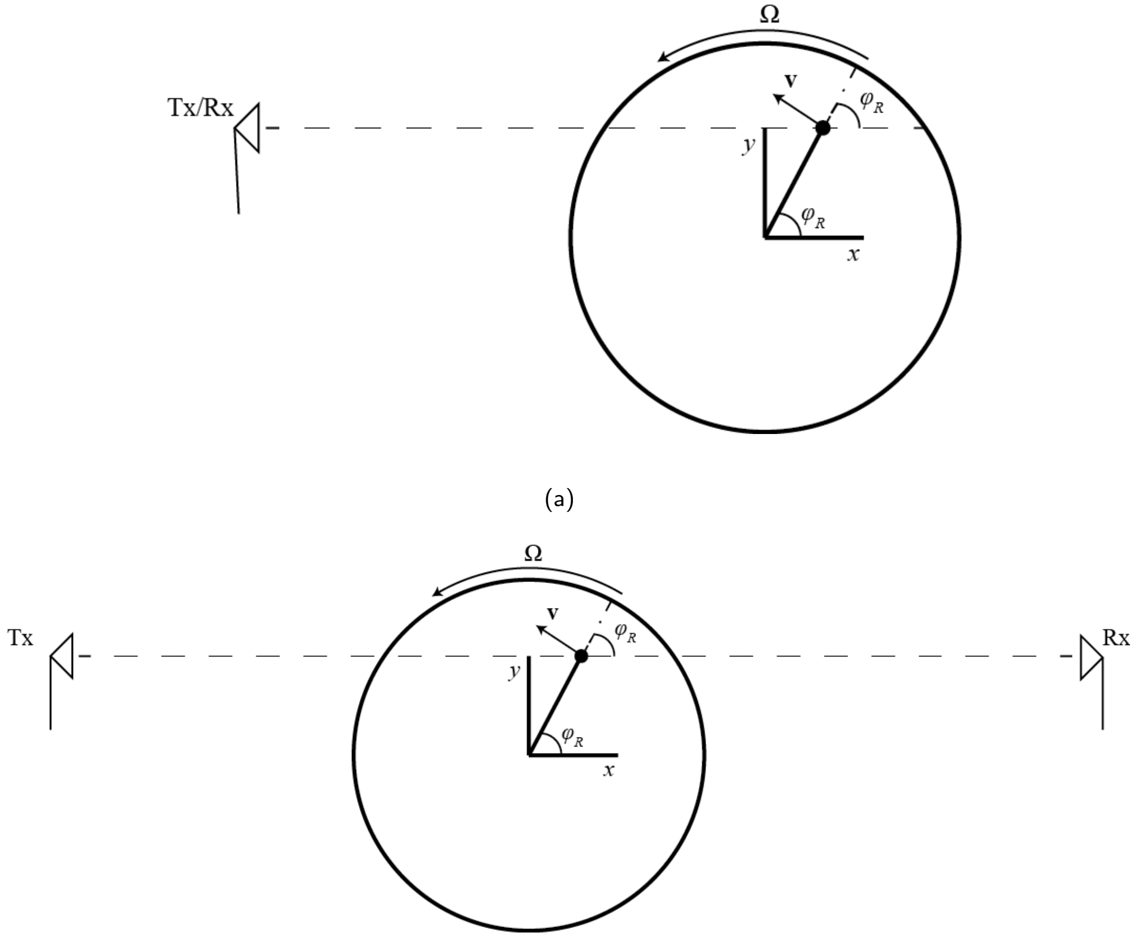

(a)

(b)

Figure 1.9: Target on a turntable in the far - field of (a) a monostatic radar, and (b) forward scatter radar.

If range-Doppler processing is then applied to the recorded signal from the rotating target whose rotating axis is perpendicular to the LOS, then the velocity coordinate can be interpreted as the cross-range resolution, δ_{cr}, given by equation 1.12. The result can, therefore, be regarded as the two-dimensional image of the target in range-cross-range domain, where the range resolution is be given by equation 1.6 (for $\beta = 0$) and the cross-range by:

$$\delta_{cr} = \frac{\lambda}{2\Delta\varphi} = \frac{\lambda}{2\Omega\tau}, \tag{1.12}$$

where $\Delta\varphi$ is the total rotational angle during the coherent observational time, τ, and Ω is the rotation speed. In the derivation of equation 1.12 it is assumed that $\Delta\varphi \ll \pi/2$, thus y being practically constant during the target observation [17, Chapter 6].

Let's assume an example, where an aircraft is rotating with an angular speed of $\Omega = 1deg/s$, relative to the radar, and has coherent integration interval of $0.5s$. Considering a radar system operating at 3 GHz (0.1 m wavelength) centre frequency and 300 MHz bandwidth, then the cross-range resolution will be:

$$\delta_{cr} = \frac{0.1}{2 \cdot 0.0175 \cdot 0.5} = 5.7m, \tag{1.13}$$

while the range resolution will be 0.5 m. Thus an image of the target can be produced with a resolution of $\propto$ 0.5 x 5.7 m.

In practice, though, that assumption will limit the coherent observation time. This is due to fluctuations of the target in range, when the total rotation angle is large, thus limiting the cross-range resolution. ISAR systems have, thus been developed with very fine range resolution (high bandwidth), to reduce the influence of range migration of rotating scattering points.

This thesis is mostly concerned with FSR and it is important to understand if ISAR is applicable to FSR, where a FS ISAR configuration for a turn-table experiment is pictorially shown in Fig. 1.9(b). But prior to this the fundamentals behind FSR will be introduced in the next section.

1.4 Aim and problem setting of the thesis

Automatic target recognition and classification is widely used in modern radar systems. Generally, such classification algorithms rely on high resolution radar images to distinguish between different targets. Forward scatter radars are known to have excellent cross-range resolution through the use of long coherent integration time as in FSR, there is fundamentally absence of range resolution [6], thus the received signals are not fluctuating as all components of the scattered EM radiation arrive at the receiver in phase. The absence of range resolution though, renders known methods for improving the resolution such as SAR, not applicable.

It is well known in literature, that the absence of range resolution ultimately allows for a target which is in the far field of both Tx and Rx to be approximated as infinitely thin and flat, due to the Physical Theory of Diffraction (PTD) [18], as discussed in Chapter 4 [19]. Using this approximation, in [1], it is shown how the FSR target signature can be mathematically described by the Physical Theory of Diffraction. This formulation is known as Shadow Inverse Synthetic Aperture Radar (SISAR). Such representation allow for the received signal to be defined in terms of the shape of the target silhouette, so that the reverse process can be performed, i.e. representation of the target silhouette by the FSR target signature. However, only a very small amount of work has been published on that topic since the introduction of SISAR. Also, no accuracy analysis of the target images has been published so far to the best knowledge of the author.

This thesis develops and investigates a novel approach to a cross-range imaging in FSR, with both modelled and experimental proof-of-concept results, which can enable the use of classification algorithms in FSR systems. The imaging method is developed based on digital holographic reconstruction, rather than theoretical diffraction methods. Also, a preliminary qualitative and quantitative accuracy analysis on the results is performed, based on comparison between target shadow and reconstructed image. The accuracy analysis was extended to take into account errors which can influence that accuracy.

1.5 Thesis outline

This thesis consists of 8 chapters.

Chapter 1 introduces common radar concepts such as range, Doppler and angle resolution, as well as, currently used methods for target imaging, such as SAR and ISAR.

Chapter 2 contains an introduction to FSR. Typical topology of the system is presented, together with brief outline of the signal formation mechanism.

Chapter 3 is concerned with the principles of diffraction and holography in the context of the thesis. Scalar theory of diffraction is briefly presented and relevant assumptions outlined. Holography is developed in this chapter and its application to FSR is discussed.

Chapter 4 presents FSR signal modelling approaches. It starts off with development of the signal model for a point-like target and extends that for extended and geometrically complex target. An approach for signal modelling based on numerical modelling of diffraction has been developed by the author in this chapter. For completeness, 2D target signal modelling in elevation and azimuth is outlined.

Chapter 5 consists of the theoretical background of imaging in FSR. An overview of the currently proposed method is presented and results are shown. Further, the novel approach proposed by the author is developed and initial simulated results are shown for both 1D and 2D cases. The properties of the reconstructed images are outlined.

Chapter 6 concerns the experimental validation of the proposed imaging method. The hardware used for the experimental validation is presented and the scenarios measured are shown. Experimental results are compared with simulated images and show good correspondence with the targets tested.

Chapter 7 consists of the accuracy analysis of the reconstructed target images. Firstly, a qualitative and quantitative measure for the accuracy of the images is done, further the influence of the error on the estimated trajectory on the target image is analysed. Auto-focusing technique is outlined based on the trajectory error analysis. The chapter also includes the estimated domain of applicability of the approach suggested by the author. To the authors best knowledge such analysis has never been performed on FSR target images before.

Chapter 8 contains the conclusions and further work proposed by the author.

CHAPTER 2

FUNDAMENTALS OF FSR

2.1 Introduction

This chapter discuses the fundamentals of FSR and the forward scatter target signals.

Forward scatter radar, as discussed in the previous section, is a particular case of bistatic radar, where the bistatic angle is close to π. The mechanism of scattering and signal reception is different than in the case of mono- and bistatic radars. It is not based on scattering off individual points on the target surface, but rather the signal is produced coherently by the whole geometrical shadow of the target, projected in the plane of movement with respect to the baseline [2].

A typical radar return can be described by two parameters - the RCS of the target and its motion. If in traditional radar the target return is characterized by the radar cross section, in FSR an equivalent role has Forward Scatter Cross Section (FSCS). The physical model behind FSCS and, thus, the target signature is different than that for the other types of radar.

The FSCS is governed by the diffraction of the incident EMW by the target's shadow, while the target's motion will introduce a Doppler-dependent phase variation, specified by the path length difference between the leakage signal and the forward scattered signal [6]. The leakage signal is defined as the strong direct path signal between the transmitter and receiver in the absence of a target on the baseline. [10]

2.2 Topology of FSR

Let us use the topology and corresponding coordinate system, shown in Fig. 2.1, for the FSR case.

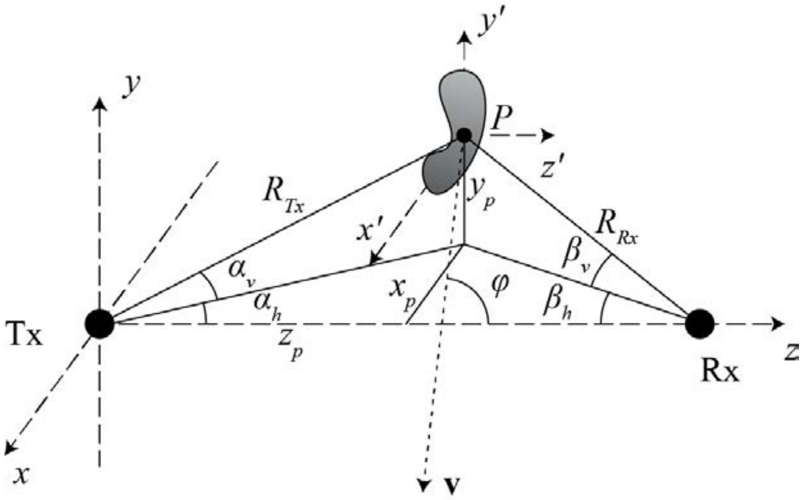

Figure 2.1: A typical FSR topology [1]. LH coordinate system is used as a convention to represent the target shadow in an x-y coordinate system where y-axis is the vertical (height) of the target.

The transmitter, Tx, is located at the origin of a coordinate system, x, y, z, and the receiver, Rx, position is $(BL, 0, 0)$, BL denoting the length of the baseline. A local coordinate system, x', y', z', with origin the geometric centre of the target, P, is parallel to the global coordinate system of the Tx and Rx and is positioned at x_p, y_p, z_p.

The distances from the centre of the target to the transmitter and receiver is denoted by

R_{Tx} and R_{Rx}, respectively. The horizontal diffraction angles are denoted by α_h and β_h, with respect to transmitter and receiver, while the vertical diffraction angles are denoted by - α_v and β_v.

The target is assumed to move in the x, z plane, i.e. no vertical motion, with velocity vector $\mathbf{v}$, intersecting the baseline at angle φ. This assumption applies to surface moving targets, which is the main research topic of this thesis.

This coordinate system will be used further in the text.

As mentioned above, the FSR signal is governed by the shadowing effect, which is discussed next in the context of FSR, according to the presented topology.

2.3 Shadowing effect: stationary target

Fig. 2.2 shows an example of a set-up to observe the shadowing effect by a stationary target.

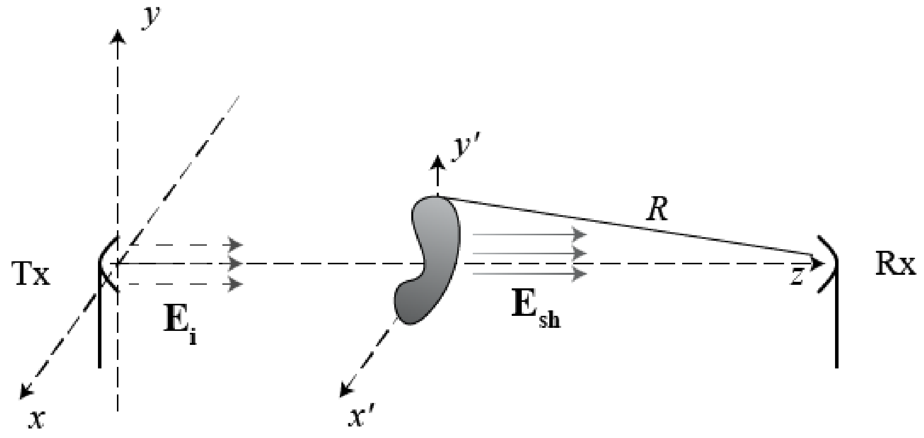

Figure 2.2: Geometry of measuring of shadow radiation by an object sitting on the baseline, between transmitter and receiver.

The shadow radiation, $\mathbf{E_{sh}}$, will be represented as the reduction of the leakage radiation, i.e. the signal, $\mathbf{E_i}$ received in an absence of a target in the vicinity of the baseline [20]. Thus, the received EM field strength at the detection point, according to Fig. 2.2, will be given by:

$$\mathbf{E_{Rx}} = \mathbf{E_i} + \mathbf{E_{sh}}, \tag{2.1}$$

where in [2] it is be shown that $|E_{sh}| \sim -|E_i|$ in the vicinity of the scattering object, which is referred to as a full shadow.

Further, according to Babinet's principle [21], the shadow radiation from an opaque object will have a phase which is 90 degrees shifted, when compared with the incident radiation. This applies to the scalar theory of diffraction and will be shown in section 3.1.6. In terms of amplitude then, equation 2.1 will be:

$$|E_{Rx}| = |E_i| - |E_{sh}|. \tag{2.2}$$

So due to the shadowing effect, the signals received in FSR are defined as a reduction of a constant leakage (further denoted as U_{LKG}), rather than the induction of a signal, as in traditional radars. So a compulsory element of FSR is the presence of direct signal at the receiver in the absence of target.

The Physical Optics approximation delivers an accurate description of the shadow radiation in the Far-Field of the opaque body, E_{sh}^{FF}, derived on the basis of Kirchhoff-Fresnel diffraction (see section 3.1.3) given by [2]:

$$E_{sh}^{FF} = \frac{i}{\lambda} \iint_A E_i \frac{\exp(-ikr)}{r} \mathrm{d}S, \tag{2.3}$$

where all terms have their usual meanings and $\mathbf{E_i}$ is the incident wave on the target, and A

is the area of the projected shadow contour (or silhouette) of the object on the observable plane integrated over the whole area of the target, d**S** is an infinitesimally small area of the target total surface and **r** is the range from that small area to the receiver.

The shadow radiation does not depend on the material of the shadowing object, assuming that it is not transparent to EMW, and is completely determined by the size and the geometry of the projected contour of the object, perpendicular to the observation axis, as shown in Fig. 2.3 [2]. This approximation in a strict sense can only be valid if the target is considered as an absolute black body, which is still valid for the general radar target, i.e. vehicles, people and animals.

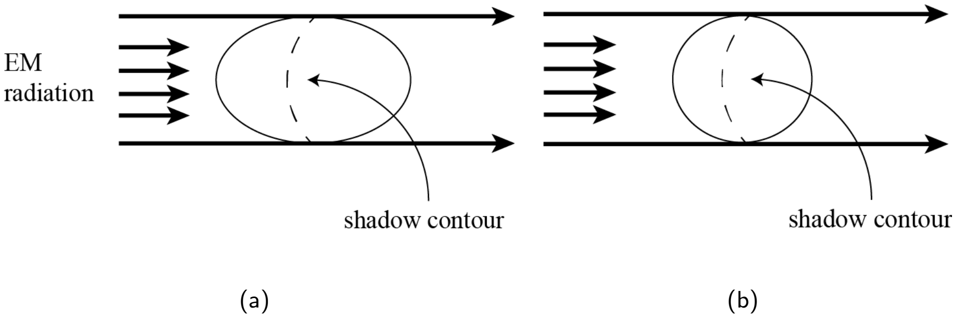

(a) (b)

Figure 2.3: Two different objects, which will yield the same shadow contour line. Directly from [2]

Another advantage of FSR over MR and BR is the increase of the FSCS with respect to the RCS of a target. This is mainly due to the fact that the FSR received signal is not affected by the scattering coefficients of the target and its shape and thus stealth coating or geometry do not reduce the FSCS. An example is shown for a sphere target of 2 m radius at 2 GHz incident CW, in Fig. 2.4. As it follows from the figure the increase of FSCS (49.5 dBm^2) in comparison with MR and BR (10 dBm^2) is 39 dBm^2.

It is important to recall the definition of near- and far-field here, before further developing the theory. Near-field in EM is defined as the region in which an emitted EM field is less

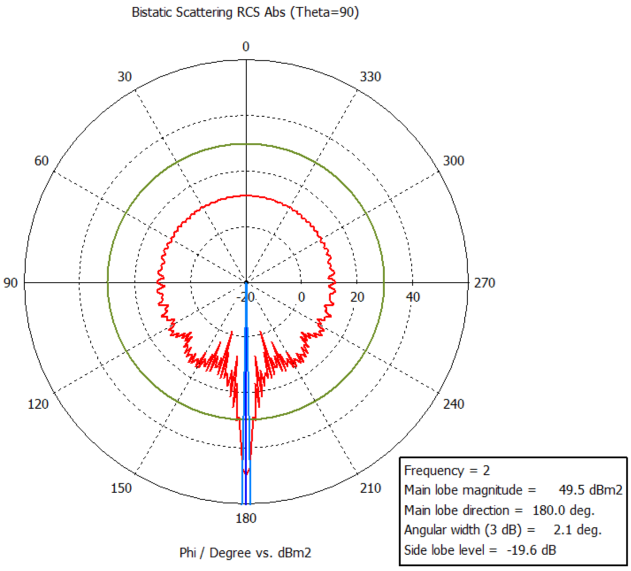

Figure 2.4: CST simulation of bistatic RCS, in dBm^2, at 2 GHz plane incident wave, in the horizontal plane, where 0 degrees is incidence direction.

than the Fraunhofer distance, $< 2R^2/\lambda$. In this region the field is acting as a combination of multipole type fields, with some phase difference between them, rather than a single-phased field.

If it can be considered that the target aperture (or silhouette) is a point-like target and in the far-field of both illuminator and receiver, i.e. observation point, then:

- $r = z + \frac{(x-x')^2+(y-y')^2}{2z}$, where x, y, z are the coordinates in the global coordinate system and x', y' are the local coordinates of the target
- E_i can be approximated as uniform across the area of the target shadow contour and
- it can be assumed that $\mathbf{r}$ is not going to significantly change over the area of that contour and
- the ranges Tx to target and target to Rx are much bigger than the largest target

dimension.

Due to the small size of the target, the $(x-x')^2+(y-y')^2$ term becomes small, going to 0, and $r=z$. Thus, both the oscillatory term, $\exp(-ik\mathbf{r})/\mathbf{r}$, and $\mathbf{E_i}$ can be considered to be constant and taken out of the integral, thus equation 2.3, can be rearranged:

$$\mathbf{E_{sh}^{FF}} = \frac{i}{\lambda}\mathbf{E_i}\frac{\exp(-ik\mathbf{r})}{\mathbf{r}}\iint_A \mathrm{d}\mathbf{S}, \tag{2.4}$$

so after integrating the area of the aperture, $\iint_A \mathrm{d}\mathbf{S} = A$, where A is the area of the aperture, projected in the direction of $\mathbf{r}$, i.e. the target silhouette:

$$\mathbf{E_{sh}^{FF}} = \frac{i}{\lambda}\mathbf{E_i}\frac{A\exp(-ik\mathbf{r})}{\mathbf{r}}. \tag{2.5}$$

If equation 2.5 is combined with equation 2.2, considering the incident wave to have a $1/r$ amplitude dependence, then an expression for the received radiation strength can be presented as:

$$\begin{aligned}|E_{Rx}| &= |E_i| - |E_{sh}^{FF}| \\ &= |U/\mathbf{r}\exp(ik\mathbf{r})| - |\frac{i}{\lambda}\mathbf{E_i}\frac{A\exp(-ik\mathbf{r})}{\mathbf{r}}| \\ &= \frac{U}{r} - \frac{iUA}{\lambda r^2} = \frac{U}{r}\left(1-\frac{iA}{\lambda r}\right) \\ &\propto |E_i|\left(1-\frac{A}{\lambda r}\right),\end{aligned} \tag{2.6}$$

where U is the amplitude of the radiation at the transmit antenna, omitting the oscillating factor, $\exp(-ik\mathbf{r})$, due to the fact that the modulus of a complex exponential equals 1. It should be noted that the mathematical description in equation 2.3 and 2.6 is only accurate within the far-field of the object, due to the assumptions used for its derivation. A further requirement for the far-field assumptions will be that $A/r \ll 1$. Under these approximations, it can be assumed that the vectors $\mathbf{r}$, $\mathbf{E_i}$ and $\mathbf{E_{sh}^{FF}}$ are going to be oriented in nearly the same direction along the z-axis, thus reducing the vector problem to a scalar one.

As an example to specify the far-field boundary, let us consider a FSR operating at frequency of 1 GHz, observing a target like a typical car of 4 m length. The far-field boundary assuming that phase difference along the target, $\Delta\varphi_{FF}$, is less than $1/12\lambda$, occurs at distance of 80 m.

So $\mathbf{E_i}$ represents the leakage signal in the receiver, while the shadowing, $\mathbf{E_{sh}^{FF}}$ represents the reduction of that leakage. If an aperture (or a target in the case of an FSR) of a finite size is situated on the baseline, some distance in the far-field from the receiver, then the shadow radiation and the received signal can be calculated via equations 2.5 and 2.6. Considering an example as illustrated in Fig. 2.5(a), where an object with aperture of area 2 m^2, a rectangle of size 2 x 1 m, is situated on the baseline, 15 m from the transmitter and illuminated by a EM wave with amplitude of 1 V/m at 1 GHz frequency. It shows both the amplitude of the unobstructed and obstructed received waves, where the difference between the two (shown in Fig. 2.5(b)), represents the signal difference, which in fact is used for target detection. It is clear that as the range increases, the shadow radiation component in $\mathbf{E_{Rx}}$, becomes smaller. The difference between the amplitudes of those two waves in absolute units, for the example considered, is shown in Fig. 2.5(b), while in Fig. 2.5(c) - in dB. From Fig. 2.5(c) it can be seen that for the particular case the power of the received signal might be in the order of -30 dB, or even less in the case of smaller targets and lower frequency (thus longer wavelength) of the incident radiation.

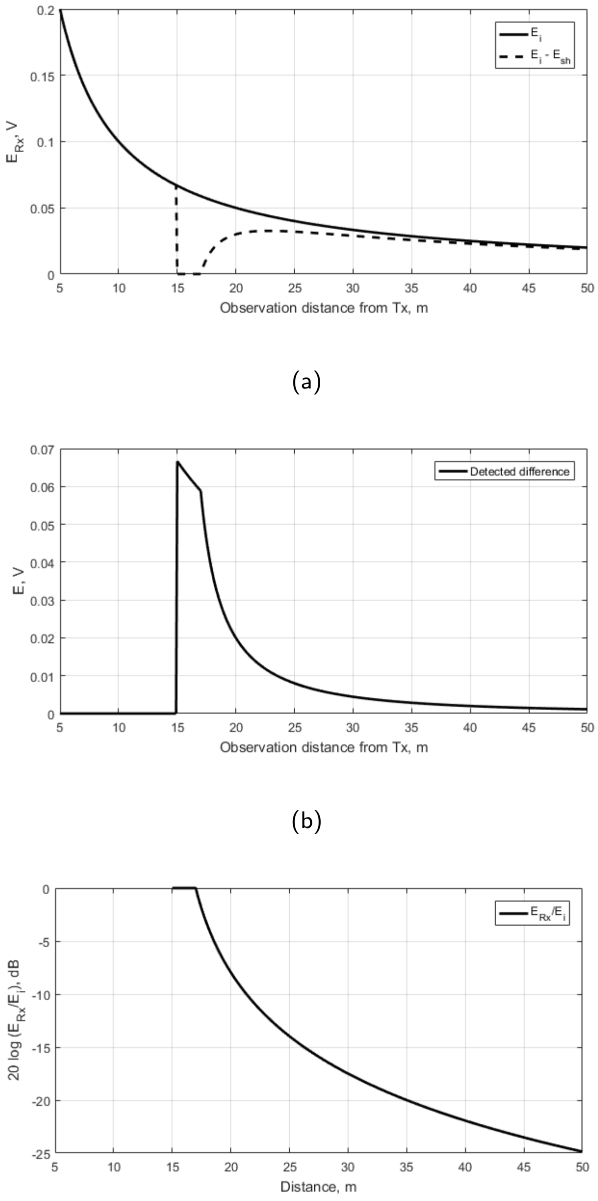

(a)

(b)

(c)

Figure 2.5: E_i and E_{Rx} calculated using equation 2.6 for an aperture with area of 2 m^2, situated 15 m from the transmitter - (a), and difference of the unobstructed E_i and the shadow radiation, representing the signal used for detection purposes in FSR - in absolute units - (b), and in dB (c). Results are calculated via equation 2.6

From Fig. 2.5(a), it can be seen that in the near-field, where r is smaller than the target dimension, there is a full shadow and the received signal E_{Rx} tends zero, where the difference between the amplitudes of the unobstructed and obstructed received waves is biggest, as seen in Fig. 2.5(b). However, in reality such darkness does not exist. This effect seen in Fig 2.5(b) is due to the fact that the near-field amplitude is calculated by equations derived for far-field assumption.

Further away from the object, the received radiation can be calculated according to equation 2.1, where the reduction from the leakage signal, shown in Fig. 2.5(b), can be used for detection purposes.

However, as said above there is a shadow signal in the near-field, which needs to be accounted for. Presence of such a near-field signal is going to be discussed below for the same parameters as the example above. For distances comparable or smaller than the largest dimension of the aperture, equation 2.3 can be approximated by the Fresnel-Kirchoff diffraction integral, equation 3.4, as suggested in [20], and is defined as follows.

If a target lying on the baseline, as shown in Fig. 2.2, can be represented in a Cartesian coordinate system, x', y', which is parallel to a x, y, z coordinate system, the origin of which is at the source of illumination, then the shadow radiation, $\mathbf{E_{sh}^{FF}}$, is given by [20]:

$$\mathbf{E_{sh}^{FF}} \cong \frac{-i\mathbf{E_i}}{\lambda} \frac{\exp(-ik\mathbf{r})}{\mathbf{r}} \iint_A \exp\left(\frac{-i\pi}{\lambda\mathbf{r}}(x'^2 + y'^2)\right) \mathrm{d}x\mathrm{d}y, \tag{2.7}$$

where it is considered that the illuminating field, $\mathbf{E_i}$ is uniform and $\mathbf{r}$ does not change much over the area of the aperture. By using equation 2.7, one can calculate both the near-field and the far-field amplitude of the shadow radiation. This is because the equation is not approximated to far-field region.

A comparison between the unobstructed and the shadow radiation, calculated by equation 2.7, for the same parameters as above, is shown in Fig. 2.6(a). Comparing Fig. 2.5(a) and

2.6(a), it can be seen that within the region of full geometrical shadow, the two approaches differ in their predictions. When near-field effects are taken into account the full shadow radiation does actually tend to $-\infty$, as $r \rightarrow 0$.

The difference between the unobstructed and the shadow radiation in dB units is shown in Fig. 2.6(b). It is clear that there is an amplification of the amplitude of the incident wave in the region $0 < r < 2$ m. In this particular case, the maximum amplification is around 25 dB.

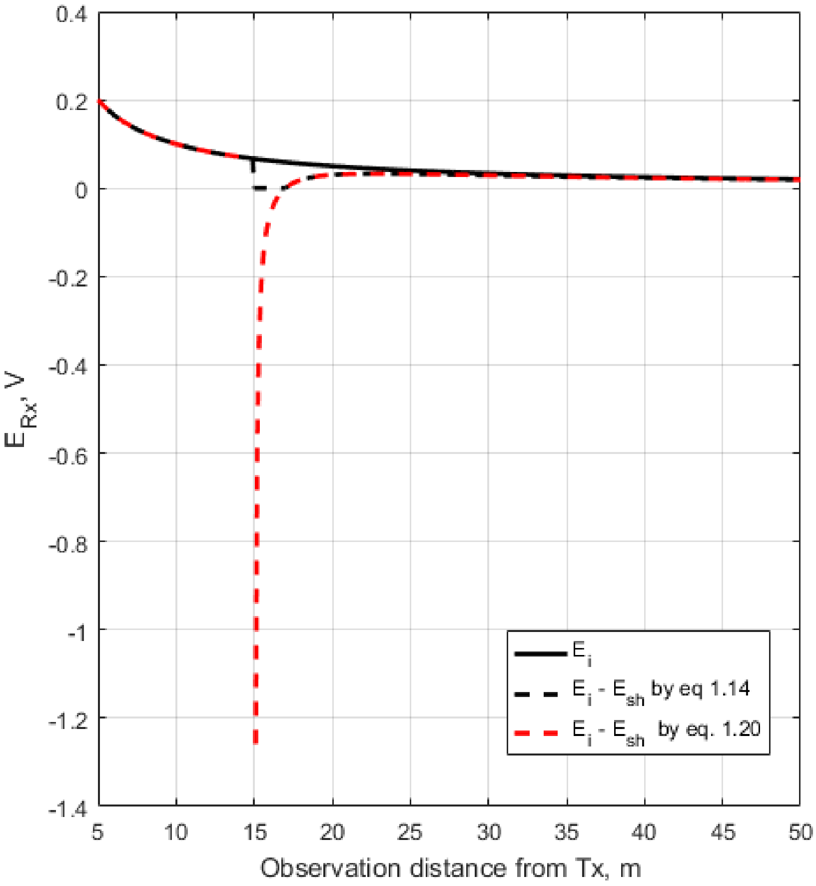

(a)

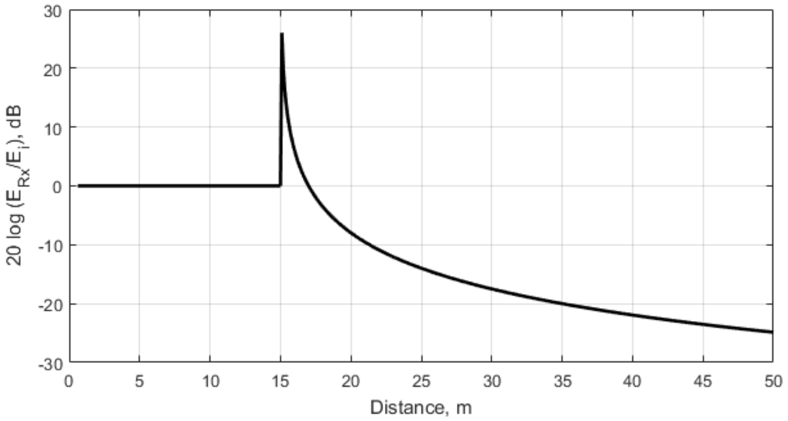

(b)

Figure 2.6: Representation of the actual shadowing in the near-field. E_i and E_{Rx} calculated for an aperture with area of 2 m^2, situated 15 m from the transmitter - (a), and difference of the unobstructed E_i and the shadow radiation, representing the signal used for detection purposes in FSR - in dB (b).

By equation 2.7, the shadow radiation in both near and far-field can be calculated. Thus the leakage signal intensity reduction, due to the presence of a target, is known, which is the basis for the calculation of target cross-section, discussed in the next section.

2.4 Shadowing effect: moving target crossing the baseline

According to the discussion above, the target presence in FSR is indicated by a reduction of the leakage signal. In the majority of cases the shadowing radiation itself is very small in comparison with the leakage signal [10] and thus it is difficult to detect a stationary target as there is no reference signal available. In radar practice we are mainly dealing with moving targets. There is an essential difference between the cases of a stationary and a moving target, which will be discussed in this section.

When a target is moving through or in the vicinity of the baseline, as shown in Fig. 2.7(a), the coordinates of the target's centre, x_p, z_p, are going to be time-dependent, and thus the amplitude of the shadow radiation at the detection point will become time-varying.

In the received signal, there will be a constant power leakage level. The shadowing due to the target presence will only occur for the time when the target is between the transmitter and receiver or their close proximity. Thus there will be a constant level in the received signal, as shown in Fig. 2.7(b), where some reduction of the leakage power is present around time 0 - the time the target is physically on the baseline. The example in Fig. 2.7(b) is modelled according a target of 2 m width, moving at a speed of 2 m/s perpendicularly towards the middle of a baseline of 50 m length.

In Fig. 2.7(a) x', y' are the coordinates of a point on the target, lying on the plane (x', y') in a Cartesian coordinate system, which has its origin in the geometric centre of the target

(x_p, y_p, z_p) and is parallel to the system axes - (x, y, z), with origin at the transmitter. The baseline between the source and the receiver is BL, while the distance from the transmitter to the target crossing point is denoted by dT. The equations of motion for a target which is moving along a known, linear trajectory in the (x, z) plane, i.e. no vertical motion of the target, are given by equations 2.8. It is important to note here that in most practical applications linearity of the trajectory is a good approximation over the observational period of the target in the FSR main lobe. For a typical surface target of length 5 m and speed of around 2 m/s, it would take 2.5 s for the target to completely cross the baseline. It is a good assumption that the trajectory would not change dramatically for most targets.

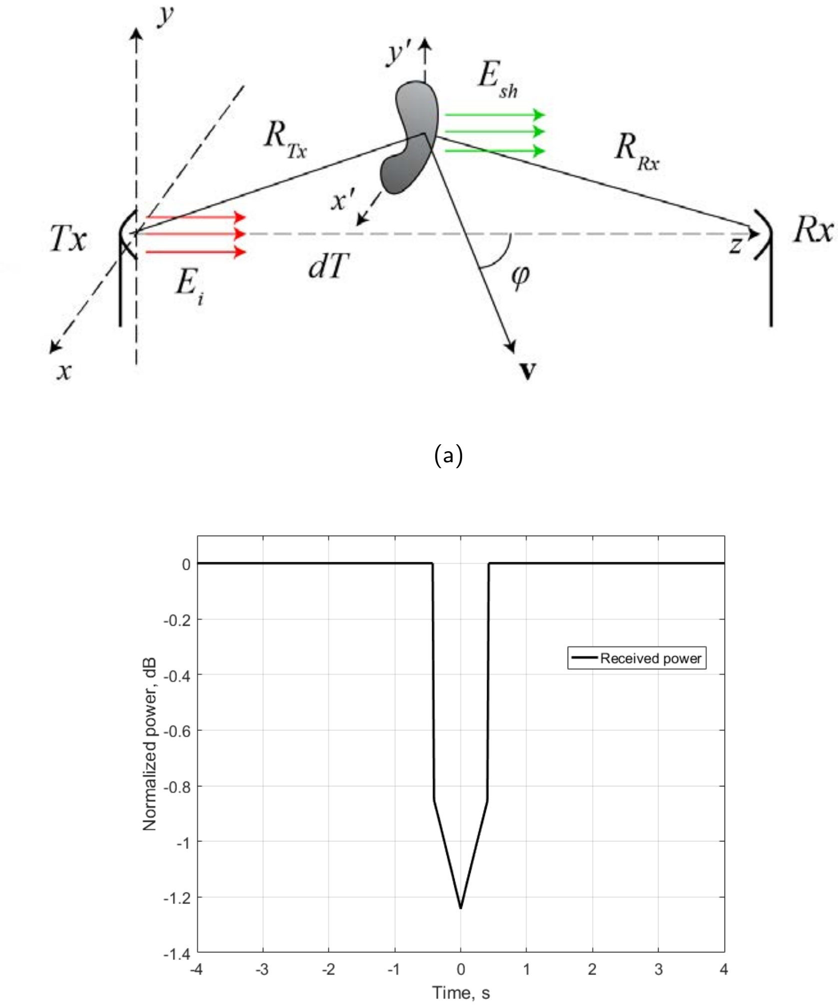

(a)

(b)

Figure 2.7: Topology of FSR when a target is moving through the baseline - (a), and the reduction in the leakage amplitude when a target moves through the baseline - (b)

$$\begin{aligned} x_p &= vt\sin(\varphi) \\ z_p &= dT + vt\cos(\varphi) \end{aligned} \tag{2.8}$$

Thus the ranges transmitter-target and target-receiver are given by equations 2.9

$$\begin{aligned} R_{Tx} &= \sqrt{(BL - dT + vt\cos(\varphi))^2 + v^2t^2\sin^2(\varphi)} \\ R_{Rx} &= \sqrt{(dT + vt\cos(\varphi))^2 + v^2t^2\sin^2(\varphi)} \end{aligned} \tag{2.9}$$

where dT is the crossing distance from the transmitter, φ is the crossing angle with respect to the baseline and v is the speed of the target.

Due to the variation of the ranges R_{Tx} and R_{Rx} with time, i.e. target's motion through the baseline, a Doppler phase signature will be produced. The total target signature, is given by the result of superposition of this phase signature and a complex envelope defined by the FSCS of the particular target, and will have the following form in the baseband [3]:

$$E_{Rx} = U_{rec}\sin(\omega_d(t)t), \tag{2.10}$$

where U_{rec} is the envelope of the signal, proportional to the forward scatter cross section and $\omega(t)$ is the time-dependent angular frequency. This angular frequency arises from the change of the path length difference, $R_{Tx} + R_{Rx}$, with time as the target moves through the observational area.

2.4.0.1 Forward Scatter Cross Section

The FSCS, which specifies the envelope of the received signal, σ_{FS} of the target is defined by the ratio between incident and shadow radiation [20] as the range to the reception point, $\mathbf{r}$, goes to zero:

$$\sigma_{FS} = 4\pi \lim_{|\mathbf{r}|\to\infty} |\mathbf{r}|^2 \frac{|\mathbf{E_{sh}}|^2}{|\mathbf{E_i}|^2} \tag{2.11}$$

FSCS, represents the amplitude of the scattered signal by the target (the signal envelope) and is given by, equation 2.13 [22], which can be derived directly from equations 2.11 and 2.7.

If it can be considered that $|\mathbf{r}|$ is large and the modulus of a complex exponential equals 1:

$$\begin{aligned}
\sigma_{FS} &= 4\pi \lim_{r\to\infty} \mathbf{r}^2 \frac{|{\mathbf{E_{sh}}}^2|}{|{\mathbf{E_i}}^2|} \\
&= 4\pi\mathbf{r}^2 \frac{\left| \frac{-i^2}{\lambda^2} \frac{\exp(-2ik\mathbf{r})}{\mathbf{r}^2} \iint_A \exp\left(\frac{-2i\pi}{\lambda r\mathbf{r}}(x'^2+y'^2)\right) \mathrm{d}x'\mathrm{d}y' \right| |\mathbf{E_i}|^2}{|\mathbf{E_i}|^2} \\
&= \frac{4\pi}{\lambda^2} \left| \iint_A \exp\left(\frac{-ik}{\mathbf{r}}\left(x'^2+y'^2\right)\right) \mathrm{d}x'\mathrm{d}y' \right| \\
&= \frac{4\pi}{\lambda^2} \left| \iint_A \exp\left(-ik(x'\frac{x'}{\mathbf{r}}+y'\frac{y'}{\mathbf{r}})\right) \mathrm{d}x'\mathrm{d}y' \right|
\end{aligned} \tag{2.12}$$

If a target-receiver geometry, as depicted in Fig. 2.8 below is investigated, then the position of each point on an imaginary mesh on the surface of the target can be expressed in terms of two angles, θ'_x and θ'_y. The range from the geometrical centre of the target to the Rx is be given by, r_P.

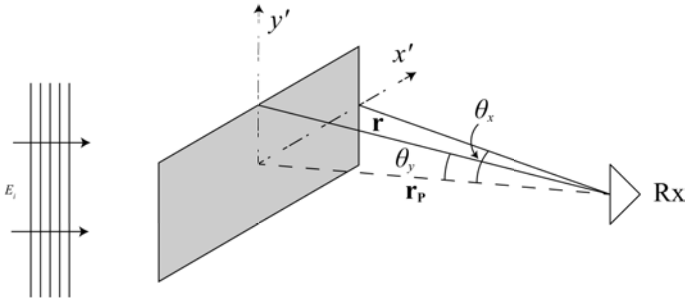

Figure 2.8: Representation of the directional angles in a target-receiver configuration, where the range from the centre of the target to the Rx is denoted by r_P

According to that, an expression for the FSCS can be written as:

$$\sigma_{FS} = \frac{4\pi}{\lambda^2} \left| \iint_A \exp\left(-ik(x' \cos(\theta'_x) + y' \cos(\theta'_y)) \, \mathrm{d}x \mathrm{d}y\right) \right|^2, \tag{2.13}$$

where all symbols have their usual meaning, $\cos(\theta'_x)$ and $\cos(\theta'_y)$ are directional cosines along x' and y', respectively. It can be deduced that the two directional cosines are given by:

$$\begin{aligned} \cos(\theta'_x) &= \frac{x'}{r} \\ \cos(\theta'_y) &= \frac{y'}{r}, \end{aligned} \tag{2.14}$$

where $r = |\mathbf{r}|$ is given by the total range $R_{Tx}+R_{Rx}$. Taking into account the target motion, equation 2.13 will be dependent on the position of the target within the observational area at each point in time. Thus it can be rewritten in a form which allows the separation of the time-dependent ranges and the target coordinates. The intermediate calculations between equation 2.13 and equation 2.15 are done by substituting equations 2.14.

$$\sigma_{FS} = \frac{4\pi}{\lambda^2} \left| \iint_A \exp\left(\frac{-ik(x'^2 + y'^2)}{R_{Tx} + R_{Rx}}\right) \mathrm{d}x \mathrm{d}y \right|^2, \tag{2.15}$$

From equation 2.13, it follows that when a target is situated on the baseline where $\cos(\theta_x)$ and $\cos(\theta_y)$ are both equal to 1, and perpendicular to the incident radiation, the FSCS is at maximum, following a well known equation [3, 23]:

$$\sigma_{FSmax} = \frac{4\pi A^2}{\lambda^2} \tag{2.16}$$

where A is the area of the target silhouette and considers the case when the target, is in the optical scattering regime, i.e. target linear dimensions are much larger than wavelength, is projected perpendicular to the receiver and is exactly in the middle of the baseline. As a result of these the FSCS will be much stronger than the monostatic RCS [6, Chapter]. This fact is easily deducible for a spherical target. For example if a sphere of radius 6λ is considered, then its FS-to-monostatic RCS ratio is:

$$\frac{\sigma_{FS}}{\sigma_{Mono}} = \frac{\frac{4\pi A^2}{\lambda^2}}{\pi r^2} = 4\pi\frac{A}{\lambda^2} = 27dB \tag{2.17}$$

Due to the complexity of equation 2.15, analytical solutions are known only for simple objects - rectangle, circle, etc., as in the case of diffraction (see section 3.1.4.1). For a rectangular target, moving along its length, i.e. x-axis, the FSCS is given by equation 3.8 in section 3.1.4.1 [3]:

$$\begin{aligned} \sigma_{FS}^{rect} = {} & \frac{4\pi}{\lambda^2} \\ & \left|\left(\operatorname{sinc}\left(\frac{\pi l}{\lambda}\sin(\varphi-\alpha_h)\sin(\alpha_h+\beta_h)\right)\right)\left(\operatorname{sinc}\left(\frac{\pi h}{\lambda}\cos(\alpha_v)\sin(\alpha_v+\beta_v)\right)\right)\right|, \end{aligned} \tag{2.18}$$

where all the symbols have their usual meanings, and A is the target area projected on the receiver, given by:$(lh)^2\sin^2(\varphi-\alpha_h)\cos^2(\alpha_v)$, where l and h are the length and height of the rectangular plate respectively, and the vertical diffraction angles, α_v and β_v, are going to be constant as the target moves through the observational area.

From equation 2.18 it can be deduced that FSCS for a rectangular target is a modulus of a sinc function, whose width depends on the ratio length-wavelength, as seen in figure 2.9, note that if the target was moving along the other direction, i.e. vertically - the FSCS will depend on the height-wavelength ratio. This coincides well with the expectation of an antenna pattern of a rectangular antenna [24].

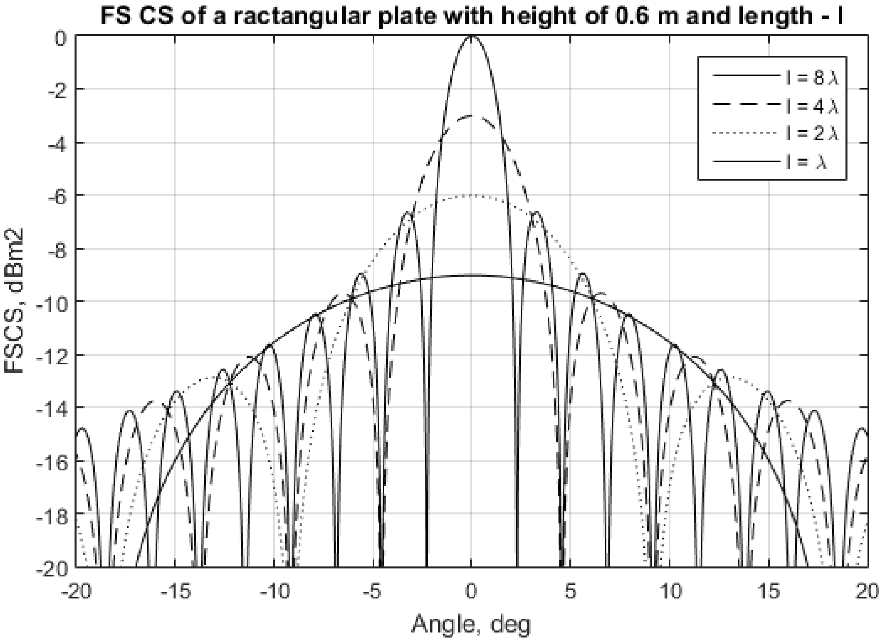

Figure 2.9: FSCS of a rectangular plate with dimensions: h = 0.6 m and changing length of target, for incident wave of 2 GHz ($\lambda = 0.15$ m). All values normalized to the RCS of target with length 1.2 m

Also, due to the movement of the target, a chirp-like signal is produced, due to the path length difference between scattered and leakage signal, at every point on the target trajectory. This is known as Doppler signature.

The FS target acts as a secondary antenna and as such the same terminology can be applied, i.e. main-lobe (ML), side-lobe (SL), etc.

2.4.1 Doppler signature

At the receiver of FSR two signals exist at the same time: the leakage, used as a reference, and the forward scattered signal from the moving target, 'modulating' the leakage [3]. The operation of FSR requires the availability of both of those signals at the input of the receive antenna.

The following discussion presents the Doppler phase signature in FSR and at this point omits the amplitude modulation caused by FSCS variation due to the target motion relevant to the baseline and possible propagation losses. Initially the phase signature of a infinitesimally small (point-like) target will be presented, which is assumed to be moving on a constant, linear trajectory.

It must be noted here that the Doppler content in the FSR target signature is fundamentally independent on the shape and size of the target in the far field, if the whole target can be considered to be in the same iso-phase contour at every single time. The Doppler phase content then will depend on the trajectory and velocity of the target [6].

The shadow radiation is cast on the receiver, as the target is moving through the observational area. The maximum amplitude shadow radiation corresponds to the point when the target is on the baseline, as shown previously in Fig. 2.7(b). Also, being in the shadow, the forward scattered signal is $\pi/2$ shifted in phase with respect to the leakage signal [3].

At the Rx antenna, there is a sum of two signals:

$$\begin{aligned} S_{Rx} &= U_{LKG} + U_{Tg} \\ &= A_{LKG}\cos(\omega_0 t) + A_{Tg}\sin(\omega_{fs} t), \end{aligned} \tag{2.19}$$

where $\omega_0 = 2\pi f_0$ is the angular frequency of the carrier signal and $\omega_{fs} = \omega_0 + \omega_d$ is the angular frequency of the scattered signal, and ω_d is the Doppler dependent angular frequency. A_{LKG} and A_{Tg} are the amplitudes of the leakage signal, U_{LKG}, and the scattered signal, U_{Tg}, respectively.

It can be assumed that A_{LKG} is not going to change over the observation time, if both Tx and Rx are stationary. A_{Tg} is proportional to the FSCS and will change over time, due to the spatial distribution of the FSCS pattern.

The Doppler frequencies in FSR generally occupy a very low-frequency band, there are two ways to detect these signals: standard I/Q processing or self-mixing heterodyne [3]. As will be discussed later, imaging in FSR requires the complex signal [1, 25], so only the first method will be discussed here.

Demodulating a signal to its quadrature components is done by mixing it with a reference function and its $\pi/2$ shifted version, in two separate mixers, so that:

$$\begin{aligned} S_{Rx_1} &= \cos(\omega_0 t)\left(A_{LKG}\cos(\omega_0 t) + A_{Tg}\sin(\omega_{fs} t)\right) \\ &= A_{LKG}/2\cos(2\omega_0 t) + A_{Tg}/2\left(\sin((2\omega_0 + \omega_d)t) - \sin(-\omega_d t)\right) \\ S_{Rx_2} &= \sin(\omega_0 t)\left(A_{LKG}\cos(\omega_0 t) + A_{Tg}\sin(\omega_{fs} t)\right) \\ &= A_{LKG}/2\sin(2\omega_0 t) + A_{Tg}/2\left(\cos(-\omega_d t) - \cos((2\omega_0 + \omega_d)t)\right) \end{aligned} \tag{2.20}$$

After passing through a LPF, and removal of DC, both quadrature components of the received FSR signal are detected:

$$\begin{aligned} S_I = S_{Rx_2} = \frac{A_{Tg}}{2}\cos(\omega_d t) \\ S_Q = S_{Rx_1} = \frac{A_{Tg}}{2}\sin(\omega_d t) \end{aligned} \tag{2.21}$$

It must be noted here that providing a reference waveform for I/Q demodulation can cause technical but not fundamental problems for systems which are operating at large baselines.

The in-phase quadrature component of a Doppler phase signal from a point-like target and the corresponding signal modulated by the FSCS pattern of a rectangular plate can be seen in Fig. 2.10, below.

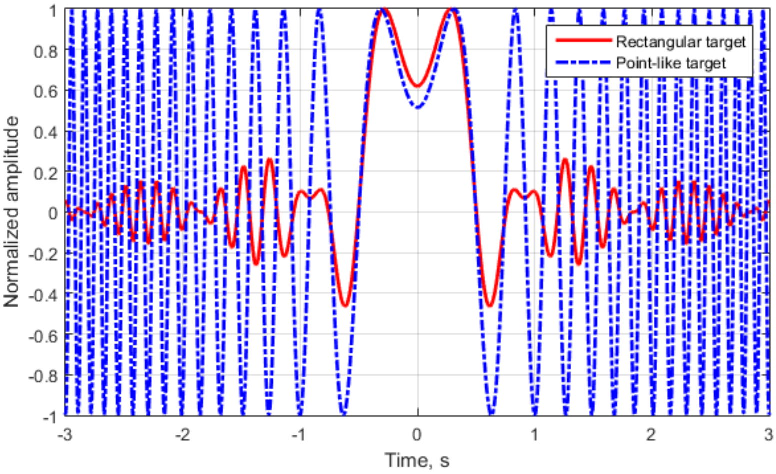

Figure 2.10: Modelled Doppler phase of a moving point like target - blue, and rectangular target - red.

As can be seen from Fig. 2.10 the carrier frequency of the two signals is the same. Therefore, it can be suggested that the Doppler frequency in the signal does not depend on the target's dimensions [19] and scattering abilities, and the Doppler angular frequency can be written as [6, Chapter]:

$$\omega_d(t) = -\frac{2\pi}{\lambda}\frac{\mathrm{d}L(t)}{\mathrm{d}t}, \tag{2.22}$$

where $L(t)$ is the sum of the time-varying ranges: target-transmitter and target-receiver, given by $L(t) = R_{Tx} + R_{Rx} - BL$ [3]. From equation 2.22 it can be noted that zero-Doppler content can be present only if the range sum is constant, i.e. the target moves on an elliptical trajectory, where the transmitter and receiver are the two focal points, or when the target is on the baseline, which is a specific case of the later, with $L(t)$ equal to the baseline length. This specific case of 0-Doppler is seen in the moment the target crosses the baseline, as well, thus the FSR loses the ability to measure range and trajectory parameters of the movement of the target [6].

According to [3], $\omega_d(t)$ can be presented as:

$$\omega_d(t) = \frac{1}{\lambda} \frac{\mathrm{d}(R_{Tx}(t) + R_{Rx}(t) - BL)}{\mathrm{d}t}, \tag{2.23}$$

where the ranges $R_{Tx}(t)$ and $R_{Rx}(t)$ are given by equation 2.9. As such the Doppler phase of a moving target in the x, z-plane will have a phase term which is generally quadratic with time [26], i.e. linear in frequency as it can be easily observed from Fig. 2.10 (blue). The figure shows the Doppler change in frequency domain for constant speed and perpendicular to the baseline and is shown for illustration purposes only.

The Doppler shift is largest, when the target moves in orthogonal direction to the middle of the baseline. It is, also, known that the Doppler signature is invariant of the target crossing position with respect to the middle of the baseline, i.e. target signatures are the same if targets cross the baseline close to either Tx or Rx, as long as the time-varying range sum, $L(t)$, is the same between crossings [3].

As an example if a point-like target, travelling with speed of 5 m/s, perpendicularly towards the middle of a baseline of length 100 m, is considered, the signature PSD will have a form like as shown in Fig. 2.11.

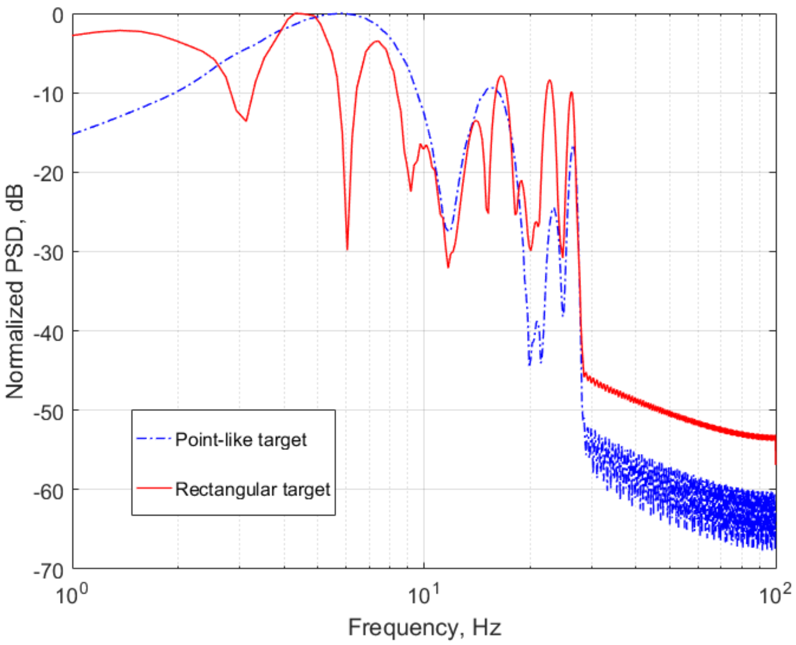

Figure 2.11: PSD of the observed Doppler signature for a point-like target (blue) and an rectangular target (red)

In Fig. 2.11 a comparison between the spectrum of the Doppler signatures observed for point-like target and an rectangular target can be seen. It clearly shows that both follow the same trend, where the significantly higher number of ”ripples” in the rectangular target spectrum is due to the contribution of the amplitude modulation due to FSCS. The sharp reduction of signal, in our case at about 3 Hz, is very typical for chirp-like signals [8].

Thus the full FSR signature is completely specified by the target trajectory and FSCS. Examples of recorded target signatures for three different targets can be seen in Fig. 2.12 [3].

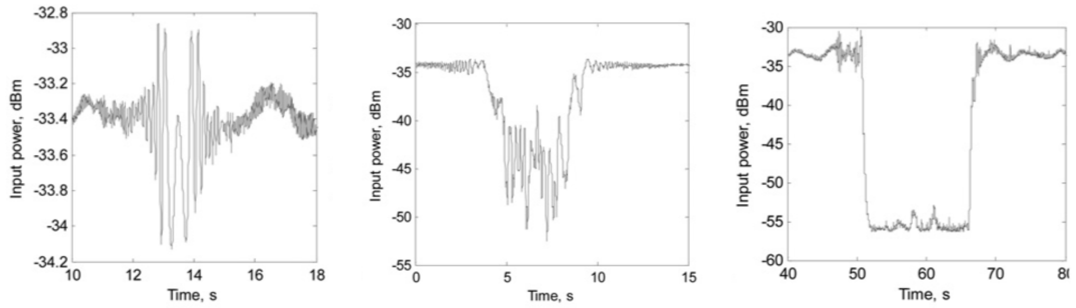

(a) (b) (c)

Figure 2.12: Doppler signatures at the input of an analogue-to-digital converter (ADC) of different sized targets (small - (a), medium - (b) and large - (c)) for a baseline of 300 m, at 7.5 GHz transmitted CW. The three target sizes are such so that they correspond to far-field diffraction - (a), boundary between far and near-field - (b), and near-field - (c). Reprinted from [3].

The amplitude of the signals shown in Fig. 2.12, correspond to the predictions (Fig. 2.6), where there is a small variation (in the order of 1 dB) between the magnitude of the shadow signal and the reference signal in the far-field - Fig. 2.12(a).

In Fig. 2.12(c) it can be seen that the signature in the near-field, is characterized by nearly complete shadowing, where the difference between shadowing and reference signals are large - in the order of 20 dB. However, in the far-field target signature (Fig. 2.12(a)), the Doppler variation due to the target motion is clearer.

It is important to acknowledge another of the main advantages of FSR over bistatic and monostatic radar systems. The forward scattered signal is characterized by absence of phase fluctuations due to range fluctuations [6, 19, 27]. This is due to the mechanism of forward scattering, i.e. the target signature is scattered by the whole of the shadow contour, rather than sum of individual scattering points on the target surface, as is the case with monostatic and bistatic radars. The FS signature is then fluctuating only as a function of the aspect angle and motion along the path of the target, i.e. the Doppler phase. However, in the near-field, as seen in Fig. 2.12(c), phase fluctuations appear in the main lobe of the forward scatter radar.

2.5 Extraction of target trajectory parameters from the signature

As it is discussed above, the target signature depends on its trajectory and FSCS, so it could be possible to extract some of the motion parameters of the target by analysis of the signature.

2.5.1 Optimal signal processing

As there is fundamentally no range resolution in FSR, the target trajectory parameters cannot be retrieved through the methods used in mono- and bistatic radar, i.e. Range-Doppler or similar processing. Thus a method for target trajectory parameter estimation in FSR, based on optimal processing, have been proposed [28]. Optimal processing is a method for extraction of parameters by match filtering the received target signature with a bank of match filters with predefined values of the parameter to be extracted, as shown in Fig. 2.13. In FSR it is mainly used for target detection and extraction of target trajectory parameters: speed, crossing angle, with respect to the baseline and crossing point with respect to either transmitter or receiver.

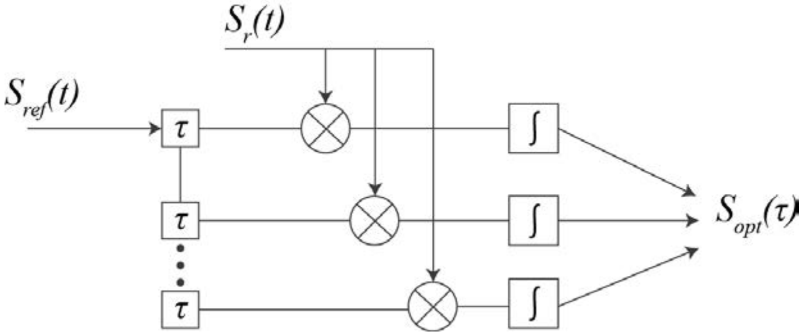

Figure 2.13: Optimal signal processing, where $S_{ref}(t)$ is a reference function, delayed by some amount of time, τ, then integrated with the received signal, $S_r(t)$

Usually optimal signal processing is used for maximization of signal-to-noise ratio (SNR) [12]. However, in the case of the further shown feasibility study of the target shadow profile reconstruction (TSPR) algorithm, high SNR was provided. The approach was, thus, used for extraction of the target motion parameters, needed to construct the propagation kernel, shown and further discussed in sections 3.2.3 and 5.2.

As can be deduced from sections 2.4.1 and 2.4.0.1, the received Doppler signature depends on the target's speed, trajectory, visibility time and FSCS, which can produce practically infinite number of target signatures.

Thus as discussed in [12] the parameters of the Doppler signature are not known, the optimal signal processing represents the process of correlation of the received signal with a set of pre-defined reference waveforms in the time-domain. It is shown that for an accurate waveform compression, via optimal processing, the envelope (FSCS) of the target signature does not need to be taken into account, because the correlation properties of the Doppler signature in FSR is mainly dependent on the Doppler phase of the signal, rather than the amplitude [12], i.e. each signature will correspond to an unique waveform. Consider an example when a Gaussian noise and its signum function are correlated, shown in Fig. 2.14. The correlation coefficient between the noise and its signum function is 0.95.

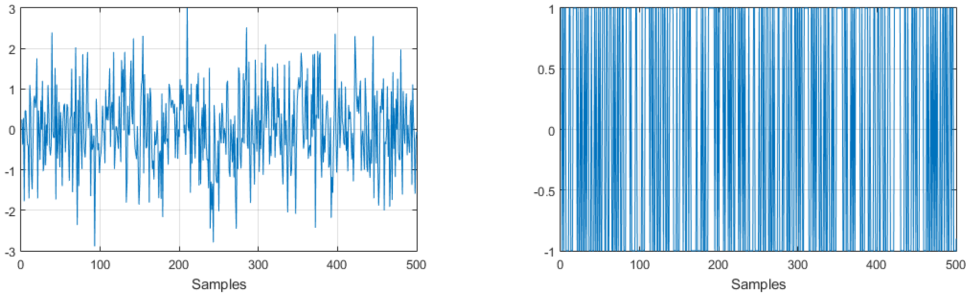

(a) (b)

Figure 2.14: Modelled Gaussian noise - (a), and its signum function - (b).

Thus in the algorithm, the processed target signal is being cross-correlated with Doppler phase only information, which removes the need of complex predictions for the envelope of the recorded signatures.

The quasi-optimal processing is achieved by correlating the received target signature by a set of reference functions, given by the oscillating term of equation 2.21, where each of the pre-defined reference waveforms is calculated for particular speed and trajectory, in a range of expected values. The usual integrating in optimal processing,

$$S_{opt}(\tau) = \int_{-T/2}^{T/2} S_r(t) S_{ref}(t-\tau)\mathrm{d}t, \tag{2.24}$$

is transformed into a discrete mathematical problem, by dividing the range of expected trajectories into equally spaced intervals, Δv, Δb and $\Delta\varphi$, for speed, crossing point with respect to the middle of the baseline and crossing angle, respectively, each of them having lengths N, M and O. The quasi-optimal procedure then produces a multi-dimensional correlation matrix of size $N * M * O$, where the maximum of the correlation will give the target's trajectory parameters, according to the Doppler content of the received signature.

However, it is shown in [12], that there will be ambiguity of the extracted crossing point, relevant to transmitter and receiver. This method for trajectory parameters estimation can be influenced by the presence of clutter or other interference in the signal, as well. Moreover, it can generate inaccurate results for surface targets, which can cross the baseline at any angle in any point. This effect is most pronounced for target trajectories close to either transmitter and receiver.

Another unsolved problem of trajectory estimation via optimal processing is the uncertainty in the target motion direction, i.e. determining the initial position on the left or the right hand side of the receiver.

2.5.2 Extraction of target trajectory parameters via analysis of the FSR spectrogram

In [29] a method of speed estimation of FSR targets, through the use of a spectrogram is presented, and will be introduced in the following section.

When FSR signals are represented via a spectrogram, the Doppler frequency variation produces a particular 'v'-shape, as shown pictorially in Fig. 2.15(a) and 2.15(b) below, for a simulated Doppler signature at 1 GHz of a target moving, perpendicularly, at 5 and 10 mps, respectively, towards the middle of a baseline of 100 m.

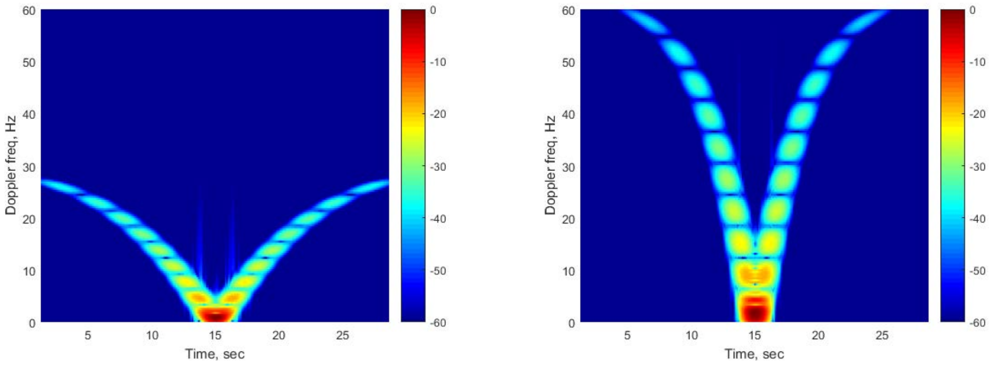

(a) (b)

Figure 2.15: Representation of a simulated Doppler signature via a spectrogram - (a) for a target moving with 5 mps and baseline of 100 m and moving at 10 mps - (b), respectively.

After applying short-time Fourier transform [30] to the target signature, the spectrogram represents a particular 'v'-shape. The slope of the 'v'-shape is dependent on the target velocity, as well as on the particular crossing angle and crossing point [29].

It is shown in [29] that the target speed towards the baseline can be estimated by the observation of that slope, via the following equation:

$$(2\Delta t)^2 v^4 - (f_d \lambda \Delta t)^2 v^2 - \left(f_d \lambda \frac{BL}{2} \right) = 0, \tag{2.25}$$

where v is the target's speed, f_d is the Doppler frequency shift, BL is the baseline and Δt is the integration time over which the Doppler shift is observed.

It is suggested that this method for speed estimation is more robust to signals with low signal-to-clutter ratio (SCR), though this has not been investigated. However, there is still going to be ambiguity of the crossing distance estimation, thus another method for target trajectory estimation using multi-static FSR system has been proposed and will be briefly introduced next.

2.5.3 Extraction of target trajectory parameters through the use of a multi-static FSR system

Multistatic FSR (Fig. 2.17) is essentially more complex system in comparison with the single line crossing FSR. Nevertheless it has essential advantages in target detection and more importantly in trajectory estimation.

Shown in [31], is a feasibility study of a multi-static FSR system, to be used for extraction of motion target parameters for low-observable targets or in the presence of interference and clutter. The availability of multiple Doppler signatures for the same target, allows for use of a different approach for target motion estimation, including accurate target tracking, without the ambiguity relevant to transmitter or receiver, which is present in the previous methods discussed.

Such configuration was first introduced in France during World War II, under the name *maille en Z*, translating as mesh of Z. It had a double Z-like shape, as shown in Fig. 2.16, below, and was used for detection of enemy bombers, reportedly measuring speed, direction and altitude of planes within 10%, 10 to 20 degrees and 1000 meters, respectively. [14].

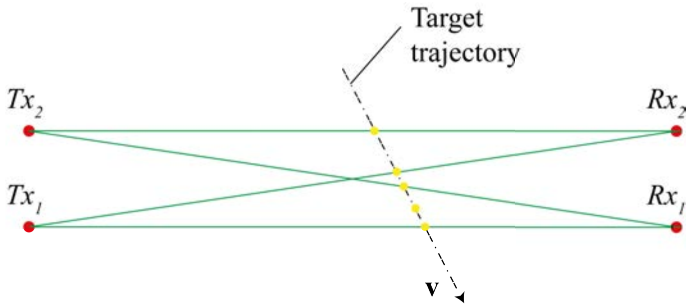

Figure 2.16: Schematic of the possible *maille en Z* configuration - the first reported *netted* FSR system

The approach is based on the accurate estimation of the crossing times of the target. Looking at Fig. 2.17, it can be deduced that if we have k transmitters and n receivers, and target is moving with constant velocity [31], each crossing time is given by:

$$t_{n,k} = \frac{(x_0 - kd_{Tx/Rx})BL - y_0(n-k)d_{Tx/Rx}}{v_y(n-k)d_{Tx/Rx} - v_xBL}, \tag{2.26}$$

where x_0 and z_0 are the target starting position with respect to the first baseline of the configuration, and v_x and v_z are the components of the speed vector in the x-axis and z-axis, respectively; $t_{n,k}$ will be referred as the crossing time for the n, k-node; $d_{Tx/Rx}$ is the distance between each and the next Tx or Rx. The four unknowns parameters of the target velocity vector can be isolated by rearranging equation 2.26 and dividing by the length of the first baseline and arranging in a matrix form [26]:

$$\begin{bmatrix} 1 & \frac{(k-n)d_{Tx/Rx}}{BL} & t_{n,k} & \frac{(k-n)d_{Tx/Rx}}{BLt_{n,k}} \end{bmatrix} \begin{bmatrix} x_0 \\ z_0 \\ v_x \\ v_z \end{bmatrix} = kd_{Tx/Rx}, \tag{2.27}$$

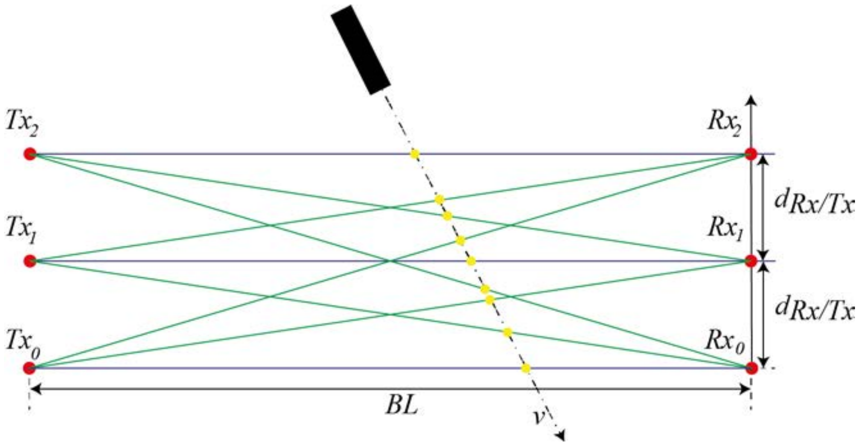

Figure 2.17: Top view of a multi-static FSR system configuration. Blue lines - direct baselines, green lines are cross baselines, for a multi-static configuration there areRx/Tx^2 crossings, i.e. 9 for the case depicted in the figure.

where the four unknowns, the trajectory parameters of the target are presented in a vector form. Thus if a minimum of four baseline crossing times are present, they will be computed as a solution to a system of equations [31]:

$$\begin{bmatrix} 1 & \frac{(k_1-n_1)d_{Tx/Rx}}{BL} & t_{n_1,k_1} & \frac{(k_1-n_1)d_{Tx/Rx}}{BLt_{n_1,k_1}} \\ 1 & \frac{(k_2-n_2)d_{Tx/Rx}}{BL} & t_{n_2,k_2} & \frac{(k_2-n_2)d_{Tx/Rx}}{BLt_{n_2,k_2}} \\ 1 & \frac{(k_3-n_3)d_{Tx/Rx}}{BL} & t_{n_3,k_3} & \frac{(k_3-n_3)d_{Tx/Rx}}{BLt_{n_3,k_3}} \\ 1 & \frac{(k_4-n_4)d_{Tx/Rx}}{BL} & t_{n_4,k_4} & \frac{(k_4-n_4)d_{Tx/Rx}}{BLt_{n_4,k_4}} \end{bmatrix} \begin{bmatrix} x_0 \\ z_0 \\ v_x \\ z_y \end{bmatrix} = \begin{bmatrix} k_1 \\ k_2 \\ k_3 \\ k_4 \end{bmatrix} d_{Tx/Rx}, \qquad (2.28)$$

where the matrix can be expanded to the number of crossing times present, to increase the accuracy of the algorithm [26]. The only variable that needs to be estimated for the solution of equation 2.28 are the crossing times of the target, and this is done on the basis of detection done by quasi-optimal processing.

Experimental and simulated results of the algorithm show good accuracy, when compared with the coherent processing discussed previously, due to the integration of additional information of the multiple crossings, thus minimizing the influence of interference and multipath on the trajectory parameter estimation [26, 32].

Results for estimation of the target trajectory shown in [31], show a mainly instrumental error of the method, for high SNR experimental data with target crossing 8 baselines. This method is also free from any ambiguity.

2.6 Conclusion

It is shown that the target signature in FSR is a superposition of a slow-varying complex envelope, dependent on the target's FSCS, and a rapidly-oscillating Doppler phase component, dependent on the target's motion.

Also, the forward scattered signal is represented by shadow radiation from an opaque aperture, whereas the FSCS is described by the physical theory of diffraction. Thus the scattering mechanism in FSR is different than that in monostatic or bistatic radars, where the received signals are produced by backscattering.

Several conclusions regarding the operation of FSR can be drawn from the discussion above. Firstly, due to the topology of the system, FSR is only operating in a fence-like configuration, in a narrow corridor around the baseline. Thus, FSR is a radar system which has been mainly used for target detection and motion parameters estimation so far. Due to the shadowing effect, the received signal is represented as a reduction of a leakage signal which can be useful for detection purposes. On the other hand, due to the Doppler phase information in the signal, trajectory parameters can be estimated with high accuracy, by any of the algorithms discussed.

Furthermore, the signal in FSR is characterised by the area of the target silhouette and by its trajectory, but not target material or 3D shape. This leads to the fundamental independence on stealth coating or geometry, and high repeatability of the received signals. Together with these advantages, the amplitude of the FSCS is generally much larger in the optical scattering regime, than monostatic or bistatic RCS, increasing the interest in FSR as a system for detection of targets with low radar cross-section, i.e. low-observable targets.

Also, direct path and scattered signals are inherently coherent due to the non-oscillating nature of the Doppler phase signature produced by the target shadow, which results in Doppler resolution inversely proportional to the target observation time (in order of tens to hundredths of a Hz). On the other hand, there is absence of range resolution, thus usual SAR/ISAR imaging methods, discussed in section 1.3, are not applicable to FSR signals directly.

This thesis discusses the idea that a target image may be obtained in the cross-range domain for FSR target signatures.

CHAPTER 3

PRINCIPLES OF DIFFRACTION, HOLOGRAPHY AND THEIR APPLICATION FOR FSR ANALYSIS

Forward scatter radar, as discussed in the previous chapter, is a particular case of bistatic radar, where the bistatic angle is close to 180 degrees. The mechanism of scattering and signal formation is different than in the case of mono- and bistatic radars, it is not based on scattering off individual points on the target surface, but rather a shadow signal is produced coherently by the whole target due to diffraction (see Fig. 3.1). Fig. 3.1 will be used throughout the chapter.

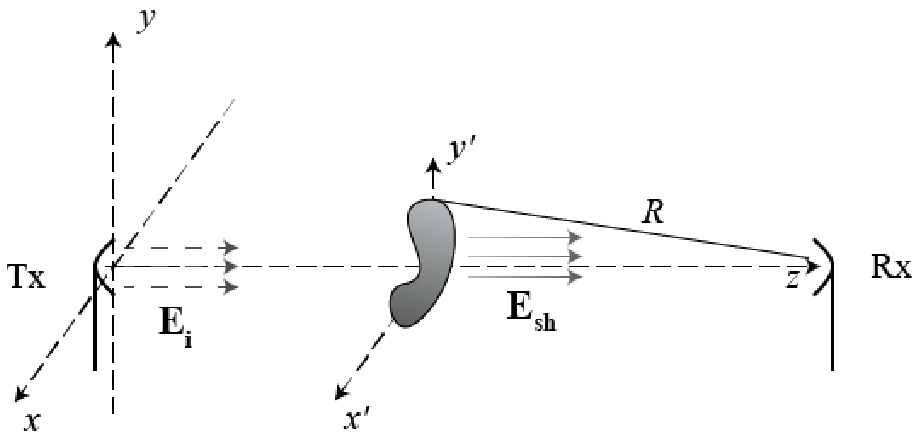

Figure 3.1: In practice at the reception point in FSR a diffraction problem is evaluated

Also, it has been discussed that the FSR signal has a holographic nature [3, 33].

Thus the fundamental properties of the FSR system, requires previous knowledge of the theory of diffraction and holography. In the following chapter, the fundamental physics behind these will be presented in the context of FSR. Firstly scalar theory of diffraction will be discussed and then a brief theory of optical holography, and specifically in-line holography. Then the principles of radio holography will be presented and compared with optical holography and the application of FSR as radio holographic system will be discussed.

This chapter is a short tutorial in diffraction and holography, intended to introduce the reader to the topics.

3.1 Scalar Theory of Diffraction

Diffraction is a theory that explain the phenomena regarding the forward motion of waves when they encounter an opening in an opaque space or an object in free space. The mathematical and physical description of diffraction is explained as the interference of wavefronts according to the Huygens-Fresnel principle [34]. The discussion below will provide with basic knowledge of the assumptions and approximations used in scalar diffraction and is only considering monochromatic waves, omits the time-harmonic term for simplicity, but without loss of generality for the research presented.

It is also, important to note that all FSR signals recorded are scalars, thus diffraction theory will be considered only it is scalar form. This is due to the fact that FS signals are generally the same polarization as the incident radiation, i.e. no depolarization effects occur on target scattering. This effect is noted by the author and colleagues in [3, 35].

3.1.1 Interference and coherence of waves

As a prerequisite of the scalar theory of diffraction, the principles of interference and coherence are first going to be presented.

Wave interference is a phenomenon, which describes their superimposition to produce a wave of higher or lower amplitude. It usually refers to waves which are coherent or partially coherent to each other, either because they come form the same source or they have exactly or roughly the same frequency [21].

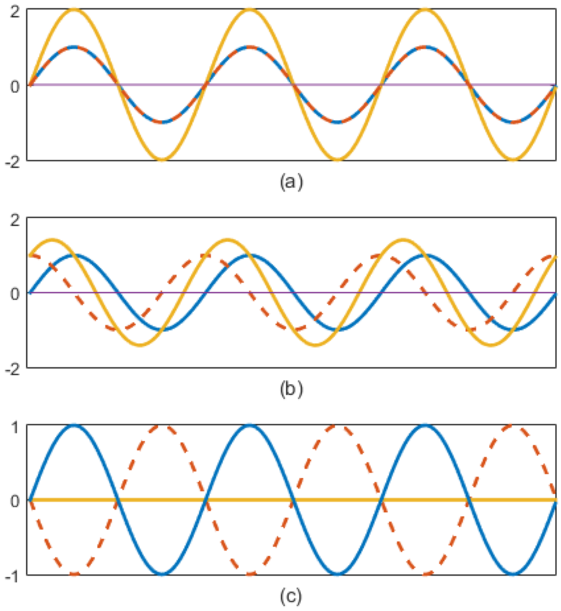

Figure 3.2: Interference of two waves of the same frequency - the two waves are in blue and red, while their interference in yellow. Three cases are shown - constructive interference - (a); mid-case - (b) and destructive interference - (c).

Fig. 3.2 shows the two extrema of interference - when phase difference between the waves is an odd multiple of π - destructive (Fig. 3.2(c)), and when it is even - constructive interference (Fig. 3.2(a)). In all other cases of phase difference between the two waves, the resulting amplitude is going to be between these maxima and minima, as in 3.2(b) [21].

Full coherence on the other hand is the property of two waves, which have a constant phase difference and the same frequency, i.e. provides constant (stationary) interference [21]. If the fluctuations of the amplitude and phase of two waves partially correlate, then the waves are said to be partially coherent.

It is known that target signatures in FSR are a sum of coherent wavefronts, scattered from the target, which interfere according to the time-varying path length of the leakage and scattered waves [3].

In the next section the Huygens-Fresnel principle of wavefront propagation will be introduced.

3.1.2 Huygens-Fresnel principle

In the mid-17th century, Huygens formulated a wave description of light. He suggested that each point a wavefront reaches becomes a source of a secondary spherical wave and the sum of all of these secondary spherical waves will represent the form of the wave at any later point in time, see Fig. 3.3. Huygens assumed that the secondary waves are travelling only in the forward direction, but there is no explanation in his formulation of why this is the case [34]. Its results have proven to be accurate, though there has been controversy about the correctness of the underlying physical phenomena. For example, Melvin Schwartz [36] wrote that to consider each point on a wavefront as a new source of radiation, and to add the radiation from all the new sources together,'makes no sense at al', since (he argues) 'light does not emit light; only accelerating charges emit light'. He concludes that Huygens' principle 'actually does give the right answer but for the wrong reasons'.

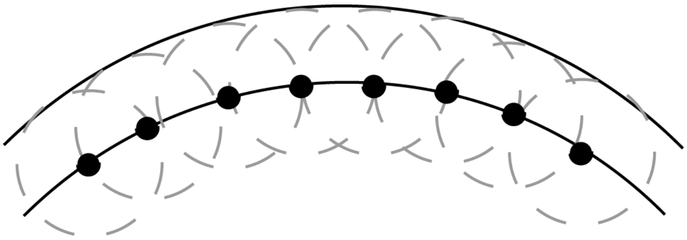

Figure 3.3: Illustration of the Huygens principle for spherical propagating wave

Albeit that, Huygens accurately described refraction and reflection with his theory of wave propagation, but failed to account for diffraction phenomena. In 1807, though, as Young performed his famous double-slit experiment, Fresnel used the Huygens principle to mathematically formulate the diffraction phenomena based on the interference between individual secondary radiators, situated around obstructions of light, see Fig. 3.1 [21, 37]. The theory is developed as follows. The electric field strength of a spherical wave, in general, can be expressed as:

$$E_{sph} \propto \frac{\exp(ikR)}{R}, \tag{3.1}$$

where R is the distance between source and detector, as pictorially shown in Fig. 3.4, and k is the wave number. The amplitude of spherical waves falls off with the distance from the emitter, while its phase is related to the distance propagated. It should be noted here that this mathematical formulation of a spherical wave is only consistent with Maxwell's laws at $R \gg \lambda$, but it is within that regime, diffraction is usually discussed. Moreover, equation 3.1 is an exact solution to the scalar Helmholtz equation, and an approximate to the vector one, considering $R \gg \lambda$ [21].

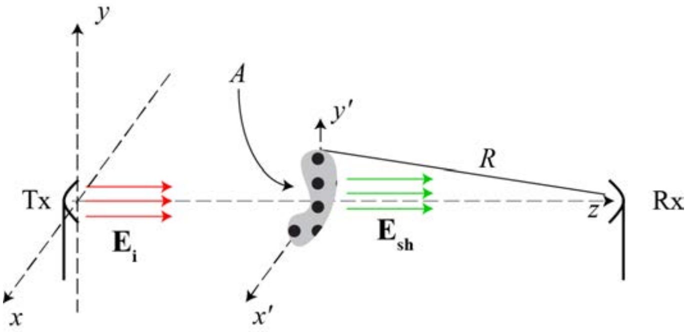

Figure 3.4: Simple illustration of diffraction, as formulated by the Fresnel diffraction theory

If a screen opening, of area A, situated perpendicular to the z plane, is considered and illuminated with a light field, E_i, then at a point, (x, y, z), away form the screen, as seen in Fig. 3.4, the field is going to be given by the sum of the contributions of all the emissions of all secondary elementary sources from each point on the area of that opening.

It must be noted here that the spacing between the elementary point sources is dependent on the wavelength of the carrier frequency used. According to theory [21], this spacing must be less than 3/4 of the wavelength.

It is important to acknowledge that due to the Huygens explanation, the diffraction phenomenon is a property of all waves for screen openings of any size [38]. Diffraction is though mainly considered in the cases for openings of sizes of at lest one wavelength [21]. Throughout this thesis, in the context of FSR, diffraction will only be considered for target dimensions larger than one wavelength.

The mathematical form of the Huygens-Fresnel diffraction for the general case, shown in Fig. 3.4, can be written as [21]:

$$E(x, y, z) = -\frac{i}{\lambda} \iint_A E_i \frac{\exp(ikR)}{R} K(\chi) \mathrm{d}x' \mathrm{d}y', \tag{3.2}$$

where $K(\chi)$ is an inclination (or obliquity) factor, which is not described in Fresnel's theory, but considered by Kirchhoff's diffraction theory, discussed in section 3.1.3. This obliquity factor is dependent on the angle between R and the z-axis, where

$$R = \sqrt{(x - x')^2 + (y - y')^2 + x^2} \tag{3.3}$$

is the range opening-screen for every secondary elementary radiator on the aperture. Equation 3.2 is known as the Huygens-Fresnel diffraction formula [21], and computes the scalar field produced by the interference of spherical waves, emitted by elementary radiators on each point (x', y') on the aperture. The $-\frac{i}{\lambda}$ term arises from the mathematical derivation of the equation, which is out of the scope of this thesis and is described in [37], and means that the secondary waves oscillate at a quarter of a cycle out of phase with respect to the incident wave, and the magnitude of the secondary waves is scaled as $1/\lambda$ with respect to the illumination wave. The phase shift between diffracted and incident waves has been previously mentioned when discussing shadow radiation in Chapter 1. The only difference being that there the waves considered were regarded as shadow and incident radiation, these terms however are identical to diffracted and incident.

An interesting fact about Fresnel's diffraction integral is that when it was presented to the French Academy of Science, a judge noticed that Fresnel's formula predicted that a bright spot should emerge in the centre of the geometric shadow behind a circular obstruction. This was then proved to be true experimentally by Arago, but the phenomenon was named after the judge that disbelieved it - Poisson, thus the name adopted was Poisson's spot. This phenomenon is observed in FSR target signatures, where the power of the signal directly behind the opaque target has the highest amplitude [6, Chapter 13].

The Huygens-Fresnel principle, gave rise to research into wave propagation through openings, i.e. diffraction theory, which was then revisited by Gustav Kirchhoff, as described in the next section.

If one needs to evaluate the electric field strength in an arbitrary point behind an illuminated object, equation 3.2 can be used. However, Kirchhoff redeveloped Fresnel's work into a mathematical form which can be numerically solved [39].

3.1.3 Fresnel-Kirchhoff (FK) diffraction theory

As shown in the previous section, the electric field strength at any point can be calculated by equation 3.2, but the so called inclination factor remains unknown. However, Fresnel-Kirchhoff (FK) (sometimes just Kirchhoff's) diffraction formula is a much simpler form of equation 3.2, but explicitly evaluates this factor. The discussion below will follow the approach presented in [21].

In 1887 Gustav Kirchhoff, showed that Huygens-Fresnel diffraction satisfies the scalar Helmholtz equation and showed the approximations used in the development of the theory, which include the approximations that the distant from the source to the aperture is much greater than the incident wavelength and that the incident radiation can only propagate through an opening. Kirchhoff used Green's theorem to derive the solution of the wave equation.

The FK diffraction integral is given as follows, according to a topology depicted in Fig. 3.4:

$$E(x,y,z) = \frac{-i}{\lambda} \iint_A E(0) \frac{\exp(ik\boldsymbol{R})}{\boldsymbol{R}} \left[\frac{1+\cos(\boldsymbol{R},\hat{z})}{2} \right] \mathrm{d}x'\mathrm{d}y', \tag{3.4}$$

where the integration is performed over the whole area of the opening, A, considering it as a mesh of secondary emitters of spherical waves, $\hat{z}$ is the vector pointing along the normal of the opening towards the receiver, and $\cos(\boldsymbol{R}, \hat{z})$ is the angle between the range to the detector and the normal to the opening. Usually diffraction is studied in on-axis configuration, where this cosine term is close or equal to 1 (see section 3.2.2). Also, this cosine term, previously called the obliquity factor is equal to zero in the reverse direction, which mathematically explains Huygens assumption of wave propagation only in the forward direction.

The Fresnel-Kirchhoff integral is quite challenging to be solved analytically, as mentioned before in section 2.4.0.1, even for uniform illumination and far-forward direction, i.e. approximating the obliquity factor as 1. Thus approximations to ease the solving process for simple shapes are introduced. These are going to be discussed in the next section.

Fresnel suggested that if the obliquity factor, $K(\chi)$, is 1 and that $R \cong |z|$, thus the denominator in equation 3.4 can be brought outside the integral. But due to the fact that small differences in R can lead to big variations in the oscillating exponential, expansion of R is performed, under the assumption that viewing distance, z, is much larger than the size of the opening, i.e. observing diffraction in the far-field:

$$R = z\sqrt{1 + \frac{(x - x')^2 + (y - y')^2}{z^2}} \cong \left[1 + \frac{(x - x')^2 + (y - y')^2}{2z^2}\right]. \tag{3.5}$$

This expansion is based on the Taylor series expansion, and the exponential in equation 3.4 can be split into x' and y' dependence:

$$\begin{aligned} E(x, y, z) \cong & -\frac{i \exp(ikz) \exp(i\frac{k}{2z}(x^2 + y^2))}{\lambda z} \\ & \times \iint_A E_i \exp(i\frac{k}{2z}(x'^2 + y'^2)) \exp(i\frac{k}{z}(xx' + yy'))\mathrm{d}x'\mathrm{d}y', \end{aligned} \tag{3.6}$$

making it easier to solve for simple shapes - rectangular or circular shaped aperture - shown in sections 3.1.4.1 and 3.1.4.2, respectively.

A further approximation is made by Fraunhofer, for the limiting case of observing the aperture from a very far distance, i.e. far-field approximation. It must be noted here that in FSR such a situation is what is typically observed.

According to Fraunhofer, in the far-field the diffraction pattern will have a mathematical form of:

$$\begin{aligned} E(x,y,z) \cong -&\frac{i\exp(ikz)\exp(i\frac{k}{2z}(x^2+y^2))}{\lambda z} \\ &\iint_A E_i \exp(i\frac{k}{z}(xx'+yy'))\mathrm{d}x'\mathrm{d}y', \end{aligned} \tag{3.7}$$

thus the pattern of the field strength depends only on the diffraction angles, given by: $\cos^{-1}(x'/z)$ and $\cos^{-1}(y'/z)$. It must be noted here that solutions of the FK diffraction integral for simple shapes, discussed below, is based on the far-field approximations.

So by equation 3.6, the calculation of the field strength at an arbitrary point in space due to the propagation of an EMW through an opening (or aperture) is simpler when compared with equation 3.4. This enables the application of numerical calculations for simulation of target signatures, which are discussed in Chapter 3.

3.1.4 Fresnel-Kirchoff diffraction integral solutions for simple shapes

The FK diffraction integral has known analytical solutions only for simple opening shapes - rectangular and circular. These are going to be shown below.

3.1.4.1 Rectangular geometry

Considering a rectangular opening of area $4lh$, where $2l$ and $2h$ are the two sides of the rectangle, as shown in Fig. 3.5, and centre P, with axes Py' and Px' parallel to the sides. Then the integration of the diffraction integral, equation 3.7, can be performed over the two independent variables - x' and y', producing a field at an arbitrary point away from the opening [21]:

$$E_{rect} = E_i \left(\frac{\sin(k(l)\sin(\theta))}{k(l)\sin(\theta)} \right) \left(\frac{\sin(k(h)\sin(\phi))}{k(h)\sin(\phi)} \right), \tag{3.8}$$

where θ and ϕ are the horizontal and vertical diffraction angles, respectively, as shown in Fig. 3.5. The full derivation of equation 3.8 can be seen in every optics textbook, eg. [21].

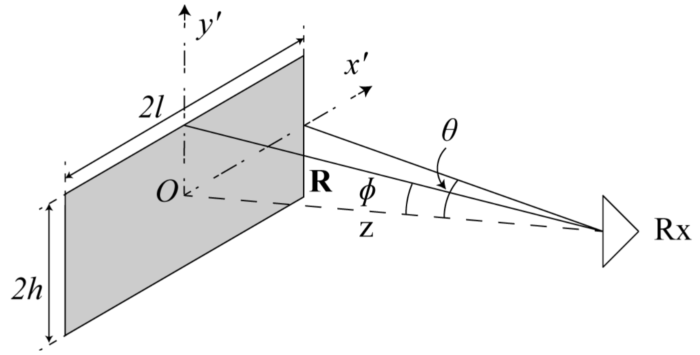

Figure 3.5: Coordinate system for observing diffraction of a rectangular opening of area $(2l)*(2h)$. Horizontal, θ, and vertical, ϕ, diffraction angles are shown with respect to a Cartesian coordinate system

The amplitude of the pattern of the diffraction is a two-dimensional sinc function, as can be seen in Fig. 3.6(a). The amplitude of the diffracted field along the z-axis is presented in Fig. 3.6(b), which shows how the diffracted pattern widens at larger observational distances, dissipating the energy along the x- and y-axis. The near-field patterns are going to be discussed in section 3.1.5, while the far-field pattern has the general shape shown in

Fig. 3.6(a). The diffraction pattern will continually evolve during the propagation along the z-direction, i.e. waves emitted from the secondary radiators will constantly interfere between each other. However, eventually it is going to form a final shape, which is going to be maintained, but increase in size proportional to the distance z, see Fig. 3.6(b) and 3.7(b). This final shape is known as the far-field pattern.

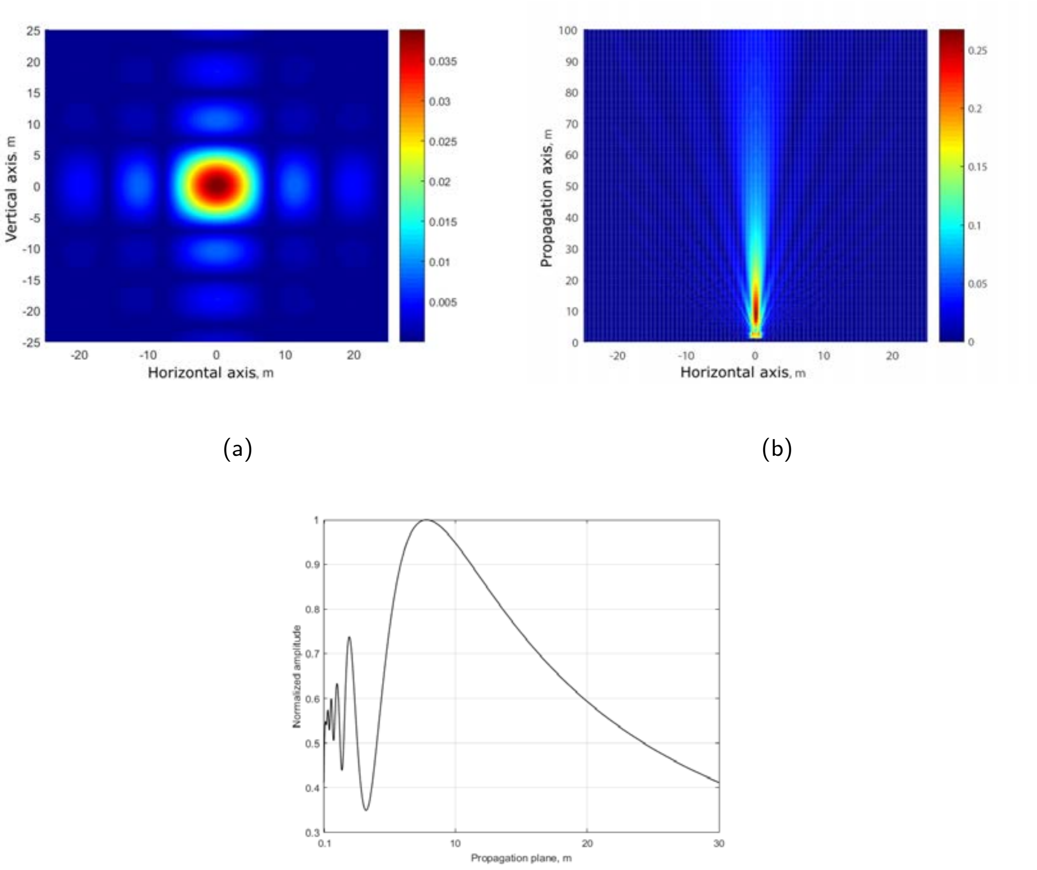

(a)

(b)

(c)

Figure 3.6: The pattern of the diffracted field for a square of side 1.8 m at 1 GHz incident frequency in x, y plane, observed at 50 m away from the receiver - (a) and the development of the diffraction pattern amplitude in the y, z plane, i.e. at different propagation distances - (b). The on-axis intensity of the diffraction pattern of the opening zoomed at shorter propagation distances - (c)

One way in which the progression of the diffraction pattern with different observation distances, shown in Fig. 3.6(b), can be analysed is by looking at the amplitude of the diffracted field at different distances from the opening, in an on-axis configuration, i.e. along the z-axis from the geometric centre of the opening. This is shown in Fig. 3.6(c) for observation distances from 0.1 to 100 wavelengths - 0.03 to 30 m. The figure clearly shows the well known and expected amplitude oscillations in the near-field due to the presence of both electric and magnetic fields [24]. Using the relationship for far-field distance calculation: $Distance = 2h^2/\lambda$, it can be computed that such distance is equal to 36 wavelengths. By inspection of Fig. 3.6(c) it can be seen that oscillations are present to a distance of around $25\lambda \approx 7.5m$ and then the intensity decays, as it spreads proportionally to the distance away from the opening, as expected by Fraunhofer theory.

As mentioned at the end of the previous section, another shape which can be solved analytically is the circle. Below is an analogous description to the above about circular openings.

3.1.4.2 Circular geometry

For a circular shaped opening the coordinates are appropriately changed to polar, thus the integrand of the Fresnel diffraction integral can be substituted by a Bessel function of the first kind. For such an aperture of diameter, r_c, the diffraction pattern, at an arbitrary point, is given by [21]:

$$E_{circ} = E_i \frac{J_1(kr_c \sin(\theta/\lambda))}{kr_c \sin(\theta/\lambda)}, \tag{3.9}$$

where J_1 is a Bessel function of the first order, and θ is the diffraction angle, given by the ratio of the observation distance and the radius of the circular aperture. The geometry is analogous to the one presented in Fig. 3.5, with the aperture shape the only difference.

The resulting pattern is known as the Airy pattern and can be seen in Fig. 3.7(a), as result of modelling of the diffraction from a circle of radius 1.8 m at frequency of 1 GHz and observation distance of 50 m. The diffraction pattern as a function of observation distance can be seen in Fig. 3.7(b). Similar conclusions can be made to the case of a circular geometry, as done for the rectangular opening above, i.e. that the energy from the diffraction dissipates in x- and y-axis, so that the total on-axis amplitude reduces as the observation distance increases.

Due to the different area between the two targets (the square has area of 3.24 m^2, while the circle - 2.54 m^2) the maximum amplitude of the diffracted waves for both targets is going to be different - about 1.3 times, comparing Fig. 3.6(a) and 3.7(a). Also, the far-field boundary theoretically will be the same, but comparing Fig. 3.6(c) and 3.7(c), it can be seen that the maximum amplitude of the diffracted wave on the z-axis is different for both cases. The difference in the value corresponds to the ratio of the area of the square and that of the circle.

Again similar conclusions can be drawn for the on-axis diffraction amplitude resulting from a circular opening. There is an oscillation of the total diffracted amplitude in the near-field, and after reaching a maximum, decays proportionally to the distance.

The solutions of diffraction for simple shapes have been presented. These can be used for the calculation of the FSCS of targets with such shapes, as shown in section 2.4.0.1.

Using FK diffraction integral, then the diffracted wave amplitude can be calculated, for a point far away from the aperture and when plane waves are perpendicularly incident on that aperture. In scenarios where these assumptions are not valid, the Rayleigh-Sommerfield (RS) diffraction theory is used for the calculation of the diffracted wave

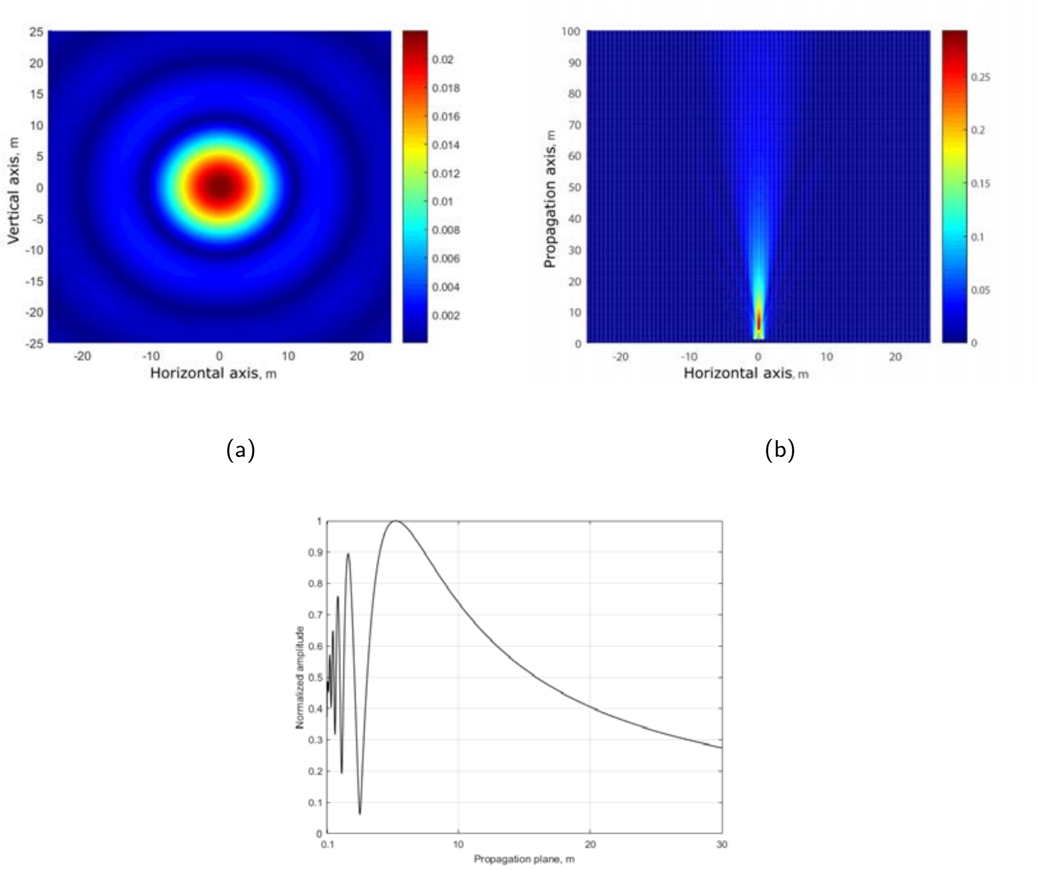

(a)

(b)

(c)

Figure 3.7: The pattern due to a circular aperture of diameter $2*1.8m$ at 1 GHz incident frequency in x, y plane, observed at 50 m away from the receiver - (a) and the development of the diffraction pattern amplitude in the y, z plane, i.e. at different propagation distances - (b). The on-axis intensity of the diffraction pattern of the opening zoomed at shorter propagation distances - (c)

amplitude. This is considered in the next section.

3.1.5 Rayleigh-Sommerfield (RS) Theory

It is widely accepted that even though Kirchhoff diffraction integrals are adequate for the solutions of many real-world problems, it is not a full solution to the diffraction problem, due to the nature of the assumed boundary conditions: perpendicular incidence on the aperture and far-field reception. [21]. So for problems, relating to systems, where the observation point is in the immediate neighbourhood, i.e. near-field, of the aperture, other more suitable mathematical description of diffraction need to be used, one of which is the so called Rayleigh-Sommerfield diffraction integrals. The full derivation process of the Rayleigh diffraction integrals is analogous to the Kirchhoff procedure, though it considers different boundary conditions [21].

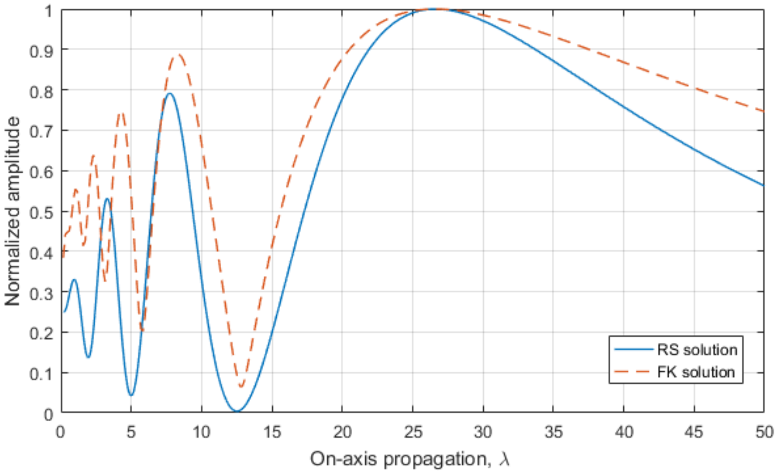

Figure 3.8: Comparison of solutions for on-axis intensity in the near field for a square aperture of size 10λ

Shown in Fig. 3.8, is a comparison between the near-field on-axis intensity of the electric field, due to diffraction of a square shaped opening of size 10λ. It shows visible differences between the solutions of the Fresnel-Kirchhoff and the Rayleigh-Sommerfield theories in the near field, as discussed in literature [21,40,41]. For this particular case the oscillating intensity stabilizes at 25λ away from the aperture, where the two solutions start to overlap in their predictions. In the scenario shown in Fig. 3.8, the far-field boundary for a opening of size 10λ is at 60λ. In reality, the two solutions will have almost the same results for the Fresnel region, extending from 10λ to 25λ in this particular case. The biggest differences between the solutions of the two theories is within the radiative near-field, below 10λ, roughly about the size of the opening itself.

In FSR a near-field effect may be observed due to:

- Targets moving close to either Tx or Rx, or
- Target size which is of the same order of the range.

In reality though, it is expected that most targets will not be in the immediate (reactive) near-field, i.e. a distance smaller than their size away from Tx or Rx, where differences between the two diffraction theories is substantial, thus in practice RS theory is not necessarily useful in FSR. This is further shown in section 4.4.2.

The Rayleigh diffraction integral of the first kind, E^{I}_{RS}, solves for a so called Dirichlet boundary value problem, while the diffraction integral of the second kind, E^{II}_{RS}, - a Neumann boundary value problem, [21] and are given by equations 3.10 and 3.11, below. The Dirichlet boundary value is exactly the same as used for the derivation of the FK diffraction integral, and considers a perpendicular plane wave incidence. On the other hand the RS integral of second kind, accounts for spherical wave incidence as well as the direction of the incident wave, but can only solve on-axis diffraction amplitude, i.e. along $z - axis$.

$$E^{I}_{RS}(x,y,z) = \frac{iA}{\lambda} \iint_A \frac{\exp(ik(r+s))}{rs} \cos(\hat{n}, \boldsymbol{r}) \mathrm{d}r \tag{3.10}$$

$$E_{RS}^{II}(x,y,z) = \frac{1}{2\pi}\iint_A \frac{\exp(ik(r+s))}{rs}\cos(\hat{n},\boldsymbol{s})\mathrm{d}r \tag{3.11}$$

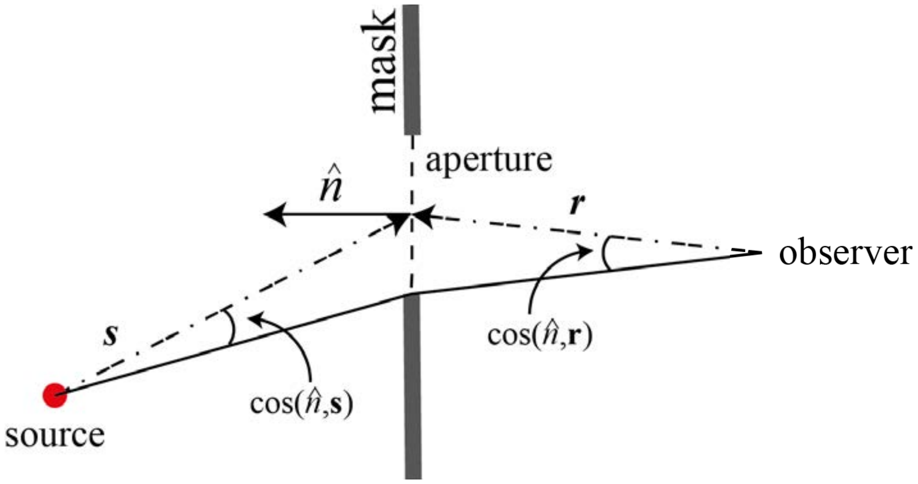

Figure 3.9: Geometry of the Rayleigh-Sommerfield solution of diffraction

In both equations 3.10 and 3.11, $\boldsymbol{r}$ is the vector along the aperture and the observation point and r is its magnitude, while $\boldsymbol{s}$ is the vector along the incident radiation, as seen in Fig. 3.9. It can be noted that the diffraction integral of the first kind solves a similar boundary condition as the FK integral, i.e. $\hat{n}$ and $\mathbf{s}$ are pointing in the same direction. The integral of the second kind, however considers that $\hat{n}$ and $\mathbf{r}$ are in the same direction.

The Rayleigh-Sommerfield diffraction integrals converge to the Fresnel-Kirchhoff expressions, when $r \gg \lambda$, $s \gg \lambda$ and small angles of diffraction and incidence. Thus away from the aperture, as the diffraction angles become smaller, there is no difference between the Fresnel-Kirchhoff and Rayleigh-Sommerfield solutions, see Fig. 3.8 after 10λ, though it is shown that the RS diffraction integrals are mathematically consistent and are holding true for near-field diffraction problems [21, 40–42]. It is, also, known that whatever the initial conditions of the diffraction, equation 3.12, below, holds true [21].

$$E_{FK} = \frac{1}{2}(E_{RS}^{I} + E_{RS}^{II}) \tag{3.12}$$

In the cases of small incidence and diffraction angles the FK diffraction integrals give similar results to either of the RS integrals [21].

For the accuracy of the FS radar target signatures, these models show good agreement with empirical observations, away from the target, as seen in Chapter 6. The Rayleigh-Sommerfield diffraction theory was used for the calculations of near-field FSR target signatures, in section 5.5.

The discussion above provides with the basic understanding of the theory of diffraction, for a receiver positioned both near and far from the aperture. It was shown that the FK integral provides with a simpler solution to the Fresnel diffraction, which can be numerically modelled. However, it does not provide with correct amplitudes for near-field observations. The advantage of using the RS diffraction integrals was shown, though due to the boundary conditions used for the derivation of the RS integral of the second order, it can only be used for calculations along the z-axis or small deviations from this axis.

It must be noted that throughout the thesis the terms aperture and opening are going to be interchangeably used. The equivalence of both an opaque aperture and transparent opening is the, so called, Babinet's principle, discussed below.

3.1.6 Babinet's principle

The diffracted EM fields was discussed above. Across the description the terms opaque and transparent apertures have been used with the same meaning. This is explained by the Babinet's equivalence theorem, first described in [43], which states that the EM field diffracted by an opening in an opaque screen will be exactly the same as the one due to a opaque object in transparent space with the same size as the slit, but with opposite phase.

This is based on a superposition technique that is used for the calculation of the diffraction field by complicated shapes and graphical representation of the idea behind that technique is shown in Figure 3.10. In the figure, the field, due to an obstruction in infinite transparent plane is regarded as equivalent to the difference between an unobstructed plane wave and the diffraction of the plane wave by an aperture of the same dimensions as the obstruction [37]. In mathematical form this principle is given by equation 3.13, where E_i is the field strength at an arbitrary observation point, O, when no screen is present, and E_1 and E_2 are the field strength due to presence of complimentary screens, i.e. openings in one correspond to opaque portions in the other [21].

$$E_1 + E_2 = E_i \tag{3.13}$$

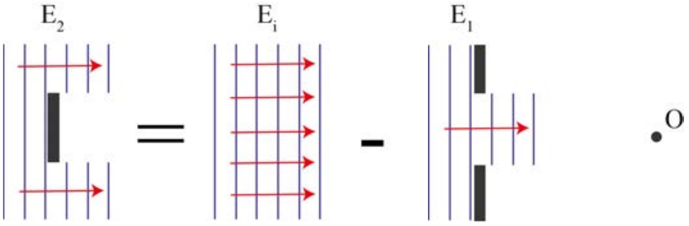

Figure 3.10: Equivalent difference of diffraction and shadow radiation

From equation 3.13 two conclusions arise [21]:

- if $E_1 = 0$, then $E_2 = E_i$, meaning that at points in space where the strength of the field is zero due to the presence of one of the screens, the strength in presence of the other is the same as if there was no screen present; and
- if $E_i = 0$, then $E_1 = -E_2$, which means that at points, where an unobstructed field

is zero, then the phases of E_1 and E_2 differ by π and the amplitudes of the field strengths due to each of the two complimentary screens are equal.

In the context of FSR, the same principle may be used, where a 3D target is represented by its shadow contour in the incident plane and then by a complimentary aperture in an opaque plane, consisting of secondary radiators according to Huygens principle [25]. Also, it should be noted that in received signatures of FS targets, which are in the optical scattering regime in the far-field, there always exists a leakage signal, which resembles the unobstructed incident radiation [3].

3.1.7 Conclusion

In the discussion above the scalar theory of diffraction was briefly described.

The Huygens-Fresnel principle was introduced, developing the approximation that the diffracted field can be considered as superposition of secondary spherical waves.

The Fresnel-Kirchhoff and the Rayleigh-Sommerfield diffraction integrals were discussed, indicating the approximations and assumptions in the physics behind each of them. The solutions of the FK diffraction integral for simple shaped apertures (rectangular and circular) were shown.

Further the Babinet's equivalence principle was introduced. It states that the diffracted field by an opaque aperture is equivalent to the one diffracted by an opening with the same size, subject to a $\pi/2$ phase shift.

It was shown how the theory of diffraction can be applied to FSR, mainly in ways of calculating the FSCS or modelling the full target signatures.

In the past century diffraction has been extensively studied for potential application in imaging and tomography. An important discovery regarding optical imaging, based on diffraction, has been discovered by Denis Gabor in 1948. This application is known as holography and it is going to be discussed next in the context of FSR and its application to FSR signals.

3.2 Basics of Holographic Imaging

Images, known to the general public, like paintings and photographs, record the intensity of scattered light, losing all phase information, i.e. optical paths [44].

Holography is the method of recording and reconstruction of holograms. A hologram represents a recording of a light field produced by the presence of a particular object or objects. It is used to display a three-dimensional image of the subject imaged. The hologram itself is not an image, but rather a recording of the interference pattern of EM radiation, and is only readable when viewed under light, which is coherent to the one used when recording the hologram [45]. The basic underlying theory of the holographic process is described below, as a prerequisite for the development of the target shadow profile reconstruction algorithm. Also, only the in-line holography geometry will be investigated due to its relation to FSR geometry.

3.2.1 Principle of holography

Standard photography is a process of recording the 2D projection of the intensity of light waves, scattered by 3D objects, so that the phase information about the EM field is not used in the process. Denis Gabor in the 1960s showed that if both phase and amplitude of the scattered EM radiation can be recorded, then an image of the object can be reconstructed and it is going to be visually indistinguishable from the object holographed. An example of a hologram and its reconstruction is shown in Fig. 3.11.

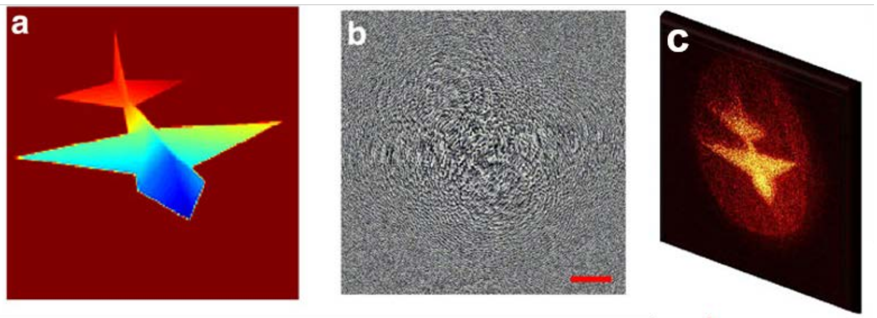

Figure 3.11: Example simulation of Gabor's holographic imaging method. The original object (wingspan - 330 μm, length - 232 μm) - (a); Hologram of the plane, taken at wavelength of 810 nm - (b); and the reconstructed image - (c). [4]

Holography is a two-step imaging process which involves the photography of the Fresnel diffraction pattern of an object (Fig. 3.11(b)) and the use of this record to construct an image of the original object(Fig. 3.11(c)). A simple block diagram, depicting these two steps is shown in Fig. 3.12.

The recorded diffraction pattern is called a hologram and bears little resemblance to the imaged object, nevertheless it contains most of the information required to construct an image of the object.

The hologram is produced by recording the Fresnel diffraction pattern on a photographic plate, as shown in Fig. 3.12(a). The light incident on the plate has a complex amplitude of which only the magnitude is recorded. Thus half of the information content of the wave is lost. The consequence is that the reconstruction is imperfect, due principally to the presence of a twin (or conjugate) image, occurring at a different focal point and thus being considerably out of focus.

The holographic process involves two steps: recording of a hologram (Fig. 3.12(a)) and

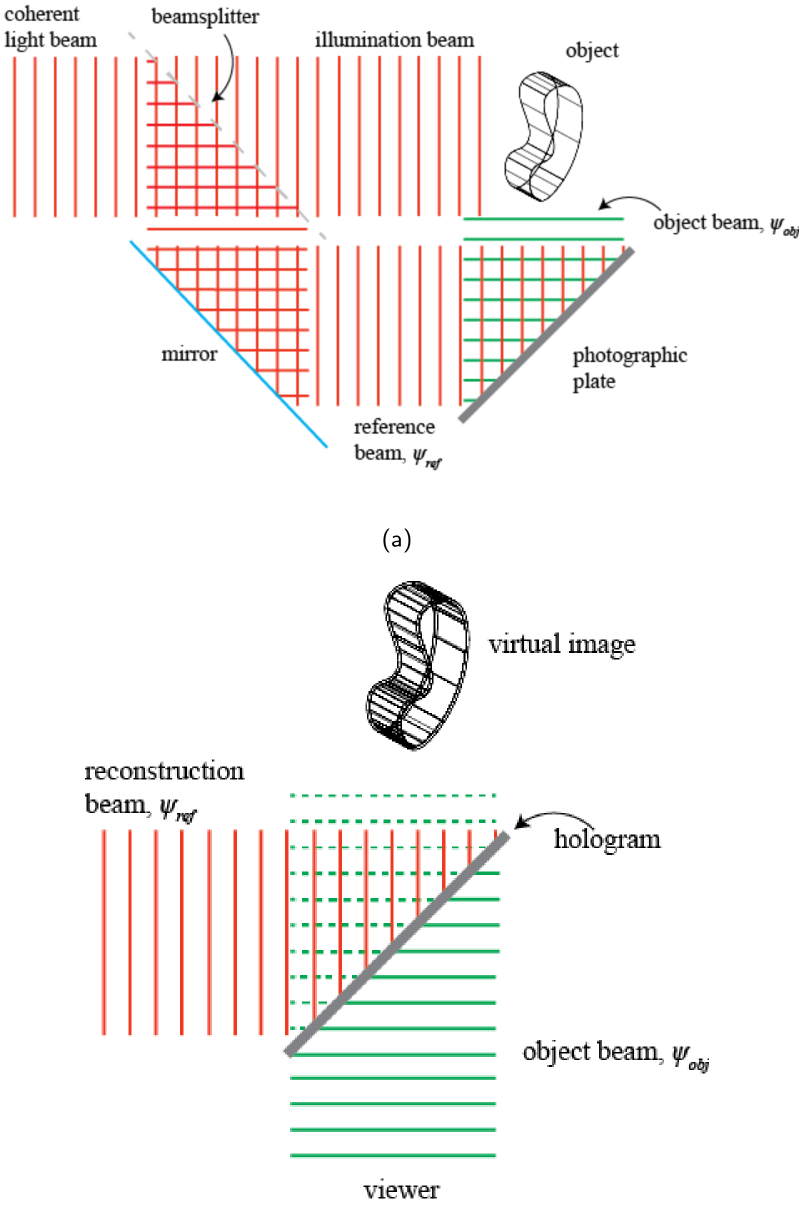

(a)

(b)

Figure 3.12: Block diagram of hologram recording - (a); and the reconstruction of the image - (b). The two diagrams show both the reference wave beam, ψ_{ref}, and the object wave beam, ψ_{obj}.

reconstruction of the image (Fig. 3.12(b)), and is developed as follows.

As light sensitive media can only record the intensity of EM waves, Gabor suggested that the phase information of the object can be encoded by recording the interference pattern of the incident and diffracted EM waves. The observed intensity in a hologram is given by [46]:

$$I(x,y) = A_{ref}^2 + A_{obj}^2 + 2A_{ref}A_{obj}\cos(\phi_{ref} - \phi_{obj}) \tag{3.14}$$

In the equation A_{ref} and A_{obj} are the amplitudes of the incident and diffracted EM radiation, respectively, while ϕ_{ref} and ϕ_{obj} are their phases. By recording this interference pattern, Gabor showed, that the object image can be reconstructed by illuminating the recorded hologram with an exact replica of the reference wave used in its recording. Today, this is done by numerical reconstruction, due to the advances in computational power [45].

Image is formed after illumination of the hologram recorded (the hologram is given by equation 3.14) with the same wave that produced it [44, 45], i.e. the reconstruction of the image, is mathematically given by:

$$\begin{aligned} A &= A_{ref} I(x,y) \\ &\propto A_{ref}(\psi_{ref}^*\psi_{ref} + \psi_{ref}^*\psi_{obj} + \psi_{ref}\psi_{obj}^* + \psi_{obj}^*\psi_{obj}) \\ &= A_{ref}I_{ref} + A_{ref}I_{obj} + I_{ref}A_{obj} + A_{ref}^2 A_{obj}^*, \end{aligned} \tag{3.15}$$

where the first two terms represent the reference wave modulated by the intensities of the incident and the diffracted waves and the third term contains the desired information about the object. The last term contains the complex conjugate of the object wave. Thus equation 3.15 shows how the complex amplitude of a scattered wave can be preserved in two-dimensional imaging [47]. The ψ terms in equation 3.15 represent the exponentials of the corresponding reference and object waves.

It should be mentioned that every part of the hologram contains the whole information about the object and object images can be reconstructed by using part of the recorded holograms, however with reduced resolution [46].

Holography can be performed in a variety of set-up geometries, with both spherical and plane waves, Gabor himself used the so-called in-line set-up, which is the relevant to the holographic nature of the FS signal. Other geometries will not be discussed, but a detailed description can be found in literature [44, 46].

3.2.2 In-line holography

The in-line geometry in holography, represents the case where the holographed object lies on the axis connecting the reference source and the recording screen and the screen is placed perpendicularly to that axis. This is the original set-up used in Gabor's first experiments, see Fig. 3.13(a).

The holographed object is placed at a distance in the far-field from the receiver and is illuminated with a wave of phase ϕ_{ref} - red wavefront in Fig. 3.13(a), propagating in the z-plane from the emitter to the screen. The incident wave diffracts due to the presence of the object and forms the object wave with phase - ϕ_{obj} - green wavefront in Fig. 3.13(a). The resulting interference between the two waves is then recorded on the screen and is called a hologram. The distance from the emitter to the object is given by equation 3.16, where R_r is the distance from the object to the detector:

$$R_t = R - R_r, \tag{3.16}$$

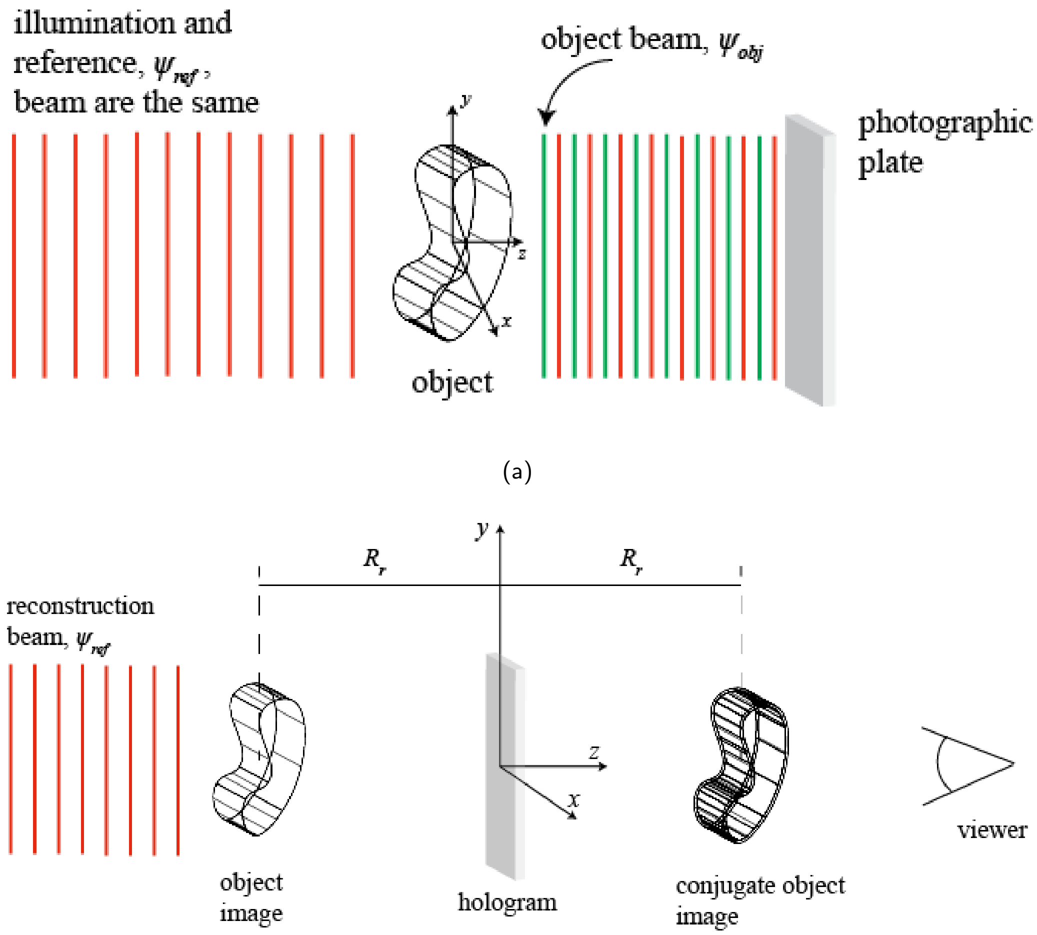

(a)

(b)

Figure 3.13: Block diagram of in-line hologram recording - (a); and the reconstruction of the image - (b)

A graphical representation of the holographic reconstruction is shown in Fig. 3.13(b), where a virtual image of the object can be seen on its original position, but at the same distance on the other side of the hologram, a real, twin-image occurs, due to the conjugate wave, resulting from the hologram reconstruction (equation 3.15) [21,44].

Considering equation 3.15:

$$A \propto A_{ref}I_{ref} + A_{ref}I_{obj} + I_{ref}A_{obj} + I_{ref}A^{*}_{obj}, \tag{3.17}$$

the first two terms deal with the reference wave, incident on the object, A_{ref}, where the first one ($A_{ref}I_{ref}$) is called the source term - consisting of both the complex amplitude and the intensity of the incident wave, while the second term ($A_{ref}I_{obj}$) is called the self-interference term. The last two terms in equation 3.17, correspond to the original object wave ($I_{ref}A_{obj}$) and its conjugate ($I_{ref}A^{*}_{obj}$) [44,46], and will be referred to as object wave and conjugate wave (or twin-image term), respectively.

When looking through the illuminated hologram, one sees an illusion of the object in three-dimensions, as if it were still present at distance R_r from the hologram. This image though can be distorted by the terms in equation 3.17. The source and self-interference terms superimpose the bright transmission on the image of the object [46]. This can however be removed through processing. On the other hand, the influence of the conjugate wave cannot be totally cancelled, as discussed below.

The twin-image term, represents a converging wave, forming a real image of the object at a distance R_r in front of the hologram (in space $z > 0$), see Fig. 3.13(b). This wave is the complex conjugate of the object wave, i.e. has opposite phase, thus the twin-image will be inverted in the z-plane. The twin-image will add to the background interference of the object image, coherently. For these reasons in-line holography is rarely used now, while off-axis geometries are preferred for microscopy applications. The conjugate image is removed through the use of off-axis set-up geometries [46].

However, it can be seen that due to the topology of facing transmit and receive antennas FSR has the same form as optical in-line holography, at radio frequencies, and so holographic principles may be applied successfully for FSR signals. This is going to be investigated later, but first lets discuss digital reconstruction of holographic images.

3.2.3 Digital in-line holography

Digital in-line holography (DIH) is the process of numerical reconstruction of the holographic image, which has the same topology like Fig. 3.13. The hologram is recorded digitally, and the reference wave is calculated numerically. A numerical calculation of the object waveform in a single plane is referred to as numerical reconstruction, each represents an image of the object focused at different depths and their combination will result in the three-dimensional image of the object [44, 46].

The reconstruction algorithm is based on the solution of the Fresnel-Kirhhoff diffraction integral, equation 3.6, which according to Fourier optics can be rewritten as [48]:

$$E(x,y,z) = K\mathcal{F}\left(A(x',y')\exp\left(-i\frac{\pi}{\lambda z}(x'^2+y'^2)\right)\right), \tag{3.18}$$

where K is the term outside of the integral in equation 3.6, so called propagation kernel or phase factor, and (x', y') is the parallel, sub-coordinate system of the object in the global coordinate system (x, y, z), as introduced in Fig. 3.4. This Fourier transform can be performed by the Fast Fourier Transform (FFT) algorithm, shown as $\mathcal{F}$ [46]. It has been shown that for the digital case, computation over a large number of matches is intense and inaccuracies arise from the approximations of the phase factor. Thus an accurate method for faster numerical reconstruction of holograms was developed by Kreuzer [44,49].

Considering the Fresnel-Kirchhoff diffraction integral, under the Fraunhofer approximation, i.e. the size of the object is much smaller than the distance to the source, and the distance object-screen is much larger than the distance object-source; the phase factor in front of the integral in equation 3.6 can be neglected. This phase factor can be considered equivalent to the exponential in equation 3.18, since it will result in a constant [49]. Also, as digital recording material, CCD and CMOS, are not continuous, the integration needs to be discretesized, and the coordinate system transformed to a form as below, according to [49]:

$$\begin{aligned} x'' &= x' \frac{R}{R_h} \\ y'' &= y' \frac{R}{R_h} \\ R_h &= \sqrt{R^2 + x'^2 + y'^2}, \end{aligned} \tag{3.19}$$

where R is the range from illuminator (Tx) to the CCD or CMOS (Rx).

To avoid boundary effects, occurring in Fourier transforms, where sharp edges are present, an effect known as ringing [50], a filter can be used to smooth the edges of the holograms. The last step of DIH is the application of the convolution theorem and the complex amplitude of the object image is given by [21,44,49]:

$$\Gamma(x, y, z) = \mathcal{F}^{-1}\{\mathcal{F}\{I\}\mathcal{F}\{K\}\}, \tag{3.20}$$

where I is the intensity distribution of the hologram, $E(x, y, z)$, and K is the convolution propagation kernel, expressed in the coordinate system given by equation 3.19. Each of the convolutions is going to produce an object image along one (x, y) plane, thus DIH algorithm allows for fast reconstructions of object image at various distances from the detector in real time [49]. It must be noted that the gain of processing time is in terms of days, compared to usage of FFT and filtering techniques, especially for moving targets [49].

A moving, 3D object can be accurately tracked and refocused for every time-frame its hologram is recorded by the application of the approach shown above. Numerical reconstruction has a major advantage to the analogue one, by enabling the reconstruction of both the amplitude and phase of the object wave, rather than only its intensity, i.e. amplitude [44]. A major advantage of the complex hologram is that only one image is produced after reconstruction, thus removing the influence of the defocused real image on the reconstruction quality [51].

The main qualitative measure of digital images is defined by the detail that a certain image holds. This measure is known as resolution. All digital approaches are resolution limited, either by the pixel resolution (CMOS or CCD pixel size and number), spectral resolution (ability to differentiate between two closely spaced lines) and spatial resolution (ability to resolve spectral features and frequencies). In the case of DIH, the resolution will be mostly affected by the pixel resolution, and will be discussed next.

3.2.3.1 Potential resolution of DIH

In digital holography the overall achievable pixel resolution of the reconstructed images is limited by the size of the receiveing screen [44]:

$$\Delta R_{DIH} = \frac{\lambda R_R}{N \Delta_S}, \tag{3.21}$$

where R_R is the distance between the screen and the object (see Fig. 3.13(b)), N is the number of pixels on the recording screen and Δ_S is the size of each pixel on the receiver. Thus in practical applications, the limiting factor is $N\Delta_S$, or the size of the receiver. Nowadays screens may have number of pixels in order of 10^7 or more, however the size of the pixel becomes smaller, thus the size of the receiver remains more or less the same.

Mostly, DIH is used in biology applications - mainly holographic microscopy. Fig. 3.14 below, show an example of a hologram of a shrimp and the reconstructed image [52].

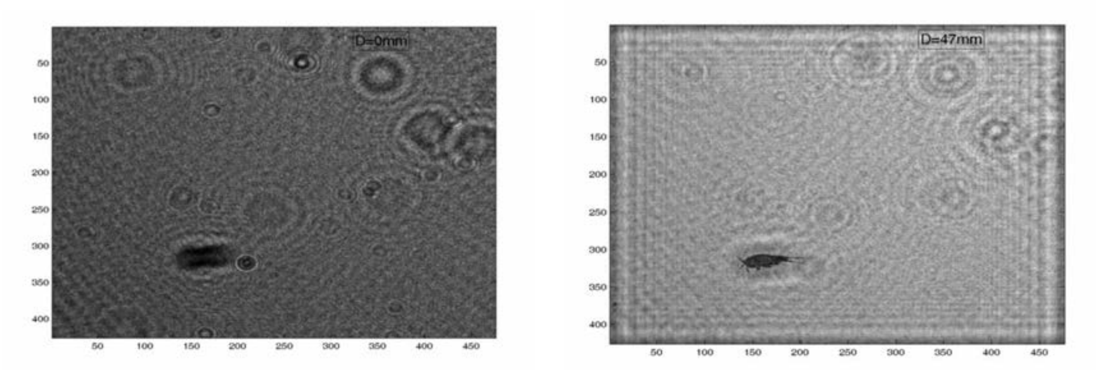

(a) (b)

Figure 3.14: Example of DIH. A hologram - (a); and its reconstruction - (b).

Holography has been usually applied to optical scenarios, and operation at RF frequencies has rarely been studied. As such, holography has been developed as strictly optical, but the same principles can be used for radio frequencies in the, so called, radio holography. The application of the theory discussed above for microwaves is going to be considered next.

3.3 Application of Holography to Radio waves

In the 1960s, after the introduction of the principle of holographic imaging by Gabor [47], there has been interest in the application of such image formation to microwave systems.

There are few main differences between waves at optical and microwave frequencies:

- Mathematical description of the interactions is identical in the scalar wave approximation, however diffraction effects are less pronounced at microwave frequencies, due to the difference in wavelength.
- Microwave frequency EM waves usually travel much further in the atmosphere, and at the same time are less energetic.
- Practically coherency is much easier achieved at microwave frequencies, also the devices used for optical waves are usually expensive and inefficient.
-

In these early stages, the main focus of research was not obtaining a true microwave hologram, but rather recording of the diffraction pattern of objects at radio frequencies and then reconstructing the image at optical frequencies [53–57].

Only a small amount of work has been done in the field of true microwave holography, that is using radio frequency radiation for both hologram recording and reconstruction [51].

However, there has been some work regarding the application of holography to radar systems [55, 58], mainly in the airborne SAR and bistatic ISAR configurations, though still optics have been used for the processing of the hologram. As such, this will not be discussed further.

In this section, a brief introduction to the previous research in microwave holography is going to be presented, together with a brief analysis of the applicability of holography in FSR.

3.3.1 Microwave holograms and optical reconstruction

In this subsection, the idea of using a microwave illumination and optical reconstruction is going to be presented, together with some of the fundamental issues of such an application.

The ability to use microwave theory for optical applications and vice versa in the context of holography, largely is due to the fact that the mathematical description of a microwave field is identical as that of the optical field when the both are considered as scalar waves [54]. This allows for usage of optical holography principles when dealing with radio frequency waves. As such, the mathematical process of recording of a hologram and the image reconstruction is going to be identical to the description in the previous section 3.2.

The main problem regarding true microwave holography in the 1960s was the fact that there was no way to accurately record the 2-dimensional diffraction pattern of an object at radio frequencies [54, 55]. Thus electrical signals from the detector (the microwave hologram) are, generally, amplified and converted to light by a lamp. The light intensity is then recorded onto a photographic film [53–55]. However, due to the usage of substantially different frequencies (the difference between optical and microwave frequencies is in the range of 10^5), the hologram has to be scaled down in spatial size proportional to the wavelength ratio.

Another fundamental issue regarding microwave holography to have been identified, when using a single receive antenna, is that the mechanical motion of the antenna needed for the scanning of the diffracted waves gives rise to scanning lines in the reconstructed images [54]. This effect can be removed by utilizing a receive array, which though increases the complexity of the system.

However, despite these issues, holograms of sufficient quality have been shown in literature

[53–55]. But still a very small amount of research has been performed in the case of true in-line microwave holography.

3.3.2 In-line microwave holography

Despite the fact that radio holography has been used in radar and tomography [58], a very small amount of research has been done with regards to the in-line configuration or usage of microwave frequencies to reconstruct the image. However, some advantages which are going to be discussed below, become apparent in true microwave holography.

Firstly, the requirement of a presence of a reference wave is removed. At radio frequencies it is possible to produce the interference pattern between the diffracted and reference wave without actually producing such a reference. This can be done by adding a locally produced reference signal before detection [51]. This is enabled due to the simpler hardware used for microwave applications and offers more flexibility to the system. However, this modelled reference needs to be phase coherent to the diffracted wave, thus phase shifters are needed to produce an accurate interference pattern.

Another major advantage is that radio frequency detectors can record both phase and amplitude, unlike optical detectors. The ability of producing a complex valued hologram is then enabled, which in turn removes the first two terms in equation 3.15, i.e. the two terms that represent the reference wave modulated by the intensities of the incident and the scattered waves [51].

The advantages outlined above, indicate that the application of holography at radio frequencies is not only possible, but in certain cases desirable. Lets next discuss the ability of a FSR system to operate as a holographic instrument.

3.3.3 FSR as a radio-holographic system

As discussed in literature holographic imaging has been used in the fields of SAR and ISAR, but not FSR [55, 58]. However, due to the fundamentals of FSR, discussed in section 2, it can be considered as a true radio-holographic system.

Recording of a radio hologram requires the use of a moving antenna or antenna array to recreate an extended imaging plane as in 3.15(a), while FSR topology naturally lends itself to radio holography due to similarity to optical set-up, where the holographic screen is inversely created through the motion of the target across the baseline, as shown in 3.15(b).

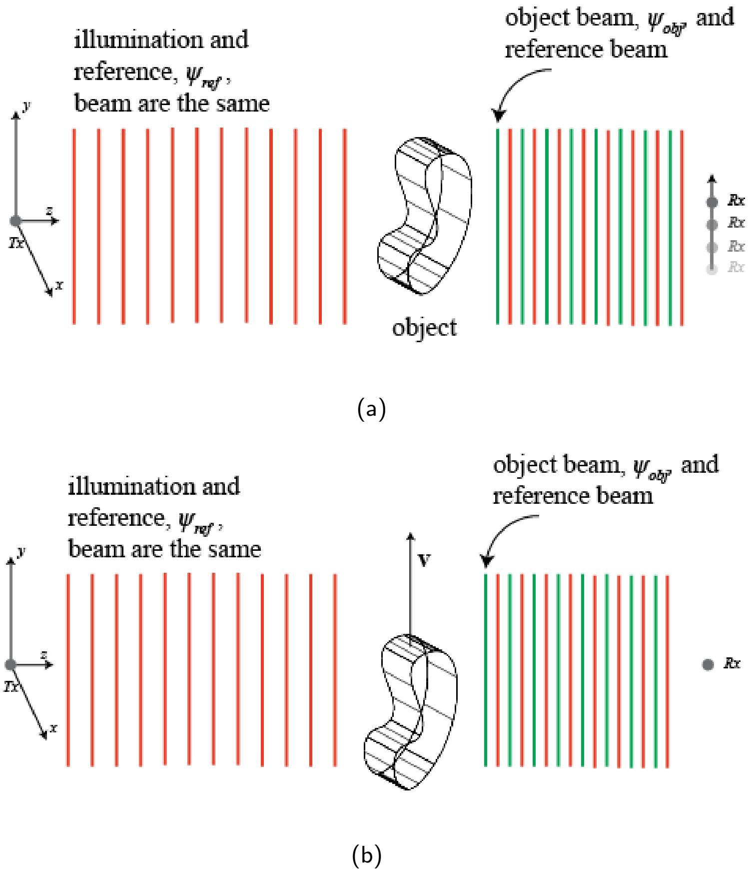

(a)

(b)

Figure 3.15: Equivalence of a moving receiver - (a), and a moving target - (b).

The reconstruction of the image is then analogous to the optical case. The main difference being, the reference re-illumination, which in the case of the moving target, would have to include a time-varying phase shift component due to the target motion. The same principle is used for radio-holography utilizing a moving receiver, rather than a receiver array [51]. This reconstruction process will be shown mathematically in chapter 3.

Another advantage is that a reference signal is present at all times in the recorded FSR signature, though labelled as leakage signal. This reduces the complexity of the hardware needed for holographic imaging. Also, through the use of a receiver capable of I/Q demodulation, a complex hologram is recorded, i.e. I and Q channel comprising both phase and amplitude information.

On the other hand, most FSR targets move in a single plane, thus creating a one-dimensional hologram. This would provide with only a single-dimension image of the target, as is later discussed in section 5.3. This disadvantage can be removed by the use of a receiving antenna array, positioned in the perpendicular plane of the target motion.

In the discussion above it can be seen that FSR is a prime candidate for a radio-holography system and this thesis is going to be dedicated to the application of holography to received target signatures in FSR.

3.4 Conclusion

In this chapter the physical background of FSR fundamentals was discussed. Scalar theory of diffraction was shown in the context of FSR, and will be further used for target signal modelling.

The scalar theory of diffraction was briefly introduced, where the Huygens-Fresnel principle was shown as a generalized description of the propagation of EM waves. The Fresnel-

Kirchhoff and Rayleigh-Sommerfield diffraction theories were developed, indicating the main approximations and assumptions used in their derivation. Solutions of the two theories were compared and conclusions on the validity of FK theory in FSR was made. Further the Babinet's principle was discussed.

Holographic imaging was introduced on the basis of the theory of diffraction. The recording of a hologram and the reconstruction of an image from that hologram was shown for the general case, as well as for the in-line geometry. Digital in-line holography was introduced and the resolution of the digitally reconstructed images was discussed.

Lastly, the application of the holographic principles at radio frequencies was discussed. It was shown that the application of a RF receiver will provide with substantial advantages over usage of optical detectors. The utilization of FSR as a radio-holographic system was then analysed. It was found that FSR target signatures are prime candidates for research into the application of holography to microwaves. This is due to the ability of RF equipment to record both phase and amplitude with relative simple hardware, compared to an optical set-up.

The holographic principle is used as a backbone for the reconstruction of the target profile in FSR, discussed in chapter 4, and the signal modelling discussed next.

CHAPTER 4

SIGNAL MODELLING IN FORWARD SCATTER RADAR

4.1 Introduction

Henceforth, the target signal or full FSR signature will be taken to mean the transmitted signal scattered from the target into the receive antenna direction. The Doppler signature will represent the phase of the scattered signal due only to the motion of the target. In the following chapter methods for the calculation of such signals are presented. These are based on the diffraction phenomenon and appropriate theory [21] where the Fresnel-Kirchhoff diffraction integral is used, together with the application of Babinet's principle.

Due to the big difference in the underlying physical phenomena governing signal formation, shown in section 2, the scattered signals in FSR modelling are different to those of bistatic and monostatic cases. Several algorithms for FSR signal simulations and relevant calculations have been proposed. These are going to be presented below, where the main advantages and disadvantages of each method will be outlined, together with examples of target signatures calculated with each of the approaches.

4.2 Model for point-like target and rectangular plate

The model of the FS signature for a point-like target is the most simple one, where the target signature is calculated on the basis of the Doppler phase due to the movement of this target [6, Chapter].

The angular frequency due to such phase is given by [3]:

$$\omega_d = \frac{2\pi}{\lambda} \frac{\mathrm{d}\left(R_{Tx} + R_{Rx} - BL\right)}{\mathrm{d}t}, \tag{4.1}$$

where R_{Tx} and R_{Rx} are the ranges target-transmitter and target-receiver, respectively, and BL is the distance transmitter-receiver, according to a typical topology of FSR, shown below, where the transmitter is located at the origin of a coordinate system, x, y, z, and the receiver position is $(BL, 0, 0)$, BL denoting the length of the baseline. A local coordinate system, x', y', z', with origin the geometric centre of the target, P, is parallel to the global coordinate system, x, y, z of the Tx and Rx and is positioned at x_p, y_p, z_p, as shown in Fig. 4.1.

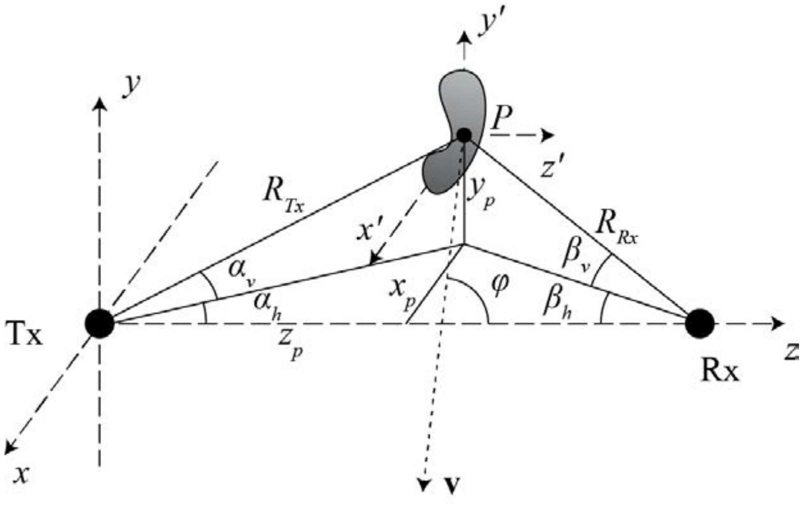

Figure 4.1: A typical FSR topology

In the case of a point target the centre of the target is the target itself. The horizontal diffraction angles are denoted by α_h and β_h, with respect to transmitter and receiver, while the vertical diffraction angles are denoted by - α_v and β_v.

The target is assumed to move in the x, z plane, i.e. no vertical motion, with velocity vector $\mathbf{v}$, intersecting the baseline at angle φ.

The complex Doppler phase signature of a point-like target at baseband, will then be given by:

$$S(t) = \exp(-i\omega_d t); \tag{4.2}$$

The model can then be extended to calculate the FS signatures of extended targets by the modulation of the Doppler phase information with the target's cross-section. The FSCS for a target is given as the time-varying diffraction pattern of the target's aperture and is given by, equation 4.3, discussed in section 2.4.0.1. The only difference between equation 2.13 and 4.3 is the labeling of the diffraction angles.

$$\sigma_{FS} = \frac{4\pi}{\lambda^2} \left| \iint_A \exp\left(-ik(x' \cos(\beta_h) + y' \cos(\beta_v)\right) \mathrm{d}x\mathrm{d}y) \right|^2, \tag{4.3}$$

As stated in sections 2.4.0.1 and 3.1.2 an analytical solution of equation 4.3 can only be found for simple targets. Thus this model is only used for modelling of the FS target signature of simple targets, like rectangles. For a rectangular plate target the FSCS is given by equation 2.18, which would produce a sinc-like function, as shown in Fig. 3.6(a). Shown in Fig. 4.2 is a modelled signature for a square target of size 1.6 x 1.6 m and a point-like target at 1 GHz incident CW wave, moving at 30 kph, perpendicularly towards the middle of a baseline of 50 m.

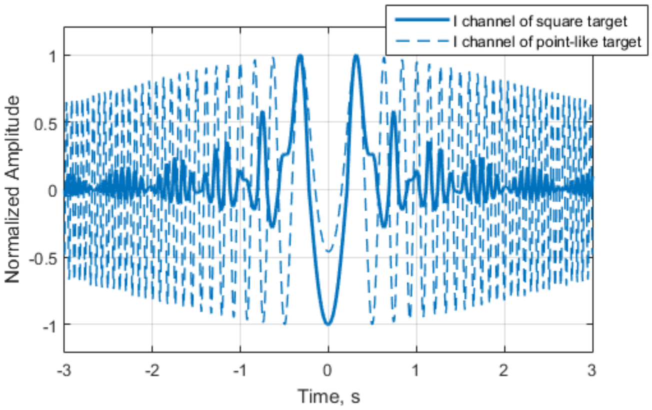

Figure 4.2: Target signature of a square and a point-like target, modelled via the free-space model briefly introduced above

The two signatures in Fig. 4.2 show the fundamental difference between the forward scatter target signatures between a point-like and an extended target. The signal from the point-like target has non-constant envelope due to the propagation loss at different distances between Rx and Tx at subsequent points in the target path. The envelope of the rectangular target's (as an example for an extended target) signature has a sinc-like shape, which is due to the FSCS.

As this model has an analytical solution only for simple shaped targets, which are not very interesting in practice from an imaging point of view. More complex simulation algorithms are proposed in the next subsections. These models will be used for testing and verification of the imaging algorithm for complex extended targets.

4.3 Signal modelling for extended target

Signal modelling methods, which account for both the diffraction of the target (and thus its shape) and the movement of the target through the baseline, are introduced in this section.

Two main methods for the calculation of the signal of an extended target, both based on the Fresnel-Kirchhoff diffraction integral, are known: Shadow Inverse Synthetic Aperture Radar (SISAR) [1] and a model based on the direct numerical solution of the FK diffraction integral [25].

4.3.1 SISAR

The SISAR model was first derived for an airborne target and as such it exploits series of assumptions for the solution of the FK integral for the particular scenario: pure far-field zone operation, small diffraction angles, optical scattering region, free space propagation [1].

The basic geometry of a FSR system is shown in Fig. 4.1. The transmitter is placed at the origin of a Cartesian coordinate system, (x, y, z), while the receiver is placed at point R at $(0, BL, 0)$. The coordinate system (x', y', z') is parallel to (x, y, z), with origin - P - the geometric centre of the target. It is assumed that the target is moving with velocity v, with trajectory, intercepting the baseline at an angle of φ. α_v and β_v are the vertical diffraction angles, while α_h and β_h are the horizontal ones.

When the Physical Optics approximation applies for the studied scenario, i.e. the target's dimensions are much larger than the wavelength, one can use the Fresnel-Kirchoff diffraction integral to calculate the forward scattered signal by the target [21].

This signal strength, according to the topology set above, can be represented as [1, 33]:

$$\begin{aligned} E(x, y, z) = {} & \frac{(\cos\alpha_h + \cos\beta_h)\exp(ikh + i\Omega^2 x_p^2)}{i\lambda R_{Tx} R_{Rx}} \cdot \\ & \int_0^{y'} H(x') exp(i\Omega^2 v^2 \sin(\varphi)^2 (\frac{x'}{v} + t)^2 dx', \end{aligned} \tag{4.4}$$

where R_{Tx} and R_{Rx} are given by equations 4.5 and 4.6 and Ω is parameter that is inversely proportional to the local Fresnel radius, r_f, given by equation 4.7:

$$R_{Tx} = \sqrt{(x' + x_p)^2 + (y' + y_p)^2 + z_p^2} \tag{4.5}$$

$$R_{Rx} = \sqrt{(x' + x_p)^2 + (y' + y_p)^2 + (BL - z_p)^2} \tag{4.6}$$

$$\Omega = \frac{\sqrt{\pi}}{r_f} \tag{4.7}$$

$$r_f = \sqrt{\lambda(x_p + BL - x_p)} \tag{4.8}$$

$H(x')$ is called the Complex Profile Function (CPF), which is dependent on the height of the target:

$$H(x') = \int_0^{y'} \exp(i\Omega^2(y'^2 + 2y'y_p)dy' \tag{4.9}$$

The CPF is the function which can generate a target profile and will be revisited further in section 5.

The signal model in the case of the surface moving target is different than in [1] as we are considering a ground moving target with smaller size, narrow diffraction angles, small elevation and arbitrary trajectory.

4.3.1.1 SISAR for the ground surface moving target

For the ground moving target we have a different approach to deriving the diffraction model, as the approximations used in [1] are not valid. In the ground case the observation period available for ground moving targets is not as prolonged as for airborne (due to the smaller length of baseline), thus the Fresnel radius, r_f is not time-independent and the dimensions of a typical ground target are relatively smaller than airborne targets.

Taking into account the assumptions for the ground moving target case, one can express the Fresnel-Kirchhoff's diffraction integral, via a Taylor series expansion of the ranges, R_{Tx} and R_{Rx}, over the coordinates of the target, shown in equation 4.10 and 4.11. Thus the diffraction integral takes the form shown in equations 4.12 [5]. This expansion is possible for the air moving target, however it is needed for the ground target due to the fact that baseline lengths are usually much shorter than in the airborne case and that the target dimensions are within a couple orders of magnitude with the baseline length.

$$R_{Tx} \approx z + \frac{(x'^2 + 2x'x_p) + (y'^2 + 2y'y_p)}{2z} \tag{4.10}$$

$$R_{Rx} \approx z + \frac{(x'^2 + 2x'x_p) + (y'^2 + 2y'y_p)}{2z} \tag{4.11}$$

$$E = \frac{|E_i|(\cos(\alpha_h) + \cos(\beta_h)}{2j\lambda R_{Tx} R_{Rx}} \iint e^{ik((\frac{1}{2R_{Tx}} + \frac{1}{2R_{Rx}})(x'^2 + 2x'x_p))} dx'dy', \tag{4.12}$$

considering $|E_i|$ as the amplitude of the incident wave, for a target moving along the x-axis we have that $x_p = vt\sin(\varphi)$, so that:

$$E = \frac{|E_i|(\cos(\alpha_h) + \cos(\beta_h)}{2i\lambda R_{Tx}R_{Rx}} e^{ikBL} \int H(x')e^{i\gamma(\frac{x'^2}{2v^2}+\frac{x't}{v})}dx', \tag{4.13}$$

where γ is the term expressing Doppler phase change (information about the trajectory) and is given by:

$$\gamma = k(\frac{1}{R_{Tx}} + \frac{1}{R_{Rx}})v^2 \sin^2(\phi) \tag{4.14}$$

The CPF, $H(x')$, is given by:

$$H(x') = \int_0^{y'} exp(ik(\frac{1}{2R_{Tx}} + \frac{1}{2R_{Rx}})(y'^2 + 2y'y_p))dy' \tag{4.15}$$

And, if a term, Q, dependent on the topology of the system is introduced, equation 4.13, can be represented as:

$$E(t) = Q \int_{-\infty}^{\infty} H(x') \exp\left(\frac{i\gamma y'^2}{2v^2}\right) \exp\left(\frac{i\gamma y' t}{v}\right) \mathrm{d}x', \tag{4.16}$$

where Q is given by:

$$Q = \frac{|E_i|(\cos(\alpha_h) + \cos(\beta_h)}{2i\lambda R_{Tx}R_{Rx}} e^{ikBL} \tag{4.17}$$

Simulated target signatures for a Range Rover-shaped (RR) target with aperture shown in Fig. 4.3 and a square of size 1.6 x 1.6 m can be seen in Fig. 4.4.

Figure 4.3: Aperture of Range Rover shaped target

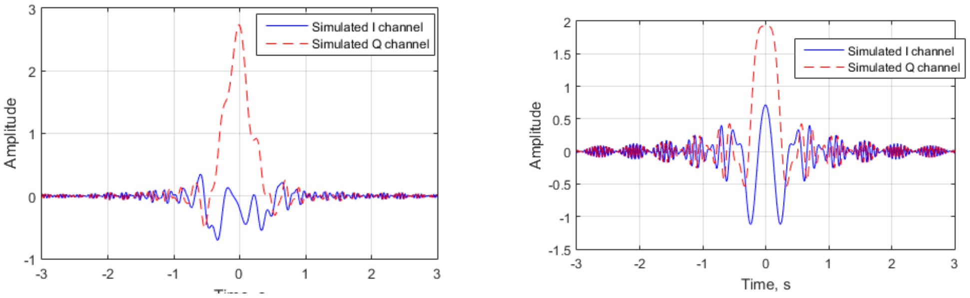

(a)

(b)

Figure 4.4: Simulated signatures for a Range Rover (RR) target (a) and square of size 1.8 x 1.8 m (b). The signatures are simulated for 1 GHz incident wave, for crossing speed of 30 kph, perpendicularly to the middle of a baseline of length of 50 m

The modelled results have been obtained by approximating the integrals into discrete sums and considering the target as a sum of thin vertical lines each of height, y'. The width of the target vertical lines was taken as 1/10 of the wavelength, i.e. 0.03 m and the integral in equation 4.16 was summed over the observation time, by steps equivalent to 0.03 m. This method is similar to the one described further in section 4.3.2.

As it can be seen when comparing the signatures for square targets, modelled with SISAR and the point-like target model, Fig. 4.2 and 4.4(b), the signatures only differ by a constant 90 degrees phase shift, which is of no consequence.

Fig. 4.5 shows a direct comparison between the solutions of both the original and modified SISAR models. As can be seen from the figure, there are small differences, the most apparent being a time-varying phase difference between the two solutions. Such an effect has been previously observed in literature. [59]

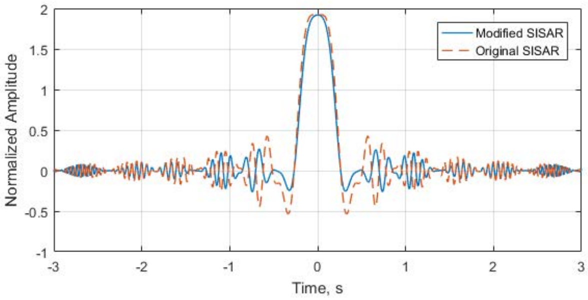

Figure 4.5: Comparison of I channel target signals modelled for a square target with both the original and modified SISAR algorithm

The envelopes of the signals shown in Fig. 4.5 do correspond to a sinc function with sidelobe levels of around -6 dB. This is similar to the results obtained for the FSCS calculation of the rectangular plate, discussed in section 2.4.0.1.

However, the SISAR model still relies on analytical (or numerical if using modelling software) solution of the FK integral. This makes it mathematically intensive for complex shaped targets.

4.3.2 Signal modelling via the numerical solution of the Fresnel-Kirchoff diffraction integral

The SISAR approach is still mathematically complex and relies on a series of assumptions in its derivation, which may not be true, especially for ground targets. Signal simulation, based on the direct numerical solution of the FK diffraction integral was proposed by the author in [25]. It is mathematically simpler than the SISAR model, shown in the previous section, and is derived based on the diffraction phenomenon, as is SISAR. However, it relies only on the direct numerical solution of FK, rather than approximate analytical solutions. As such the model can be used in all practical cases without the need of complete redevelopment, however only the free-space model has been shown below. As shown in chapter 6 the accuracy is sufficient even in cases where multipath may be present.

The assumptions behind its derivation are going to be outlined below and the practical application of the approach is going to be presented.

Firstly Babinet's principle (section 3.1.6) is used to represent the target shadow silhouette from a opaque target in transparent space, into an aperture of the target's dimensions, lying into opaque space, as shown in Fig. 4.6. After that the assumption that a target is a black body and that it is lying on a single plane, i.e. not curved target, is applied. The latter assumption is applied so that a plane wavefront can be modelled to scatter off the target at the same time in all space.

Then the target signature is modelled on the basis of Fresnel-Huygens principle, where the target aperture is divided into secondary elementary radiators (see Fig. 4.8(b)) and the signal is calculated as the sum of the response of all of these secondary elementary radiators. In this way the target's FSCS is taken into account by the discrete version of the Fresnel-Kirchhoff diffraction integral, which is used for the calculation of the response of the elementary radiators on the target aperture. For a complex target the secondary front is formed by the radiation of a number of secondary elementary radiators, thus for the correct description of the FS signature, a minimum elementary area must be defined which corresponds to the desired accuracy of the shadow radiation pattern and, therefore, FSCS of the target. Assuming that the shadow aperture with distributed secondary radiators represents an aperture antenna, according to the antenna theory, the area of each of the

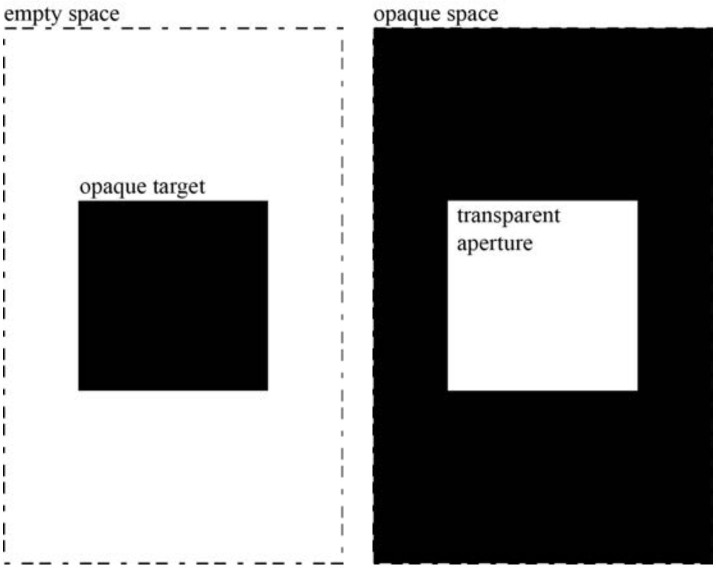

(a) (b)

Figure 4.6: Graphical representation of the Babinet's principle. Opaque target in empty space (a) is represented by a transparent aperture in opaque space (b).

secondary radiators should be related to the carrier wavelength. There exists literature regarding the limits of the grid size of the mesh of secondary radiators, the maximum grid size was defined to be $(0.166\lambda)^2$, corresponding to the discussion in [60]. In most numerical application of the Huygen's principle, though, much finer mesh grid is used.

Considering a stationary aperture, as shown in Fig. 4.7, the Fresnel-Kirchhoff diffraction integral in the on-axis approximation is given by [21], where $E(x, y, z)$ is the E-field at the receiving antenna:

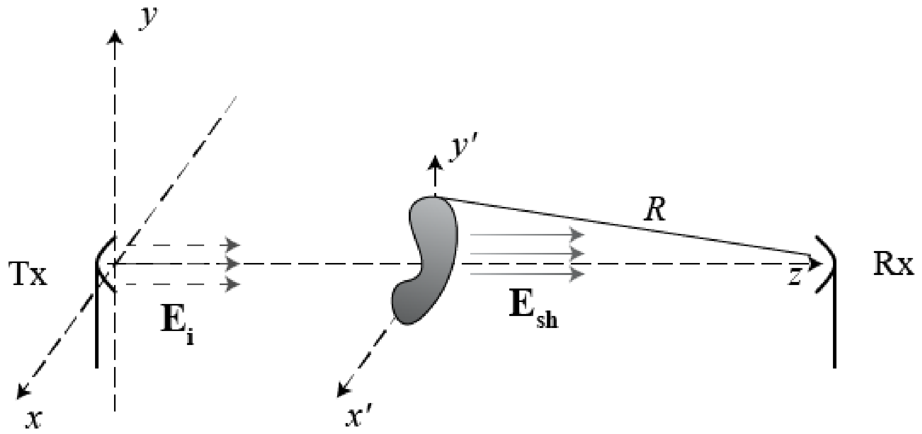

Figure 4.7: Geometry of measuring of shadow radiation by an object sitting on the baseline, between transmitter and receiver.

$$E(x,y,z) = \frac{-i}{\lambda}\iint_A E_i \frac{\exp(ikR_{Rx})}{R_{Rx}} \mathrm{d}x'\mathrm{d}y', \tag{4.18}$$

where E_i is the incident EM wave, R_{Rx} is the range from aperture to the detector, A is the total area of the aperture, which is in x', y' Cartesian coordinate system, parallel to a x, y, z coordinate system, the origin of which is the transmitter. Equation 4.18 is based on the following assumptions: observation plane is perpendicular to and its middle intersects the z-axis and operation in the far-field, meaning that the target is in the far-field of the transmitter and the receiver is in the far-field of the target.

For the sake of simplicity, but without loss of generality henceforth the incident field is going to be considered to be constant, uniform of a unit strength, i.e. $E_i = 1V/m$.

Thus for an infinitesimally small point on the aperture of area $dA = \mathrm{d}x'\mathrm{d}y'$, taking the imaginary part of the wave:

$$\mathrm{d}E(t) = \frac{-i\mathrm{d}x'\mathrm{d}y'}{\lambda R_{Rx}} \exp(i\omega t) \tag{4.19}$$

The field calculated by 4.19 is only due to a single point, positioned at the baseline, as such the $(x-x')^2 and (y-y')^2$ terms are close to 0.

Now if the equivalent problem of a moving point aperture, rather than moving detector is considered, some time-varying Doppler phase due to the change of range, is going to be introduced. It must be noted here that such phase differences are only observed at small diffraction angles. Such a geometry is depicted in Fig. 4.7, and 4.19 will transform into:

$$E(t) = \frac{i\mathrm{d}x'\mathrm{d}y'}{\lambda R_{Rx}} \exp(i(\omega + \omega_d(t))t), \tag{4.20}$$

where $\omega_d(t)$ is the angular frequency due to the rate of change of the range at each time on the trajectory of the moving point.

Thus the signal produced by many (NxM) radiating points, resembling an extended aperture, will be the sum of the scattered fields of all the points on the aperture, weighted by their area - $\mathrm{d}x'\mathrm{d}y'$, for each point n, m respectively:

$$E(t) = \frac{i}{\lambda R_{Rx}} \sum_{n=0}^{N} \sum_{m=0}^{M} \mathrm{d}x'\mathrm{d}y' \exp(i(\omega + \omega_{d_{n,m}}(t))t), \tag{4.21}$$

where N and M are the total number of points along the target's length, l, and height, h, respectively. The target's length is assumed to be along the x' axis, while the height - along y'.

We are considering a ground FSR system with maximum baselines of the order of a hundred meters [23, 25, 61], so the diffraction process cannot be approximated as on-axis. Thus, the horizontal diffraction angles, α_h and β_h, have to be taken into account.

Complex signal scattered by an extended target, at baseband, is given by 4.22 , corresponding to a generic FSR scenario, shown in Fig. 4.1.

$$E(t) = \sum_{n=0}^{N}\sum_{m=0}^{N} \frac{i}{\lambda R_{Rx}} \mathrm{d}A \cos(\alpha_{h_{n,m}}) \cos(\beta_{h_{n,m}}) \exp(i\omega_{d_{n,m}}(t)t) \tag{4.22}$$

where all notations are analogous to the ones used in equation 4.21. The area of the individual secondary radiator is given by $\mathrm{d}A$.

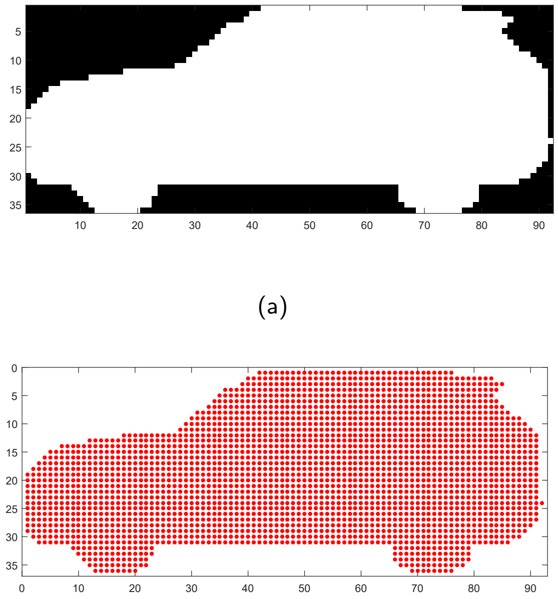

(a)

(b)

Figure 4.8: Range Rover target representation in terms of Babinet's principle - (a) and Huygens-Fresnel principle - (b)

An example of the signals that are calculated by the algorithm are seen in Fig. 4.9 for a Range Rover (RR) target of size 4.6 m x 1.8 m for an incident plane wave with frequency of 1 GHz. The target is represented first by its aperture (Fig. 4.8(a)) and then by points of size 0.05 x 0.05 m (Fig. 4.8(b)), which represent the secondary radiators on the surface of the target aperture. The area of each secondary elementary radiator is thus assumed to be $(0.16\lambda)^2$. The target in these simulations is moving perpendicularly to the middle of the baseline with speed of 30 kph.

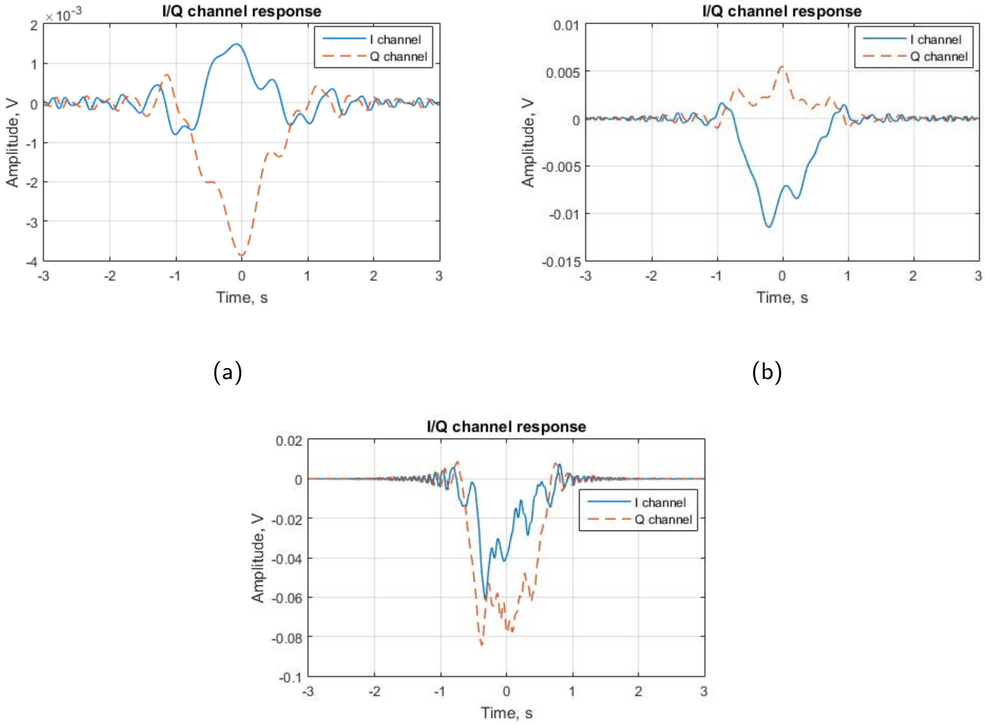

(a)

(b)

(c)

Figure 4.9: Modelled Range Rover target Doppler signatures for different baseline lengths: (a) - 100 m; (b) - 50 m; (c) - 10m

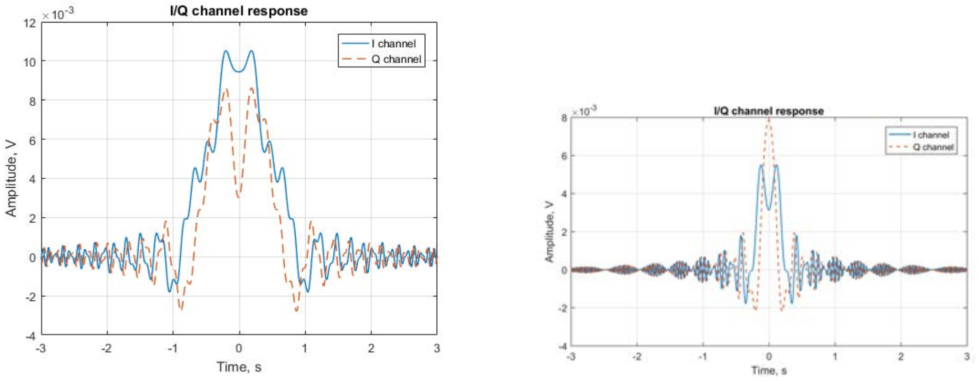

(a) (b)

Figure 4.10: Modelled signal for a rectangular target of size 4.6 x 1.8 m - (a) and size 1.8 x 1.8 m - (b); for 50 m baseline at 30 kph speed

Considering the signatures shown in Fig. 4.9, a direct comparison between Fig. 4.2, 4.4 and 4.10 can be made for the square target. It can be noted that the envelopes of all the signatures for the 1.8m square target resemble a sinc function and the first sidelobe level of all the signals is around -6 dB.

Comparing Fig. 4.9(b) and 4.10(a), one can observe the differences between the target signature of a rectangular (uniform) target and an asymmetrical target of the same size. It can be seen that the envelope of the rectangular target signal is symmetrical, following the symmetry in the target's aperture. The real car signature, however, is not symmetrical. This is due to the asymmetry in the FSCS of the car.

Comparing the signatures simulated with SISAR and the model described above, Fig. 4.4 and 4.9(b), respectively, it can be seen that the two models have a subtle but constant phase difference, though the shape of the main lobe is very similar.

The difference in amplitude between the signatures at 100 m (Fig. 4.9(a)) and 50 m (Fig. 4.9(b)) baselines is approximately half, but the amplitude difference between the

50 m (Fig. 4.9(b)) and the 10 m (Fig. 4.9(c)) baseline signatures is around an order of magnitude, the signal is fully shadowed, with a much bigger amplitude than the far-field target signals, in accordance to the discussion in section 2.3. The signal shown in Fig. 4.9(c) is however not fully accurate, due to it being a near-field signal, as discussed in section 3.1.5.

Also, it can be seen that the FS target signal of a fully shadowing target will resemble the shape of the target itself, as discussed previously in literature [3].

Simulated signatures are compared to experimentally obtained FS signals in Chapter 5. The modelling for one-dimensional target signatures for extended targets has been described. Next modelling of the two-dimensional signals is going to be presented.

4.4 Modelling of two-dimensional target signatures

In the following section the above method of signal modelling is going to be extended to two-dimensional target signature calculations. Two-dimensional here assumes that received signal strength can be recorded in both x and y axis, similar to holography. These modelling results will be used in the estimation of the resolution of target profiles in chapter 7.

The recording of such two-dimensional target signatures will require a vertical receiver array, which will need to have a substantial height, as seen in the analysis of the reconstructed 2D target profiles in chapter 4 and the accuracy analysis in chapter 7.

The algorithm discussed below assumes that the target lies in free space and that a receiver array can be of length -30 to 30 m, where 0 m is the geometrical centre of the target. For the calculation of the signals two solutions are used - based on the Fresnel-Kirchhoff diffraction integral and the Rayleigh-Sommerfield diffraction integral, where the latter is used for near-field calculations only.

4.4.1 Fresnel-Kirchhoff diffraction integral based two-dimensional target signature

Modelling of two-dimensional target signatures, using the Fresnel-Kirchhoff based modelling, section 5.5, is done on the basis of an array of receivers in the vertical plane, recording the FS Doppler signature of a target moving in the horizontal plane, or equivalently, a two dimensional array of receivers with a stationary target. A graphical representation of the later scenario is shown in Fig. 4.11.

Sampling is done in space, rather than time, for faster calculation of the signature, according to a minimum separation between receiver points, given by $\Delta z = \Delta y \leq 1/4\lambda$.

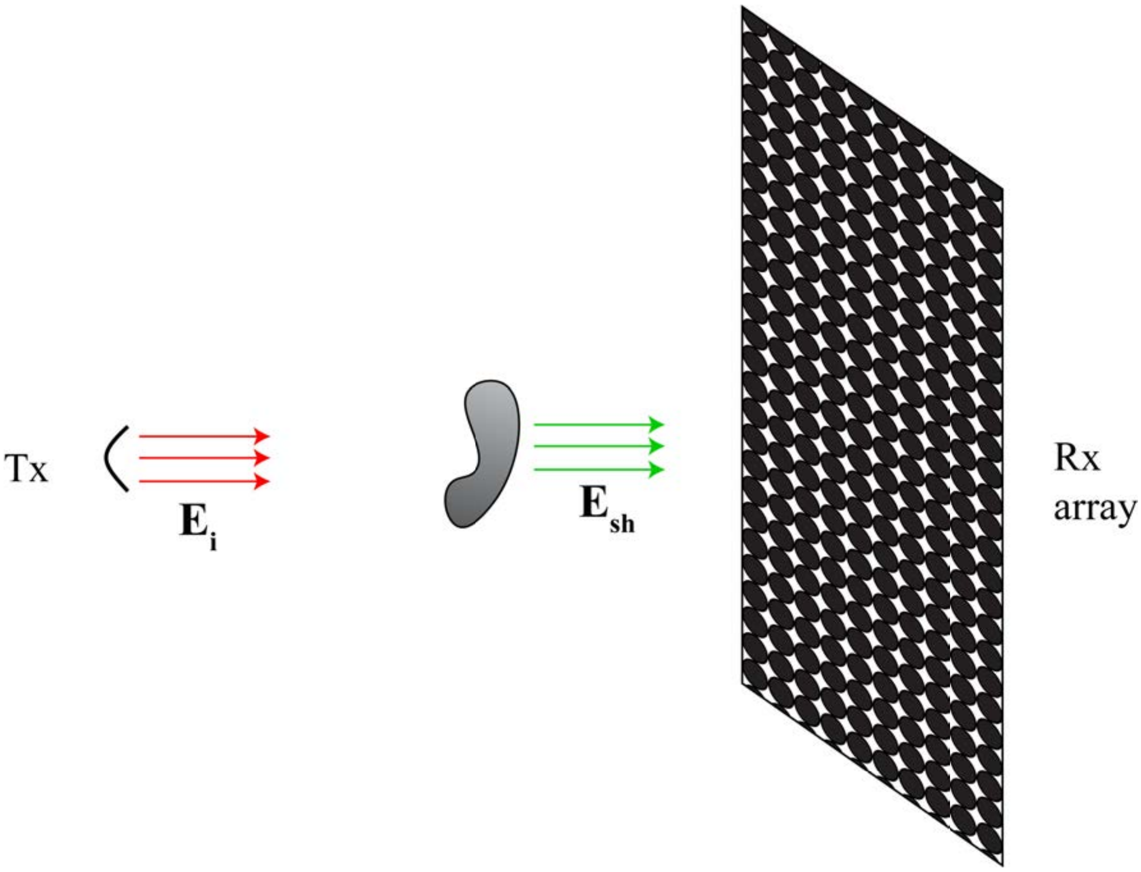

Figure 4.11: Simple schematic of a 2D FSR configuration with a Rx array.

Example modelled signatures for square (1.6 m x 1.6 m) and Range Rover Sport target (4.6 x 1.8 m, whose aperture is shown in Fig. 4.13), are shown in Fig. 4.12 and 4.14, respectively, below. The target is modelled intercepting a 100 m baseline perpendicularly in the middle with speed of 30 kph. The signals are calculated via the method described in section 4.3.2, where target signals are calculated at every point of the receiver array.

Figure 4.13: Range Rover Sport aperture

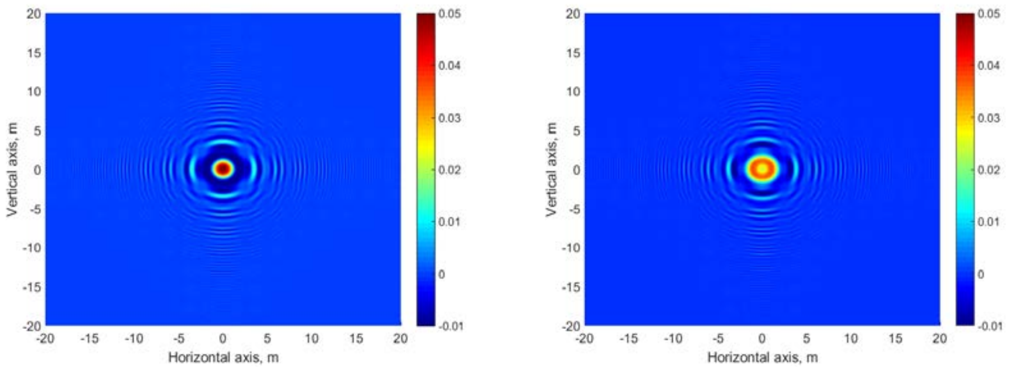

(a) (b)

Figure 4.12: Two-dimensional target signature from a square target of size 1.6 x 1.6 m, at 1 GHz incident frequency. Real (a) and imaginary (b) parts of the signature are shown.

As analytical solutions exist for the case of rectangular target is available, thus logically a signal modelled according to the discussion in section 3.1.4.1 is shown below and compared with the method proposed in section 4.3.2. It must be noted that the signatures in Fig. 4.15 do not have Doppler content due to the motion of the target, but are only showing the real part of the envelope of the signal.

The analytical and proposed solutions provide with very similar results as shown in Fig. 4.15. This implies the results of the proposed method used for signal calculation coincide with the theoretical expectations.

In practice Fig. 4.12 and 4.14 are RF holograms of the apertures of the two targets, calculated through the FK diffraction integral.

From Fig. 4.12 and 4.14 the difference in the aperture of the two targets can be clearly seen, where the signal due to the presence of a square target is symmetric in both the horizontal and vertical axes, while the signal due to the Range Rover target follows the asymmetry in the shape of the aperture.

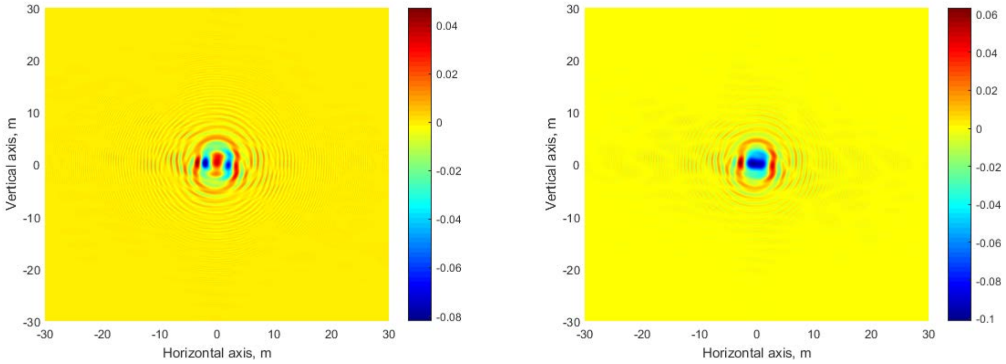

(a) (b)

Figure 4.14: Two-dimensional target signature from a shadow of a Range Rover Sport target of size 4.6 x 1.8 m (a), at 1 GHz incident frequency. Real (b) and imaginary (c) parts of the signature are shown.

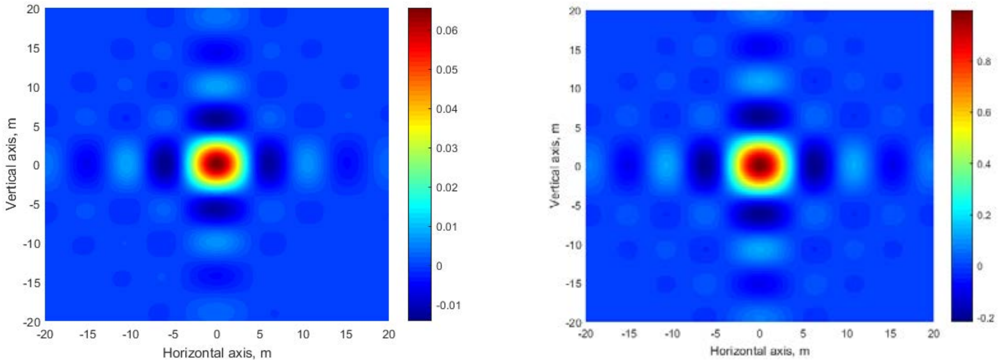

(a) (b)

Figure 4.15: Real part of the two-dimensional target signature from a stationary square target of size 1.6 x 1.6 m, at 1 GHz incident frequency. Solution according to the proposed signal modelling method (a) and analytical solution (b).

These two dimensional target signatures can enable two dimensional target imaging of targets, moving in the Fresnel and far field zones. However for near-field signatures, these signals must be calculated by the Rayleigh-Sommerfield diffraction integral. It must be noted here that far-field for the Range Rover as given by the well known equation ($D_{FF} = \frac{2D^2}{\lambda}$, where D_{FF} is the far-field distance and D target dimension) is 140 m, while for the square is 17 m.

4.4.2 Rayleigh-Sommerfield (RS) diffraction integral based two-dimensional target signature

In reality FSR targets can be expected to be moving in the near-field of either the transmitter or receiver. Thus calculations for the 2D target signature were done for near-field operation, as well, using the same outline as above, but the calculation is performed via the RS integral.

The model uses the same approximations as the previously described Fresnel-Kirchhoff calculations, but uses the RS diffraction theory, specifically the RS integral of first kind, equation 3.10.

Target signatures, shown in Fig. 4.16, are simulated for similar parameters - 1 GHz incident EM wave, 10 x 10 screen, for a square target of size 1.6 x 1.6 m, 3 m baseline. The area of the middle peak of the calculated field by the RS integral - Fig. 4.16(b), corresponds to the area of the target.

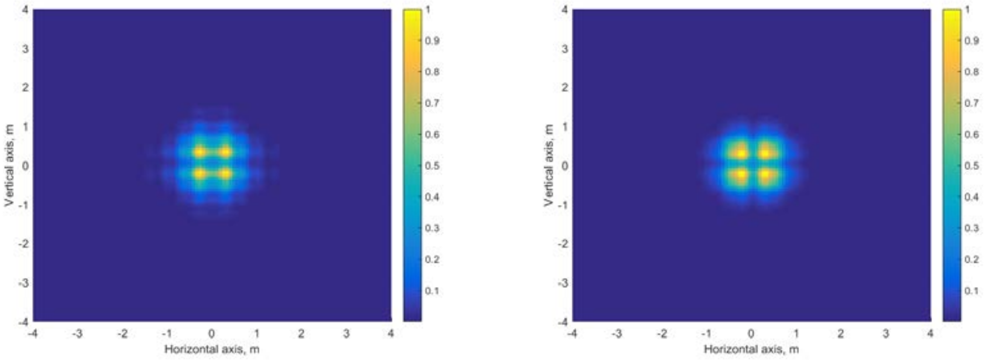

(a) (b)

Figure 4.16: A comparison of the normalized absolute value of the solutions of the FK - (a), and RS - (b), 2D square target. The signals are simulated for 1 GHz incident CW wave, 10 x 10 m observation screen, positioned 3 m away from the aperture.

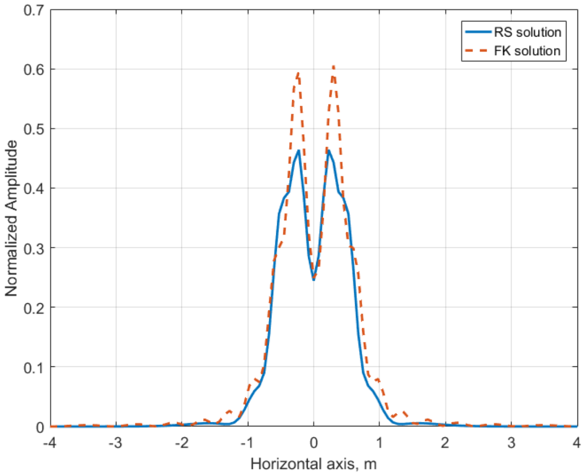

Figure 4.17: Comparison between the solution of the FK and RS theories. Only the horizontal plane is considered

As can be seen from Fig. 4.16, even when the distance target - receiver is less than the target size, there are very limited differences for the solutions in near-field between the RS and FK solutions. Also, this is further shown in Fig. 4.17, where only the horizontal plane is considered for an on-axis solution in the vertical plane. The main difference between the two solutions is the amplitude of the peaks, however, in the context of imaging, the shape of the envelope, rather than the amplitude is the more interesting. Thus, henceforth only the far-field and Fresnel near-field signals are going to be discussed, i.e. only the FK solutions are going to be studied.

4.5 Conclusion

In this chapter algorithms for signal modelling in Forward Scatter Radar are presented. Firstly, solutions proposed in literature were considered, together with examples of already published results. The topic was introduced by a model developed for calculation of the signal of a point-like target, where FSCS is separately calculated and as such is only available for simple shapes.

A model for the calculation of the signal of an extended target, already published, has been introduced. This model, known as SISAR, was firstly derived for airborne targets and as such is shown to be somewhat incorrect for calculation of a ground moving target signal. A modified version of SISAR, developed by Hu [5], was described. Example signatures were shown for both cases.

Following that, a novel model for calculation of the FSR signals is presented based on the direct numerical solution of the FK diffraction formula. The mathematical and thus computational effectiveness of the novel model has been briefly discussed. Further simulation results were compared with already published ones, showing good agreement.

Full holographic modelling based on the novel approach (together with analogously derived model based on RS theory) has been introduced for the purpose of 2D target signature calculations. It is based on the availability of a vertical array of receivers. Example signatures for a square and car targets has been shown. Also, a comparison between the RS and FK solutions was made, concluding that in real world scenarios FK would provide with sufficient accuracy for the modelling of target signatures.

In the discussion above it was shown how the target signatures in FSR are practically obtained from the target aperture. In the next chapter the inverse problem - obtaining the target aperture from the signal, is going to be discussed.

CHAPTER 5

IMAGING IN FSR AND DEVELOPMENT OF TARGET SHADOW PROFILE RECONSTRUCTION

Due to the phenomenology, traditional SAR/ISAR imaging is not applicable in the case of FSR. However, imaging in FSR is an important addition to the capabilities of the system, already researched [12, 31, 62, 63]. This section will deal with the transformation of 1D target signature in 1D target profile, where 1D is meaning a line connecting two or more points. Thus instead of imaging, in FSR the process is going to be called profile reconstruction.

By considering the target signature as a combination of a time-varying diffraction pattern of the target shadow and a Doppler phase signal due to the movement of the target, as shown in section 2.4.1, one can use Holographic algorithms to extract information about the target shape from the received complex target signal. In this section two models are discussed, the first one is the shadow inverse synthetic aperture radar (SISAR) [1] and the other one is a novel approach, proposed by the author, which is the main theme of the thesis and takes advantage of the principle of Holography, described in section 3.2 and is referred to as Target Shadow Profile Reconstruction (TSPR).

5.1 State of the art of target imaging in FSR

5.1.1 SISAR

The SISAR model, first published in western journals in 2000 [1], but developed in the 1980s is the first model to predict how information about the target shape and size can be extracted from a FS signature. It was derived for an airborne target and as such it exploits a series of assumptions, which are not valid for the general case of a ground-moving target. These assumptions include operation in free-space and in the far-field with very narrow diffraction angles, and, also, a purely optical scattering region.

In SISAR the imaging (profile reconstruction) corresponds to the extraction of the so called complex profile function (CPF), $H(x')$, from the target signal.

The SISAR transform has the form of a spatial Fourier transform, and is given by: [1, 33]

$$H(x') = \frac{\gamma}{2\pi v Q} \int_0^{T_{obs}} E(x, y, z) exp(j\frac{\gamma y'^2}{2v^2}) exp(j\frac{\gamma y' t}{v}) \mathrm{d}t, \tag{5.1}$$

where y' is the position of the target along its trajectory towards the baseline, γ is given in equation 4.14, Q is amplitude scaling, due to the geometry of the particular topology and is given by:

$$Q = \frac{|E_i|(cos(\alpha_h) + cos(\beta_h)}{2j\lambda z^2} e^{jkBL}, \tag{5.2}$$

where α_h and β_h are the diffraction angles with respect to transmitter and receiver, respectively. $E(x, y, z)$ is the received complex FSR signal and T_{obs} is the total observation time.

The algorithm is dependent on the accuracy of estimating the target velocity and trajectory, so that the coordinate system around the transmitter and receiver as well as the complimentary coordinate system (x', y', z') of the target can be built accurately. Inaccuracy in the estimation of the trajectory parameters will lead to inaccurate profile reconstructed, as discussed in [64]. The actual height of the reconstructed profile, Γ_{SISAR}, is given by the amplitude of the CPF, for the ground target [5, 33]:

$$\Gamma_{SISAR} = |H(x')| \tag{5.3}$$

The SISAR reconstruction model is used in integral form, integrating the received signal scattered from the target over time from 0 to T_{obs}.

However, due to the assumptions in the derivation of SISAR, it is not applicable to the ground moving case, as discussed in section 4.3.1. Thus a modified version has been introduced and will be discussed next.

5.1.2 Modified SISAR

As discussed in the previous section, the original SISAR imaging model was derived for airborne targets. As such under the assumptions made it is not valid for application to surface targets, as it is expected that there is presence of multi-path propagation and due to the smaller baseline - near-field effects and wide diffraction angles operation influence the reconstruction, as well as, possible presence of clutter. Also, due to the sufficiently smaller electrical size of ground targets, operation in higher Mie scattering regions, is also possible.

A modification to the SISAR model has been introduced in [5] to correct the inaccuracies arising from the assumptions of the original model, discussed in the previous section.

As shown in [59] the modified model will correct results of the original model. It is based on the modified SISAR signal model, discussed in section 4.3.1.1.

Considering the received signal to be given by equation 4.13:

$$E(t) = Q \int_{-\infty}^{\infty} H(x') \exp\left(\frac{i\gamma x'^2}{2v^2}\right) \exp\left(\frac{i\gamma x' t}{v}\right) \mathrm{d}x', \tag{5.4}$$

where $H(x')$ can be estimated from equation 5.4 [5], to be:

$$H(x') = \frac{\gamma}{2\pi v Q} \exp\left(\frac{i\gamma x'^2}{2v^2}\right) \int_{-T_{obs}/2}^{-T_{obs}/2} E(t) \exp(-i\gamma x' t/v) \mathrm{d}t, \tag{5.5}$$

where the integration is performed over time so that the crossing of the baseline corresponds to 0 seconds. The target profile will then be given by the absolute value of the CPF [5]:

$$\Gamma_{ModSISAR} = |H(x')| \tag{5.6}$$

Multiple results have been published [5, 59, 65] suggesting that the modified model generates more accurate results, due to the phase corrections introduced by the Taylor expansion of the coordinates.

In Fig. 5.1, below, an example of reconstructed profiles by the original and modified SISAR method are shown, for a truck. The target was moving at 20 m/s, perpendicularly, towards the middle of a baseline of 300 m. The incident frequency was set to 0.9 GHz.

As can be seen from Fig. 5.1, the target profile can be successfully reconstructed with the

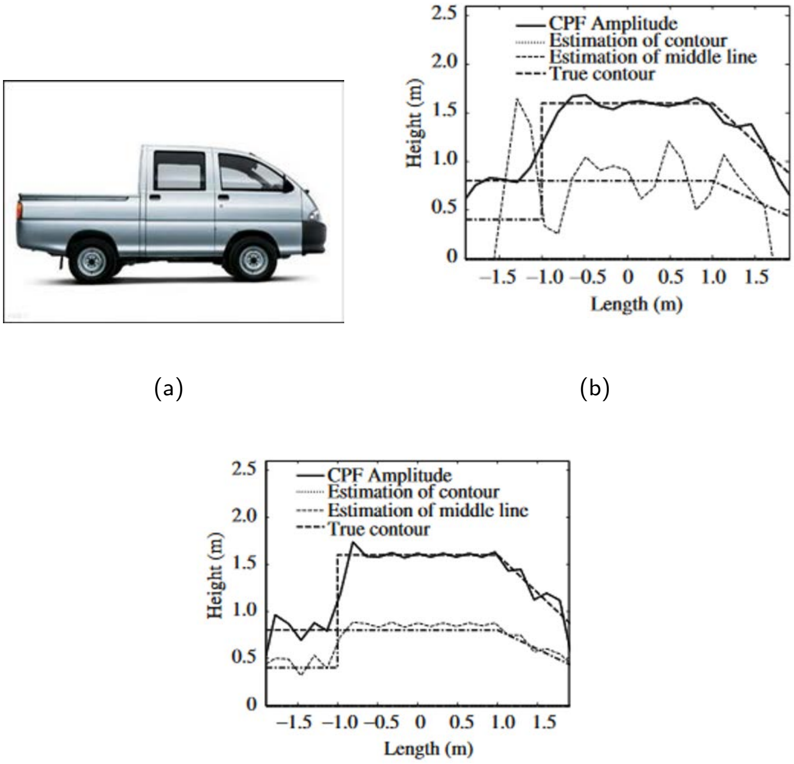

(a) (b)

(c)

Figure 5.1: Target simulated - (a); reconstruction result of the SISAR imaging algorithm - (b); reconstruction result of the modified SISAR algoirithm - (c). It should be mentioned that the results are from simulation, thus target trajectory parameters are accurately known [5]

SISAR algorithm. The result for the original model can be considered worse after visual comparison, suggesting that the modifications do improve the algorithm.

However, SISAR imaging is still mathematically (analytically) intensive and as discussed above requires modifications to be applied to surface moving targets. A novel approach developed by the author and based on holographic imaging is discussed below.

5.2 Target Shadow Profile Reconstruction algorithm

The target shadow profile reconstruction (TSPR) model is derived on the basis of the FSR signal formation and basics of holographic reconstruction. The development of this method is motivated by the apparent mathematical complexity of the SISAR model and the unavailability of any experimental results except for the ones shown in the publications of Cheng Hu et al., where only two targets are shown in a very controllable experimental scenario. TSPR is intended for easier implementation into signal processing algorithms, so that practical aspects of FSR target imaging can be further investigated.

The model is developed on the equivalence between a moving probe receiver and a moving target, as seen in Fig. 5.2.

The physical derivation behind the TSPR along with the assumptions made is going to be discussed below, while the practical implementation is going to be discussed after that.

5.2.1 FSR signal as a hologram

A form of the FSR signature, comparable to the holographic signals, should be established before the suggested holographic reconstruction is applied. Such a form, based on the Fresnel approximation will be formulated in this subsection.

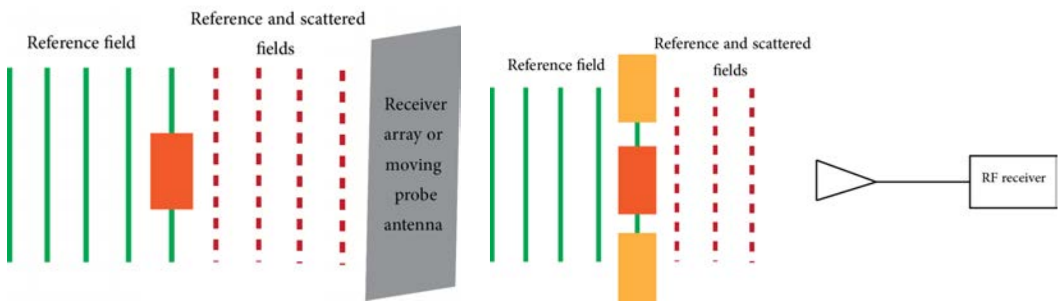

(a) (b)

Figure 5.2: Phenomenology of holography in the static-target case with an array of receivers - (a), and moving-target case with a single receiver - (b). The resulting received signals are going to be equivalent

In the mathematical description below, the target signals are going to be considered 2-dimensional, for completeness and easier direct analogy to holography.

Let a target, move on a plane, P_1, situated at $z = 0$ of a Cartesian coordinate system and have transmittance of $s_b + s_r(x', y')$, where s_b is a constant average value over the whole plane, while $s_r(x', y')$ is the transmittance of the target, as shown in Fig. 5.3, below.

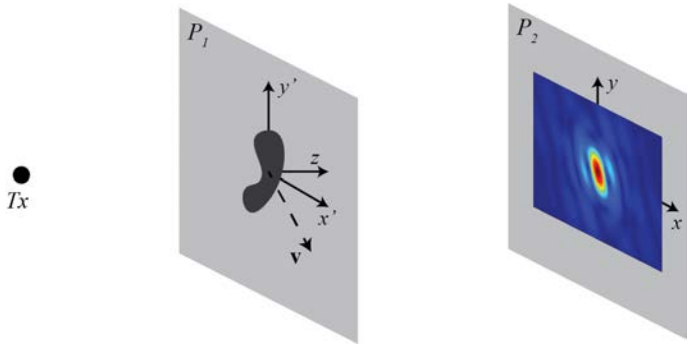

Figure 5.3: Recording of a RF hologram

A monochromatic plane wave which will propagate from negative to positive z, after interacting with the plane P_1 will have a form of:

$$E_{holo} = [s_b + s_r(x', y')] \exp(i\omega t), \tag{5.7}$$

where ω is the angular frequency term of the incident monochromatic wave and the exponential term correspont to the propagation delay. At a plane, P_2, in $z > 0$, an "out-of-focus" image, i.e. Fresnel diffraction pattern of the target is observed [57]. That structure, $\chi(x, y)$, can be calculated via the Fresnel-Kirchhoff diffraction integral, discussed in section 3.1.3, for small diffraction angles [57]:

$$\chi(x, y) = \frac{i}{\lambda z} \iint [s_b + s_r(x', y')] \exp\left(\frac{-ik}{2z}\left((x - x')^2 + (y - y')^2\right)\right) \mathrm{d}x'\mathrm{d}y' \tag{5.8}$$

According to [57] equation 5.8 can be considered to be a convolution of the target transmittance with an impulse function, $f(x, y)$, given by:

$$f(x, y) = i/\lambda z \exp[-\frac{-ik}{2z}(x^2 + y^2)]. \tag{5.9}$$

Since s_b represents the constant leakage signal, then it would correspond to a plane wave, which will propagate unaltered, except due to the effect of edge diffraction on the boundaries of the target contour. If this effect can be considered negligible, then s_b would represent a constant DC level (so called leakage) in the Fresnel pattern, so that:

$$\chi(x, y) = s_b + s_r(x', y') * f(x, y). \tag{5.10}$$

It must be noted here that the only difference between the planes x', y' and x, y is their separation z as suggested in [57]. Also, according to the reference, equation 5.10 can be represented in terms of a Fourier transform:

$$\chi(x,y) = s_b + \mathcal{F}[S_r(\xi,\eta)F(\xi,\eta)], \tag{5.11}$$

where ξ and η are the spatial frequencies corresponding to $x(x')$ and $y(y')$, respectively, and $S_r(\xi,\eta)$ and $F(\xi,\eta)$ are the Fourier transforms of s_r and f, respectively. The production of the Fresnel pattern is thus representing a multiplication of the spectrum of the target transmittance by a phase factor:

$$F(\xi,\eta) = \exp\left(\frac{i}{4k}(\xi^2+\eta^2)\right) \tag{5.12}$$

It is, also, considered that both the amplitude and phase of $\chi(x,y)$ are recorded. This is the FS signature from the target, also called FS hologram from here onwards, where the oscillatory nature of the Doppler phase in the signature represents the phase factor: $f(x,y) = \mathcal{F}(F(\xi,\eta))$.

Now, if the FS hologram is placed on the plane P_1 and illuminated with the same monochromatic wave: $\exp(i\omega t)$, and the hologram moves on the opposite direction of the target on that plane, in order to compensate phase in the signal, i.e. the phase factor will be the complex conjugate of $f(x,y)$, then, at screen P_2, using equations 5.11 and 5.12:

$$\begin{gathered}(s_b + s_r(x',y') * f(x,y)) * f(x,y)^* = \\ \mathcal{F}^{-1}\left((s_b + \mathcal{F}[S_r(\xi,\eta)F(\xi,\eta)])\, F(-\xi,-\eta)\right) \cong \\ \mathcal{F}^{-1}\left(S_r(\xi,\eta)\right) = s_r(x',y'),\end{gathered} \tag{5.13}$$

reconstructing the original transmittance, $s_r(x',y')$, of the target. This manner of reconstruction is possible if and only if $f(x,y)$ is symmetrical, which is true in the case of FSR.

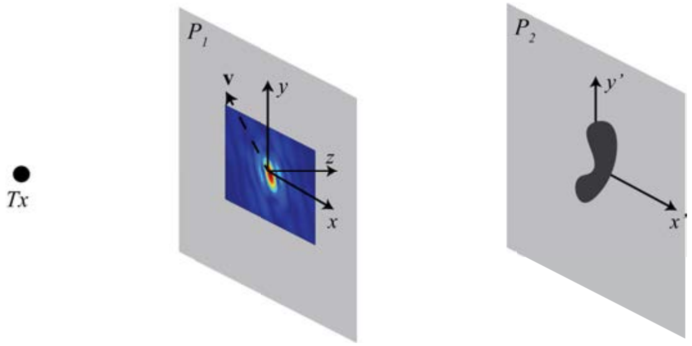

Figure 5.4: Reconstruction of a RF hologram

The discussion above mathematically develops microwave holographic reconstruction, which can be applied to FSR signatures. In the next section the practical application of the method will be presented.

5.2.2 Application of holographic reconstruction to FSR signatures

Considering the theoretical description outlined above, a practical approach to profile reconstruction can be developed on the basis of holographic reconstruction. In the discussion below it will be shown how to apply such algorithm to FSR signatures. In the following description the target signal and reconstructed image are going to be considered one-dimensional.

If the complex FSR received signal at a single receiver of a moving target, without presence of DC, noise or interference at baseband, can be written as, see section 2.4.1:

$$E_{Rx} = \sigma_{FS} \exp(i\omega_d t), \tag{5.14}$$

where σ_{FS} is the target's FSCS - the diffraction pattern of the target's aperture and ω_d is the target Doppler angular phase. The FSCS can be considered to represent the target's transmittance and the Doppler oscillatory term - the impulse function, both of which in the cases of a practical FSR are one-dimensional, i.e. having a system with a single receiver. Equation 5.14 corresponds to equation 5.8, where the imaginary part of the signal is considered and constant scaling factors are not considered.

The conjugate of the Doppler oscillatory term will correspond to $f(x,y)^*$ in equation 5.13, and will be given by:

$$K(t) = \exp(-i\omega_d t), \tag{5.15}$$

and is further referred to as TSPR propagation kernel.

According to the discussion above (equation 5.13) the target image will be given by:

$$\begin{aligned} \Gamma_{TSPR} &= |E_{Rx} * K(t)| \\ &= |\mathcal{F}^{-1}\{\mathcal{F}\{E_{Rx}\}\mathcal{F}\{K(t)\}\}|. \end{aligned} \tag{5.16}$$

The convolution in equation 5.16 can be regarded as a Doppler cancellation, similar to SAR/ISAR processing. This "removal" of Doppler content requires high accuracy of target trajectory parameter estimation, which is discussed in section 7.5. Also, note that $K(t)$ needs to have opposite phase from the Doppler phase of the received signal, i.e. the complex conjugate.

Fig. 5.5 below compares the result of the modified SISAR algorithm, as seen in Fig. 5.1(c), and TSPR for the same target and simulation parameters: 300 m baseline, target speed of 20 m/s, crossing the baseline perpendicularly in the middle, 0.9 GHz incident radiation. It must be mentioned here that the orientation of the reconstructed profile around the x-axis is due to the phase difference between the Doppler signature and the propagation kernel, and does not represent the actual orientation of the target.

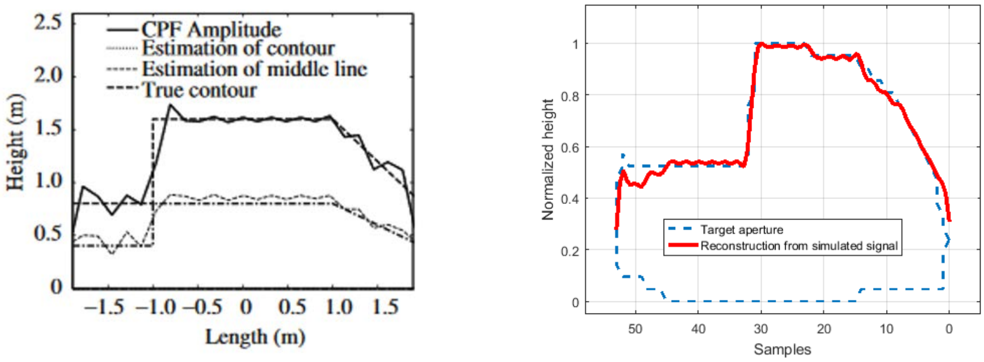

(a) (b)

Figure 5.5: Comparison of the reconstruction result of the modified SISAR algorithm - (a) [5] and TSPR algorithm - (b). The meaning of the midline is going to be discussed in the next subsection

As can be seen in Fig. 5.5 the result of TSPR follows the outline of the target shadow.

Results of the TSPR algorithm can be seen in Fig. 5.6 for simulated signals of a Range Rover target at 1 GHz CW incident radiation and 50 m baseline, and target moving along a single horizontal axis, i.e. no vertical motion, perpendicularly to the middle of the baseline with speed of 30 kph. The signals were simulated at sampling rate of 200 Hz.

The meaning of the x-axis in Fig. 5.6(c) and 5.6(d) is samples in time after convolution of the two signals - the target signal and the propagation kernel. The result in Fig. 5.6(d) show two bumps in the profile at around sample 20 and 70. These are going to be discussed in the next subsection. Otherwise the reconstructed target profile indicates good agreement with the target aperture.

It must be noted here that the extraction of the complex envelope of the target can only be performed after accurately determining the crossing time of the target, i.e. the moment the target is on the baseline. This is a matter which has not been researched, though a simple mechanism of target crossing time estimation based on the short-time Fourier

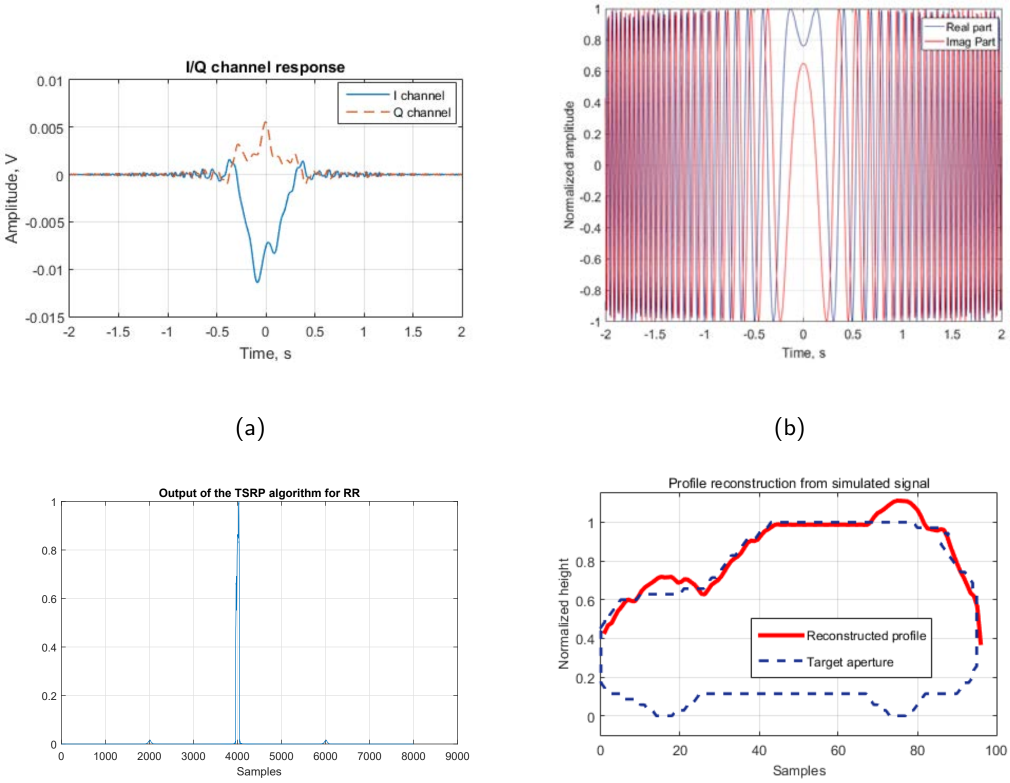

(a) (b)

(c) (d)

Figure 5.6: Target shadow profile reconstruction for a simulated signal of a Range Rover target: (a) - time-domain signal, modelled according to 5.5; (b) - propagation kernel for the trajectory parameters of the target; (c) - output of the TSPR algorithm; (d) - zoomed reconstructed profile and the original target aperture

transform (STFT) of the recorded signal was developed and can be seen in Appendix A. Already developed target detection algorithms and optimal processing can also be used.

In the above section it was shown that FSR target image can be obtained through holographic processing of the signal. Comparison of already known methods for such imaging was shown. From here onwards, only the TSPR model will be considered for FSR imaging. Next the properties of the reconstructed images (profiles) will be discussed.

5.3 Properties of the reconstructed profiles

The outline of the target shadow profile reconstruction algorithm has been discussed above, with examples showing that it has good accuracy for simulated signals. However, the properties of the reconstructed profiles have to be analysed, before the experimental validation and accuracy analysis of the images generated.

From Fig. 5.5(b) and 5.6(d), it can be seen that the result of the TSPR algorithm clearly resembles the contour of the target. In practice, through observation it can be noted that the TSPR algorithm reconstructs the height-difference profile of the target, i.e. contour according to the absolute value of the height of the target at each point along its length, as shown in Fig. 5.7, where the target is represented as the sum of secondary emitter points for a finite width of the target's aperture. It should be noted that the TSPR algorithm would reconstruct the vertical profile of the target, if the target is moving along a vertical axis, so from now on the axis of movement will be considered as the imaging axis.

Because of the one-dimensionality of the TSPR algorithm its results will posses ambiguity for different targets which are the same around their mid-line in the imaging axis. A mid-line in the context of target profiles is half of the height at every point in the length of the target. In practice such targets rarely exist for the surface moving case but it is easy to deduce the fact that inaccurate target recognition can result from this one-dimensionality, as seen in Fig. 5.8, where the results of the TSPR algorithm for two identical trapezoids, rotated by 180 deg are shown.

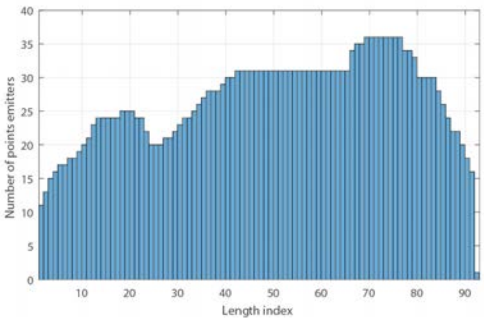

Figure 5.7: Histogram of the number of points at each index in the length of the profile of RR target

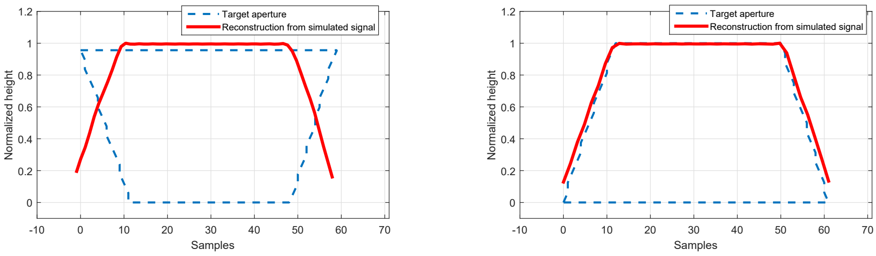

(a)

(b)

Figure 5.8: TSPR result for a boat-like trapezoid target, clearly the output of the TSPR is the same for both targets, despite the difference between them

It should be noted that for ground targets, the scope of the issue with one-dimensionality is greatly reduced compared with the result presented in Fig. 5.8, as different ground targets tend to not be the same around their horizontal axis, i.e. all such targets will have either wheels or tracks on their lower half.

Also, from Fig. 5.5(b), 5.6(d) and 5.8 several assumptions for the shape and form of the reconstructed profiles can be deduced:

- A correct target profile will have the greatest gradient on its edges, i.e. the target profile will have straight and nearly vertical edges (depending on the target observed)
- A correct target profile will have small amplitude oscillations, due to the convolution with the rapidly oscillating term in $K(t)$

where a correct target profile means accurate. A more comprehensive explanation of the meaning of a 'correct' profile will be presented in chapter 7.

As small errors might be present in the estimated trajectory of the target or the position of the phase centres of antennas, which would result in big discrepancies in the rapidly oscillating exponential upon which the propagation kernel is built, a quasi-auto-focusing process for the reconstructed profiles can be implemented. It will be based on the aforementioned properties of the reconstructed profiles and will be further explained in chapter 7, along with a preliminary analysis of the dependence of the accuracy of the reconstructed profiles on clutter and errors in the trajectory estimation.

The issue of the one-dimensionality can greatly reduce the applicability of the approach. However, two dimensional target imaging can be analysed, as well. This will be discussed next in the context of the TSPR algorithm.

5.4 Two-dimensional profile reconstruction

In the previous subsection it was shown that some target information can be extracted from the 1D target signal. In this section true 2D target imaging will be discussed, as a means for improving the generated target images. Here a 2D target image means that the expected result is an image in x- and y-axis, rather than an outline of the profile, as shown above.

Two dimensional signatures of the FS target are produced by the simulation models, discussed in section 4.4, for an array receiving the target signal, as shown in Fig. 5.9. An example of a target signature and the corresponding image can be seen in Fig. 5.10, below. It shows very good resemblance with the target shadow, with a further accuracy analysis of the 2D images done in chapter7. For 2D target imaging the accuracy analysis is done only in the form of resolution analysis, as such configurations are impractical. In the discussion below it can be seen that the vertical array required will be of the order of a few target heights.

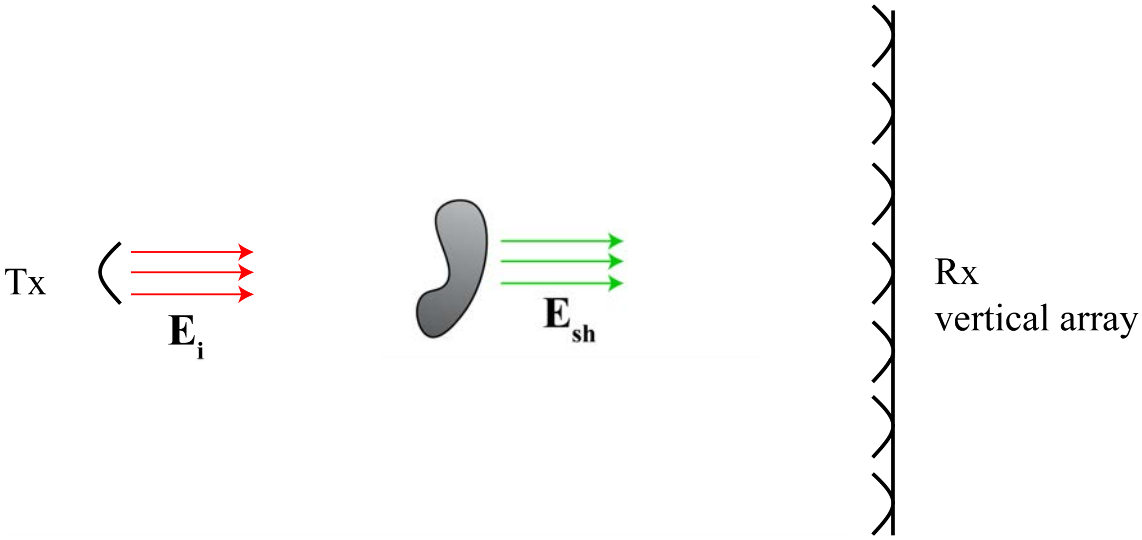

Figure 5.9: Simple schematic of a 2D FSR configuration with a vertical Rx array.

The TSRP algorithm was applied to the modelled two-dimensional target signatures of a Range Rover Sport (RR) target. Simulated signals and profile reconstructions for a RR target are seen in Fig. 5.10, 5.11 and 5.12 for three different frequencies - 100 MHz, 1 GHz and 2 GHz.

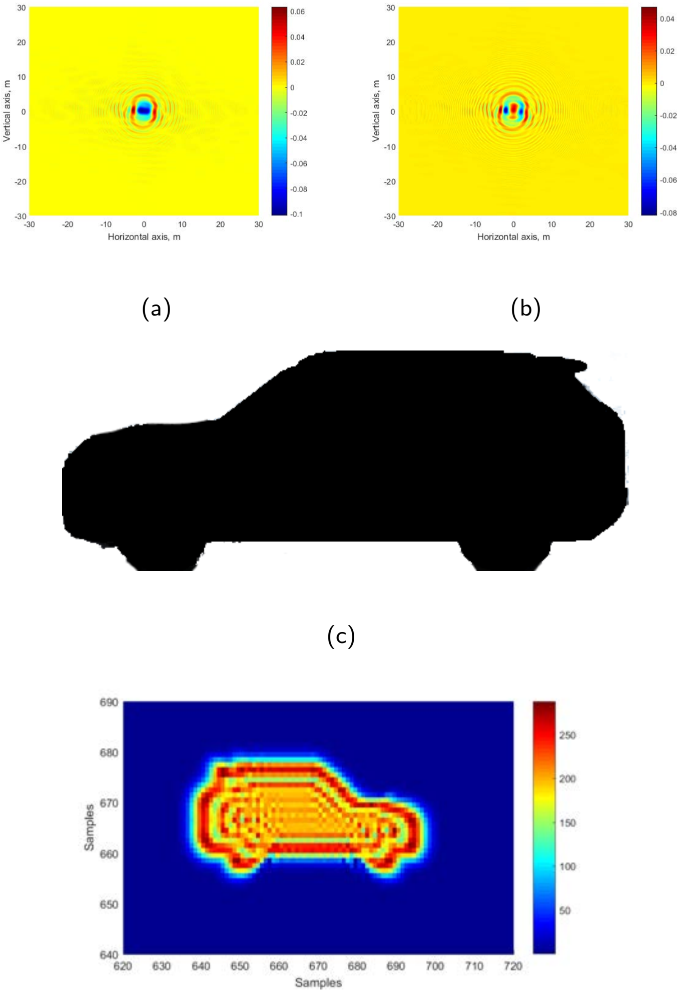

(a)

(b)

(c)

(d)

Figure 5.10: Two-dimensional FSR imaging for a Range Rover Sport target of size 4.6 x 1.8 m at 1 GHz incident frequency. Real part (a) and imaginary part (b) of the complex signal are shown. Also, the target shadow - (c) and the reconstructed image - (d). Receive array dimension is equivalent to the dimension of the vertical axis in (a) and (b) - 60 m

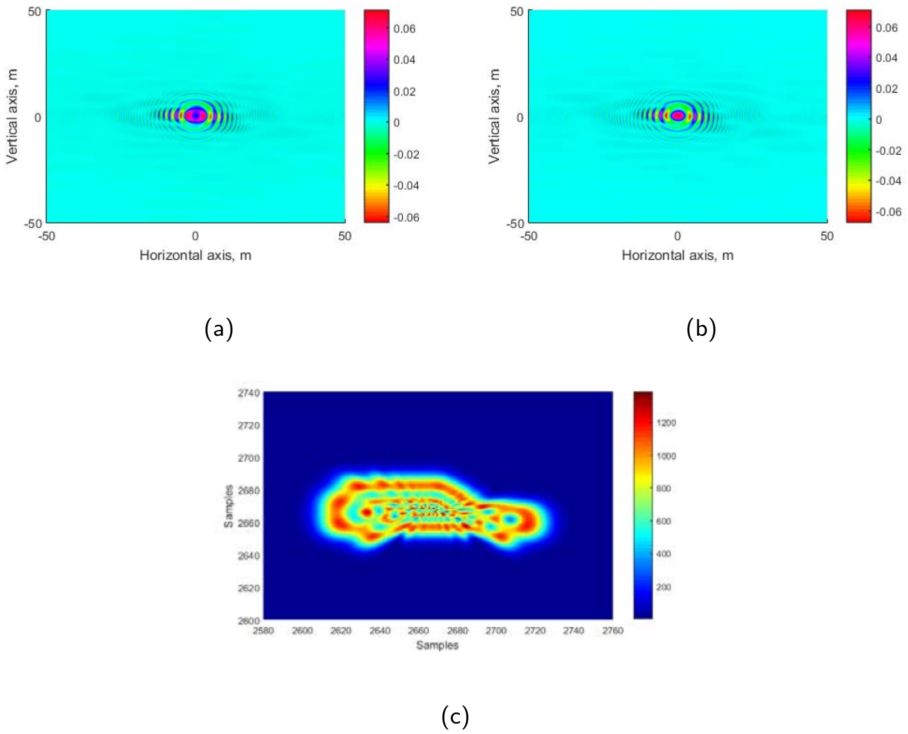

Figure 5.11: Two-dimensional FSR imaging for a RR target of size 4.6 x 1.8 m at 100 MHz incident frequency. Real part (a) and imaginary part (b) of the complex signal are shown. Also, the reconstructed image - (c). Receive array dimension is equivalent to the dimension of the vertical axis in (a) and (b) - 100 m

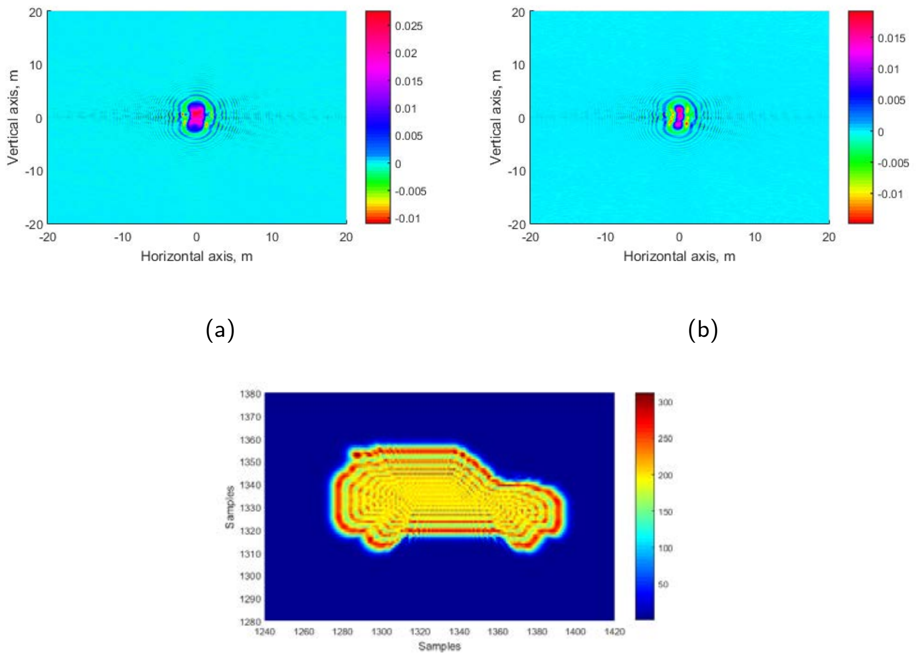

(a)

(b)

(c)

Figure 5.12: Two-dimensional FSR imaging for a RR target of size 4.6 x 1.8 m at 2 GHz incident frequency. Real part (a) and imaginary part (b) of the complex signal are shown. Also, the reconstructed image - (c). Receive array dimension is equivalent to the dimension of the vertical axis in (a) and (b) - 40 m

As it can be seen from Fig. 5.11, the resolution of TSPR 2D images is acceptable even at 100 MHz ($\lambda = 3m$). The resolution of the target images will be discussed further in chapter 5.

Also, according to the modelled results, a method for interpolation of the 2D target signature from multiple 1D signatures can be analysed, a multiple-input-single-output (MISO) system, as discussed in section 5.4.

This system will have to rely on the analysis of the 2D image resolution, governed by the Holography principle, 3.2.3. The system will have to deploy multiple receivers in the vertical dimension, to be able to produce the required resolution for recognition of the target and, also, preserve the phase information of the FSCS of the target.

Thus a sufficient number of receivers needs to be present, spaced accordingly. Modelling of the 2D diffraction patterns of the targets were analysed, where a few receivers in the vertical dimension are modelled, thus receiving a number of signals, each consisting of a FS target signature for the same target. The resulting vectors are then interpolated, so that spacing between receivers in the vertical axis corresponds to $\Delta y \leq 1/4\lambda$. This spacing between interpolated waves is chosen through qualitative comparison between the solutions of a number of modeled results based on different spacings. It was chosen as a best result for both speed of the solution and the accuracy of the result.

Analysis of this technique can provide with a minimum number for receivers, to provide a visually recognisable target image. Also, considering the resolution equation for DIH, equation 3.21, and target height of 1.8 m, it is expected that for a vertical array of 5.5 m size, the reconstructed image is going to be only two pixels in height, as seen in Fig. 5.13, where a 2D target signature is interpolated across vertical space from ground (0 m) to 5.5 m, by 5 receivers spaced 1.1 m apart (same result is obtained by simulating 4 receivers spaced by 1.385 m).

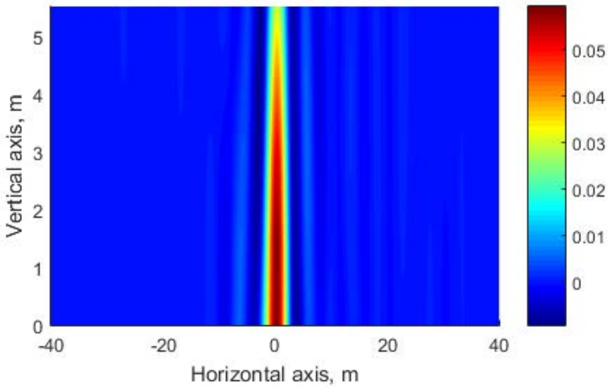

(a)

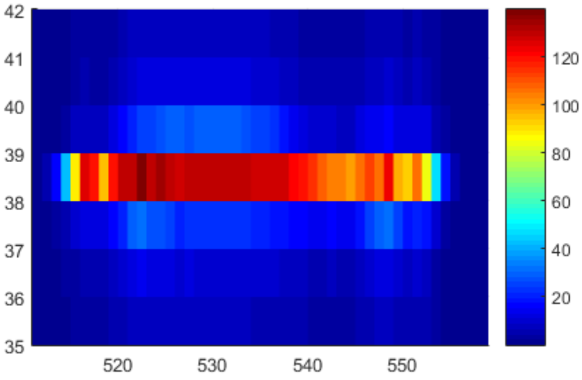

(b)

Figure 5.13: Real part of a two-dimensional target signature - (a), recorded by a sparse array of vertical receivers and the 2D target image reconstructed - (b), for a RR target (4.6 x 1.8 m) for 1 GHz incident radiation at 30 m from receiver.

Thus a relatively large array would be needed for the accurate extraction of 2D target profiles via this method. However a smaller array will still produce a 2D image, which can be used in conjunction with the 1D reconstructed profile. As seen from Fig. 5.13(b), the outline reveals where the top and bottom (wheels) of the car is. The wheels are positioned around 520 and 550 sample on the horizontal axis and haev magnitude of around 50. As previously mentioned analysis of the number of sidelobes required for the correct extraction of the target profile can be seen in section 7.2.2. The results indicate that at least three sidelobes should be analysed. According to aperture diffraction a width of a lobe is approximately given by:

$$\Delta\Theta = \frac{2\lambda}{h}, \tag{5.17}$$

where $\Delta\Theta$ is the spacing between nulls in radians and h is the height of the aperture considered. For the example considered, the width of a lobe for a target of 1.8 m height is around 9 degrees. This would result in minimum receiver height (for the recording of three sidelobes) of around 5 m at a 30 m observation distance.

The analysis regarding the height of the receiver array is based on the analysis of the minimum length of signal needed for the accurate reconstruction done in Chapter 7, where the conclusion is made that at least 3 sidelobes must be recorded.

In this subsection 2D target imaging was discussed. However, there are constraints which do not allow for 2D target imaging in practical applications of FSR, such as the availability of high vertical array of Rx antennas.

In the section the different methods for target imaging (profile reconstruction) in FSR were discussed. It was shown that a novel approach based on holographic principles has at least the same accuracy than previously published SISAR model. The properties of the reconstructed images was discussed, together with the availability of 2D target imaging. In the next section example results for simulated target signatures will be presented.

5.5 Initial results from simulations

The TSPR algorithm for one- and two-dimensional target signatures have been shown above, together with the initial analysis of the properties of the reconstructed target profiles. Further analysis of the output of the TSPR algorithm for different targets can be done based on modelled target signatures. In this section simulation results of TSPR for one-dimensional target signatures will be presented. The targets used in the modelling results below are chosen specifically to analyse different properties of the TSPR algorithm like gaps in the shadow (human walking and car with a trailer) and are geared towards the experimental scenarios used further in the thesis.

In the following simulated time-domain FS target Doppler signatures, the sampling rate is 200 Hz and the target is considered as an array of points, as shown in Fig. 4.8(b), of size 0.05 m x 0.05 m. The incident radiation has frequency of 1 GHz and the target is moving with constant velocity of 30 kph perpendicular to the middle of the baseline.

Firstly simulations are done for simple shape, like square and a human, see Fig. 5.14 and 5.15, in order to prove the feasibility of the TSPR algorithm.

In Fig. 5.14(a), the simulated time-domain signature for a square target is shown and the resemblance with the signal simulated by the model described in section 4.2, Fig. 4.2 can be clearly seen.

Further results are shown for other interesting ground moving targets: a bike riding human (Fig. 5.16); and two cars with different shapes - BMW 3 series (Fig. 5.17) and Ford Fiesta (Fig. 5.18).

Looking at the two car results - figures 5.17(b) and 5.18(b), the difference in shapes of the cars can be clearly seen in the simulated signatures. The presence of the bumps on

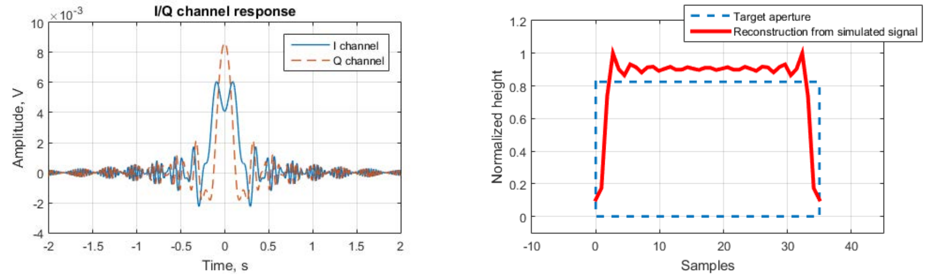

(a) (b)

Figure 5.14: Target shadow profile reconstruction and a simulated signal of a simple square target of size 1.8 x 1.8 m: (a) - time-domain signal; (b) - zoomed reconstructed profile and the original target aperture

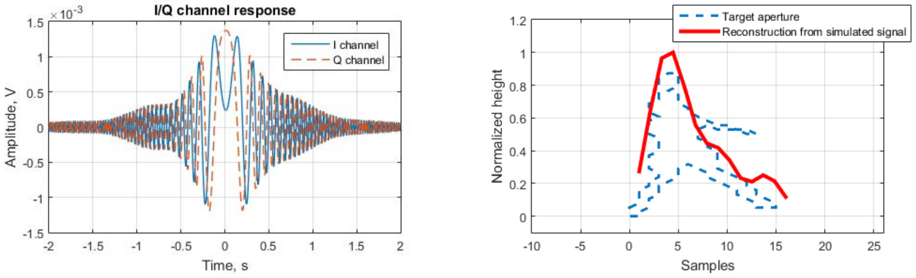

(a) (b)

Figure 5.15: Target shadow profile reconstruction and a simulated signal of a human target walking of height 1.8 m: (a) - time-domain signal; (b) - zoomed reconstructed profile and the original target aperture

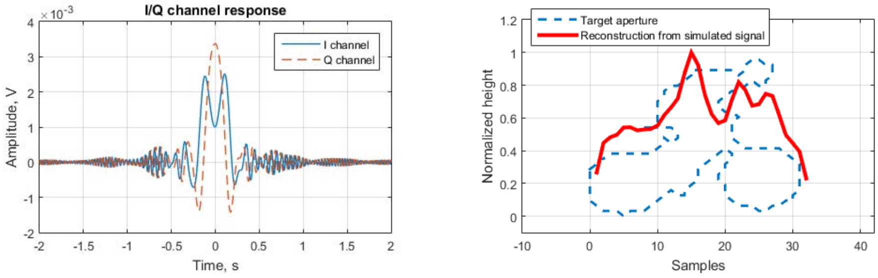

(a) (b)

Figure 5.16: Target shadow profile reconstruction and a simulated signal of a human target riding a bike of height 1.8 x 1.5 m: (a) - time-domain signal; (b) - zoomed reconstructed profile and the original target aperture

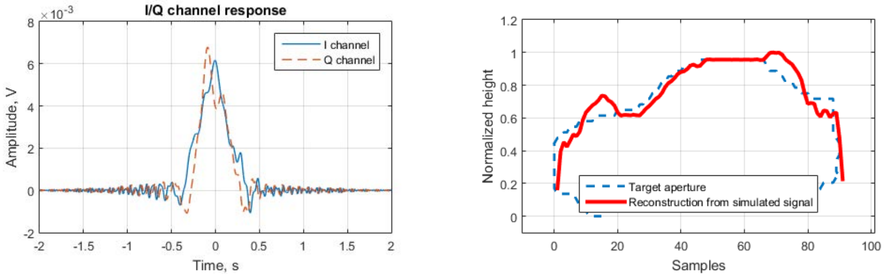

(a) (b)

Figure 5.17: Target shadow profile reconstruction and a simulated signal of a BMW 3 series target of size 4.6 x 1.4 m: (a) - time-domain signal; (b) - zoomed reconstructed profile and the original target aperture

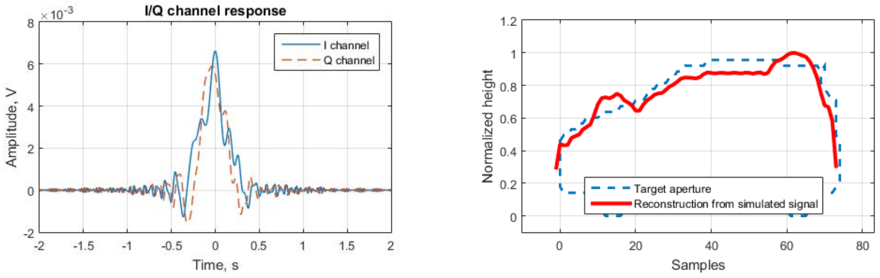

(a) (b)

Figure 5.18: Target shadow profile reconstruction and a simulated signal of a Ford Fiesta target of size 3.8 x 1.4 m: (a) - time-domain signal; (b) - zoomed reconstructed profile and the original target aperture

the top of the reconstructed profiles, is due to its one-dimensionality and was discussed in section 5.3, and represent the wheels of the cars.

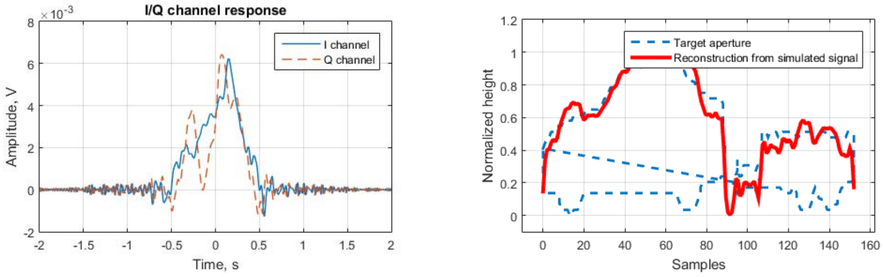

(a) (b)

Figure 5.19: Target shadow profile reconstruction and a simulated signal of a BMW 3 series target, towing a trailer target of size 3.4 x 1.5 m: (a) - time-domain signal; (b) - zoomed reconstructed profile and the original target aperture

From Fig. 5.19 it can be seen that the profiles of two targets in convoy (which in this case are the trailer and the car) can be reconstructed accurately, as long as the targets can be estimated to be in the same isophase contours along their movement, and thus their FSCS main-lobes coincide.

5.6 Conclusion

In the previous chapter the theory behind target imaging, i.e. profile reconstruction, in FSR has been shown. Firstly, the already published SISAR and its modified version were shown with examples for each one. Some of the differences between the two methods are outlined.

Further, the holography nature of the FSR signal was discussed, where the received target signal was described as a microwave hologram.

Further, the novel imaging method proposed by the author was developed. Holography methods were used to describe the FSR signal and thus the availability of the holographic approach for image reconstruction was developed. The method is computationally effective, following on the digital holography methods, only requiring a matrix multiplication and a Fourier transform to reconstruct the target image. This method for holographic reconstruction at microwave frequencies was referred to as TSPR.

A practical application of the holographic reconstruction method was discussed, together with the properties of the reconstructed profiles: one-dimensionality and behavior at edges. Multiple TSPR results of simulated signatures are shown.

An approach for a two-dimensional target imaging using a vertical receiver array has been developed as a method for high resolution target imaging and removal of the horizontal ambiguity of the target image due to the one-dimensionality of the original approach.

CHAPTER 6

EXPERIMENTAL VALIDATION OF TARGET SHADOW PROFILE RECONSTRUCTION ALGORITHM

In the previous chapter the TSPR algorithm was discussed and results were shown for simulated target signatures. It was shown that the TSPR can accurately reconstruct a target's profiles. In this chapter the algorithm will be applied to experimentally obtained target signatures.

A number of systems were employed for the experimental validation of the imaging algorithm, including both single node and multi-static configurations. In the following chapter the hardware of the systems used is going to be described and the parameters of the experimental measurements will be quoted.

Several scenarios were studied, where quadrature signatures were recorded for targets of different sizes and material compositions. Initial results for each of the systems will be presented, for the different targets measured.

It must be mentioned here that some of the reconstructed profiles will be inverted on the x-axis compared with the rest. This is due to a 90 degree phase shift between the Doppler kernel and the recorded target signature. However, this is of no consequence to the accuracy of the results.

6.1 Hardware used for experimental verification

Two major hardware set-ups were used for experimentation: one custom built and one built upon a Software Defined Radio (SDR) - the USRP-2950R. Each of these will be discussed below. The operational frequency was about 1.2 GHz in both cases. In the following two subsections the hardware will be briefly described, with more details found in Appendix B.

6.1.1 Single-node FSR system for ground moving target

As the goal of this section is the experimental confirmation of the theoretically developed 1D algorithm in chapter 5 using moving target, crossing a single baseline.

The custom built system block diagram is shown in Fig. 6.1 and consists of a transmitter and a receiver with baseband I/Q channel signal output. A more detailed description of the hardware used can be seen in Appendix B.1 where the results of a preliminary power budget calculation are shown, as well.

The transmitted waveform is a CW non-modulated waveform, generated by a MiniCircuits ZX95-1410-S voltage-controlled oscillator and amplified by MiniCircuits ZX60-V82 amplifier to achieve a transmit power of 18 dBm. The transmitted signal was then passed through a low-loss RF cable (Belkin RG-8/U) of length up to 60 m to the transmit antenna, representing the maximum separation between transmitter and receiver. This enables synchronization to be done precisely by the same oscillator, allowing for the accurate I/Q demodulation, without the need of phase-locked loops and separate local oscillators.

The receiver allowed for extraction of both Received Signal Strength Indicator (RSSI) and I/Q channels. The RSSI channel signal was extracted through the use of a Log-Amp detector, while the I/Q channels were demodulated in the usual manner, briefly introduced below.

The received signal was mixed by two copies of the transmitted signal, one $\pi/2$ shifted, to generate the two quadrature components of the chirp-like Doppler signature. These were LPF filtered to 100 Hz, i.e. providing maximum Doppler frequency of 100 Hz - sufficient for surface moving target observation [3]. The received signal was then passed to a USB-FS1608 ADC, and signals recorded by a laptop, with a sample frequency of 200 Hz.

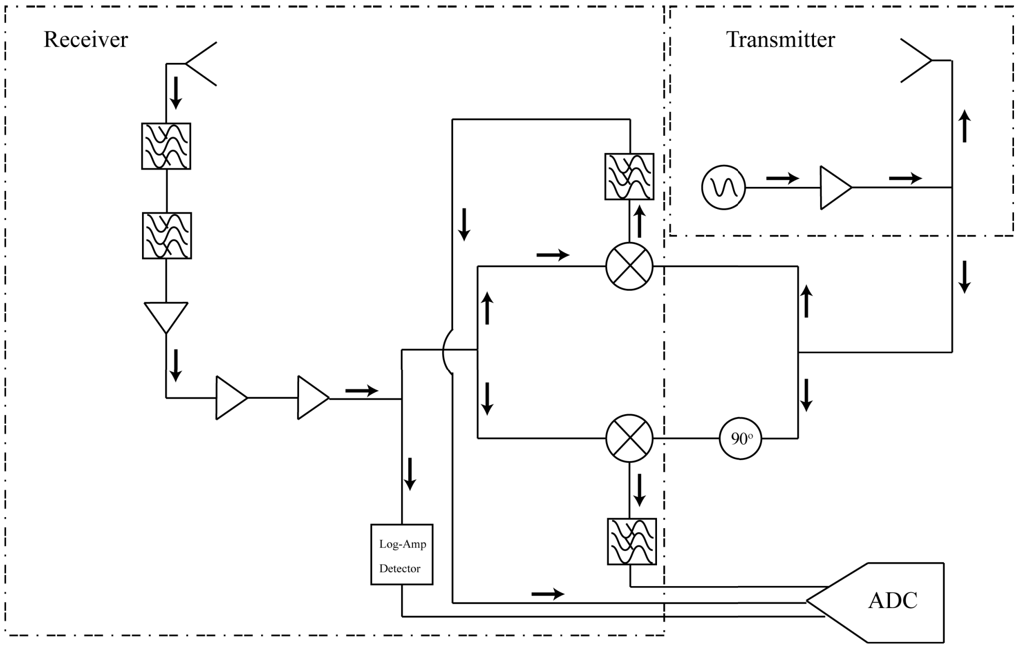

Figure 6.1: Schematic of hardware used for experimental verification of the TSRP algorithm

In Fig. 6.2(a), a photo of the transceiver is shown, where from now on it shall be referred to as 'black box' (BB). In the experimental measurements horn antennas were used - the

Q-Par WBH1-18S antenna, which operates at frequencies between 1 and 18 GHz, shown in Fig. 6.2(b). These antennas have gain of around 1.5 dBi at the operational frequency and -3 dB beamwidth of 80 degrees [66].

(a) (b)

Figure 6.2: Picture of the single-node FSR transciever - (a); and the WBH1-18S Q-Par horn antenna used in measurements - (b).

This system was proven to have high phase accuracy and was used as calibration for the rest of the hardware used.

The above described proof-of-concept single-node FSR system was developped and designed in the MISL laboratory by Dr. Edward Hoare.

Another scenario studied in the measurements undertaken was a 2x2 multistatic system that was based on a SDR - the NI USRP-2950R orgnaized in FSR configuraion. A brief description of the device is introduced next.

6.1.2 Software defined radio

The Universal Software Radio Peripheral (USRP) is a computer-hosted system, a part of a group defined as Software Defined Radio (SDR). It represents a digital system, preprogrammed to be used as a radio controller, thus giving the ability for RF transmitters or receivers to be built comparatively inexpensivly and simply. The USRP family of hardware was designed for open and easy access to radio technology.

The general structure of USRPs consists of a motherboard, containing the hardware for the digital signal processing and host PC controllers, and one or more daughterboards, representing the RF front-end. The motherboard consists of a Field-Programmable Gate Array (FPGA) used as a digital signal processor, USB or Ethernet controller for the communication with the host PC, ADCs and DACs, crystal oscillator for precise frequency control, a flexible clock (from 10 to 64 MHz), and power regulators. The daugherboard, generally, consists of filters, low noise amplifiers and IQ modulator/demodulator.

Initial feasibility experiments for the application of such devices as FSR systems were made with the USRP B100, and sample results can be seen in [67]. The conclusion of the publication being that USRP devices can be used as FSR systems, however due to a somewhat high noise figure (also discussed in [67]) would require additional RF front-end to be fitted to the device.

During the research an USRP with higher specification was obtained which was used in further experiments. The details of the device - NI USRP-2950R, can be seen below.

6.1.2.1 USRP-2950R

The 2950R has the same general structure as outlined above, but with further added calibration tables for higher SNR and lower harmonic distortions. Also, for more accurate and stable reference the clock is locked to GPS. A full schematic of the device can be found on [68].

Another difference is that there are two daughter-boards on the device, each capable of transmitting and receiving signals from 50 MHz to 2.2 GHz. This can allow for multi-static measurements in 2x2 configurations, providing 4 baseline crossings rather than a single one.

The 2950R's motherboard consists of a Xilinx Kintex-7 FPGA, which digitally down converts the signal and has free gates which allows for the application of FPGA programming. This can allow for easier implementation of initial signal processing algorithms on the device, thus reducing the amount of post-processing needed, but was not studied in the context of TSPR application.

The 2950R has a maximum transmitted power of +15 dBm and +31.5 dB maximum amplification of the received signals and maximum RF bandwidth of 40 MHz. The device can be connected to the host PC via three different methods, each having its own advantages and disadvantages:

- 1 Gbps Ethernet - quick and easy to set-up, but limited to 10 MHz RF bandwidth due to the maximum of the data-flow of 125 MBps.
- ExpressCard - limited to 20 MHz bandwidth due to the restriction of data-flow of PCIe x1 slot of ExpressCard connectors, but can customize FPGA code and is designed for use with laptops, which allows for mobility of the system
- PCIe x4 card - can utilize full bandwidth and can take advantage of the customizable FPGA, but can only be used with a tower PC

Firstly, for the initial set-up and callibration of the system, the PCIe x4 card was used in a Dell T7400 PC, which allowed for the receiving of the full bandwidth of the 2950R. This connection type proved to be good choice for the utilisation of the full potential of the device, but due to the lack of mobility, it was decided that 1 Gbit Ethernet and

ExpressCard PCIe connections will be used for the experimental processes.

The hardware was controlled via LabVIEW 2014 and LabVIEW 2015 software, using the NI-USRP 14.0 and 15.0 driver, respectively. A screenshot as an example of the front-view of the software used in the experiments can be seen in Fig. 6.3.

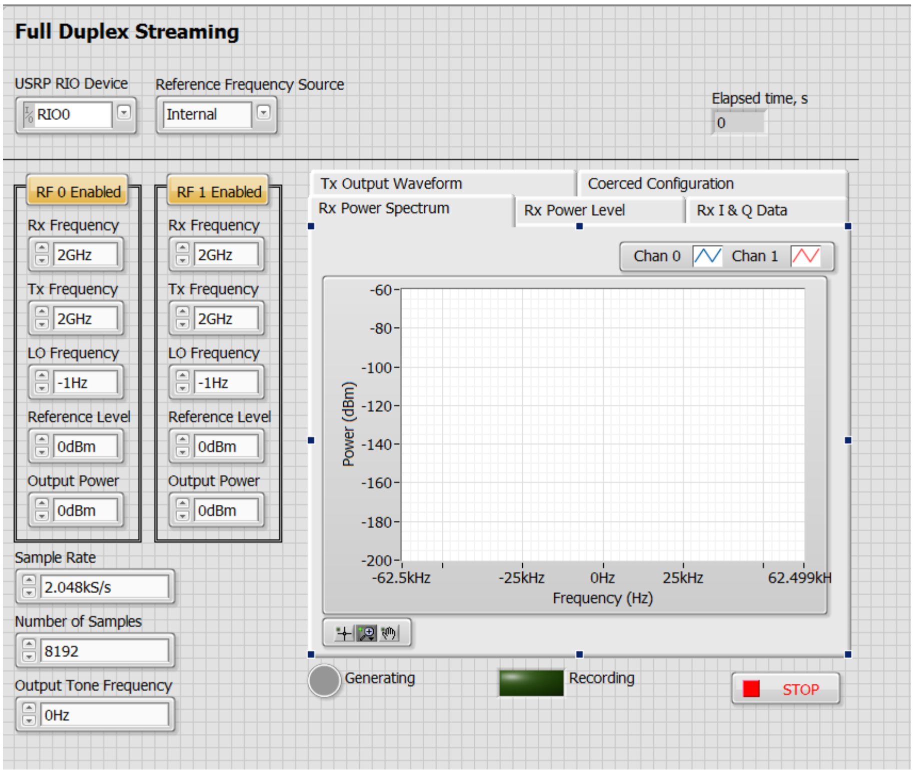

Full Duplex Streaming

USRP RIO Device: RIO0
Reference Frequency Source: Internal
Elapsed time, s: 0

RF 0 Enabled
Rx Frequency: 2GHz
Tx Frequency: 2GHz
LO Frequency: -1Hz
Reference Level: 0dBm
Output Power: 0dBm

RF 1 Enabled
Rx Frequency: 2GHz
Tx Frequency: 2GHz
LO Frequency: -1Hz
Reference Level: 0dBm
Output Power: 0dBm

Sample Rate: 2.048kS/s
Number of Samples: 8192
Output Tone Frequency: 0Hz

Figure 6.3: Top view of the LabVIEW program used for initial 2x2 MIMO measurements with USRP-2950R

The device was used with 4 in-house made patch antennas (designed by Mr Liam Daniel, MISL staff member). The centre frequency of the antennas was 1.19 GHz and some of the properties of the 4 antennas can be found in App. B.2.

A power calibration over the whole band of the device was performed, as part of the study. The results can be seen in Appendix B.3.

Multiple experiments were made with each of the two hardware configurations discussed above. Thus, TSPR was applied to signatures recorded with both the 1.2 GHz BB single-node FSR and 2x2 multi-static system, using the USRP-2950R. The results are going to be shown in the next section.

6.2 Experimental results

Experimental measurement to experimentally validate the TSPR algorithm were done using both of the hardware systems described above. An overview of the measurements undertaken can be seen in Table 6.1.

Firstly, scaled measurements which are highly repetitive were done with electrically smaller targets (size of the order of few wavelengths, but still in high Mie scattering regime). These were done for both validation of the hardware through its design iterations and quick proof of the signal modelling technique introduced by the author in section 4.3.2.

After that initial measurements with car targets were done, where 5 different cars were used - Land Rover Discovery 2 (LR), Range Rover Sport (RR), BMW 3 series coupe, Ford Fiesta (FF), Smart Fortwo. The target signatures were measured with both the BB and the USRP-2950R hardware. Following the validation of the TSPR algorithm, more complex measurement scenarios were used. These included targets with open and closed windows and a multistatic measurement.

The results obtained from the experiments with open and closed windows were used for initial analysis of the effect of the material composition of the targets, while the multistatic measurements were used for initial analysis of simultaneous imaging at different aspect angles.

Table 6.1: Overview of the experimental details

Date	Hardware Used	Baseline	Antennas height	Target	Trajectory
03.05.13	BB	10 m	0.3 m	saturation test measurements	perpendicular
12-16.07.13	BB	12 m	0.3 m	T1, T2, T3	perpendicular
07.12.13	BB	50 m	1 m	BMW, LR, Smart	perpendicular
19.07.14	BB	65 m	1 m	BMW, LR, FF, human	perpendicular
09.08.14	BB	60 m	1 m	FF, RR	perpendicular
20.12.14	BB	55 m	2 m	LR, FF, BMW	perpendicular
29.05.15	USRP 2x2	61 and 65 m	1 m	BMW, LR	perpendicular and 68 degrees

6.2.1 Initial experimental results with plates

Initial experiments were made, recording the I/Q demodulated FSR target signatures of smaller targets, to prove the concept of the TSRP algorithm and test the equipment. The transceiver used was the BB, referred to in section 6.1.1, transmitting 1.2 GHz CW signal, corresponding to a wavelength, λ, of 0.25 m. The antennas used were identical Q-Par horn antennas.

The experiments were done on a car park in the main campus of the University of Birmingham, as shown in Fig. 6.4, which was chosen for the low clutter environment and low interference. Baselines ranged between 8 and 12 m, and the target was the chassis of a remote controlled toy car, travelling with speed around 1 m/s, with a conducting asymmetrical plates secured on this chassis. Thus different asymmetrical shapes could be investigated.

Three target shapes were used, all of them "interesting" to target imaging - two rectangles with different sizes taped together, a triangle and one with a rectangle taped to the triangle. The sizes and pictures of the targets can be seen in Table 6.2 and Fig. 6.5, respectively. As seen in Table 6.2, all the used targets fall within the optical scattering regime, i.e. follow the approximation that:

$$\frac{2\pi D}{\lambda} \geq 10, \tag{6.1}$$

where D is the largest dimension of the target.

Target signatures have been repeatedly recorded on a number of occasions, and show high degree of repeatability - an inherent property of FSR.

The target signatures were modelled according to the model outlined in section 5.5 and

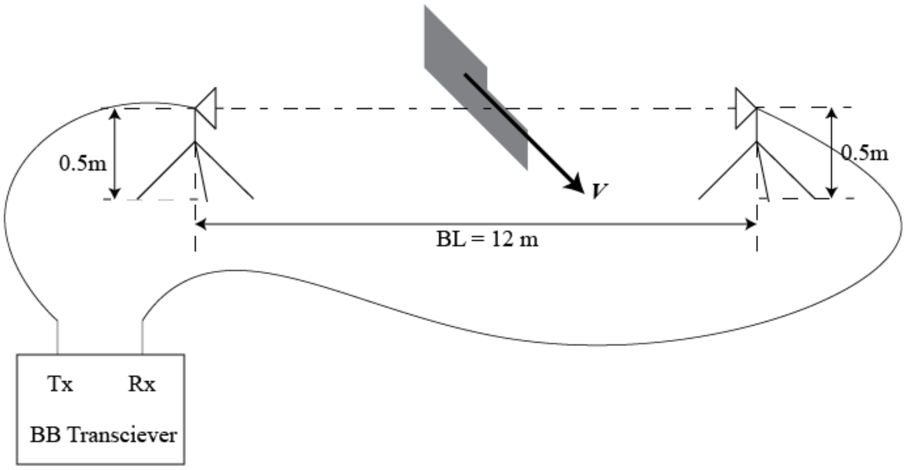

(a)

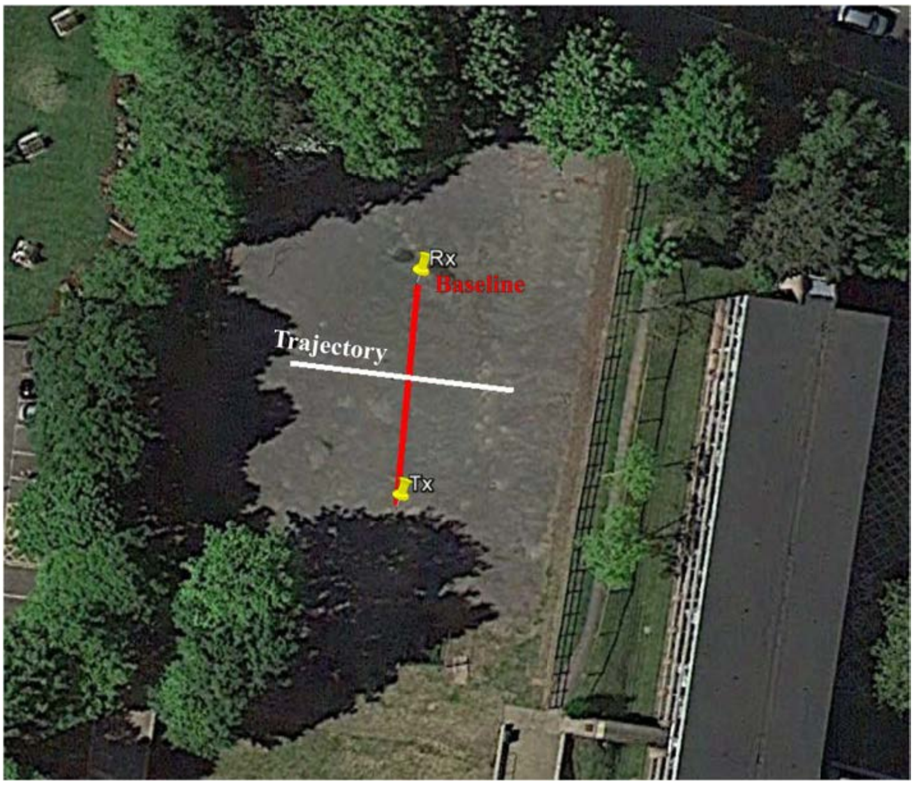

(b)

Figure 6.4: Location of the initial experiments, with smaller electrical size targets.

(a) (b) (c)

Figure 6.5: The three different targets used for initial prove of the TSRP model: T1 - (a); T2 - (b) and T3 - (c).

Table 6.2: Table of size of the targets used in the initial experimental tests

Target	Size (h x l), m	El. size, according to eq. 6.1
T1, Fig. 6.5(a)	0.68 x 0.76	15.91
T2, Fig. 6.5(b)	0.76 x 0.72	15.91
T3, Fig. 6.5(c)	0.76 x 1.1	23.03

are compared to the measured ones in Fig. 6.6, below, for the same target motion and baseline - baseline of 12 m, antenna elevation of 0.5 m and target crossing the baseline perpendicularly in the middle at speed of around 1 m/s.

The simulated target signatures for the three targets used in the initial measurements shown good correspondence with the recorded signatures. However, the main purpose of the measurements was the confirmation of the TSPR algorithm and as such the recorded signatures were processed by the TSPR algorithm. Examples of the reconstructed target profiles from the signatures seen above can be seen in Fig. 6.7, below.

As seen in Fig. 6.7 reconstructed target profiles can provide with information about the general shape of the targets, though because the features on the targets are small, the wavelength is not sufficiently small to accurately extract the accurate target profile.

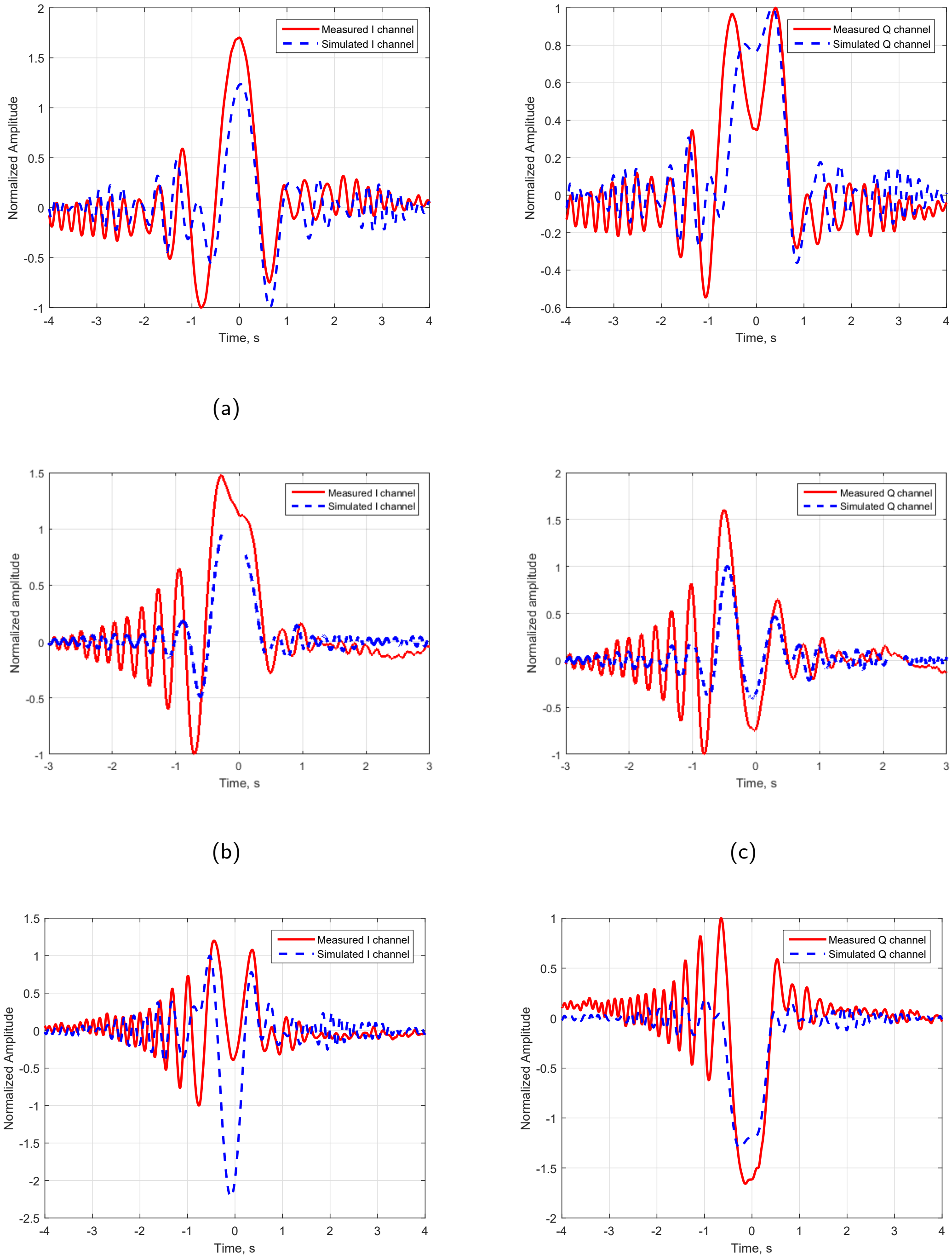

(a)

(b)

(c)

(d)

(e)

Figure 6.6: Simulated and recorded (suing BB hardware) complex signatures for the three electrically small targets: T1 - (a) and (b); T2 - (c) and (d); T3 - (e) and (f)

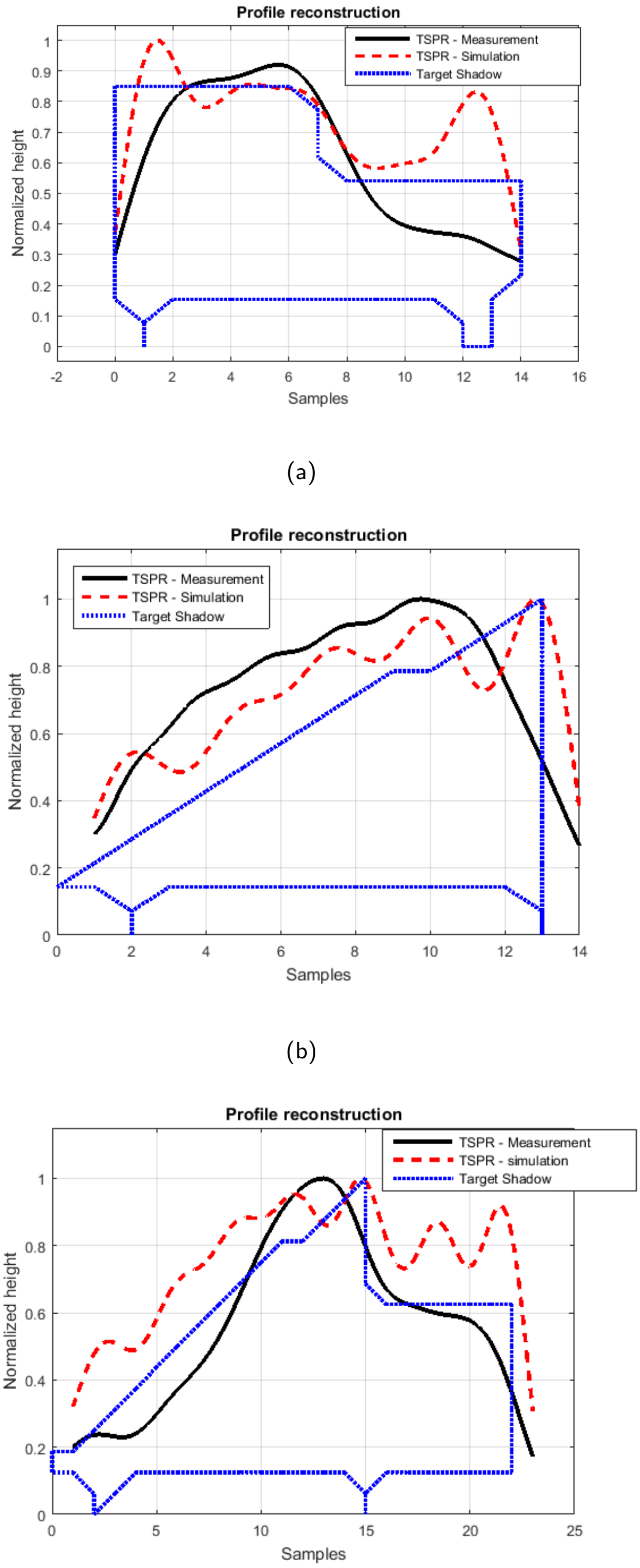

(a)

(b)

(c)

Figure 6.7: Profile reconstruction results for the targets shown in Fig. 6.5. T1 - (a); T2 - (b) and T3 - (c).

This can be confirmed by visual inspection of the influence of the target wheels (the wheels of the chassis). It can be seen that the target profile obtained from the simulated signals are influenced by the presence of the wheels to a greater extent than those for the measured signatures. This is most evident from the reconstruction of target T1 (Fig. 6.7(a)). Also, differences between the target model and the measurement results for this target can be seen in the regions where the target is low above ground (the end of the target) with height of about 0.4 m (less than 2 wavelengths of height). The remainder of the reconstructed profile of target T1 corresponds to the target shadow contour and the results of the simulation. The total height of the target was around 3 wavelengths.

In terms of the second target used in the initial measurements - T2, the measured result follows the modelled result well, where the latter can be seen to have more 'unstable', oscillatory nature than the result from measurements. Both follow the observations obtained for target T1, where there is biggest difference between target shadow and TSPR result in the regions where the target has the smallest height. It must be mentioned that in terms of target T2, the wheels had a smaller influence on the simulated results than for target T1. This might be due to the constant gradient on the contour of the target, rather than a flat line like it is with the previous target discussed.

Target T3 represents a combination of both the targets previously discussed as its shadow contour has both a straight line and a line which is gradually increasing. The reconstructed profiles follow the observations for the previous two targets, where in the regions of flat line (end of the target) there is influence of the wheel of the chassis in the simulated profile, while it has an oscillatory nature in the rest of the target. The measured result follows the target shadow, where it has lower agreement in the parts where the target has a lower height. The flat part of target T3 is above 2 wavelengths in height, while the full height is around 3.

Further experiments were done with bigger targets to ensure system operation in the high optical region of forward scattering. Further analysis of the accuracy of the target profiles will be performed in the next chapter.

6.2.2 Initial experimental results with car targets

Multiple experiments were done on the Pritchatts Road Car Park, within the main campus of University of Birmingham, UK, to experimentally prove the results of the TSRP algorithm for ground moving targets. The geometry of these experiments is shown in Fig. 6.8, where the target was crossing the middle of the baseline (red line), along a perpendicular trajectory (white line). A view of the experimental set-up from the position of the target can be seen in Fig. 6.9.

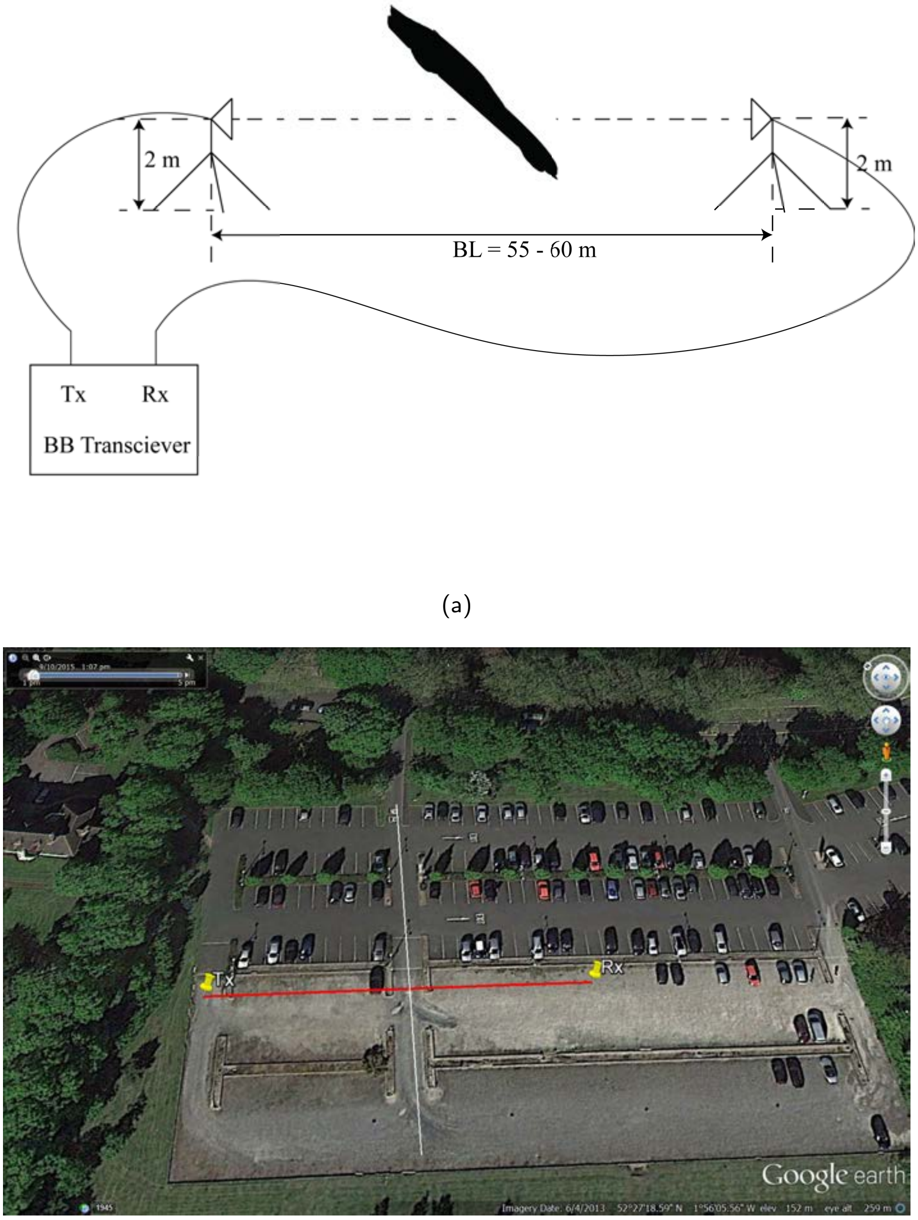

(a)

(b)

Figure 6.8: Geometry of single-node experiment configuration. A schematic in (a) and an overlay on Google Earth in (b).

Table 6.3: Description of experimental recordings

Date (mm/yy)	Targets	Baseline
08/14	FF, RR	60 m
07/14	BMW, FF, LR	65 m
12/13	BMW, LR, Smart	50 m
12/14	BMW, FF, LR	55m

Figure 6.9: Target's point of view of the experimental set-up.

The target signatures were recorded on multiple occasions, Table 6.3, gives the main experiments undertaken. The main purpose of these experiments was to prove the previous results of the TSPR algorithm, including the difference in the reconstructed profiles for targets with opened and closed windows.

During all the measurements target speeds were between 10 and 20 kph, target trajectories were continuously recorded via a GPS logger and the target crossing was recorded using a few GoPro Hero cameras. The equipment used was the BB transceiver of section 6.1.1, with two wideband horn Q-Par WBH 1-18S antennas at height of 2 m.

Several targets were used - BMW 3 series, Land Rover Discovery 2 (with roofrack), Ford Fiesta, Range Rover and Smart Fortwo. Pictures of the targets are shown in Fig. 6.10.

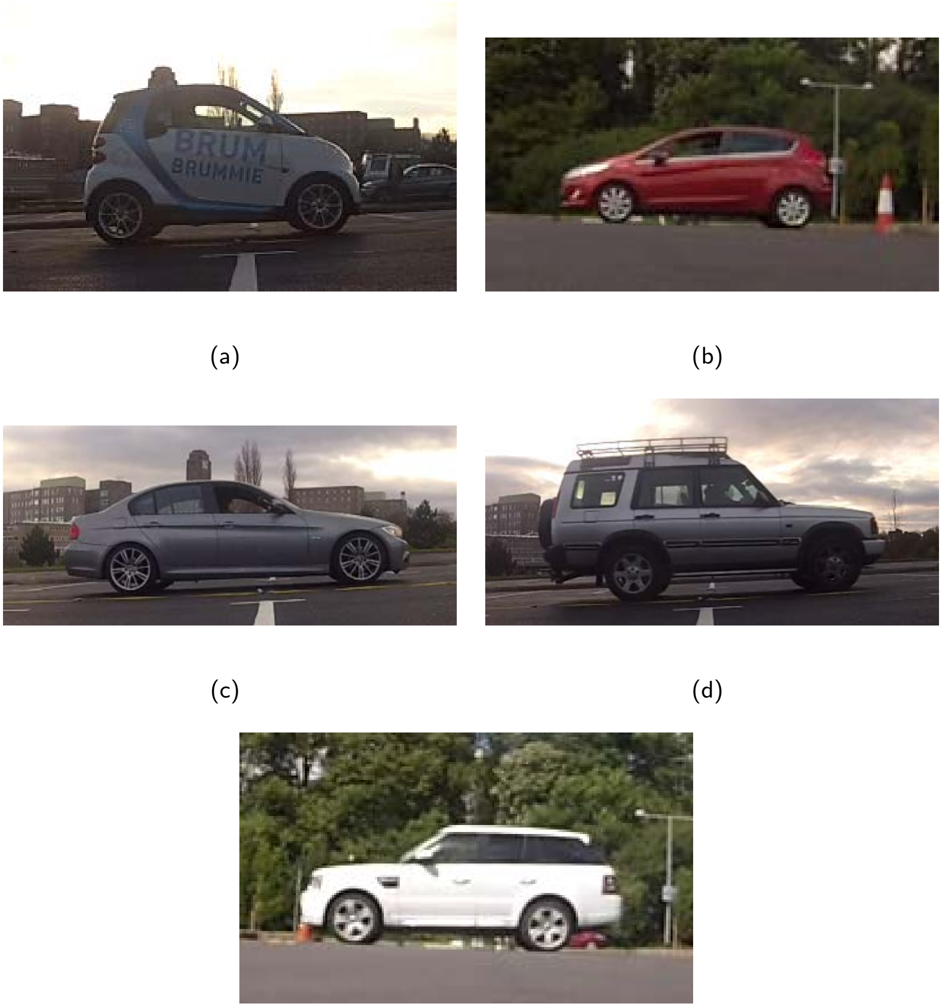

(a) (b)

(c) (d)

(e)

Figure 6.10: The different targets used for initial experimental proof of the TSRP model. Smart Fortwo (2.7 x 1.5 m) - (a); Ford Fiesta (4 x 1.5 m) - (b); BMW 3 series (4.6 x 1.4 m) - (c); Land Rover Discovery 2 (4.7 x 2 m) - (d) and Range Rover (4.7 x 1.8 m) - (e)

Examples of the signatures recorded for the five targets can be seen in Fig. 6.11, 6.12, 6.13, 6.14 and 6.15 together with simulated signatures, using the modelling described in section 5.5.

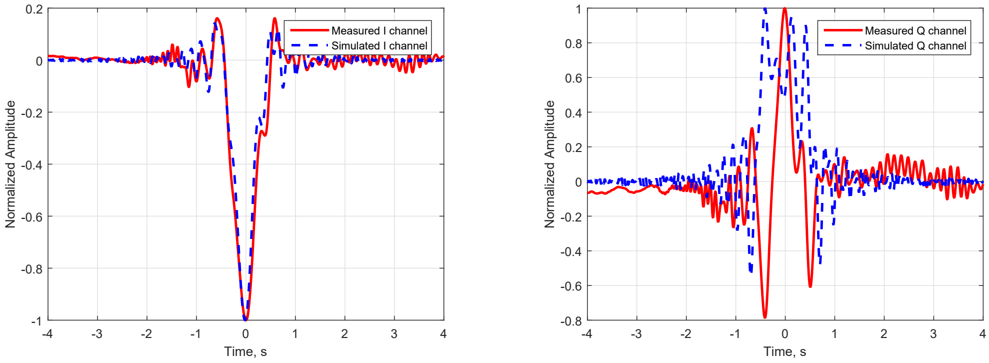

(a) (b)

Figure 6.11: Recorded signatures and the simulated signatures corresponding to the recording parameters for Smart Fortwo - I - (a) and Q - (b).

Figs. 6.11, 6.12, 6.13, 6.14 and 6.15 show the recorded time-domain signatures of five different targets compared to modelled signatures. The targets were moving with the following speeds during those measurements: Smart Fortwo ≈ 3 m/s (11 kmph); Ford Fiesta ≈ 2.2 m/s (8 kmph); BMW 3 series coupe ≈ 2.5 m/s (9 kmph); Land Rover Discovery 2 ≈ 5 m/s (18 kmph) and Range Rover Sport ≈ 3.6 m/s (13 kmph). These speeds were extracted from the video and GPS ground truth. An analysis of the effect of the error in the estimated speed on the reconstructed profile will be presented in section 7.3.

The simulated signatures for the targets used, coincide to reasonable degree of accuracy with the experimentally recorded signatures and specifically within the main lobe. Discrepancies outside the main lobe may be result of bistatic scattering from the sides of the car, for the recorded signatures, or difference in the Doppler phase. This Doppler difference can be from a small error in the estimation of the target speed. However, these

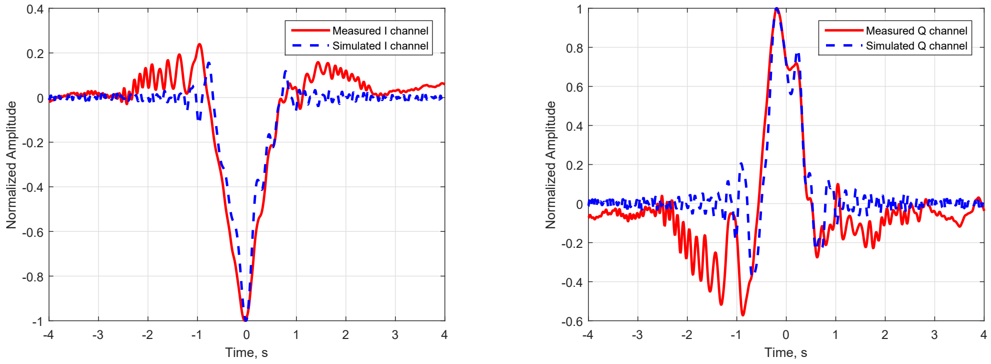

(a) (b)

Figure 6.12: Recorded signatures and the simulated signatures corresponding to the recording parameters for Ford Fiesta - I - (a) and Q - (b).

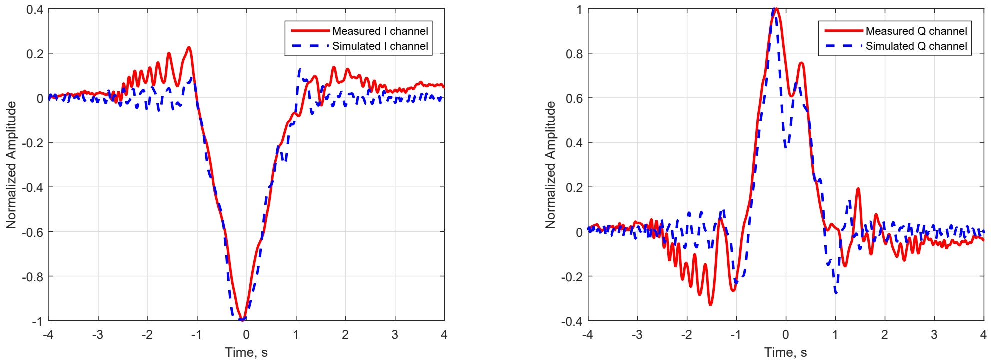

(a) (b)

Figure 6.13: Recorded signatures and the simulated signatures corresponding to the recording parameters for BMW 3 series coupe - I - (a) and Q - (b).

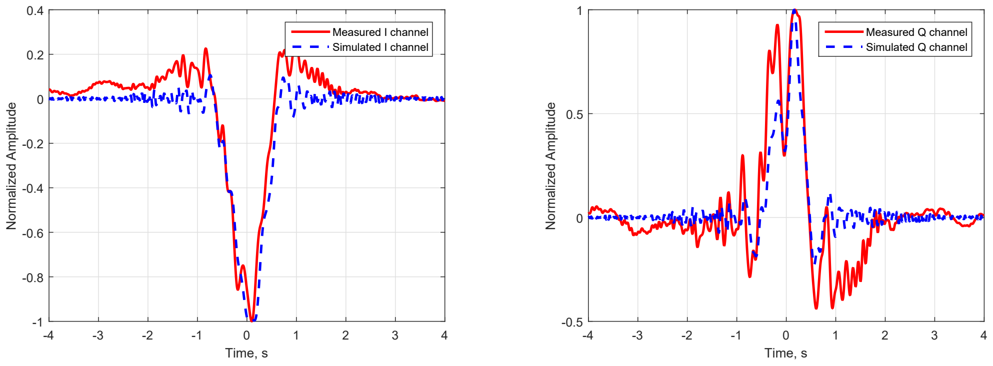

(a) (b)

Figure 6.14: Recorded signatures and the simulated signatures corresponding to the recording parameters for Land Rover Discovery 2 - I - (a) and Q - (b).

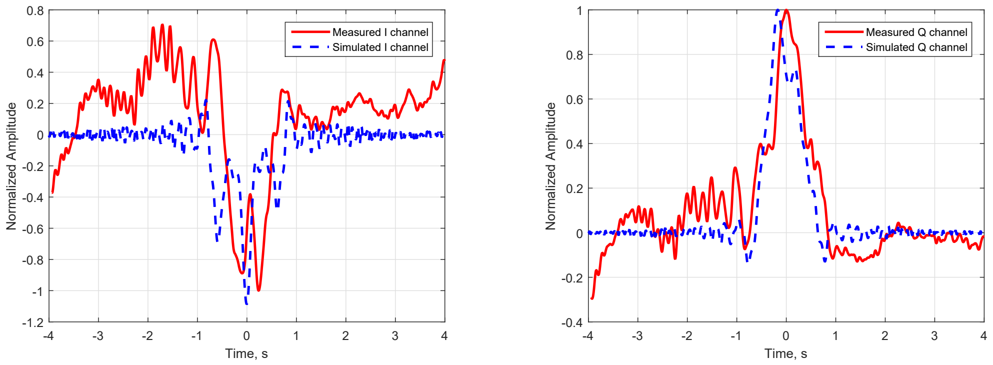

(a) (b)

Figure 6.15: Recorded signatures and the simulated signatures corresponding to the recording parameters for Range Rover Sport - I - (a) and Q - (b).

discrepancies have little consequence on the result of the TSPR algorithm further away from the main lobe of the target signature. This is further discussed in Chapter 7. Also, some discrepancies between the modelled and recorded signatures may arise from the approximations made in section 4.3.2, mainly far-field operation and plane wave incidence on the target. This effect was not studied further in the thesis, however is a topic for further work.

It can, also, be seen that there is generally good agreement between the simulated and modelled results except for the cases of Fig. 6.11(b) and 6.15(a). In both cases the simulated target signatures look more oscillatory within the main lobe than the corresponding recorded signals. For the rest of the signatures it can be said that the main discrepancies are outside of the main lobe and specifically the variable DC level around the main lobe. This effect can be an effect from the multipath or some clutter interference. The modelled results do not take into account the multipath, and as such this cannot be proven at this stage of the research.

The I and Q channel signatures of the smaller targets - Smart and FF, can be said to be less oscillatory within the main lobe, when compared to the bigger targets - LR and RR. This is especially evident from the I channel signals of all the targets.

The TSRP algorithm was applied to the signals presented in the figure above and the reconstructed profiles for the five targets can be seen in Figs. 6.16, 6.17, 6.18, 6.19 and 6.20.

Firstly, comparing the results of the two main measurements - electrically smaller targets (Fig. 6.7) and real world targets, it can be visually determined that the accuracy of the reconstructed profile for the big targets (cars) is much higher than that of the electrically smaller targets. Table 7.7, shows the parameters of the accuracy of the reconstructed

Figure 6.16: Reconstructed profile of Smart Fortwo

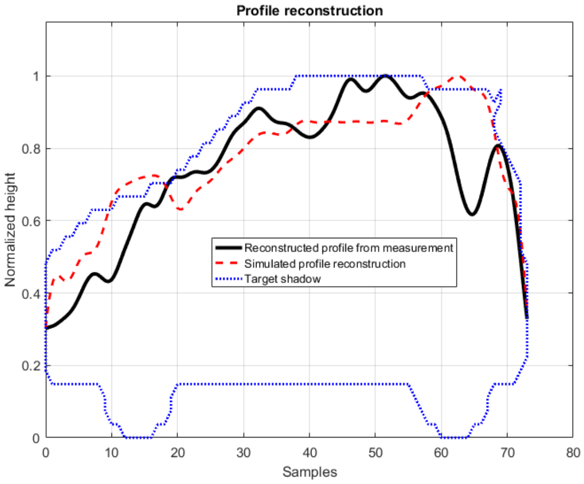

Figure 6.17: Reconstructed profile of Ford Fiesta

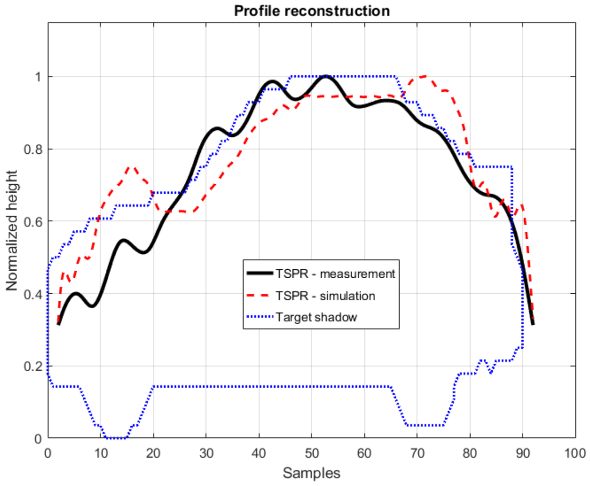

Figure 6.18: Reconstructed profile of BMW 3 series coupe

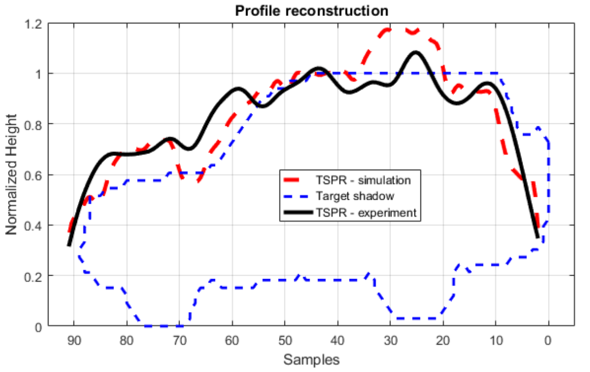

Figure 6.19: Reconstructed profile of Land Rover Discovery 2

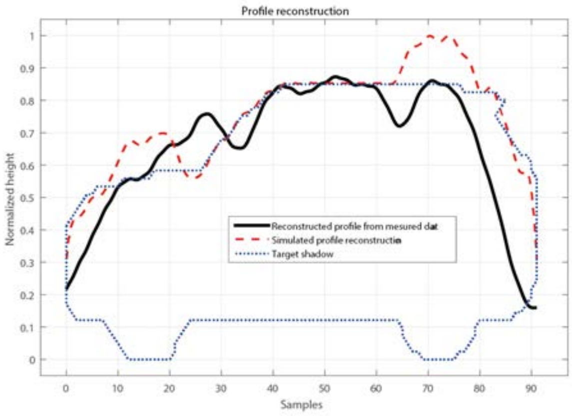

Figure 6.20: Reconstructed profile of Range Rover Sport

profiles of the cars. This is expected as the typical car is in the optical region of the FSR system used.

Secondly, from the results presented in the figures above, it can be noted that in reality the wheels on the bottom of the target have much less influence on the experimentally obtained target profiles, compared with the modelled results. This might be due to the influence of the two-ray propagation, where the received target signal power is proportional to at least $1/\text{height}^4$, where height is the height of a point on the target.

The last two remarks are a subject to a further fundamental study, which should focus on the composition of the target's studied.

It must be noted here again that samples in the x-axis of the reconstructed profiles correspond to time domain samples, dependent on the speed of the car and the sampling rate. This issue is further discussed in section 7.2.1. In practice the length in samples can be converted to the actual length of the vehicles, however, this has not been investigated further during the feasibility study of the TSPR algorithm. The profiles shown are, also, rescaled where a sample in the x-axis corresponds to the area of the secondary radiators used in the modelling - each sample corresponds to 0.05 m.

The experimental results for the profile reconstruction of targets show that the method is accurate and reconstructs the target image to some degree of similarity for a single node system with targets crossing the baseline perpendicularly in the middle. As further validation a 2x2 multistatic system based on the NI USRP-2950R was used to record FS target signatures and will be presented next.

6.2.3 Results of 2x2 multi-static configuration

An experiment with a 2x2 multi-static configuration using the NI USRP RIO-2950R, was performed on the Pritchatts Road Car Park of the University of Birmingham, with the geometry shown in Fig. 6.21. The technical parameters of the measurements are given in Table 6.4, the antennas used were in-house built patch antennas with centre frequency of 1.17 GHz, and their properties are shown in Appendix B.2.

The main purpose of the measurements was to investigate how the reconstructed target profile will change when a target is moving at some angle with respect to the baseline and compared with the perpendicular crossing. As such, the 2x2 system provided with two cases of each, where the targets were crossing the baseline at 90 and at around 60 degrees. A final goal would be to fuse the results in a reconstructed target model to improve accuracy. This has not been investigated in this thesis, however the difference in the reconstructed profiles for the different crossing angles are shown. This fusing technique can be based on averaging or other similar techniques to reduce the oscillations of the reconstructed profiles, or fuse the profiles in three dimensional space as shown for modelled results in Fig. 6.28.

Also, the measurements provided with somewhat more accurate measurement of the target trajectory parameters, according to the previously published methods discussed in section 2.5.3.

As stated above, the geometry will provide two perpendicular crossings and two 68 degree crossings of the baseline for the same target, which can improve the data extraction. Two targets were used in the experiments - a Land Rover Discovery 2 (Fig. 6.10(d)) and a BMW 3 series coupe (Fig. 6.10(c)). The corresponding lengths of the target shadows with 22 degrees projection will be: 4.11 and 4.00 m. The 22 degrees projection is relevant to a

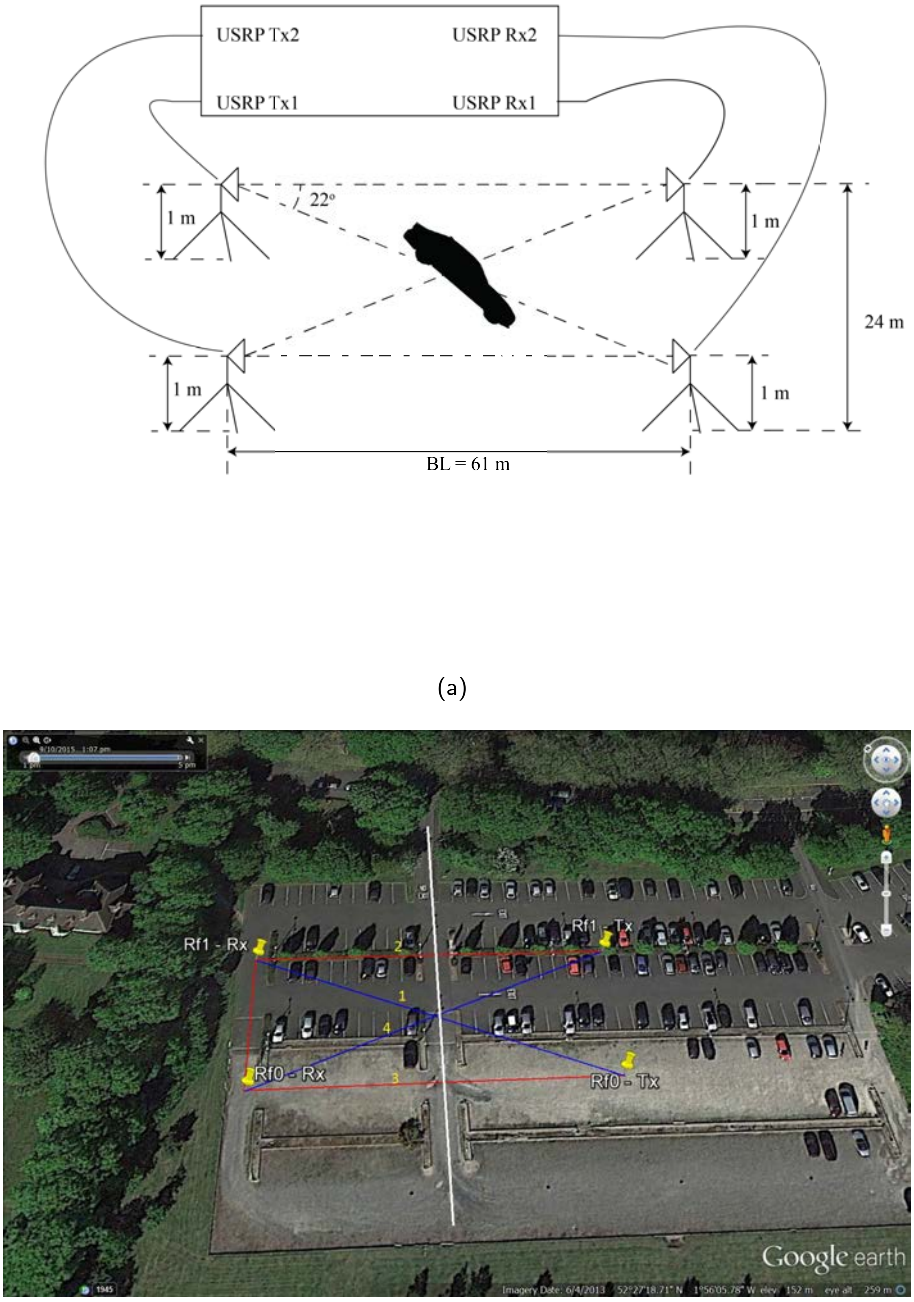

(a)

(b)

Figure 6.21: Geometry of 2x2 multi-static configuration, the baseline lengths are 61 m and 65.5 m, while distance between Tx/Rx pairs was 24 m. The four antennas had height of 1 m. Figure shows a schematic in (a) and an overlay of the geometry on a Google Earth image in (b)

Table 6.4: Technical parameters of the 2x2 MIMO measurements.

Parameter	Value
Receivers centre frequency	1.1800155 GHz
Transmitter 1 centre frequency	1.1800157 GHz
Transmitter 2 centre frequency	1.1800146 GHz
Sampling rate	3 kHz
Tx power	15 dBm
Rx Gain	30 dB

line perpendicular to the baseline, as graphically explained in Fig. 6.22. The projections expected are shown in Fig. 6.23, below.

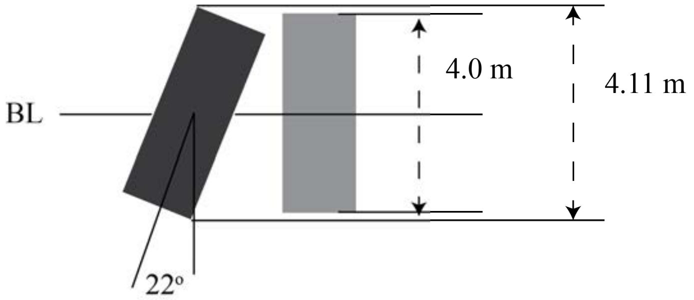

Figure 6.22: Change of target shadow length due to its projection angle with respect to the baseline

The crossing speed of the targets has been calculated to be 4.1 and 5.3 m/s (15 and 19 kph) for the perpendicular crossing for the BMW 3 series and Land Rover Discovery 2 targets, respectively. This is the crossing speed at the perpendicular crossings and it is assumed that the targets are moving with more or less constant speed through the area observed.

Examples of the signatures of the two targets for the four different baseline crossings are shown in Fig. 6.24(a) and 6.24(b). Comparing the signatures recorded by the BB hardware

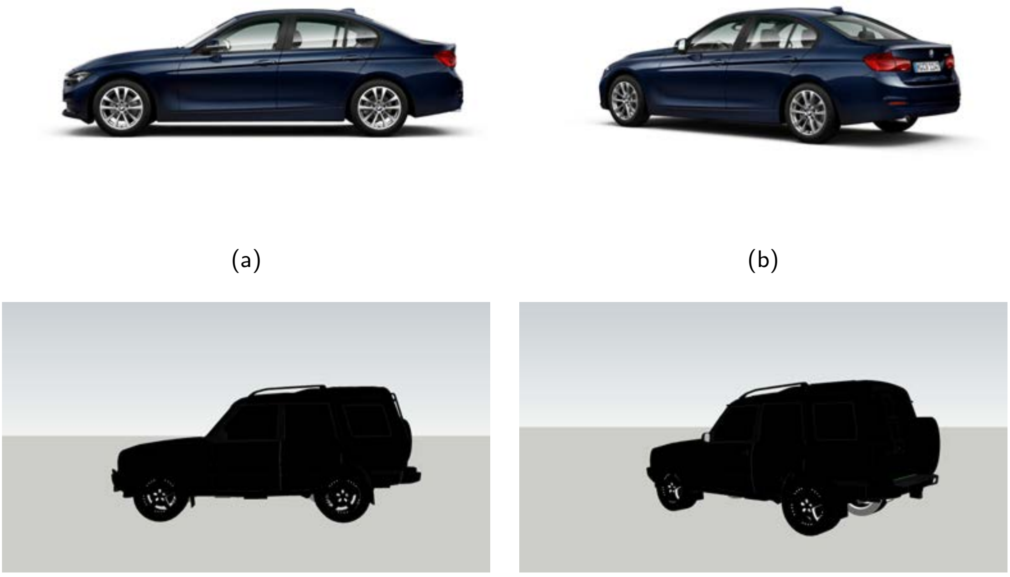

(a) (b)

(c) (d)

Figure 6.23: The four expected projections of the two car targets - BMW 3 series and Land Rover Discovery 2. Perpendicular projections for the two targets are shown in (a) and (c), respectively, while the projections at 22 degrees are shown in (b) and (d)

(Fig. 6.13(a) and 6.13(b) for BMW target and Fig. 6.14(a) and 6.14(b) for LR target) it can be seen that the signals recorded for the 2x2 MIMO resemble the previously recorded signatures for the same targets, but have lower received power, and the signatures of the targets for the cross-receiver case are deteriorated. This suggests that the USRP has a high noise figure (also suggested in [67]) and thus should be fitted with RF front-end, consisting of additional amplifiers and filters, for future measurements.

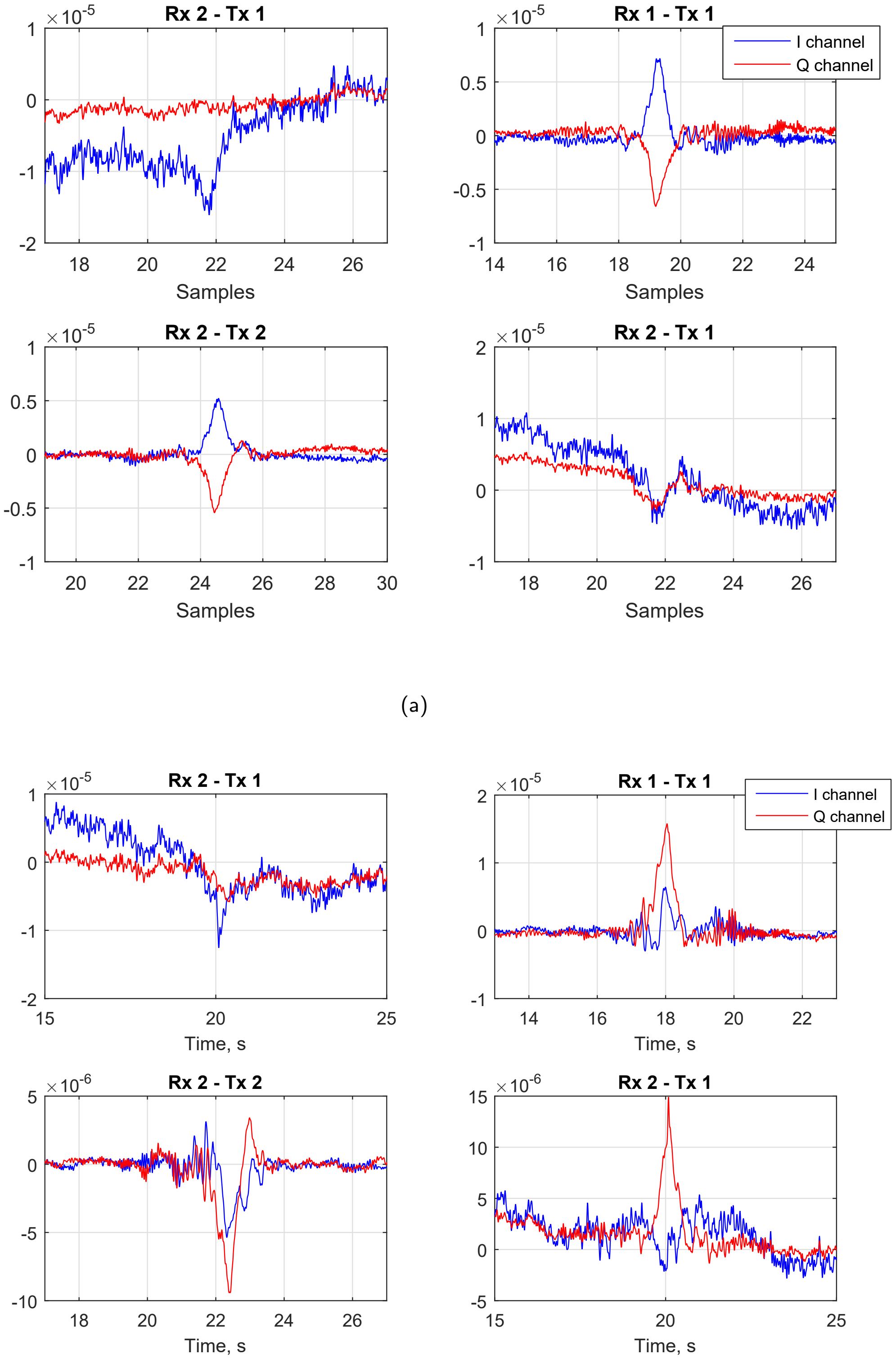

(a)

(b)

Figure 6.24: Example of the signatures recorded for BMW 3 series coupe - (a) and Land Rover Discovery 2 - (b), for the four target crossings.

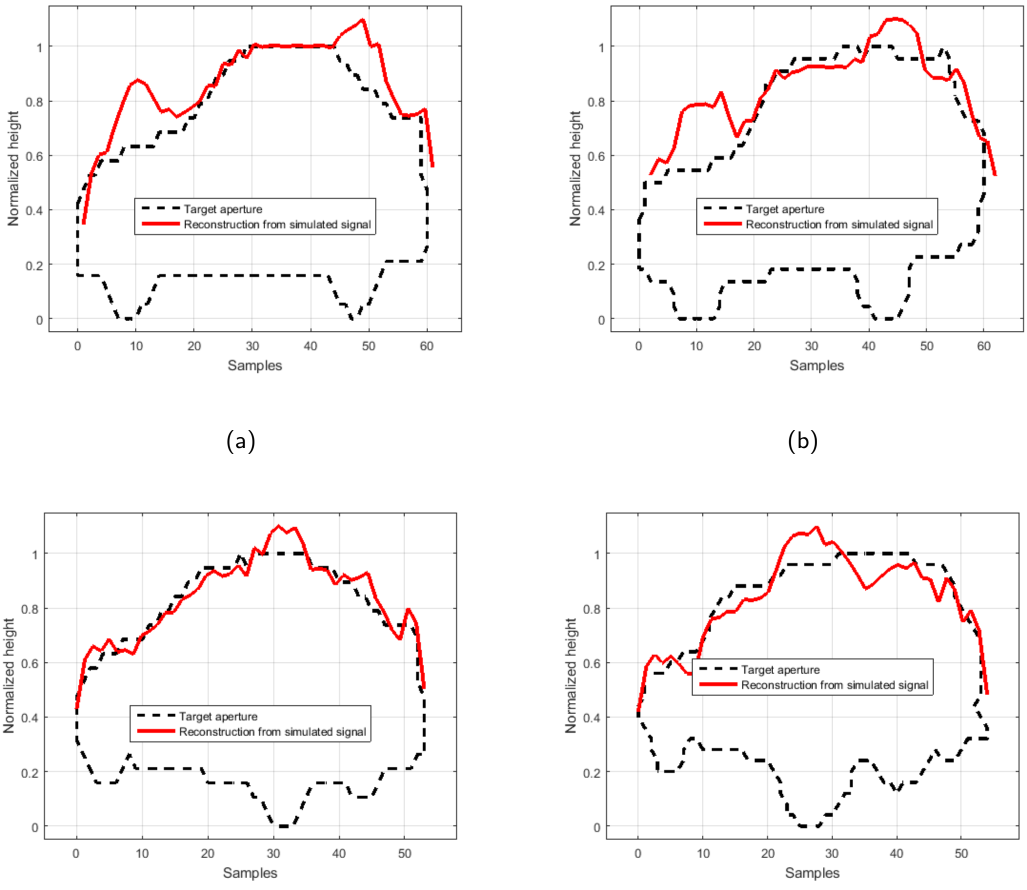

(a)

(b)

(c)

(d)

Figure 6.25: Simulated target profiles for the two targets used in the two projections: BMW 3 series 90 degree projection - a) and 22 degree projection - b); and Land Rover Discovery 2 at 90 degrees - c) and 22 degrees - d)

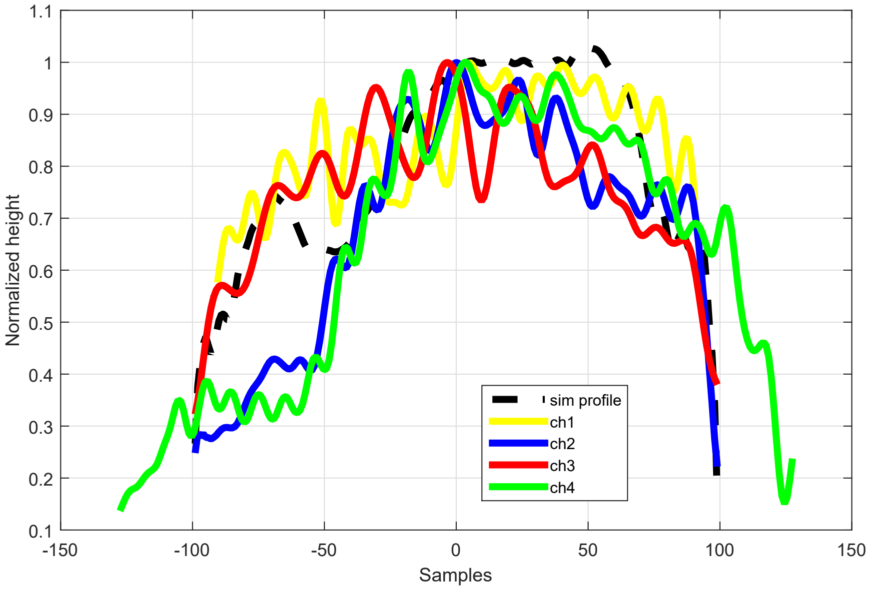

Figure 6.26: Results of profile reconstruction for all channels - 1,2,3 and 4, for the BMW 3 series coupe

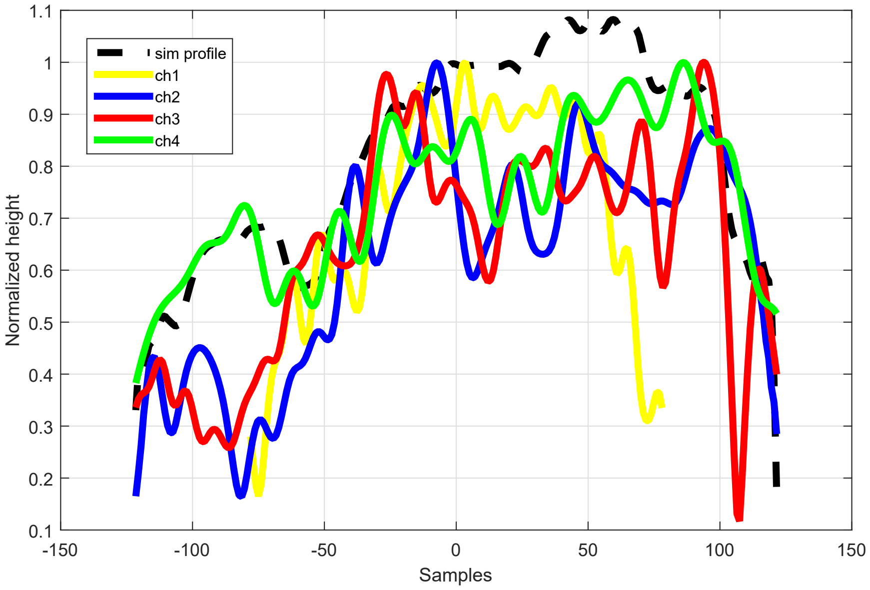

Figure 6.27: Results of profile reconstruction for all channels - 1,2,3 and 4, for the Land Rover Discovery 2

The reconstructed target profiles were done for all channels for both targets and can be seen in Figs. 6.26 and 6.27. From the two figures it can be seen that the profiles recorded for 22^0 aspect angle (channels 1 and 4) have different length and shape than those for the perpendicular crossings (channels 2 and 3). This is expected due to the different size and shape of the shadow of the target in both cases, which can be seen in Fig. 6.25, where the target shadows are presented in both 90 degrees and 22 degrees projections.

As can be seen from Fig. 6.26 (and less in 6.27), the reconstructed profiles can be grouped in two pairs through visual observation. One of the pairs corresponding to perpendicular crossing and the other for crossing at 68 degrees angle (22 degrees projection). The main difference between the two sets being the lower apparent height of the front of the target and absence of a bulge due to the front wheels. These properties can be seen in the modelled results in Fig. 6.25, as well. The main features of the reconstructed profiles in the multistatic case follow the logic of the single node measurement results, discussed previously.

The two sets of target profiles have the same length, due to the fact that they were normalized to the same length, for easier visualization when plotted together. An exception is the Ch1 image in Fig. 6.27, which had some additional noise and thus the automatic rescaling did not provide with a proper scaling factor.

The perpendicular crossings, however, correspond to the previously seen data obtained with the single node transceiver, shown in Fig. 6.18 and 6.19 for the BMW and LR targets, respectively. The 22 degrees projection results show that sufficient differences in the target profiles are introduced that more information regarding the 3D geometry of the target can be obtained through measurements with angular offset.

Thus if a comprehensive data fusion technique is developed, the four reconstructed profiles can be rearranged and fused, so that they represent a higher dimensional model of the target, rather than just a 1D outline. Such fusion can yield a result similar to the one showed in Fig. 6.28, below, where different simulated target outlines are 'fused' together to form a somewhat 3D outline of a target. The three images were fused only to provide visual example of a result. The fusion was done based on exact knowledge of the modeled target profiles' aspect angles. Then rotating the vectors of the results accordingly in a three dimensional matrix.

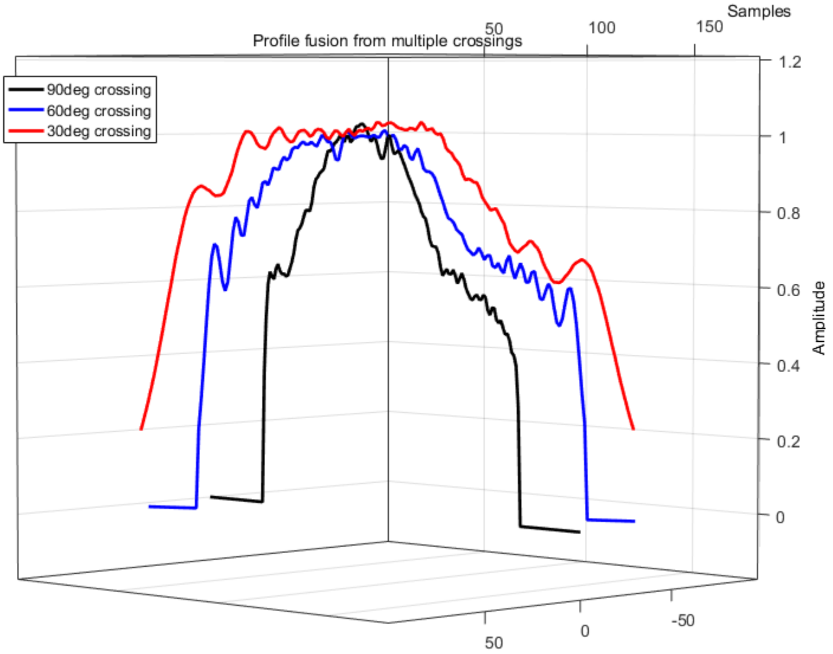

Figure 6.28: A result of simple data fusion of target profiles for BMW 3 series reconstructed profiles at 3 different crossings

Also, it must be noted here that averaging can be done on the target profiles reconstructed for signals recorded by a multistatic or a MIMO system, in order to increase their accuracy.

6.2.4 Profile dependence on state of windows of car targets

Experimental measurements were done for cars which windows are either opened or closed. This was done as a part of an accuracy analysis, which, though, is a subject to another fundamental study of the TSPR performance in real-world scenarios.

It is expected that target profiles will be influenced by the opened windows, but that influence is not going to be substantial, because the change is going to be small in terms of wavelength. Also, it is clear that most influential will be the effect of the opened back windows, as the presence of a driver on the front will still create a shadow, whether or not there is an opening.

Reconstructed target profiles for targets with opened and closed windows can be seen in Fig. 6.29, where the difference in the target profiles can be clearly seen. The two targets - BMW 3 series and Land Rover Discovery 2, were moving with speeds of 19 and 15 kmph, respectively, crossing the baseline perpendicularly.

As can be seen when comparing the figures above the results where target has opened windows (Fig. 6.29(a) and 6.29(b)) there is a reduction in the height of the reconstructed profile compared with the previous results. This is apparent in the reconstructed profiles for both targets investigated.

A further analysis of the BMW target profiles suggests that the difference is very close to the expected as the ratio of the full height to vertical window size of the car is around 0.22 (around 0.35 m for a target of 1.4 m height). The result in Fig. 6.29(b) shows a decrease between the modelled result for closed windows and the experimental result for open windows of around 0.2 at around sample number 50.

It can be noted that the ratio between the total height and vertical size of window of the Land Rover Discovery 2 is around 0.2, as well. Such reduction can be seen around samples 20 and 50.

The properties of the reconstructed profiles in the different conditions measured match the

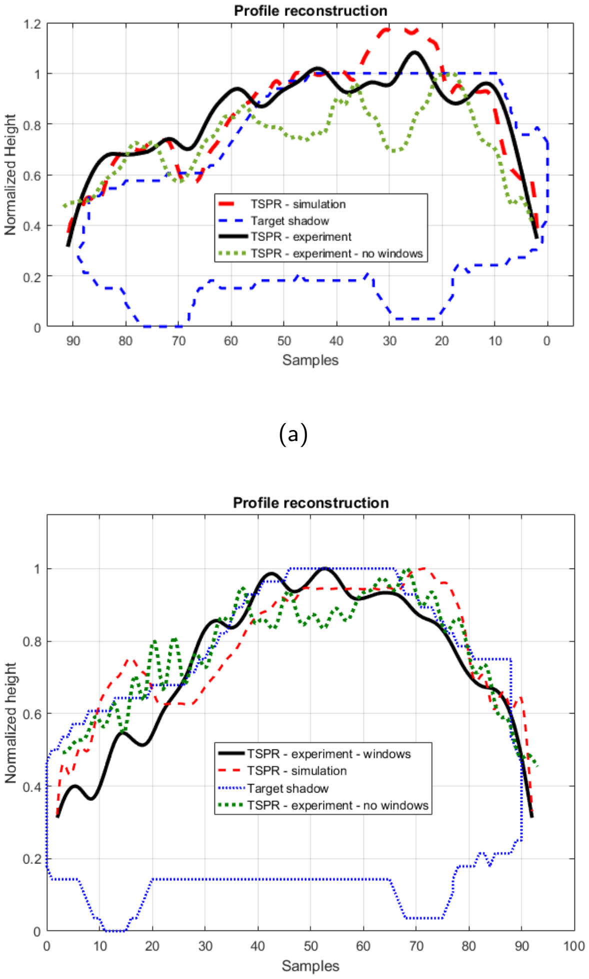

(a)

(b)

Figure 6.29: Comparison between measurement results of TSPR imaging of targets with closed and lowered windows, in Land Rover Discovery 2 - (a); and in BMW 3 series - (b)

expectations, based on the previous results, but further optimization studies on the shape and composition of different targets must be done. FSR signal is described in literature as independent on the target materials, however, using the reconstruction results differences depending on the composition of the target may arise.

6.3 Conclusion

Several hardware systems were used for the experimental measurements of this PhD. These include a 1.2 GHz CW single-node FSR system (BB) and a USRP device NI USRP-2950R used in multistatic measurements. The hardware properties of both the devices are only briefly discussed, as this is not within the main scope of the thesis. However, supplementary calibration measurements and antenna measurements are shown in the Appendix.

Two main sets of targets were used: electrically small targets (used for scaled experiments which are rapidly reproducible) and car targets (which validate the TSPR results for a real-world application). The main features of all the targets can be identified visually from the obtained results. Most particular difference between the target shadows and the reconstructed target profiles are the oscillations on the TSPR results which are due to inaccuracies in the propagation kernel, used to cancel the Doppler phase from the signal.

It was, also, noted that electrically larger targets will yield relatively better results than smaller targets. The results discussed above were only qualitatively analysed through the visual resemblance of the reconstructed profiles with the expected target shadow projection. A more quantitative study will be presented in the next chapter.

The influence of the composition of the targets was briefly discussed, through the difference in the results obtained for car targets with opened and closed windows, however it was noted that this is a subject for a future study.

A 2x2 multi-static system has been used to measure target signatures for two targets - a BMW 3 series coupe and a Land Rover Discovery 2. Results show that the TSPR algorithm does produces 4 different target profiles, which can be correctly classified into two groups through visual observation. These are compared with simulated results, and show some agreement with the modelling. The main purpose of these measurements was to investigate possible data fusion, however this was not implemented on real results during the research conducted.

In the next chapter an initial accuracy analysis of the results shown in chapter 4 (simulated results) and the measurements results discussed above will be presented.

CHAPTER 7

INITIAL ACCURACY ANALYSIS OF PROFILE RECONSTRUCTION

7.1 Introduction

Results of the Target Shadow Profile Reconstruction (TSPR) algorithm application for both simulated and measured signals were shown in the previous two chapters. They demonstrated good visual correspondence with the expected target outlines. However, as a requirement for the development of the novel approach proposed in this study for target imaging in FSR, an accuracy analysis must be done. The overall accuracy of the target profile must be quantitatively estimated, and the resolution of the reconstructed images must be analysed.

Further, many real-world issues might deteriorate the performance of the TSPR algorithm. These include, but are not limited to:

- Incorrect estimation of the target trajectory parameters, and especially speed
- Low SCR or/and SNR of the recorded target signature

- Acceleration of the target's movement in any of the axes during the target visibility
- Electric size and composition of the target
- Operation in near-field of the FSR system

All of the dependencies identified to be deteriorating to the TSPR output will be analysed in the following chapter. Also, a study of the quantitative and qualitative accuracy of the reconstructed target profiles is shown.

7.2 Accuracy of the target profile

Criteria for the estimation of the accuracy of the reconstructed target images need to be formulated. Such constraints, discussed in the following section, will be based on analysis of the resolution of the reconstructed target profiles and further on the similarity between the target shadow and its reconstructed profile.

To the best of the author's knowledge, such analysis has not been investigated and published before for FSR reconstructed target profiles.

7.2.1 Resolution of reconstructed target profile

According to the resolution analysis of Digital In-line Holography (DIH) [44] in section 3.2.3, the resolution of reconstructed microwave holograms should depend on the size of the screen used as detector ($N\Delta_s$), the incident wavelength, λ and the distance between the aperture and the screen, R_{Rx}, according to [46]:

$$\Delta R_{DIH} = \frac{\lambda R_{Rx}}{N\Delta_s}, \tag{7.1}$$

where N is the number of pixels (or independent samples) on the recording screen and Δ_s is the separation between them.

Equation 7.1, can be checked through the modelled results for 2D target signatures. We can consider as an example a 2D BMW target, which is 1.4 m at its highest point, and counting the number of points on the widest part of the reconstructed 2D images, shown in section 5.4, where Fig. 7.1 is shown as an example. The number of points should correspond to the expression: $\Delta R_{2D} = h/N_{points}$, meaning that the resolution would be equal to the height of the target, divided by the number of points on the image. Through observation it was found that the resolution in the image corresponds to resolution of DIH for the same parameters, as can be seen in Table 7.1 below.

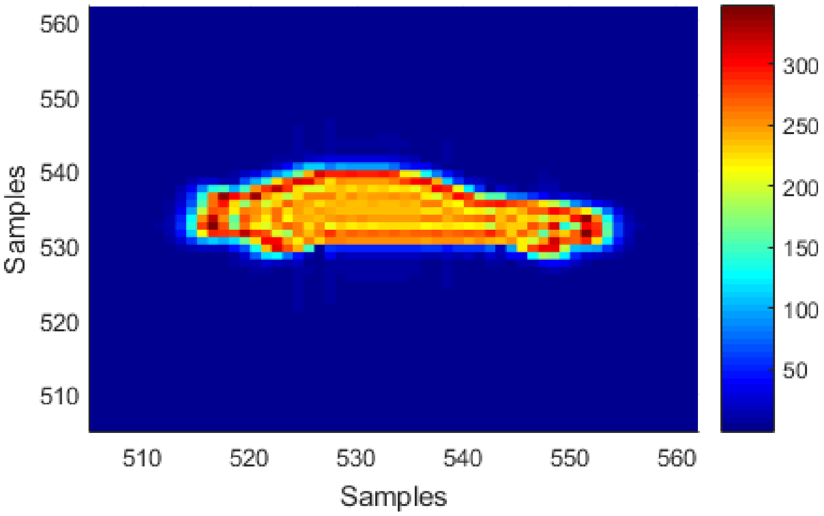

Figure 7.1: An 2D reconstructed image of a BMW, where its microwave hologram is recorded on a screen of size 80 x 80 m at 1 GHz.

It can be seen that the resolution of 2D target images corresponds to the resolution of holography images. However, in most practical scenarios FSR signatures are one dimensional, specifically one-dimensional along the length of the target. As such the term resolution would represent the spacing between (ability to separate) two points on the curve. This

Table 7.1: Table of resolution results for two-dimensional target images

Frequency	Screen Size	Number of image pixels	Resolution	Resolution by eq. 7.1
500 MHz	100x100 m	7	0.200 m	0.180 m
1 GHz	80x80 m	11	0.1136 m	0.1125 m
5 GHz	40x40 m	29	0.048 m	0.045 m

would not provide with a meaningful description of the ability of the one-dimensional result to follow the shape of the target contour.

As the TSPR algorithm for one-dimensional signals is going to produce one-dimensional profiles as was discussed in chapter 4, the resolution of the profile will be dependent on other relationships between different variables, which are going to be investigated empirically next. It is expected that sampling rate of the received signal is going to be one of the variables, by inspection of equation 7.1.

Due to the unavailability of such one dimensional holograms, the analysis below is done empirically. According to the results seen in Table 7.2 the resolution in length of the profiles can be described to be dependent on the speed of the target and the sampling rate used, according to:

$$\Delta R_{L_{1D}} = \frac{v}{f_s}, \tag{7.2}$$

thus the resolution of the reconstruction itself does not depend on the incident wavelength and the length of the baseline (see Table 7.2), but on the other hand in order to resolve features of the profile, the scattering wavelength must be at least of the order of the target features, as described by the theory of diffraction, see section 3.1.2 [21], and antenna theory [69].

Table 7.2: Table of resolution results for one-dimensional target profiles reconstructed from simulated signals

Frequency GHz	Speed mps	Sampling rate Hz	Baseline m	Resolution according to eq. 7.2, m	Ratio of length of profile and number of samples, m
1	10	200	60	0.050	4.6/92
1	10	200	120	0.050	4.6/92
1	10	200	250	0.050	4.6/92
0.1	10	200	60	0.050	4.6/101
0.5	10	200	60	0.050	4.6/93
2	10	200	60	0.050	4.6/93
1	10	50	60	0.200	4.6/24
1	10	100	60	0.100	4.6/47
1	10	400	60	0.0250	4.6/187
1	1	200	60	0.005	4.6/990
1	5	200	60	0.0250	4.6/188
1	20	200	60	0.100	4.6/47

In this subsection the resolution of the reconstructed target images (in the case of 2D signals) and profiles (in the case of 1D) was investigated.

The dependence on the incident frequency and baseline length is going to be referred to as feature resolution of the reconstructed profiles, whose effects for the one-dimensional target profile can be seen when quantitatively estimating the accuracy of the reconstructed target image. This will be discussed next.

7.2.2 Criteria of accuracy estimations of target profile

As the sampling information in the vertical direction is lost due to the one-dimensional signal recording, the term resolution is not consistent with the quantitative accuracy analysis of the one-dimensional target profile. In reality accuracy can be given only by means of estimation of the similarity between the actual target shadow and the result from TSPR. There are a few methods that can be used for a quantitative expression of the accuracy of the target profile reconstruction algorithm output, including:

- Goodness of fit parameters between the target aperture and the reconstructed profile
- Dynamic Time Warping (DTW), using Procrustes analysis for the minimization of the DTW output [70]

Both methods, will be discussed below and constraints on the accuracy in terms of the fit parameters and DTW distance will be defined at the end of each subsection. It must be mentioned here that the analysis was done by comparing the real contour to the results of modelling.

Table 7.3: Table of validation fit parameters for different frequency values for the same target

Frequency, GHz	Baseline, m	Validation SSE	Validation RMSE
0.1	50	2.4912	0.1646
0.2	50	0.7419	0.0898
0.5	50	0.2725	0.0544
1	50	0.1806	0.0443
2	50	0.1393	0.0389

7.2.2.1 Fit of TSPR output and target aperture

Because of the analytically complex functions which would represnt the target profile, a fitting function cannot be simply done. However, as part of the accuracy study only cooperative targets were used, i.e. the target profile is inherently known.

Thus the target profile is fitted via shape preserving interpolant fit, and then the fit is matched to validation data which is the normalized sum of the number of secondary emitters on the target aperture, see Fig. 5.7.

In Table 7.3, SSE is the sum of squared errors of the reconstruction and RMSE is the root-mean-square error. Figures of some of the cases in the Table can be seen in Fig. 7.2 and 7.4.

It is expected that smaller frequency will resolve less of the fine features of the target, as already discussed in section 6.2.1. The difference in the accuracy can be seen in Fig. 7.2 for frequencies between 0.1 and 2 GHz, where the results of modelling for a Range Rover Sport target are shown. Here it should be noted that though there are substantial unresolved parts of the profiles in Fig. 7.2(d) and 7.4(d), the length of the reconstructed

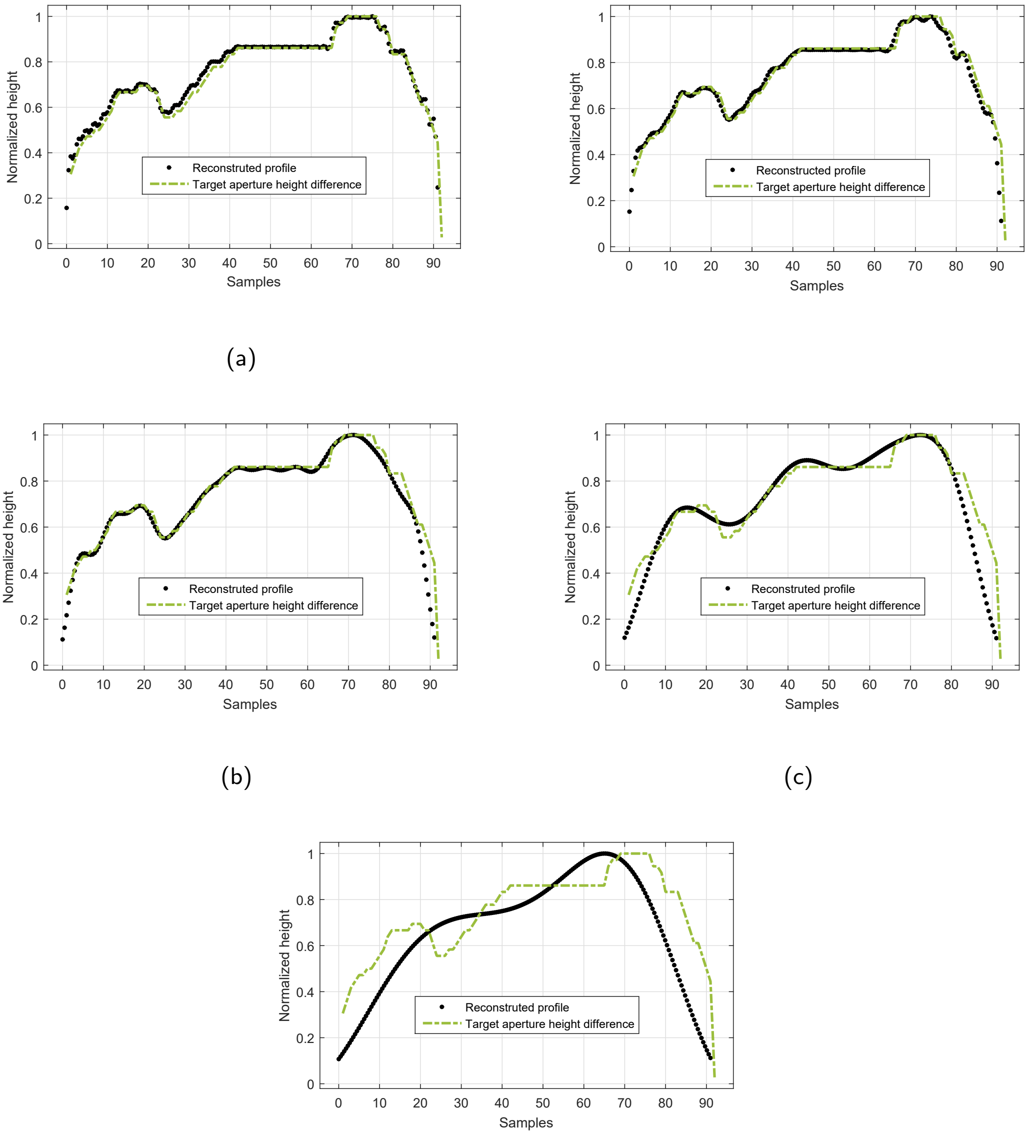

(a)

(b)

(c)

(d)

Figure 7.2: Simulated profile reconstruction for a Range Rover target moving perpendicularly and to the middle of the baseline with speed of 5 mps, at 50 m baseline for different operational frequency - (a) - 2 GHz; (b) - 1 GHz; (c) - 500 MHz; (d) - 200 MHz; (e) - 100 MHz.

profiles is the same, thus the resolution is the same.

On the other side, the reconstructed profile can lose the resolving ability depending on the number of sidelobes present in the target's FS Doppler signature recorded. Initial analysis shows that for the accurate target profile reconstruction the main and first 8 sidelobes, i.e. 4 sidelobes each side, need to be recorded, as seen in Fig. 7.3, though target features can be identified by the analysis of signatures containing only the 2 first sidelobes, but with reduced accuracy.

This would mean that for a recording of 30 s of a target moving with 10 m/s, the results will yield inaccuracy when the baseline is increasing (between 50 and 1000m), as shown in Fig. 7.4 and Table 7.4. It must be noted that the results do not depend on the baseline itself, but rather on the number of sidelobes seen.

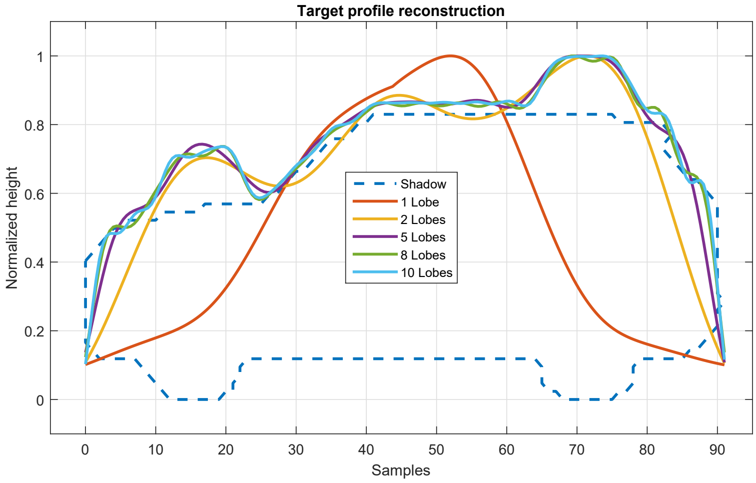

Figure 7.3: Profile reconstruction of RR target for signals of different length

Fig. 7.3 shows reconstruction of the target profile from modelled signatures of different length in terms of sidelobes, ranging from 1 to 10 sidelobes.

By visual interpretation of the results shown in Fig. 7.2 and 7.4 and tables 7.3 and 7.4 a

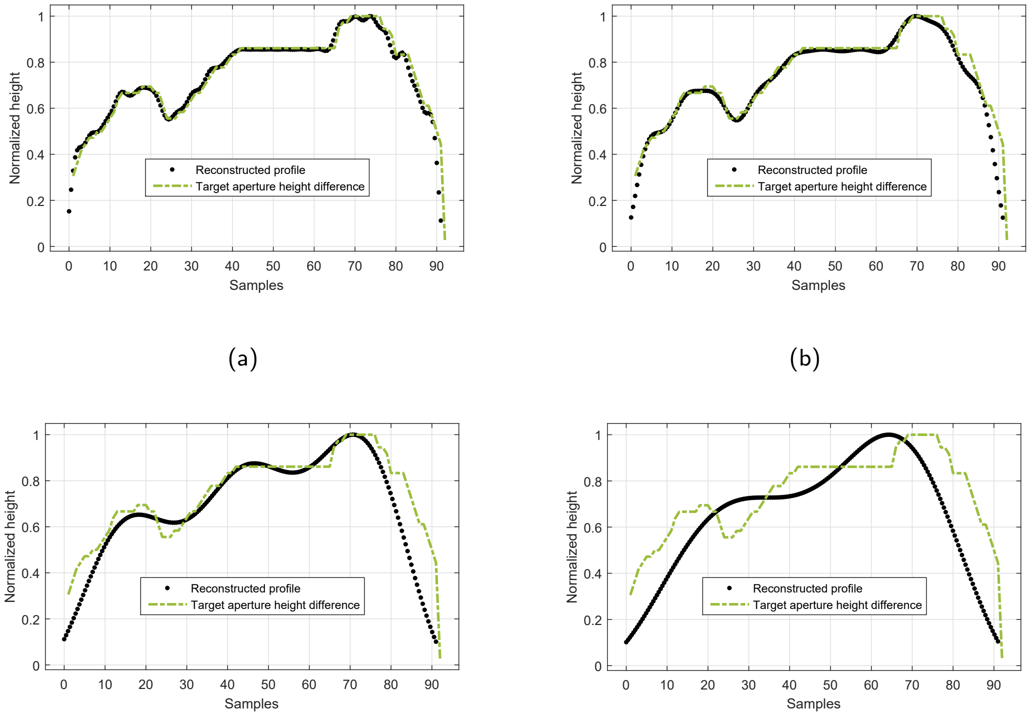

(a)

(b)

(c)

(d)

Figure 7.4: Simulated profile reconstruction for a Range Rover target moving perpendicularly and to the middle of the baseline with speed of 5 mps, at 1 GHz operational frequency for different baseline lenghts - (a) - 50 m; (b) - 200 m; (c) - 750 m; (d) - 1000 m.

Table 7.4: Table of validation fit parameters for different baseline values

Frequency, GHz	Baseline, m	Number of sidelobes	Validation SSE	Validation RMSE
1	50	15	0.1806	0.0443
1	100	10	0.1672	0.0426
1	200	8	0.2826	0.0426
1	500	5	0.07803	0.0921
1	750	2	1.2644	0.1172
1	1000	1	2.9096	0.1778

constrain on the validation SSE and RMSE values can be estimated, which would be used as an estimate of the accuracy of the profile obtained from both simulated and measured signatures.

These will be defined as follows:

- a reconstructed profile which has a validation SSE of lower than 0.3 will be considered as accurate
- a reconstructed profile with a validation RMSE of lower than 0.05 will be considered as accurate

The constraints presented above can be sufficient for this initial research. However, such qualitative analysis can be performed via dynamic time warping, as well, discussed below.

7.2.2.2 Dynamic Time Warping (DTW), using Procrustes analysis

Another method which can be used for the estimation of the accuracy of the reconstructed targets is DTW. It provides with another estimate of accuracy.

The analysis in this subsection is done for the same reconstructed profiles used in the previous subsection, though the similarity between the TSPR output and the target shadow outline is defined by DTW. The target profiles are passed through Procrustes analysis, using the function integrated in Matlab, to minimise the DTW result for each of the profiles. Only then, DTW is performed. The procedure is going to be discussed in more detail below.

To compare shapes of two curves, these curves must be first optimally superimposed. The Procrustes superimposition determines a linear transformation (translation, reflection, rotation and scaling) between two curves. This is done in order to obtain two curves of similar size and placement, by measuring the shape difference, or Procrustes distance, between them. An example of such superimposition can be seen in Fig. 7.5, below.

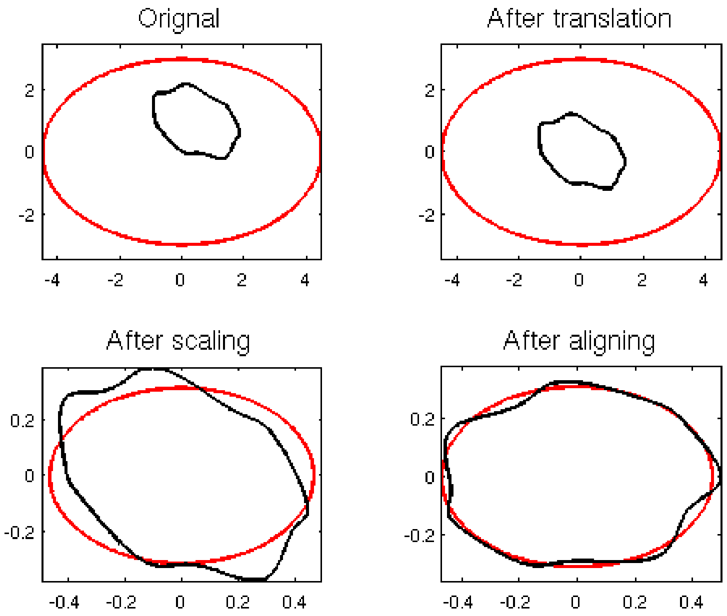

Figure 7.5: Procrustes superimposition of two curves, showing the result after each step of translation, scaling and rotation

After the Procrustes superimposition, the two curves will match exactly if their shapes are the same. The Procrustes superimposition, generates a transformed curve Z given by [70]:

$$Z = bY(t)T + \epsilon, \tag{7.3}$$

where Z is the transformed curve, b is the scale component of the linear transformation, ϵ is the translation component, T is the rotation and reflection component and $Y(t)$ is the curved which is tested. The transformed curve, Z, is then matched to the target shadow by DTW.

DTW is an algorithm for measuring the similarity between two temporal sequences which may vary in speed or time, i.e. local and total sampling between the two sequences may be different [71].

In general, DTW is a method that calculates the optimal match between two sequences. The sequences are 'wrapped' non-linearly in the time domain to determine a measure of their similarity, independent of non-linear variations between the two sequences in time [71].

Considering two curves - A and B of sizes m and n, respectively. DTW will calculate a matrix of size m x n, where each cell consists of a distance measurement of the height difference between the corresponding elements of the two curves. The best match between the two curves is then the path through the matrix, which will minimise the total distance between them. This is done by calculating all the paths through the grid and finding the smallest sum of each. An example of DTW for arbitrary curves can be seen in Fig. 7.6, below.

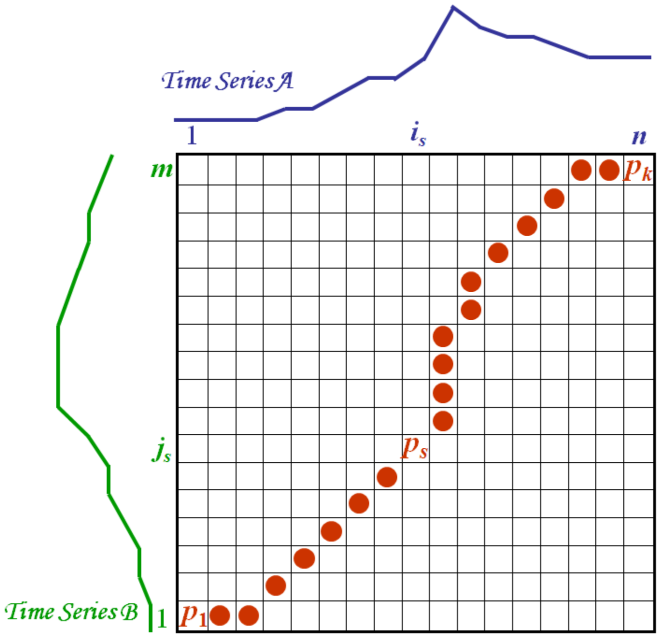

Figure 7.6: An example of DTW, where curve A is matched to curve B. The result of the DTW is the grid path denoted by the red dots.

Table 7.5: Results for the accuracy of the reconstructed profiles, for DTW

Frequency, GHz	Baseline, m	b	T	ϵ	DTW
1	50	1.0118	1	-0.0067	0.0875
1	200	0.9318	1	0.0657	0.0930
1	750	0.7494	1	0.2255	0.1622
1	1000	0.6146	1	0.3389	0.2365
0.5	50	0.9353	1	0.0613	0.0944
0.2	50	0.7888	1	0.1697	0.1596
0.1	50	0.6376	1	0.3173	0.2231

There are constraints on the acceptable paths along the grid, including [71]:

- Monotonic condition - the path will not turn back on itself, i.e. both indexes of the matrix are either increasing or staying the same, but never decrease
- Continuity condition - the path advances one step at a time
- Boundary condition - the path starts at the point corresponding to $A(1)$ and $B(1)$
- Warping window condition - a good path is unlikely to wander too far from the diagonal
- Slope constraint condition - the path should not be too steep or too shallow - a requirement that prevents short sequences matching long ones.

After Procrustes analysis, the DTW result should be minimized, though the shape of the curve is not changed, thus the reconstructed profiles are first Procrustes superimposed on the target shadow, and the matched to the target shadow outline by DTW. The results of the DTW for the profiles reconstructed in figures 7.4 and 7.2 can be seen in Table 7.5.

Table 7.5, indicates that there is no rotation done during the Procrustes superimposition of the matched curves.

By visual inspection of the profiles reconstructed in Fig. 7.2 and 7.4, and the results of DTW analysis in Table 7.5, a maximum value for the DTW can be deduced to be a threshold for accuracy of the reconstructed profiles from simulated signatures. This value is going to be defined by the reconstructed profiles at 1 and 0.5 GHz frequency (Fig. 7.4(a) and 7.2(b), respectively), as 0.10. This means that reconstructed profiles which will have a DTW value when compared with the original target shadow of more than 0.10 will be considered inaccurate or wrong.

Henceforth, accurate target profile will mean that the TSRP output has passed the three constraints when compared with the target shadow. These are very conservative values, as simulated results are characterized by the absence of environmental and hardware noise, inaccuracies in the measurements of target trajectories, presence of bistatic scattering of the target, etc. However, through the analysis above, constraints on the accuracy of the modelled target profiles can be defined as:

- validation SSE of lower than 0.3
- validation RMSE of lower than 0.05
- DTW distance of lower than 0.10

and each reconstructed result which follows these constraints will be considered accurate.

As can be seen from Table 7.5, the output of the Procrustes analysis on simulated profiles for different baseline and frequency is larger for larger wavelengths. The same can be said for the output of the DTW after its minimization. Thus it may be further affirmed that larger wavelengths generate less accurate TSRP output for the same target.

Table 7.6: Parameters of accuracy for the reconstructed profiles of small targets

Target	Baseline, m	DTW	Validation SSE	Validation RMSE
T1	12	0.3623	8.1588	0.2280
T2	10	0.1468	2.4464	0.1856
T3	12	0.4957	9.5606	0.2351

It is important to stress here that the choice of operational wavelength will provide the feature detection, while the baseline is not going to affect the accuracy of the profile, if enough of the FS target signature can be recorded. Thus an optimal frequency/baseline configuration must be determined for a practical application of FS systems for TSPR, as higher operational frequency of FSR will provide with a narrower FSCS pattern.

7.2.2.3 Qualitative accuracy analysis of TSPR output of measured signatures

Having defined constrains for the accurate output of the TSPR, apart from visual similarity, the results for the measured target signatures were compared with their corresponding target shadows, according to the two methods of error estimation discussed above.

The two tables, 7.6 and 7.7, contain the mean DTW and fit values for the accuracy of the reconstructed profiles for each target used in the experimental measurements.

From Table 7.6 it can be seen that for electrically smaller targets, the results at 1.2 GHz do not fit the constrains defined previously: DTW < 0.10; SSE < 0.3 and RMSE < 0.05. This can be explained by the fact that the wavelength (0.25 m) is too large to enable fine feature resolution of these targets.

However, Table 7.7 shows that for bigger targets the accuracy becomes better, where the reconstructed target profiles can be considered close to accurate for Smart, FF and LR,

Table 7.7: Parameters of accuracy for the reconstructed target profiles

Target	Basline, m	DTW	Validation SSE	Validation RMSE
BMW(07.12)	55	0.3013	2.0943	0.0800
Smart(07.12)	55	0.0763	1.9653	0.1325
FF (09.08)	50	0.0811	1.7521	0.1074
LR(07.12)	55	0.1478	1.5072	0.0935
RR (09.08)	55	0.6461	4.3258	0.1493

taking into account only DTW distances. The validation SSE and RMSE even for these bigger targets is larger than the constraints set-up for the simulated results. Thus it can be considered that the constraints set are very conservative, though they will be used further in this chapter, as most of the analysis is to be done on simulated signatures.

After this qualitative analysis of the output of the TSPR algorithm, analysis of the effect of inaccurate estimation of variables of the target motion will be performed and will be discussed in the next section.

7.3 Effect of trajectory estimation errors on the reconstructed results

Currently the main parameter identified to influence the accuracy of the reconstructed profile is the inaccurate estimation of the target motion parameters, thus leading to an inaccurate extraction of Doppler phase, as also suggested in [64]. Analysis of the influence of the estimation of untrue trajectory parameters was performed, where all three of the parameters - speed, crossing angle and crossing point, were taken into account. This analysis was performed for both simulated and measured Doppler signatures and also produced the preliminary constrains for automatic profile selection, explained in section 7.4.

7.3.1 Error in estimation of speed

Analysis of the influence of untrue estimation of speed on the TSPR was performed for both simulated and measured signatures. The signatures of a Range Rover and Ford Fiesta target were passed through a bank of TSPR algorithms, which were accounting for slightly different target crossing speed, ranging from -50% to $+50\%$ of the actual crossing speed. The reconstructed profiles are shown in Fig. 7.7 below. In the figure it can be seen that the reconstructed profiles show more robustness when experimental signals are used for the reconstruction, though the experimental results have lower accuracy than the simulated ones for the exact trajectory parameters.

It was found that the model is reasonably robust to errors in the estimation of the speed, within an absolute error of 0.2 m/s speed, meaning that for targets moving at around 5 m/s (like in the examples), the error margin is 5%.

7.3.2 Error in estimation of crossing angle

The intersecting angle between the target trajectory and the baseline is another of the main variables of motion influencing the target signature.

A target trajectory intersecting the baseline at an angle different from 90 degrees results in assymetric instantaneous Doppler frequency along the movement of the target in the narrow corridor around the baseline and the shadow aperture of the target will have different size due to the projection on the y-axis, thus an incorrect estimation of the crossing angle may result in a substantial error of the reconstructed profile.

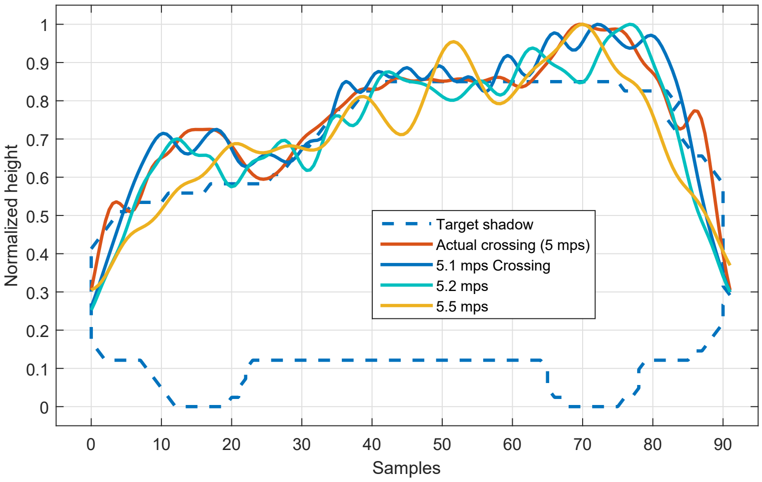

(a)

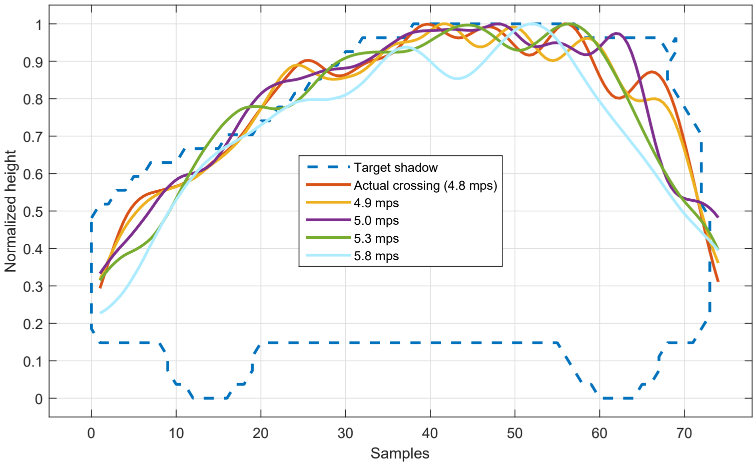

(b)

Figure 7.7: Reconstructed profiles for errors in speed of target - a) simulation; b) experimental results

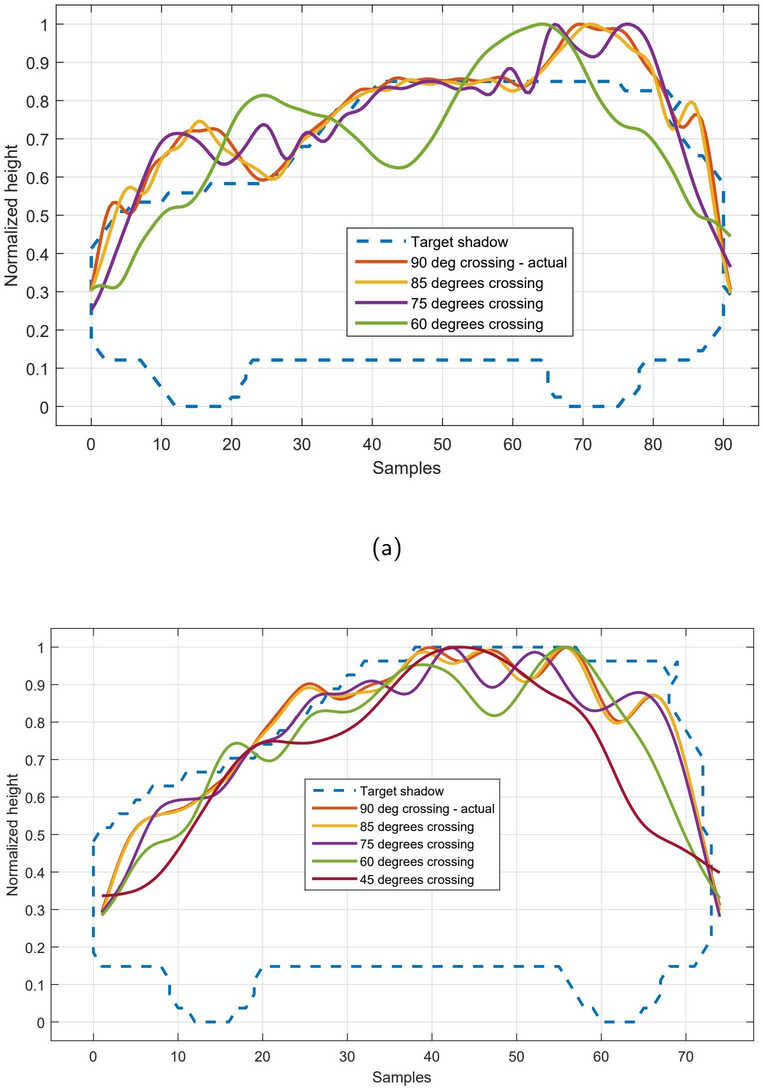

(a)

(b)

Figure 7.8: Reconstructed profiles for errors in crossing angle of target - a) simulation; b) experimental results

Again, simulated and measured signature of Range Rover and Ford Fiesta targets, respectively, were passed through a bank of TSPR algorithms, extracting Doppler phases, where speed was fixed, but crossing angle was incrementally changing with 5 degrees frokm 0 to 90. It has been found that within a margin of ±15 degrees for the perpendicular trajectory, the target profile is accurate and degrades outside this margin. This can be visually confirmed by inspection of Fig. 7.8.

It has to be noted here that, also, in this analysis it can be seen that experimentally obtained target profiles are more robust to errors in the estimation of target crossing angle, which is similar as for the errors in the crossing speed, shown in the previous section. This is probably due to the fact that modeled results use approximated theory and higher order phase factors are present in the recorded signal, however, this is a subject for further research.

7.3.3 Error in estimation of crossing point

The crossing point of the target defines the diffraction region the system will operate, thus inaccuracy in the trajectory crossing point may generate an untrue profile for sufficiently large inaccuracies in the estimation of crossing point.

Also, due to the absence of range resolution in FSR, obtaining an estimate for the crossing point is ambiguous. The following assumes that the propagation kernel is going to be the same whether the error is towards the receiver or the transmitter. Due to the kernel dependence on ω_d and the fact that ω_d does not depend on the individual ranges - Tx-to-Target and Rx-to-Target, but their sum, it is a valid approximation.

The TSPR algorithm was found to be very robust to errors in the estimation of crossing point, see Fig. 7.9, as long as the Doppler content of the propagation kernel, $K(t)$, does not refer to a target in the near-field of either Rx/Tx, for a target which is in reality crossing in the middle of the baseline and in the far-field.

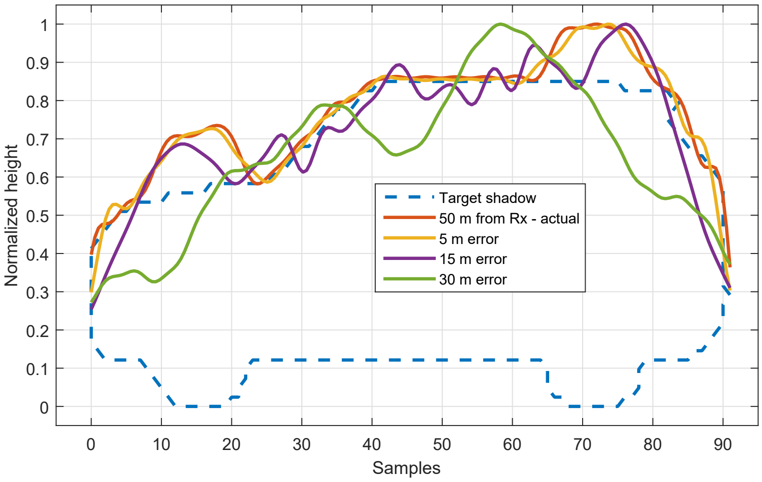

(a)

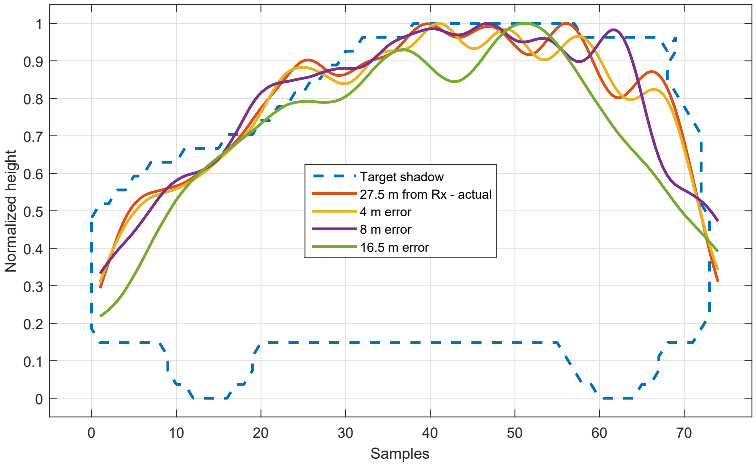

(b)

Figure 7.9: Reconstructed profiles for errors in crossing point of target - a) simulation; b) experimental results

In this section, the robustness of the TSPR output with regard to errors in the estimation of the target motion parameters, i.e. inaccuracy of the propagation kernel, $K(t)$, was analysed. It was shown that the reconstructed target profile can be considered accurate for errors in the target speed of up to 5%, crossing angle of up to ±15 degrees. A robustness have been identified with errors in the crossing point. These are going to be a base for the auto-focusing algorithm discussed next.

7.4 Auto-focusing of the TSPR algorithm output

According to the observations in the previous section, 7.3, and the properties of the reconstructed profiles, outlined in section 5.3, a quasi-auto-focusing processing for the reconstructed profiles can be developed.

This processing relies on particular properties of reconstructed target profiles, which are an output of the algorithm for the most true Doppler frequency extraction, and include:

- Highest frequency of oscillations of the curve
- Straightest edges
- Highest accuracy, according to DTW and fit.

Thus an algorithm which can select the profile which posses these properties, would select the reconstructed profile with highest focus, which would be resultant from the most accurate Doppler information. Such a process can be basis for quasi-optimal trajectory estimation of the target, as well, though this is not within the scope of this discussion.

The auto-focusing of the reconstructed profile is done in stages, where Doppler signatures are modelled on the basis of predefined values of speed, crossing point and crossing angle. Knowledge of the dependence of the reconstructed target profile on errors in the estimation of target trajectory parameters (discussed in the previous subsection) will influence the number of Doppler signatures to be created. This auto-focusing technique is dependent on inherent knowledge of a rough estimate of the target speed, which can be performed

Table 7.8: Table of selection of extracted trajectory parameters by auto-focusing of TSPR output

Data File	Target speed estimated by auto-focusing of TSPR output, mps	Ground truth speed, mps
LR_1	5.34	5.24
LR_3	3.00	2.94
LR_4	3.34	3.54
LR_5	3.70	3.58
LR_6	3.23	3.32

by any of the methods outlined in section 2.5.

The model is similar in operation to the quasi-optimal processing discussed in section 2.5.1 and the contrast maximisation model described in [72]. Its trajectory parameter output will be corresponding to the most accurate extraction of the complex envelope of the target, rather than the true Doppler information, i.e. if there are unaccounted phases due to clutter or other interference in the signal the output of a target trajectory estimation method based on these TSPR constraints may not produce the actual target trajectory parameters. This is not an issue to the TSRP method, though, as it is not important to model the actual target movement in the step of extraction of complex envelope, but the one that cancels out the correct phases in the signal.

The method was found to correctly estimate the target trajectory parameters, within the errors estimated in the previous section 7.3. A selection of the extracted speed of experimentally measured signatures of a Land Rover targets can be seen in Table 7.8.

This is a subject to further studies and analysis. Next the analysis of the TSRP output for different target trajectories will be examined. This will define the domain of application of the algorithm.

7.5 Dependence on target trajectory

Target crossing at arbitrary trajectories, namely crossing point and angle, can introduce a substantial asymmetry in the Doppler phase around the zero-Doppler point. This can generate an error in the target profile reconstruction due to the influence of that asymmetry on the complex envelope. For a non-cooperative, real-world operation of a ground-based FSR system it is expected that targets will cross the baseline at such arbitrary trajectories.

The performance of the TSPR algorithm was tested for simulated signatures of target trajectories intercepting the baseline at different angles and locations, relative to perpendicular in the middle, both independently and as a combination. This analysis will provide with the geometrical domain that the TSPR algorithm proposed will be applicable.

7.5.1 Crossing point

Simulated signatures for targets crossing the baseline at different crossing points, ranging from near field of the transmitter/receiver to the middle of the baseline, have been analysed (see Fig. 7.11). The simulated signatures can be seen in Fig. 7.10.

This analysis was done to establish weather the TSPR algorithm can generate correct target profiles in the reactive near-field. The viewing distance needed for this region for a RR target of size (4.6 x 1.8 m) for 1 GHz FSR system with 50 m baseline will be given by [21]:

$$L_{NF} \leq 0.62 \frac{\sqrt{D^3}}{\lambda} \leq 8.2m, \tag{7.4}$$

where D is the largest dimension of the target and L is the viewing distance.

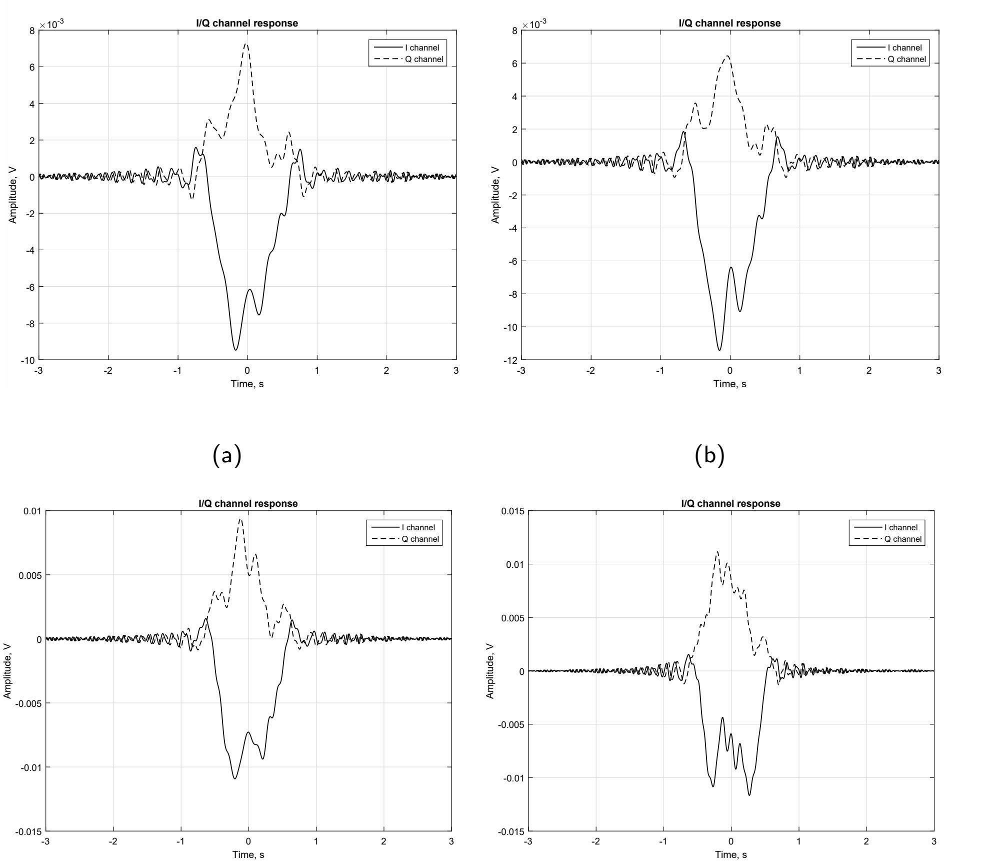

(a) (b)

(c) (d)

Figure 7.10: Zoomed target signatures for a RR target crossing a baseline of 50 m, perpendicularly at different points - middle (a); 10 m from the middle (b); 15 m from the middle (c) and 20 m from the middle (d)

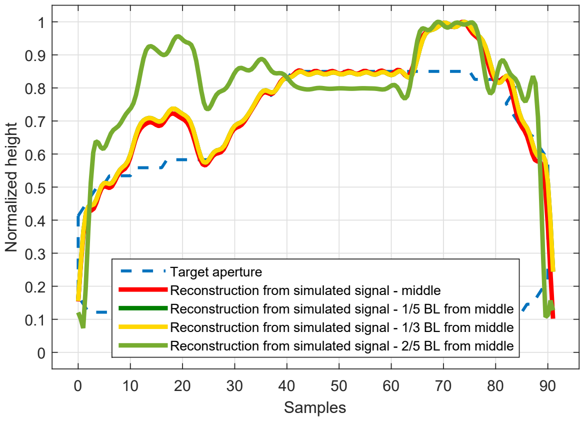

Figure 7.11: Results of target profile reconstruction for RR target, crossing the baseline at 90 deg, at different points, the simulation was done for a baseline of 50 m for 4 distances from Tx: 25 m, 15 m, 7 m and 5 m

The results shown in Fig. 7.11, confirm that the TSPR algorithm does not generate correct target profiles in the reactive near-field, though there is no qualitative or quantitative change of the reconstructed profiles for the rest of the considered distances.

7.5.2 Crossing angle

As a continuation on the estimation of the minimal distance needed between target and Tx/Rx, similar analysis is done for a RR target crossing a baseline of 50 m in the middle at different angles, ranging from 10 to 90 deg. Target signatures were simulated for 1 GHz single node FSR and they can be seen in Fig. 7.12, below.

The shape of the signatures of targets crossing the baseline at different angles, see Fig. 7.12, was found to be in good correspondence between each other, where the main lobe of the time-domain signature is longer, due to the lower speed in the y-direction.

The reconstructed profiles on the other hand, seen in fig 7.13, show that reconstructed

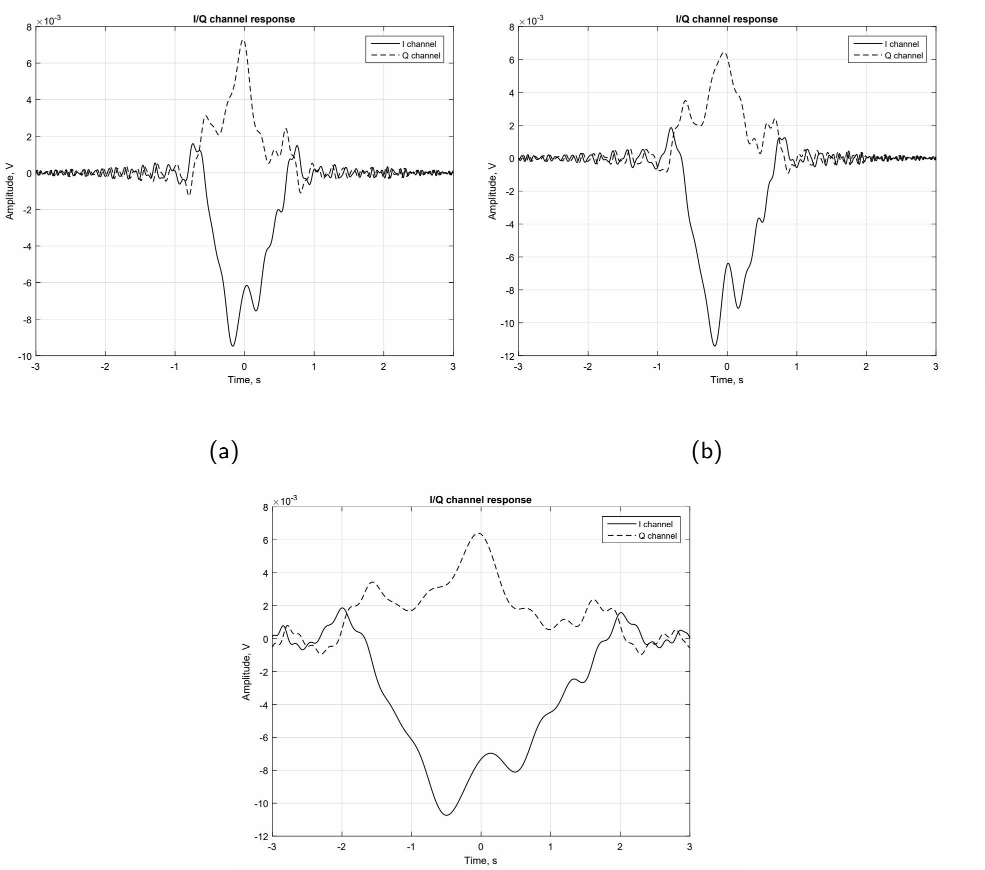

(a)

(b)

(c)

Figure 7.12: Zoomed simulated target signatures for a RR target crossing a baseline of 50 m, in the middle at different angles - perpendicularly (a); 60 degrees (b); 20 degrees (c)

profiles for a Range Rover target do have reduced accuracy for lower crossing angle, possibly due to the lower instantaneous Doppler phase, though the shape of the target can still be obtained.

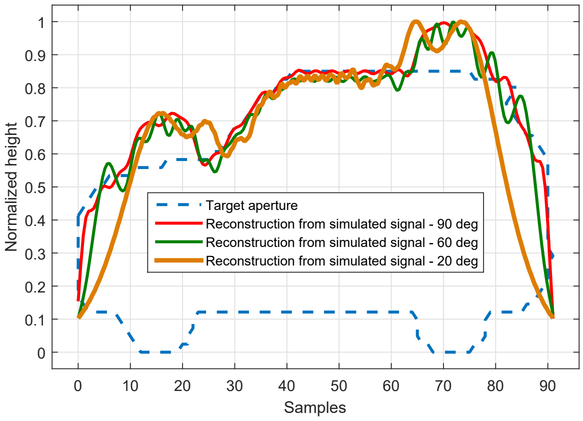

Figure 7.13: Results of target profile reconstruction for RR target, crossing the baseline at in the middle, at different angles, the simulation was done for a baseline of 50 m

So far it has been shown that the TSRP is applicable in the Fresnel and Fraunhofer regions and at any crossing angle independently. However, a full analysis will require the discussion of the scenarios where a target crosses both not in the middle and at an angle different than 90 degrees.

7.5.3 Arbitrary motion of target

Signals were simulated for target with trajectory with non-perpendicular intersection and crossing the baseline not in the middle. Reconstruction of the profiles for arbitrary cases of an arbitrary trajectory of a target, seen in Fig. 7.14, shows that TSPR has a much reduced accuracy, though some features of the target profile can be extracted. The signatures were simulated for 1 GHz CW system, with baseline of 50m and target speed of 5 mps.

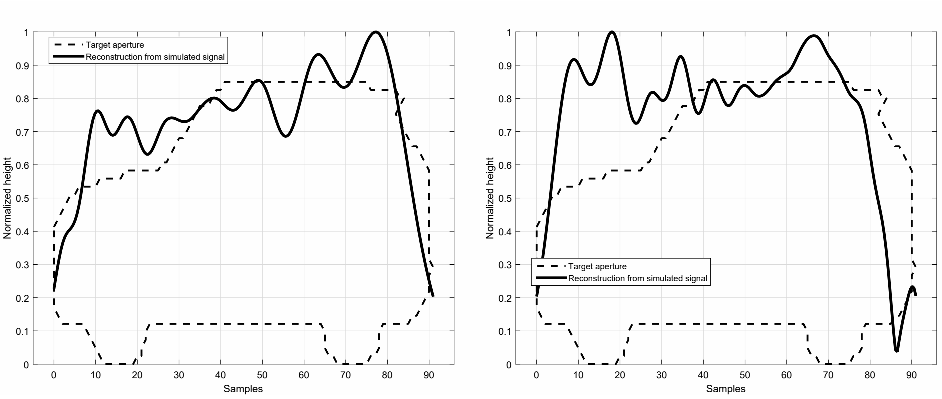

(a) (b)

Figure 7.14: Reconstructed target profiles for a combination of different crossing angles and crossing points - 60 deg crossing 10 m away from middle of baseline (a) and 80 deg crossing 15 m away from the middle of the baseline (b).

This requires further research into the formation of the FSCS and the TSPR algorithm, in order to identify the reasons for the reduced accuracy for arbitrary moving targets, as in practice the surface moving targets are known to be highly manoeuvrable, thus able to change their motion rapidly.

A suitably zig-zag spread multi-static FSR configuration can thus be deployed to ensure that there is at least a single crossing at an angle larger than 60 deg or close to the middle of the baseline, as shown in Fig. 7.15.

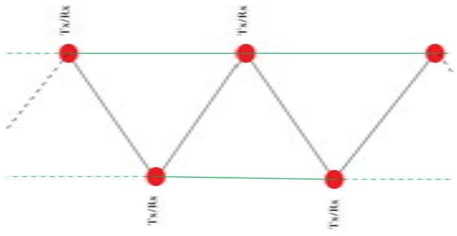

Figure 7.15: A zig-zag shaped FSR multistatic geometry

Also, it must be mentioned here that, profiles of targets which are accelerating in a straight line movement through the baseline, can be reconstructed accurately, provided that the acceleration is known, thus modelled into the Doppler phase, used in the extraction of the complex envelope.

In this subsection the dependence of the target motion parameters on the output of TSPR model was investigated, with results showing that the algorithm has reduced accuracy for targets which have arbitrary motion with respect to the normal to the middle of the baseline.

Next the influence of clutter interference in the target signature on the reconstructed profiles will be discussed.

7.6 Influence of clutter on the image reconstruction

Until now few parameters were investigated on their influence on the accuracy of the output of the profile reconstruction algorithm: inaccurate extraction of parameters and arbitrary motion of target.

Another fundamental system variables that can reduce the accuracy of TSPR for a surface-based FSR system is the clutter interference on the measured signature. This can introduce errors in the estimation of target trajectory parameters, thus the extraction of Doppler phase and reconstruction of target RCS, but, also, it can introduce unaccounted phase to the complex envelope, thus influence the reconstructed profile. Only the latter is discussed below, as trajectory parameter estimation is not within the main scope of this thesis.

It has been noted in previously published results in [73–76] that surface based forward scatter signals can be severely influenced by clutter. In the case of surface moving target observations the main clutter sources can be either vegetation (for ground moving targets) and sea clutter (for maritime targets). It has been shown in [73, 74, 77] ,that sea surface clutter is repetitive with a spectrum peaking at below 1 Hz. Also, it was shown that the intensity distribution is Gaussian.

Vegetation clutter has not been studied as extensively as sea clutter in the case of forward scatter radars. However, published results in [75, 76], show that vegetation clutter has similar properties when compared to sea clutter, i.e. spectrum limited to low frequency components of around 1 Hz.

As discussed in Chapter 5, the information required for the profile reconstruction algorithm is the low frequency FSCS component of the FS signal. As such, random low frequency components of the clutter spectrum can interfere with the FSCS component and introduce phase discrepancies. These phase changes can result in an incorrectly reconstructed target profiles, due to the inability to accurately cancel the clutter phases in the received signal. Analysis of the influence of vegetation clutter on the TSPR results has been done for modelled signatures.

7.6.1 Simulation results

Clutter simulated according to the vegetation clutter model developed in [76, 78] enabled analysis of the reconstruction performance in presence of vegetation clutter. Fig. 7.16 shows the signals generated by the addition of clutter to the target signature of RR target, moving perpendicularly to the middle of the baseline of length 50 m at speed of 5 mps.

Presence of clutter might significantly deteriorate the performance of the TSPR, so it was tested against different SCR and results and the presented in Fig. 7.17. It can be seen that for SCR of less than 15 dB, the random phase of the clutter influences the reconstruction of the profile. Thus, preliminary signal processing, such as whitening filter, have to be used before application of the TSPR algorithm in highly-cluttered environments.

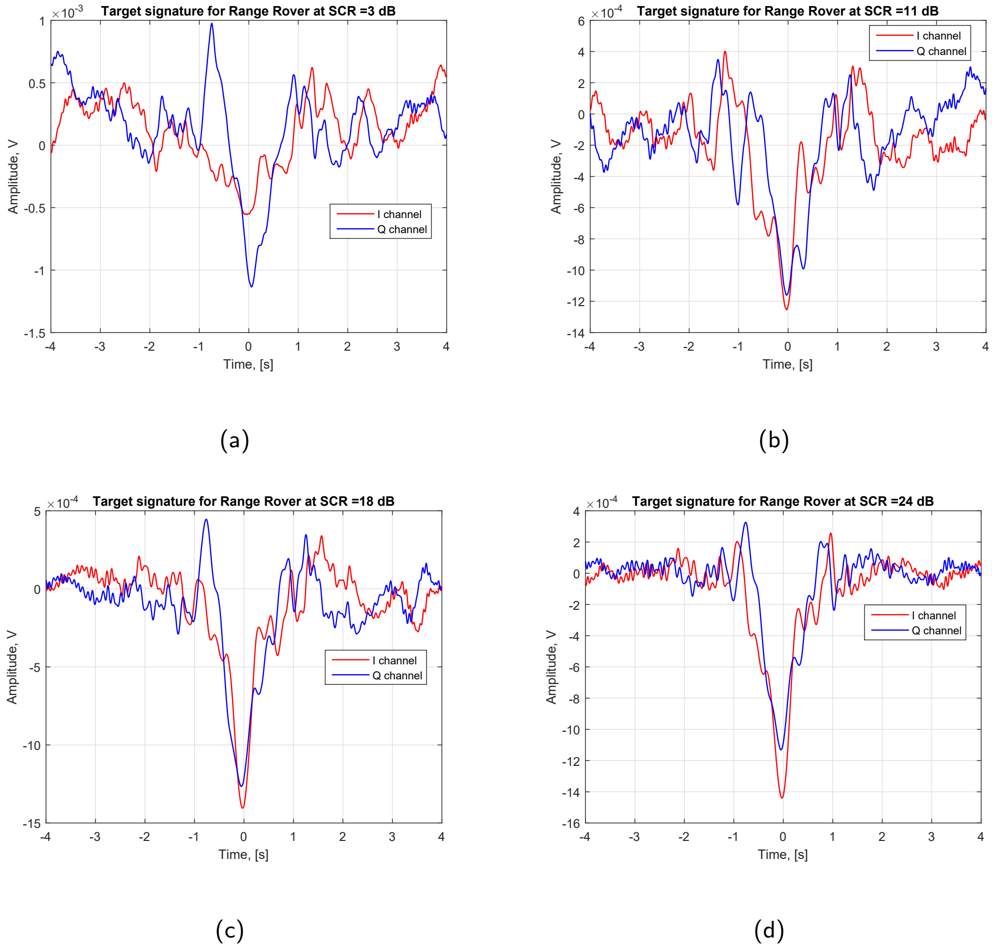

(a) (b) (c) (d)

Figure 7.16: RR target signatures simulated for different SCR: 3 dB - (a); 11 dB - (b); 18 dB - (c) and 24 dB (d).

This is a subject of special fundamental and optimisation studies, and current results are presented as part of the initial analysis of the algorithm sensitivity to the clutter. It is worth to note that in reality we can expect 20-40 dB SCR, a range in which TSPR results show good stability.

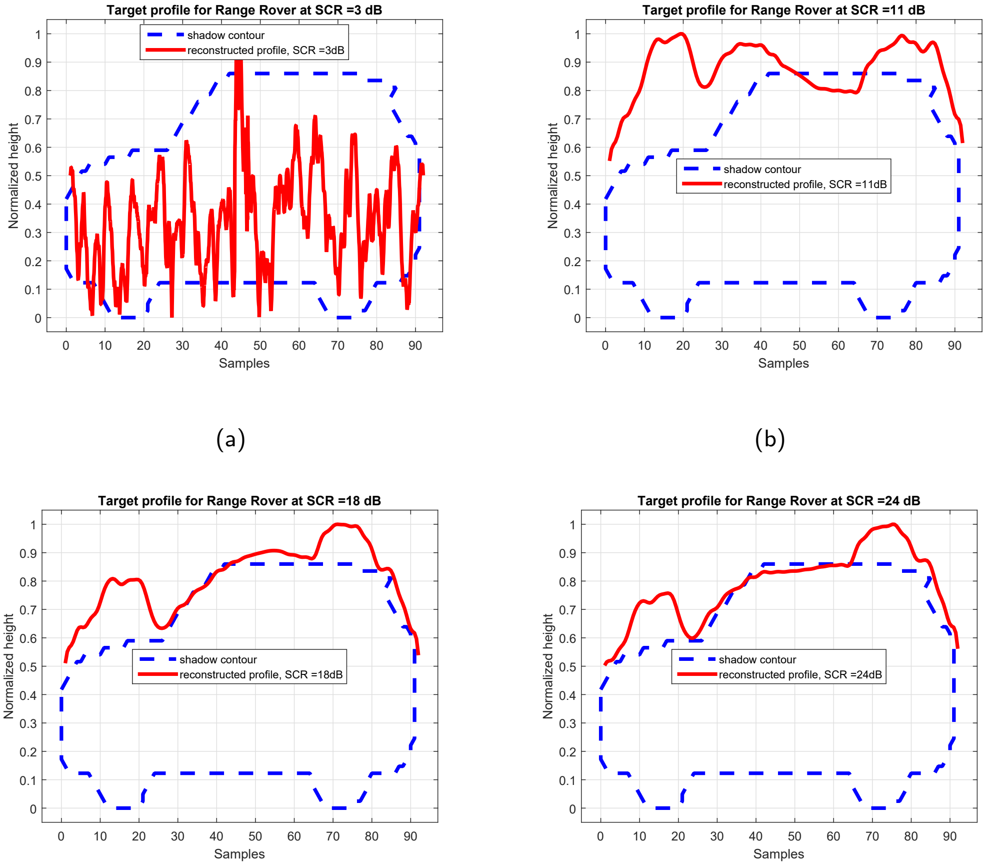

(a)

(b)

(c)

(d)

Figure 7.17: Reconstructed target profiles for RR target at different SCR: 3 dB - (a); 11 dB - (b); 18 dB - (c) and 24 dB (d).

7.7 Conclusion

A comprehensive qualitative and quantitative accuracy analysis of the output of the TSPR algorithm was done. The similarity of reconstructed target profiles to the actual target shadows were analysed and constraints on the accuracy of the model were developed. These were based on two main similarity criteria - goodness of fit and dynamic time warping.

Relationships for the resolution of one- and two-dimensional target image reconstructions were shown and analysed. It was shown that for one dimensional target profiles the resolution does not depend on the wavelength used, however the feature extraction ability does depend on the frequency/baseline relationship. This is a topic that was investigated through modelled results and as such would require further analysis in future work on the topic.

The TSPR output was shown to have accuracy stability over different factors which might deteriorate its performance. It was shown that accuracy of the reconstructed target profiles does not depend on the target crossing point, as long as the target and modelled kernel are both either in the near-field or the far-field. Also, accuracy is shown for Doppler extraction via untrue trajectory motion parameters, where the reconstructed profile does pass accuracy tests for error margins of 5% m/s and 15 degrees for speed and crossing angle, respectively.

The dependence of the target profile on the actual target trajectory was estimated. It was shown that target trajectory angle and crossing do not influence the feature resolution of the reconstructed profiles, but when used in combination they will introduce sufficient errors, so that the TSPR output will not be accurate. A domain of applicability of the method proposed has been defined regarding both frequency/baseline relation and trajectory of the target. A Z-shape multistatic topology was suggested to extend applicability of the system for arbitrary target trajectories.

The profile reconstruction algorithm was tested for simulated signatures of targets within a cluttered environment. A vegetation model, [76, 78], was used to simulate signals with SCR between 3 and 24 dB, and the TSPR algorithm showed good stability over the range between 24 and 15 dB. In reality a SCR of between 20 and 40 dB is expected. Experimental confirmation of this finding should be part of future work regarding the TSPR algorithm.

CHAPTER 8

CONCLUSION AND FURTHER WORK

8.1 Conclusion

The aim of this thesis was to present and show first preliminary results of a method for cross-range target imaging in forward scatter radar. Due to the absence of range information in FSR currently used methods for improving the resolution of radar outputs are not applicable and as such automatic target classification algorithms based on target images cannot be used in FSR. The existing FSR imaging method was described and its shortcomings outlined in Chapter 5.

A novel method for target imaging was introduced in this thesis. The method, called target profile shadow reconstruction, is based on digital holographic image reconstruction, thus has a mathematically and computationally simpler form. Simulation results were shown for both 1D (azimuth) and 2D (azimuth and elevation) cases. The performance was compared with other FSR imaging methods which are published.

Preliminary experimental validation was performed with two radar systems, shown in Chapter 6. The results obtained show good correspondence with the targets observed.

Effects of the target structure and size were briefly analysed.

Initial analysis of the accuracy of the reconstructed images was performed, resulting in the definition of criteria for acceptable accuracy. The domain of applicability of the approach was done. The accuracy analysis performed includes two topics which can influence the results: errors in target trajectory estimations and vegetation clutter. The imaging method showed reasonable robustness to modelled vegetation clutter and less so for trajectory estimation errors. It was found that target speed miscalculation will result in the largest errors. Requirements for the system topology and the baseline/frequency combination are presented. To the best knowledge of the author such analysis has not been performed on FSR imaging methods before.

8.2 Summary

This thesis presents the PhD research done on a novel approach of SISAR imaging - target shadow profile reconstruction (TSPR).

Chapter 1 is mainly interested in the basics of radar systems operation and different types of radars. Also in this chapter derivations of the range and Doppler frequency resolution of monostatic and bistatic radar systems is presented, along with the radar equation for bistatic geometries. A literature survey of radar imaging, formulating the differences between RAR, SAR and ISAR was done.

Theoretical background of FSR is presented in chapter 2, including derivation of FSCS from physical optics for a stationary and moving targets, target Doppler signature formation, algorithms for extraction of target trajectory parameters. Lastly, PhD problem setting and aims, together with the thesis structure is discussed.

Chapter 3 concerns with the theory of diffraction and holography. Diffraction theories as derived from Huygens-Fresnel principle are presented and are used to show the relationship between FSCS and diffraction, together with the Babinet's principle. Further, the basics of holographic imaging is discussed in the context of in-line geometry. Digital in-line holography is presented and its main properties shown, as a prerequisite to the development of TSPR. Lastly, the application of holographic processing to radio waves is presented, giving examples of other uses of such technology in literature.

Chapter 4 is dedicated to the development of signal modelling on the basis of the theory of diffraction, specifically the Fresnel-Kirchhoff diffraction integral. Firstly, different signal models are shown starting from the model for a rectangular target, then examples of the SISAR modelling and, finally, a novel approach, based on the Fresnel-Kirchoff diffraction integral, for modelling of the signatures of complex shapes, together with examples of signatures modelled for different targets. Also, modelling of two dimensional target signatures is shown, together with examples for a square target and a car - Range Rover Sport.

The TSPR imaging algorithm is developed on the basis of holography in chapter 5. The approach is explained, together with the properties of reconstructed profiles, including:

- One-dimensionality;
- Geometrical properties.

Further in the section, a method of extraction of the mid-line of the profile, i.e. the real target profile, rather than the height-difference of the target shadow, is presented, together with examples for simulated signatures of a BMW 3 series for different height of Tx and Rx antennas. This method is only used for simulated signatures in this thesis.

A model for 2D reconstruction of the target image is presented, where the 2D images are reconstructed from a 2D target signature modelled by the previously mentioned algorithm.

Finally, chapter 5 is concluded by examples of both one- and two-dimensional target signature simulations and TSPR images for each case.

In chapter 6 the hardware used for experimental measurements is presented, including a 1.2 GHz single-node FSR system (BB) and the NI USRP-2950R. Measurement scenarios for electrically small targets are presented, measured with the BB hardware, showing the reduced accuracy of the TSPR algorithm for electrically small targets, which are close to the Rayleigh scattering regime. Target signatures were, also, recorded for car targets - BMW 3 series, Range Rover, Land Rover, Ford Fiesta and Smart Fortwo, using the BB 1.2 GHz hardware, showing good accuracy of the target profile reconstruction algorithm. A 2x2 multistatic system was tested with the BMW 3 series and Land Rover targets, using the NI USRP-2950R, showing that the TSPR algorithm accurately reconstructs the target's profile for crossing at 22 degrees, where the profiles take into account the difference in length and shape of the profiles, due to the different projection of the target's shadow at different angles.

Lastly, a brief explanation of an algorithm for the extraction of passive FSR signatures is presented, along with results for different non-cooperative and cooperative targets.

Chapter 7 concerns with the accuracy of the output of the TSPR algorithm. This chapter includes qualitative and quantitative measures of the accuracy of the target profile, including resolution and criteria of the accuracy of the reconstructed target profile. Resolution of 2D target images has been shown to correspond to the resolution of holograms, acquired by digital in-line holography, while the resolution of one-dimensional reconstructed target profiles have been shown to be dependent on the target speed and sampling frequency, i.e.

the length of the target signature in samples.

Several criteria of the accuracy of the reconstructed target profiles have been analysed, including fit parameter estimation between reconstructed profiles and target shadow and dynamic time warping. It is shown that the TSPR algorithm requires availability of 9 lobes of the target's FSCS in order to produce accurate results for simulated signatures and thus an appropriate frequency/baseline ratio must be present for each FSR system deployed, in order to generate accurate reconstructed target profiles for the expected targets.

Further in chapter 7, the dependence of the target profile on errors in the estimation of the target motion parameters - speed, crossing angle and crossing point, has been analysed. It has been shown that the method is reasonably stable over errors in crossing angle and crossing point, as long as the propagation kernel is not modelled for a target moving in the near-field of Tx or Rx of the FSR. It has been shown that the algorithm is stable over errors of the target speed less than 5%. After that, a quasi-auto-focusing method is presented on the basis of the geometric properties of the reconstructed target profiles and the results of the dependence of the reconstructed profiles on errors in the trajectory parameters.

Chapter 7, also, includes the dependence of the TSPR output on the trajectory of the target, where it has been shown that the TSPR algorithm can be applied with accurate results for targets moving at all angles and points with respect to the baseline, but generates an untrue output for targets moving at near-field of the Tx or Rx of the FSR system. Also, arbitrary (quasi-random) motion of targets, where the previous constraints were combined, is presented in this section. It was shown that the TSPR algorithm does not generate accurate results when targets are crossing at a trajectory which crosses the baseline at angles smaller than 60 degrees and away from its middle. Thus it was suggested that in practice FSR systems for surface targets must be multistatic and set-up in a zig-zag geometry. It was shown that targets which are accelerating their straight line speed and moving vertically do not influence the TSPR output, as long as the acceleration is detected and modelled or falls within the limit of 5% and the FSCS main lobe does fall on the Rx antenna.

Finally, the influence of presence of clutter on the reconstructed profiles is investigated. Target signatures were modelled for a range of SCR, ranging from 3 to 24 dB, and results indicate that the reconstructed profiles are accurate for SCR above 18 dB, which is reasonable for surface based FSR systems.

8.3 Further work

This thesis developed and investigated a novel approach for target imaging in FSR. As an initial step for further development of the TSPR model, the shortcomings of the theory presented have to be analysed. The signal modelling is developed on the basis of plane wave incidence and far-field operation, however in most of the ground based FSR cases that is not the case. The effect of these approximations on the phase of the FSR signal must be investigated.

The imaging method is not based on area of applicability, however the theoretical development, assumes that there is a plane wave incidence on the target. This can generate phase errors in the near-field regions and introduce significant errors in the reconstructed images. Also, edge diffraction is not taken into account.

The experimental results and the accuracy analysis performed revealed further topics for research in the areas of:

- Some of the results shown in chapter 6, show reconstructed target profiles which have high lobes in the regions just before and just after the target crossing. According to the author this is most likely due to bistatic scattering of the front and back of the targets which is received. The influence of these can be big for targets which are not flat on the front and back and thus scatter higher amplitude signals into the receiver, through the bistatic scattering. The main issue with such scatterings is that there is going to be a low-level and low-frequency Doppler phase content which will not be cancelled out by the FSR propagation kernel.
- Analysis of the clutter influence on the reconstruction accuracy was very limited and considered only modelled results based on an empirical model for vegetation clutter. Further analysis has to be made, with inluence on multipath and experimental validation of the modelled results. Also, this imaging method can be applied for other surface moving targets, thus sea clutter analysis must be performed, as well.
- The analysis of the domain of applicability and baseline/frequency restrictions was only done based on modelled signals, thus experimental test of the conclusions made has to be performed.

Section 6.2.4 shows initial results on the influence of target material structure on the TSPR results, based on a brief analysis of the results obtained for cars with open and closed windows. Further study has to be made regarding other possible influences on the reconstruction generated by complex targets with different material compositions.

It is suggested in literature that SISAR imaging can be performed with single channel FSR recorded signals, i.e. I or Q, through the use of a segmented Hilbert transform, which was not investigated during the PhD research, but is a main point of research for the future.

Finally, ATC algorithms, based on TSPR images, can be adopted to improve the results of already available classification methods.

APPENDIX A

CROSSING TIME ESTIMATION

The accurate modelling of the Doppler phase corresponding to the target's motion, requires the accurate knowledge of the crossing time of the target. This is the practice of target detection in FSR.

In FSR this is ultimately done via quasi-coherent processing (section 2.5.1), but another approach can be, also used.

This novel approach for detection of the target crossing time depends on the very usual for FSR signals 'v'-shape of their spectrogram, seen in fig. A.1 [29]. In practice the target crossing is going to happen at 0 Hz, where the maximum of FSCS is, and there is no Doppler or range resolution, as shown in section 1.2.2.

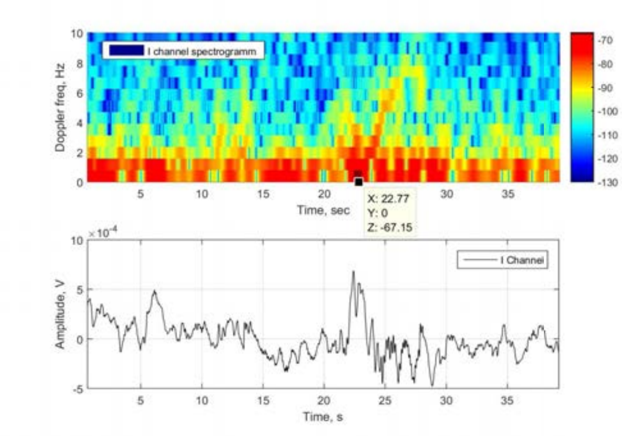

Figure A.1: A spectrogram and a time-domain signal of a RR target crossing the middle of the baseline perpendicularly at 3.6 mps. The maximum of the spectrogram is at 0 Hz and corresponds to the actual crossing of the target.

This 0 Hz point can be found by finding the local maximum on the 1st line of the matrix of values - corresponding to 0 Hz. This is where target signal is strongest and at 0 Hz.

It should be noted that in the presence of substantial amounts of clutter, the approach is not going to be useful, as there might be low-frequency peaks, higher than the targets main lobe, thus whitening filter must be applied before using this technique.

APPENDIX B

HARDWARE PROPERTIES

B.1 1.192 GHz single node FSR transceiver

A detailed schematics of the hardware can be seen in figure B.2, while a picture of the device can be seen in fig. B.1. There are two components that are not off-the shelf in the built, whose properties were measured via a VNA. The rest of the components can have their properties seen on the MiniCircuits webpage.

Figure B.1: Picture of the inside of the BB receiver.

Table B.1: Components of the BB hardware

Name	Type of component	Model
F1	BPF	built in-house
F2	BPF	VBFZ-1065-S
U4	LNA	ZX60-P162LN
U1	LNA	ZX60-1215-LN-S+
U2	Amp	ZX60-V82-S+
F3	BPF	built in-house, same as F1
F4	LPF	100 Hz 1 order built in-house
F5	LPF	100 Hz 1 order built in-house
U3	Amp	ZX60-V82-S+
OSC1	VCO	ZX95-1410-S

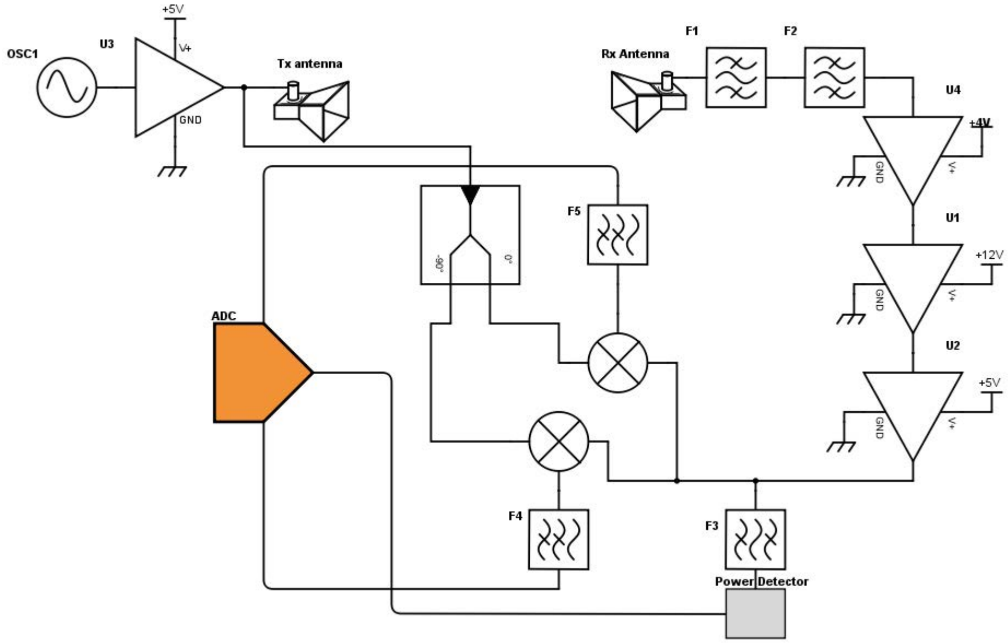

Figure B.2: Schematic of the BB transceiver. The properties of each of the elements is given in table B.1 below

The in-built BPF have been measured by a VNA and its properties can be seen in fig. B.3

and B.4. This BPF is fitted to reject the communication frequencies which would pass through VBFZ-1065-S filter.

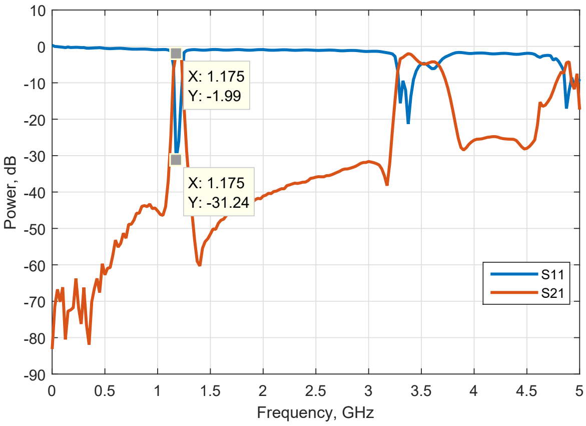

Figure B.3: A plot of measured S11 and S21 parameters of the in-house built band-pass filter

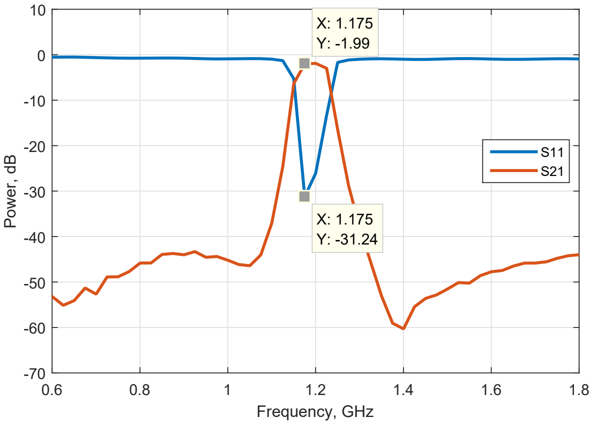

Figure B.4: A plot of measured S11 and S21 parameters of the in-house built band-pass filter, zoomed at 0.6 to 1.8 GHz range

The BB hardware was powered by a Tracer 12V 22Ah Lithium Polymer battery.

The power calibration curve of the RSSI channel of the BB can be seen in Fig. B.5, below.

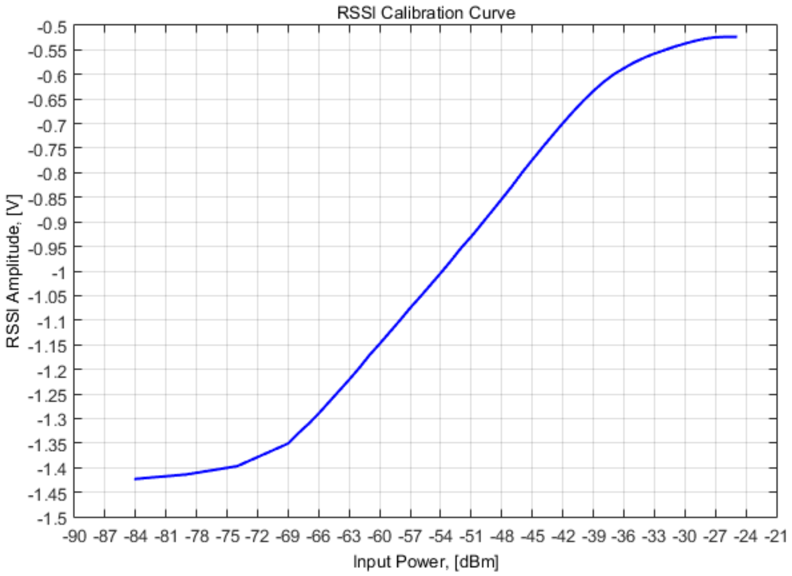

Figure B.5: CAlibration curve of the RSSI channel of the BB receiver

B.1.1 Power budget calculation

Short cables and connectors were used to connect all the components together, but their loss is not going to be accounted for in the estimations below. Their total loss is estimated to below 5 dB.

The transmit chain power is defined by the power of the ZX95-1410-S VCO, the ZX60-V82 amplifier and the loss due to the ZX10-2-12. Thus [79]:

$$P_{Tx} = 8.07 + 14.43 - 3.86 = 18.64 dBm. \tag{B.1}$$

The received chain has more components, table B.2 gives the power gain/loss of each of the components [79].

Then for the RSSI channel, the gain of the receive chain is going to be:

Component	Gain, dB
BPF	-2
VBFZ-1065-S	-1.8
ZX60-P162LN	21.12
ZX60-1215LN	14.45
ZX60-V82-S+	14.43
ZX10-2-25	-4
ZX05-5-S	-7
ZX10Q-2-12	-3.65

Table B.2: Gain figures for the components in the receiver chain of the BB transceiver

$$G_{RxRSSI} = -2 + -1.8 + 21.12 + 14.45 + 14.43 + -4 + -2 = 40.2dB, \tag{B.2}$$

while for the I/Q channels, up to the LPF:

$$G_{RxI/Q} = -2 + -1.8 + 21.12 + 14.45 + 14.43 + -4 + -4 + -7 = 31.2dB. \tag{B.3}$$

This would generate the following received signal levels at different baseline lengths, quoted in Fig. B.6. These show that the RSSI channel will be below the minimum signal level at the baselines at which the experiments were done (60 m). This is what has been observed, however since the research was not investigating the RSSI channel data, it was discarded.

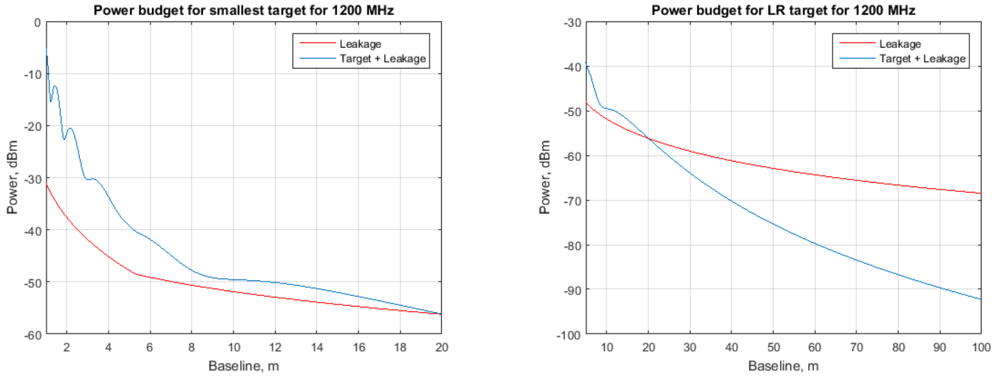

Figure B.6: Power budget calculations for both the smallest target used (the two rectangles of size 0.68 x 0.76 m) - (a) and a Range Rover of size 1.8 x 3.6 m - (b).

B.2 Patch antennas designed by Liam Daniel

Four identical patch antennas were designed by Liam Daniel and produced within the school's PCB facilities. The S11 parameters of all 4 antennas are shown in fig B.7, where in fig. B.8 the same plot is shown zoomed around the frequency of operation of the antennas - 1.17 GHz.

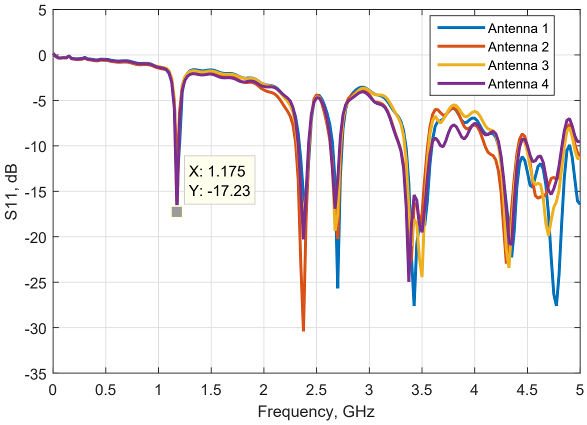

Figure B.7: Measured S11 for the 4 antennas for the band between 300 kHz and 5 GHz

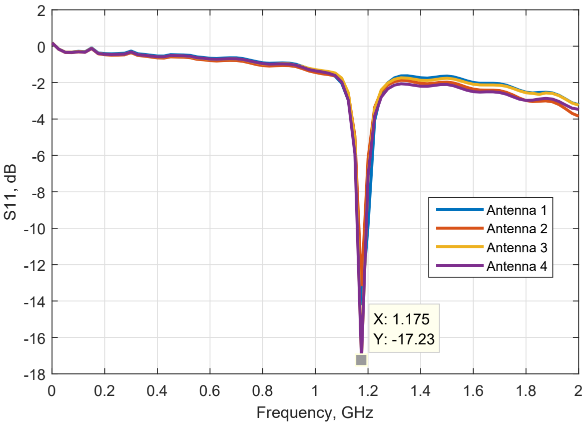

Figure B.8: Measured S11 for the 4 antennas, zoomed from fig. B.7

The antennas were also measured in an anechoic chamber, where a WBH1-18S was used as both a transmitting and a reference antenna. A simple figure of the measurement set-up is shown below.

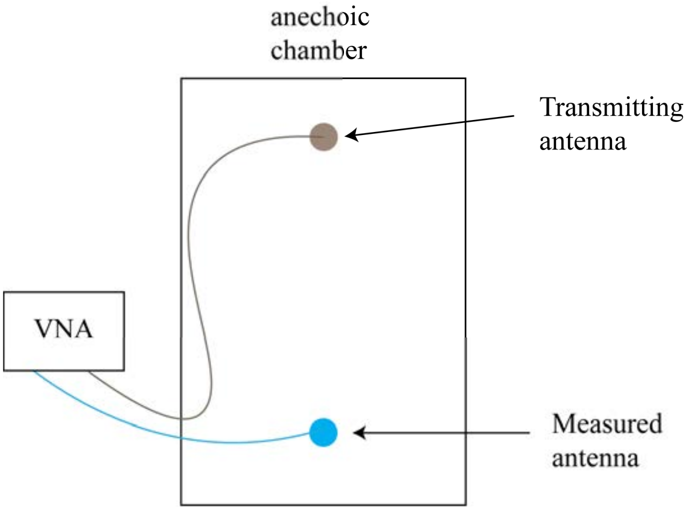

Figure B.9: A simple graphical presentation of the set-up used to measure antennas. The antenna under test is located on a rotating table

The results of the measurements are shown below, where they are normalized to the output of the WBH1-18S, which has around 1.5 dBi gain at 1.2 GHz.

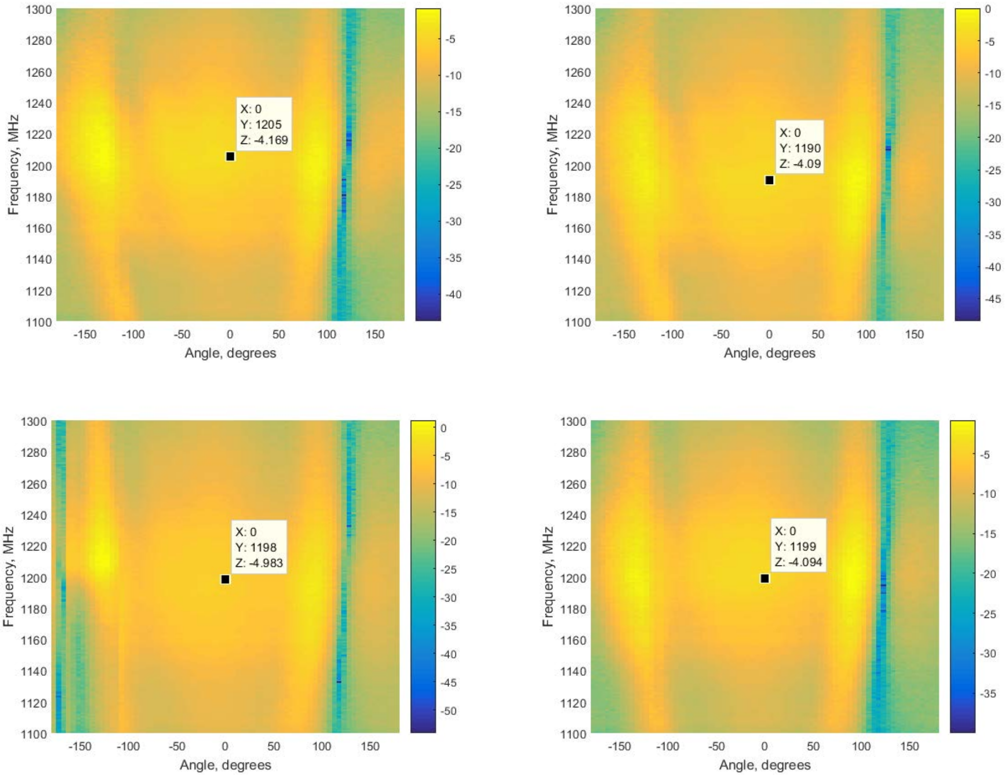

Figure B.10: Results of the measurement of the in-house made patch antennas (Antenna 1 - (a); 2 - (b); 3 - (c) and 4 - (d)). Received power is in dB and normalized to output of WBH1-18S.

As can be seen from Fig. B.10, the main lobe of the manufactured antennas is in the region of -2 to -3 dBi.

These antennas were used in the 2x2 multistatic measurements, described in sec 6.2.3.

B.3 Power Calibration of the USRP-2950R

Power calibration of the USRP over the whole frequency range was done as part of the initial study of the device. Due to the availability of two receiver ports on each of the RF daughterboards, multiple configurations were used. These can be seen in Fig. B.11, below.

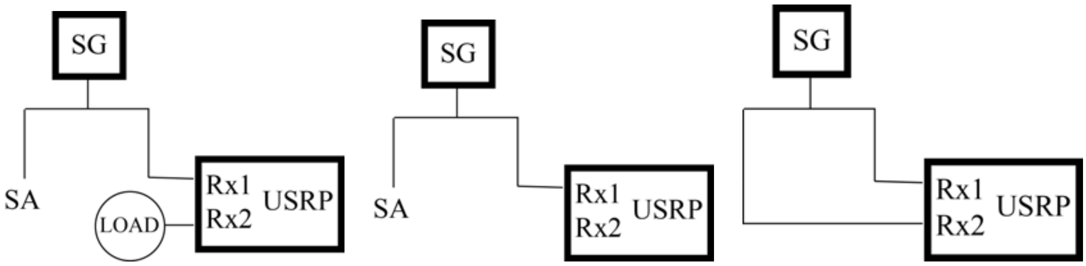

Figure B.11: Three configurations used for the power calibration of the USRP-2950R

Firstly, a matching 50 Ω load is used as the input to one of the channels (Fig. B.11(a)), then the input is left opened (Fig. B.11(b)). These were done for both Rx1 and Rx2. Finally, the input from the signal generator (SG) was connected to both inputs. It must be mentioned here that the measurements were matched to the reading of a Rohde & Schwarz FSH3 and Field Fox spectrum analyzers.

A MiniCircuits ZFSC-2-2500 power splitter was used to enable the simultaneous use of spectrum analyser and USRP. The splitter was checked on a VNA and was flat over all of the range of used frequencies (50-2200 MHz).

Each of the Rx channels on a single daughterboard was tested for received power for the range of operational frequencies (50-2200 MHz). Results indicate that the Rx1 channel is not calibrated to be used as receiver, as received power is significantly different than the Rx2 channel, see Fig. B.12. The results are normalized to FieldFox power readings.

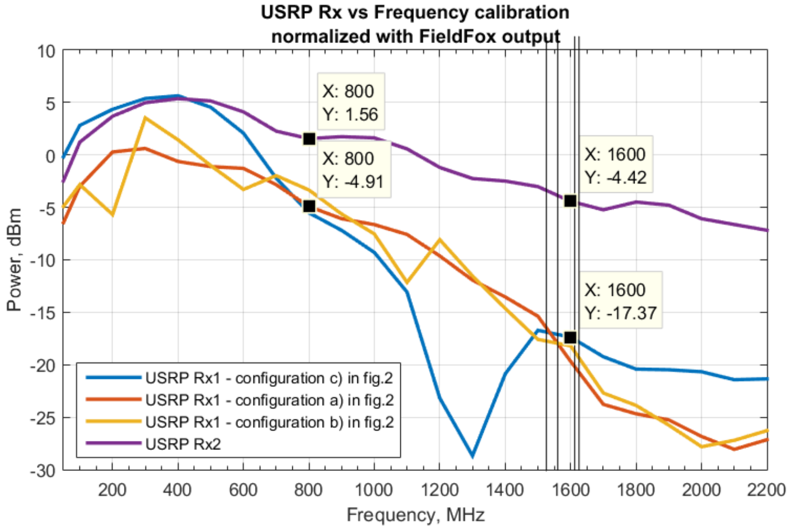

Figure B.12: USRP Rx power calibration versus frequency

Also, difference in the power level in Rx1 was noted when both Rx1 and Rx2 were connected to the output of the power splitter and signals were being transmitted from the signal generator. ALso, Rx1 was tested with a load connected to it, as well, with similar discrepancies between transmitted and received values. However, such differences were not observed in Rx2 channel in any of the configurations shown in Fig. B.11.

The gains of the LNAs in the receiver part of the USRP daughterboard were tested for their linearity over the operational frequency range. The gains used were 7 incremental steps of 5 dB from +0 to +30 dB. Results (Fig. B.13) indicate that the gain inside of the USRP is linear over the operational frequency range. It was observed that there is -1 dB total offset between +0 and +30 dB, i.e instead of +30 dB the power is amplified with 29 dB. This is over the whole range of frequencies. Same difference of received power was observed between Rx1 and Rx2.

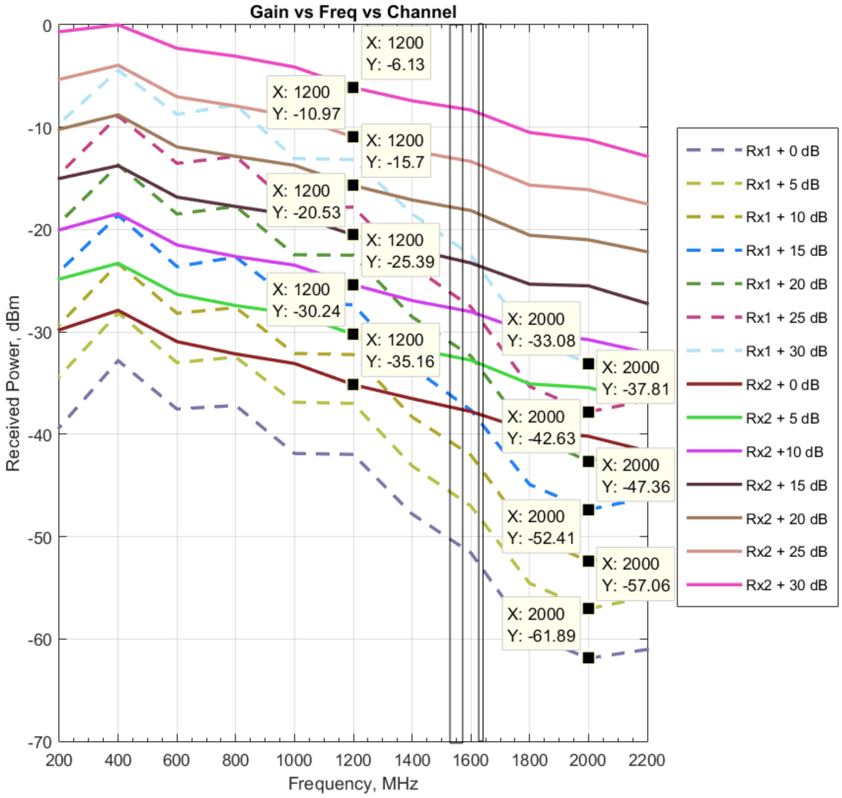

Figure B.13: USRP Rx LNA gain vs frequency

The above calibration was taken into account during all the measurements done. Only Rx 2 port was used as a receiver on each of the daughterboards.

APPENDIX C

PUBLICATIONS

The publications done by the author are as follows:

S. Hristov, L. Daniel, and M. Gashinova, Software defined radio for profile reconstruction in Forward Scatter Radar," in European Radar Conference (EuRAD), 2014 11th, Oct. 2014.

S. Hristov, L. Daniel, E. Hoare, M. Cherniakov, and M. Gashinova, Target shadow profile reconstruction in ground-based forward scatter radar," in Radar Conference (RadarCon), 2015 IEEE, May 2015

Second author of a number of papers connected to the work done for this PhD:

M. Ritchie et al., "Simultaneous data collection of small maritime targets using multistatic radar and forward scatter radar," in IET Radar, Sonar & Navigation, vol. 11, no. 6, pp. 937-945, 6 2017.

M. Contu et al., "Passive Multifrequency Forward-Scatter Radar Measurements of Airborne Targets Using Broadcasting Signals," in IEEE Transactions on Aerospace and Electronic Systems, vol. 53, no. 3, pp. 1067-1087, June 2017.

A. De Luca, M. Contu, S. Hristov, L. Daniel, M. Gashinova and M. Cherniakov, ”FSR velocity estimation using spectrogram,” 2016 17th International Radar Symposium (IRS), Krakow, 2016, pp. 1-5.

A number of papers based on the experimental results and accuracy analysis of the TSPR approach proposed by the author are in preparation.

REFERENCES

[1] V. Chapurskiy and V. Sablin, "SISAR: shadow inverse synthetic aperture radiolocation," in *Radar Conference, 2000. The Record of the IEEE 2000 International*, 2000, pp. 322 –328.

[2] P. Ufimtsev, "New Insight into the Classical Macdonald Physical Optics Approximation," *Antennas and Propagation Magazine, IEEE*, vol. 50, no. 3, pp. 11 –20, Jun. 2008.

[3] M. Gashinova, L. Daniel, V. Sizov, E. Hoare, and M. Cherniakov, "Phenomenology of Doppler forward scatter radar for surface targets observation," *IET Radar, Sonar and Navigation*, vol. 7, no. 4, pp. 422–432(10), Apr. 2013.

[4] L. Huang, X. Chen, H. Mhlenbernd, H. Zhang, S. Chen, B. Bai, Q. Tan, G. Jin, K.-W. Cheah, C.-W. Qiu, J. Li, T. Zentgraf, and S. Zhang, "Three-dimensional optical holography using a plasmonic metasurface," *Nature Communications*, vol. 4, 11 2013, "This work is partly supported by the Engineering and Physical Sciences Council of the United Kingdom under the scheme of NSF/EPSRC Materials Network.".

[5] C. Hu, X. Li, T. Long, and C. Zhou, "An accurate sisar imaging method of ground moving target in forward scatter radar," *Science China Information Sciences*, vol. 55, no. 10, pp. 2269–2280, 2012. [Online]. Available:

http://dx.doi.org/10.1007/s11432-012-4584-9

[6] M. Cherniakov, Ed., *Bistatic Radar: Principles and Practice.* Wiley, 2007.

[7] M. Richards, J. Scheer, J. Scheer, and W. Holm, *Principles of modern radar*, ser. Principles of Modern Radar. SciTech Publishing, Incorporated, 2010, no. v. 1. [Online]. Available: https://books.google.co.uk/books?id=nD7tGAAACAAJ

[8] M. Skolnik, *Radar Handbook, Third Edition*, ser. Electronics electrical engineering. McGraw-Hill Education, 2008. [Online]. Available: https://books.google.co.uk/books?id=76uF2Xebm-gC

[9] M. Richards, W. Melvin, W. Holm, and J. Scheer, *Principles of Modern Radar: Advanced Techniques*, ser. EBSCO ebook academic collection. Institution of Engineering and Technology, 2012. [Online]. Available: https://books.google.co.uk/books?id=G_O9GAAACAAJ

[10] M. Gashinova, L. Daniel, E. Hoare, V. Sizov, K. Kabakchiev, and M. Cherniakov, "Signal characterisation and processing in the forward scatter mode of bistatic passive coherent location systems," *EURASIP Journal on Advances in Signal Processing*, vol. 2013, no. 1, p. 36, 2013.

[11] A. Blyakhman, A. Myakinkov, and A. Ryndyk, "Tracking algorithm for three-dimensional bistatic forward scattering radar with weighting of primary measurements," in *Radar Conference, 2005. EURAD 2005. European*, Oct. 2005, pp. 153 –156.

[12] C. Hu, V. Sizov, M. Antoniou, M. Gashinova, and M. Cherniakov, "Optimal Signal Processing in Ground-Based Forward Scatter Micro Radars," *Aerospace and Electronic Systems, IEEE Transactions on*, vol. 48, no. 4, pp. 3006–3026, Oct. 2012.

[13] F. Kovalev, “Estimating the coordinates of a moving target from the Doppler data measured by forward-scatter radar systems,” *Journal of Communications Technology and Electronics*, vol. 52, no. 3, pp. 313–321, 2007.

[14] N. Willis, *Bistatic Radar*, ser. Electromagnetics and Radar. Institution of Engineering and Technology, 2005. [Online]. Available: https://books.google.co.uk/books?id=U0XG5WB-vY8C

[15] A. M. Kinghorn and A. Nejman, “Picosar- an advanced lightweight sar system,” in *Radar Conference, 2009. EuRAD 2009. European*, Sept 2009, pp. 168–171.

[16] G. Krieger, A. Moreira, H. Fiedler, I. Hajnsek, M. Werner, M. Younis, and M. Zink, “Tandem-x: A satellite formation for high-resolution sar interferometry,” *IEEE Transactions on Geoscience and Remote Sensing*, vol. 45, no. 11, pp. 3317–3341, Nov 2007.

[17] R. Sullivan, *Radar Foundations for Imaging and Advanced Concepts*, ser. Electromagnetics and Radar Series. Institution of Engineering and Technology, 2004. [Online]. Available: https://books.google.co.uk/books?id=cPpd96ttEFcC

[18] P. Y. Ufimtsev, *Fundamentals of the Physical Theory of Diffraction.* Wiley, 2007.

[19] A. Myakinkov, A. Kuzin, M. Gashinova, V. Sizov, and M. Cherniakov, “Inverse Forward Scatter SAR,” in *Proc. of 2010 Int. Conf. on Synthetic aperture sonar and radar*, Jun. 2010, pp. 1–5.

[20] V. Schejbal, O. Fiser, and J. Pidanic, “Comparisons of approximate and exact solutions for forward scattering,” in *Proceedings of the 5th European Conference on Antennas and Propagation (EUCAP)*, Apr. 2011, pp. 2318–2322.

[21] M. Born, E. Wolf, A. Bhatia, D. Gabor, A. Stokes, A. Taylor, P. Wayman, and W. Wilcock, *Principles of Optics: Electromagnetic Theory of Propagation, Interference and Diffraction of Light*. Cambridge University Press, 2000. [Online]. Available: http://books.google.co.uk/books?id=oV80AAAAIAAJ

[22] J. Glaser, “Bistatic RCS of Complex Objects near Forward Scatter,” *Aerospace and Electronic Systems, IEEE Transactions on*, vol. AES-21, no. 1, pp. 70 –78, Jan. 1985.

[23] M. Gashinova, K. K. L. Daniel, E. H. V. Sizov, and M. Cherniakov, “Phenomenology Of Signals In FSR For Surface Targets Detection,” in *Radar 2012*, 2012.

[24] C. Balanis, *ANTENNA THEORY: ANALYSIS AND DESIGN, 3RD ED (With CD)*. Wiley India Pvt. Limited, 2009. [Online]. Available: https://books.google.co.uk/books?id=ibDCbwAACAAJ

[25] S. Hristov, L. Daniel, E. Hoare, M. Cherniakov, and M. Gashinova, “Target shadow profile reconstruction in ground-based forward scatter radar,” in *Radar Conference (RadarCon), 2015 IEEE*, May 2015, pp. 0846–0851.

[26] M. Contu, D. Pastina, P. Lombardo, A. De Luca, M. Gashinova, L. Daniel, and M. Cherniakov, “Target motion estimation via multistatic Forward Scatter Radar,” in *Radar Symposium (IRS), 2015 16th International*. IEEE, 2015, pp. 616–621.

[27] R. Abdullah, M. Rasid, M. Azis, and M. Khalafalla, “Target prediction in Forward Scattering Radar,” in *Applied Electromagnetics, 2007. APACE 2007. Asia-Pacific Conference on*, Dec. 2007, pp. 1 –5.

[28] C. Hu, M. Antoniou, M. Cherniakov, and V. Sizov, “Quasi-optimal signal processing in ground forward scattering radar,” in *2008 IEEE Radar Conference*, May 2008, pp. 1–6.

[29] A. De Luca, M. Contu, S. Hristov, L. Daniel, M. Gashinova, and M. Cherniakov, "FSR velocity estimation using spectrogram," May 2016.

[30] J. Allen, "Short term spectral analysis, synthesis, and modification by discrete fourier transform," *IEEE Transactions on Acoustics, Speech, and Signal Processing*, vol. 25, no. 3, pp. 235–238, Jun 1977.

[31] M. Gashinova, L. Daniel, M. Cherniakov, P. Lombardo, D. Pastina, and A. De Luca, "Multistatic Forward Scatter Radar for accurate motion parameters estimation of low-observable targets," in *Radar Conference (Radar), 2014 International*, Oct. 2014, pp. 1–4.

[32] M. Gashinova, V. Sizov, N. A. Zakaria, and M. Cherniakov, "Signal detection in multi-frequency Forward Scatter Radar," in *Radar Conference (EuRAD), 2010 European*, 2010, pp. 276–279.

[33] C. Hu, C. Zhou, T. Zeng, and T. Long, "Radio holography signal reconstruction and shadow inverse synthetic aperture radar imaging in ground-based forward scatter radar: theory and experimental results," *Radar, Sonar Navigation, IET*, vol. 8, no. 8, pp. 907–916, Oct. 2014.

[34] C. Huygens, *Traité de la lumière: où sont expliquées les causes de ce qui luy arrive dans la reflexion, & dans la refraction, et particulierement dans l'etrange refraction du cistal d'Islande.* Chez Pierre vander Aa, 1690.

[35] M. Contu, A. D. Luca, S. Hristov, L. Daniel, A. Stove, M. Gashinova, M. Cherniakov, D. Pastina, P. Lombardo, A. Baruzzi, and D. Cristallini, "Passive multifrequency forward-scatter radar measurements of airborne targets using broadcasting signals," *IEEE Transactions on Aerospace and Electronic Systems*, vol. 53, no. 3, pp. 1067–

1087, June 2017.

[36] M. Schwartz, *Principles of Electrodynamics.* Courier Corporation, Apr. 2012.

[37] M. Ware and J. Peatross, *Physics of Light and Optics*, Feb 2015.

[38] H. A. Bethe, "Theory of diffraction by small holes," *Phys. Rev.*, vol. 66, pp. 163–182, Oct 1944.

[39] R. Longhurst, *Geometrical And Physical Optics.* Orient BlackSwan, 1986. [Online]. Available: https://books.google.co.uk/books?id=gpwmf3zufz4C

[40] J. C. Heurtley, "Scalar rayleigh-sommerfeld and kirchhoff diffraction integrals: A comparison of exact evaluations for axial points," *J. Opt. Soc. Am.*, vol. 63, no. 8, pp. 1003–1008, Aug 1973.

[41] G. D. Gillen and S. Guha, "Modeling and propagation of near-field diffraction patterns: A more complete approach," *American Journal of Physics*, vol. 72, no. 9, pp. 1195–1201, 2004.

[42] A. S. Marathay and J. F. McCalmont, "On the usual approximation used in the rayleigh–sommerfeld diffraction theory," *J. Opt. Soc. Am. A*, vol. 21, no. 4, pp. 510–516, Apr 2004.

[43] A. Babinet, 1837.

[44] R. Barth, "Digital in-line x-ray holographic microscopy with synchrotron radiation," Ph.D. dissertation, Combined Faculties for the Natural Sciences and for Mathematics of the Ruperto-Carola University of Heidelberg, 2008.

[45] M. Heydt, "Theory of Holography," in *How Do Spores Select Where to Settle?* Berlin, Heidelberg: Springer Berlin Heidelberg, 2011, pp. 5–11.

[46] P. Hariharan, *Basics of Holography.* Cambridge University Press, 2002.

[47] D. Gabor *et al.*, “A new microscopic principle,” *Nature*, vol. 161, no. 4098, pp. 777–778, 1948.

[48] J. Goodman, *Introduction to Fourier Optics*, ser. McGraw-Hill Series in Electrical and Computer Engineering: Communications and Signal Processing. McGraw-Hill, 1996.

[49] H. Kreuzer, “Holographic microscope and method of hologram reconstruction,” USA Patent US Patent 6,411,406, Jun 25, 2002, uS Patent 6,411,406.

[50] Q. Wu, F. Merchant, and K. Castleman, *Microscope Image Processing*, ser. Electronics & Electrical. Elsevier/Academic Press, 2008. [Online]. Available: https://books.google.co.uk/books?id=Z8P0nQEACAAJ

[51] G. Deschamps, “Some remarks on radio-frequency holography,” *Proceedings of the IEEE*, vol. 55, no. 4, pp. 570–571, April 1967.

[52] “MIT 3D optical systems group,” accessed: 16/06/16. [Online]. Available: http://web.mit.edu/optics/www/dhi.htm

[53] R. P. Dooley, “X-band holography,” *Proceedings of the IEEE*, vol. 53, no. 11, pp. 1733–1735, Nov 1965.

[54] Y. Aoki, “Microwave holograms and optical reconstruction,” *Appl. Opt.*, vol. 6, no. 11, pp. 1943–1946, Nov 1967. [Online]. Available: http://ao.osa.org/abstract.cfm?URI=ao-6-11-1943

[55] R. W. Larson, E. L. Johansen, and J. S. Zelenka, “Microwave holography,” *Proceedings of the IEEE*, vol. 57, no. 12, pp. 2162–2164, Dec 1969.

[56] D. E. Duffy, “Optical reconstruction from microwave holograms,” *J. Opt. Soc. Am.*, vol. 56, no. 6, pp. 832–832, Jun 1966. [Online]. Available: http://www.osapublishing.org/abstract.cfm?URI=josa-56-6-832

[57] E. N. Leith and J. Upatnieks, “Reconstructed wavefronts and communication theory∗,” *J. Opt. Soc. Am.*, vol. 52, no. 10, pp. 1123–1130, Oct 1962. [Online]. Available: http://www.osapublishing.org/abstract.cfm?URI=josa-52-10-1123

[58] R. W. Larson, J. S. Zelenka, and E. L. Johansen, “A microwave hologram radar system,” *IEEE Transactions on Aerospace and Electronic Systems*, vol. AES-8, no. 2, pp. 208–217, March 1972.

[59] L. X. Liang, H. Cheng, Z. Yu, L. Teng, and M. Cong, “The imaging research of the ground moving targets in forward scattering radar,” in *Signal Processing (ICSP), 2010 IEEE 10th International Conference on*, Oct. 2010, pp. 2019 –2022.

[60] A. Ludwig, “Computation of radiation patterns involving numerical double integration,” *IEEE Transactions on Antennas and Propagation*, vol. 16, no. 6, pp. 767–769, Nov 1968.

[61] V. Sizov, M. Cherniakov, and M. Antoniou, “Forward scattering radar power budget analysis for ground targets,” *Radar, Sonar Navigation, IET*, vol. 1, no. 6, pp. 437–446, 2007.

[62] M. Cherniakov, M. Salous, V. Kostylev, and R. Abdullah, “Analysis of forward scattering radar for ground target detection,” in *Radar Conference, 2005. EURAD 2005. European*, Oct. 2005, pp. 145–148.

[63] M. Cherniakov, R. S. A. R. Abdullah, P. Jancovic, M. Salous, and V. Chapursky, “Automatic ground target classification using forward scattering radar,” *Radar,*

Sonar and Navigation, IEE Proceedings, vol. 153, no. 5, pp. 427–437, 2006.

[64] Z. Chao, Z. Canyan, H. Cheng, and Z. Tao, “Accuracy analysis of sisar imaging algorithm in forward scatter radar,” in *Wireless Communications Signal Processing (WCSP), 2012 International Conference on*, Oct 2012, pp. 1–4.

[65] H. Cheng, Z. Chao, Z. Canyan, L. Haibo, and Z. Tao, “Forward scatter radar sisar imaging: Theory and primary experimental results analysis,” in *Radar Symposium (IRS), 2013 14th International*, vol. 2, June 2013, pp. 643–648.

[66] “Q-par miniature single polarization 1-18 ghz horn antenna manual,” accessed: 03/12/15. [Online]. Available: http://intermera.ru/files/docs/WBH1-18_Datasheetnew1_web.pdf

[67] S. Hristov, L. Daniel, and M. Gashinova, “Software defined radio for profile reconstruction in Forward Scatter Radar,” in *European Radar Conference (EuRAD), 2014 11th*, Oct. 2014, pp. 573–576.

[68] “Ettus research technical documentation website,” accessed: 03/10/13. [Online]. Available: http://code.ettus.com/redmine/ettus/projects/public/documents

[69] L. Blake, *Antennas*, ser. Wiley series in electronic engineering technology. Wiley, 1966. [Online]. Available: https://books.google.co.uk/books?id=KCRTAAAAMAAJ

[70] I. L. Dryden and K. V. Mardia, *Statistical shape analysis.* Wiley Chichester, 1998, vol. 4.

[71] H. Sakoe and S. Chiba, “Dynamic programming algorithm optimization for spoken word recognition,” *Acoustics, Speech and Signal Processing, IEEE Transactions on*, vol. 26, no. 1, pp. 43–49, Feb 1978.

[72] Y. Luo, D.-l. Hu, B.-f. Luo, and Q. Zhang, “Motion compensation for SISAR based on contrast maximization,” in *Synthetic Aperture Radar, 2007. APSAR 2007. 1st Asian and Pacific Conference on*, Nov. 2007, pp. 431 –434.

[73] K. Kabakchiev, L. Daniel, E. Hoare, M. Gashinova, and M. Cherniakov, “Near zero grazing angle forward-scatter sea clutter measurement statistical properties,” in *Radar Symposium (IRS), 2013 14th International*, vol. 2, Jun. 2013, pp. 620–624.

[74] K. Kabakchiev, L. Daniel, M. Gashinova, E. Hoare, M. Cherniakov, and V. Sizov, “Radar parameters influence on the clutter in maritime forward scatter radar,” in *2014 11th European Radar Conference*, Oct 2014, pp. 113–116.

[75] N. Rashid, P. Jancovic, M. Gashinova, M. Cherniakov, and V. Sizov, “The effect of clutter on the automatic target classification accuracy in FSR,” in *Radar Conference, 2010 IEEE*, May 2010, pp. 596–602.

[76] V. Sizov, C. Hu, M. Antoniou, and M. Cherniakov, “Vegetation clutter spectral properties in VHF/UHF bistatic doppler radar,” in *Proc. of the 2008 IEEE Radar Conference*, 2008, pp. 26–30. [Online]. Available: http://www.researchgate.net/profile/Vladimir_Sizov3/publication/224385077_Vegetation_clutter_spectral_properties_in_VHFUHF_bistatic_doppler_radar/links/541ff56a0cf2218008d42572.pdf

[77] M. Gashinova, K. Kabakchiev, L. Daniel, E. Hoare, V. Sizov, and M. Cherniakov, “Measured forward-scatter sea clutter at near-zero grazing angle: analysis of spectral and statistical properties,” *Radar, Sonar Navigation, IET*, vol. 8, no. 2, pp. 132–141, February 2014.

[78] M. Gashinova, M. Cherniakov, N. A. Zakaria, and V. Sizov, “Empirical model of vegetation clutter in forward scatter radar micro-sensors,” in *Radar Conference, 2010*

IEEE, 2010, pp. 899–904.

[79] "Minicircuits website," http://194.75.38.69/homepage/homepage.html, accessed: 03/12/2015.